Ultrashort Fiber Laser Platform for Seeding of 1-um Laser Amplifier Systems

Dissertation
zur Erlangung des Doktorgrades
an der Fakultät für Mathematik, Informatik und Naturwissenschaften
Fachbereich Physik
der Universität Hamburg

vorgelegt von

Yi Hua

Hamburg

07.2020

Eidesstattliche Versicherung / Declaration on oath

Hiermit versichere ich an Eides statt, die vorliegende Dissertationsschrift selbst verfasst und keine anderen als die angegebenen Hilfsmittel und Quellen benutzt zu haben.

Die eingereichte schriftliche Fassung entspricht der auf dem elektronischen Speichermedium.

Die Dissertation wurde in der vorgelegten oder einer ähnlichen Form nicht schon einmal in einem früheren Promotionsverfahren angenommen oder als ungenügend beurteilt.

Hamburg, den 24.07.2020

_____
Unterschrift der Doktorandin / des Doktoranden

Abstract

Diode-pumped Ytterbium-doped (Yb-doped) amplifier systems at 1-µm wavelength supporting high-energy pulses at high average power are becoming the workhorses for ultrafast science, including soft X-ray generation [1], optical parametric chirped-pulse amplifier pumping [2], terahertz radiation generation and amplification as well as high-brightness photo-injectors for laser-wakefield acceleration or free-electron lasers [3]. Room temperature (RT) Yb: ytterbium aluminum garnet (Yb: YAG) laser systems are commonplace for producing high average power and high energy sub-ps optical pulses due to their quantum-limited emission efficiency, superior thermo-mechanical properties, and broadband emission spectrum [4], [5]. The long fluorescence lifetime and large emission cross-section of Yb: YAG enable a significant over-all gain [6]. At cryogenic temperature, Yb: yttrium lithium fluoride (Yb: YLF) shows its advantages regarding the average power scalability due to the transition from a quasi-three-level to a four-level laser system, and also significant improvements of thermos-optical material properties. It supports sub-ps pulse amplification due to its several-nanometers flat gain bandwidth [7], [8].

To operate an Yb-doped solid-state laser amplifier system reliably and efficiently, a suitable seed laser operating at 1-µm central wavelength is essential. A Ti: sapphire laser can be used as the seeder for its broadband emission bandwidth covering the 1-µm spectral slot [9]. However, spectral filtering the 1-µm signal from its broadband output leads to pulses with low energy and low efficiency. Building an ultrafast seeding source based on Yb-doped crystals would be expensive and hard to maintain [10]. Therefore, a fiber-based seed source at 1-µm is desired for its low-cost and reliability, incorporating the advantage of a small footprint and alignment-free, turn-key operation [11]. In this thesis we investigate and expand the parameter space of the ultrafast Yb-based fiber laser system for the purpose of seeding Yb-doped solid-state laser. The output parameters of the fiber laser system in terms of pulse energy, spectral center wavelength, laser stability and noise performance are customized to match the solid-state laser material. Four essential elements are investigated through this thesis, including an all-polarization maintaining fiber oscillator, nonlinear wavelength conversion methods and its noise characteristics, the linear/ nonlinear amplification of short wavelength ultrafast pulses, and the design of low noise front-end laser system. We achieved an ultrashort fiber laser platform with the merit of alignment-free, turn-key operation, and high stability. As a seed source at 1 µm, it offers a tunable output signal for different types of Yb-based solid-state amplifier systems.

Zusammenfassung

Dioden-gepumpte, Ytterbium-dotierte optische Laserverstärker, die hoch energetische Pulse bei gleichzeitig hoher mittlerer Leistung in einem Wellenlängenbereich von 1 µm generieren können, werden heute in vielen Bereichen eingesetzt, wie z.B. bei der Röntgenstrahl erzeugung, beim pumpen von optischen parameterischen Verstärkern (OP(CP)A) Systemen, Erzeugung und Verstärkung von Terahertzstrahlung sowie bei Photoinjektoren in Freien-Elektronen-Lasern. Bei Raumtemperatur betriebene Yttrium-Aluminium-Granulat (Yb:YAG) Laser sind durch ihre quantenlimitierte Emissionseffizienz, guten thermo-mechanischen Eigenschaften und dem breitbandigen Emissionsspektrum zum Standard geworden, wenn Pulse im sub-ps Bereich erzeugt werden sollen. Die lange Lebensdauer und der große Emissionswirkungsquerschnitt ermöglichen eine signifikant höhere Verstärkung. Auf kryogene Temperatur (~80K) gekühlt, zeigt Yb: Yttrium Lithium Flourid (Yb:YLF) eine Änderung vom Quasi-Drei-Niveausystem zum Vier-Niveausystem und eine damit einhergehende Verbesserung der thermo-optischen Eigenschaften, welche Vorteile bei der Skalierbarkeit der mittleren Leistung und der Verstärkung von sub-ps Pulsen mit sich bringt.

Um einen Yb-dotierten Festkörperlaser effizient und zuverlässig betreiben zu können, ist ein Seedlaser mit einer zentralen Wellenlänge von 1µm erforderlich. Zu diesem Zweck könnte ein Titan-Saphire Laser mit dessen breitbandigem Emissionsspektrum im 1µm Bereich verwendet werden, jedoch würde dies eine spektrale Filterung notwendig machen und damit die Ausgangsenergie und Effizienz deutlich reduzieren. Eine weitere Option wäre die Konstruktion einer auf Ytterbium Kristallen basierenden ultraschnellen Seedquelle, welche allerdings teuer und schwer zu warten ist. Die Lösung bieten faserbasierende Seedlaser, die geringe Kosten und hohe Zuverlässigkeit bei gleichzeitig kleiner Größe und einfacher Bedienung ermöglichen. Das Thema dieser Dissertation beinhaltet die Entwicklung von ultraschnellen Yb-basierten Faserlasern deren parameter auf Yb-basierte Hochleistungs-Festkörperlaser angepasst sind, wie etwa die Pulsenergie, zentrale Wellenlänge, Stabilität und Rauscheigenschaften. In der Arbeit werden grundsätzlich vier fundamentale Bereiche untersucht: der polarisationserhaltende Faseroszillator , die nicht-lineare Umwandlung von Wellenlängen, die lineare und nicht-lineare Verstärkung von kurzwelligen, ultraschnellen Pulsen und das Design eines rauscharmen front-end Lasersystems. Es wurde ein ultraschneller, leicht bedienbarer Faserlaser mit hoher Stabilität und veränderbaren Parametern zum Seeden von verschiedenen, auf Yb-Kristallen basierenden, Festkörperverstärker eltentwicket.

Acknowledgement

I want to thank my supervisor Professor Franz X. Kärtner, for supporting me during my Ph.D. time. The discussion with Prof. Kärtner is always so helpful and enlightens me to think differently. I am impressed by his tremendous amount of knowledge and enthusiasm for research. I appreciate that Prof. Kärtner gave me this chance to have such an enjoyable experience in my life working and researching in the high-tech lab with a bunch of talented people.

I want to thank my supervisor Dr. Guoqing Chang for his help and support. He is one of the best teachers based on my memory. He is very knowledgeable and also has his way of explaining everything clearly and insightfully. I can remember those days that he distributed papers and books on our desks. I learn so many things from him, not only the knowledge but also his research and teaching habits.

I want to thank Dr. Michael Hemmer, who is a lovely and energetic officemate. The talking with him is always so joyful and inspiring. He has his ability to see the good side of things and people. Even though he is quite busy with laser building, he never feels tried to help others and answer questions. Apart from being an enjoyable person, he is also a gifted and hard-working scientist, who I want to keep up with.

I want to thank Dr. Mikhail Pergament for his effort to team up the laser group. I worked in his subgroup for one year and already felt the changing of surroundings. In this subgroup, everyone helps each other and celebrate each one's achievement. As a very busy man, Mikhail never fails to handle things successfully. I appreciate his caring and enthusiasm to solve every problem.

During my Ph.D. years, I receive a lot of help from my friends, who company me both in good time and bad time. Yizhou is my officemate; he is very kindhearted to listen to people and help others. I am always impressed by how he achieved these years. His willful to handle different and challenging tasks influence me a lot. Qian, Yudong, and Yunyun are my ski and Texas poker buddies, with who I spent a lot of casual time. They never failed to give me a hand when I fell. For the last year, Marvin joined our group as a bachelor student. I am so impressed by his talent and his hard-working when I was his supervisor. I learn a lot from him as well while working and discussing with him.

Finally, I want to thank my family for their endless love. They make me know that there is always a beautiful place where I can rest and put back myself.

Table of Contents

Table of contents

List of Publications

PUBLICATIONS IN REFEREED JOURNALS

[1]. **Y. Hua**, Y. Z. Liu, U. Demirbas, M. Pergament, F. X. Kärtner, "Tunable ultrafast Yb-fiber laser for efficient seeding of cryogenic Yb:YLF amplifiers," Manuscript in preparation.

[2]. **Y. Hua**, G. Zhou, W. Liu, M. Xin, F. Kärtner, and G. Chang, "Femtosecond two-color source synchronized at 100-as-precision based on SPM-enabled spectral selection," Opt. Lett., May 2020, doi: 10.1364/OL.391161.

[3]. **Y. Hua**, W. Liu, M. Hemmer, L. E. Zapata, G. Zhou, D. N. Schimpf, T. Eidam, J. Limpert, A. Tünnermann, and F. X. Kärtner, "87-W 1018-nm Yb-fiber ultrafast seeding source for cryogenic Yb: yttrium lithium fluoride amplifier," Optics letters, vol. 43, no. 8, pp. 1686–1689, 2018.

[4]. **Y. Hua**, G. Chang, F. X. Kärtner, and D. N. Schimpf, "Pre-chirp managed, core-pumped nonlinear PM fiber amplifier delivering sub-100-fs and high energy (10 nJ) pulses with low noise," Optics express, vol. 26, no. 5, pp. 6427–6438, 2018.

[5]. G. Cirmi, H. Çankaya, P. Krogen, A.-L. Calendron, **Y. Hua**, B. Debord, F. Gérôme, F. Benabid, and F. X. Kärtner, "Novel method for the angular chirp compensation of passively CEP-stable few-cycle pulses," Opt. Express, vol. 28, no. 3, p. 3171, Feb. 2020.

[6]. U. Demirbas, H. Cankaya, **Y. Hua**, J. Thesinga, M. Pergament, and F. X. Kärtner, "20-mJ, sub-ps pulses at up to 70 W average power from a cryogenic Yb: YLF regenerative amplifier," Optics Express, vol. 28, no. 2, pp. 2466–2479, 2020.

[7]. H. Cankaya, U. Demirbas, **Y. Hua**, M. Hemmer, L. E. Zapata, M. Pergament, and F. X. Kärtner, "190-mJ cryogenically-cooled Yb: YLF amplifier system at 1019.7 nm," OSA continuum, vol. 2, no. 12, pp. 3547–3553, 2019.

[8]. D. Zhang, A. Fallahi, M. Hemmer, H. Ye, M. Fakhari, **Y. Hua**, H. Cankaya, A.-L. Calendron, L. E. Zapata, N. H. Matlis, et al, "Femtosecond phase control in high-field terahertz-driven ultrafast electron sources," Optica, vol. 6, no. 7, pp. 872–877, 2019.

[9]. D. N. Schimpf, H. T. Olgun, A. Kalaydzhyan, **Y. Hua**, N. H. Matlis, and F. X. Kärtner, "Frequency-comb-based laser system producing stable optical beat pulses with picosecond durations suitable for high-precision multi-cycle terahertz-wave generation and rapid detection," Optics express, vol. 27, no. 8, pp. 11037–11056, 2019.

[10]. D. Zhang, A. Fallahi, M. Hemmer, X. Wu, M. Fakhari, **Y. Hua**, H. Cankaya, A.-L. Calendron, L. E. Zapata, N. H. Matlis, et al, "Segmented terahertz electron accelerator and manipulator (STEAM)," Nature photonics, vol. 12, no. 6, pp. 336–342, 2018.

[11]. A.-L. Calendron, J. Meier, M. Hemmer, L. E. Zapata, F. Reichert, H. Cankaya, D. N. Schimpf, **Y. Hua**, G. Chang, A. Kalaydzhyan, et al, "Laser system design for table-top X-ray light source," High power laser science and engineering, vol. 6, 2018.

[12]. F. X. Kärtner, F. Ahr, A.-L. Calendron, H. Çankaya, S. Carbajo, G. Chang, G. Cirmi, K. Dörner, U. Dorda, A. Fallahi, et al, "AXSIS: Exploring the frontiers in attosecond X-ray science, imaging and spectroscopy," Nuclear Instruments and Methods in Physics Research Section A: Accelerators, Spectrometers, Detectors and Associated Equipment, vol. 829, pp. 24–29, 2016.

PROCEEDINGS OF REFEREED CONFERENCES

[1]. F. X. Kärtner, D. Zhang, M. Fakhari, **Y. Hua**, H. Cankaya, A.-L. Calendron, L. Zapata, and N. H. Matlis, "Terahertz Acceleration," in International Photonics and OptoElectronics Meeting 2019 (OFDA, OEDI, ISST, PE, LST, TSA) (2019), paper TW5B.1, Nov. 2019, p. TW5B.1.

[2]. **Y. Hua**, Y. Liu, U. Demirbas, M. Pergamenta, F. X. Kärtnera, "Tunable ultrafast Yb-fiber laser for efficient seeding of cryogenic Yb:YLF amplifiers." In Ultrafast Optics XII 2019.

[3]. G. Cirmi, H. Çankaya, P. Krogen, A.-L. Calendron, **Y. Hua**, B. Debord, F. Gérôme, F. Benabid, and F. X. Kärtner, "Novel method for CEP-stable seeding of few-cycle OPCPAs," in Advanced Solid State Lasers, 2019, pp. AM2A–3.

[4]. M. Hemmer, H. Olgun, U. Demirbas, **Y. Hua**, A.-L. Calendron, H. Çankaya, and F. X. Kärtner, "Efficient Extraction From a Multi-Pass Yb:YAG Amplifier Via Multi-Pulse Amplification," in 2019 Conference on Lasers and Electro-Optics Europe and European Quantum Electronics Conference (2019), paper ca_9_1, Jun. 2019, p. ca_9_1.

[5]. H. T. Olgun, W. Tian, D. N. Schimpf, **Y. Hua**, A. Kalaydzhyan, N. H. Matlis, and F. X. Kärtner, "Efficient multicycle THz generation using a dedicated frequency-comb laser," in Conference on Lasers and Electro-Optics (2019), paper JTu2A.105, May 2019, p. JTu2A.105.

[6]. D. Zhang, A. Fallahi, M. Hemmer, X. Wu, M. Fakhari, **Y. Hua**, H. Cankaya, A.-L. Calendron, L. E. Zapata, N. H. Matlis, and F. X. Kärtner, "Segmented Terahertz driven device for ultrashort electron acceleration, compression, focusing and streaking," in Conference on Lasers and Electro-Optics, San Jose, California, 2018, p. SM4A.4.

[7]. F. X. Kärtner, D. Zhang, A. Fallahi, M. Hemmer, M. Fakhari, **Y. Hua**, H. Cankaya, A.-L. Calendron, L. E. Zapata, and N. H. Matlis, "Compact THz Accelerators: From Fiction to Reality," in 2018 43rd International Conference on Infrared, Millimeter, and Terahertz Waves (IRMMW-THz), Sep. 2018, pp. 1–3.

[8]. **Y. Hua**, G. Zhou, W. Liu, M. Xin, F. X. Kärtner, and G. Chang, "100-as-level synchronized two-color source based on SPM-enabled spectral selection," in CLEO Pacific Rim Conference 2018 (2018), paper Tu3B.2, Jul. 2018, p. Tu3B.2.

[9]. **Y. Hua**, G. Zhou, W. Liu, F. X. Kärtner, and G. Chang, "Tightly synchronized two-color femtosecond source based on low-noise SPM-enabled spectral selection," in CLEO: QELS_Fundamental Science, 2018, pp. JTh2A–162.

[10]. M. Hemmer, L. E. Zapata, **Y. Hua**, and F. X. Kärtner, "Addressing spectral narrowing in cryogenic Yb: YAG: a 10 mJ cryogenic Yb: YLF regenerative amplifier," in Advanced Solid State Lasers, 2016, pp. ATh4A–3.

[11]. **Y. Hua**, W. Liu, M. Hemmer, L. E. Zapata, G. Zhou, D. N. Schimpf, T. Eidam, J. Limpert, A. Tünnermann, and F. X. Kärtner, "87-W, 1018-nm Yb-fiber ultrafast seeding source for cryogenic Yb: YLF amplifier," in CLEO: Science and Innovations, 2016, pp. SM4Q–5.

List of figures

List of Figures

List of figures

List of figures

CHAPTER 5

List of Tables

List of Abbreviations

AC	Autocorrelation
AMP	Amplifier
AOFS	Acousto-optic frequency shifter
AOM	Acousto-optic modulator
ASE	Amplified spontaneous emission
BBO	Beta barium borate
BPD	Balanced photodetector
BOC	Balanced optical cross-correlator
BPF	Bandpass filter
CEP	Carrier-envelope phase
CPA	Chirped-pulse amplification
CW	Clockwise
CCW	Counter-clockwise
CFBG	Chirped fiber Bragg grating
DE	Delay element
DM	Dichroic mirror
DS	Dissipative soliton
DSR	Dissipative-soliton-resonance
DMS	Dispersion-management-soliton
FWHM	Full width at half maximum
FBG	Fiber Bragg-Grating
GD	Group delay
GDD	Group delay dispersion
HWP	Half-wave plate
HOM	High-order mode
MOPA	Master-oscillator-power-amplifier
NPR	Nonlinear polarization rotation
NOLM	Nonlinear optical loop mirror
NALM	Nonlinear amplifying loop mirror
OPO	Optical parametric oscillator

List of abbreviations

PBS	Polarizing beam splitter
PB	Phase bias
PM	Polarization-maintaining
PMF	Polarization maintaining fiber
PI	Proportional-integral
PCMA	Pre-chirp managed amplification
PCF	Photonic crystal fiber
PZT	Piezoelectric transducer
QWP	Quarter-wave plate
RS	Raman soliton
RT	Room temperature
RIN	Relative intensity noise
RTJ	Relative timing jitter
RMS	Root-mean-square
SSFS	Soliton self-frequency shift
SESS	SPM-enabled spectral selection
SPM	Self-phase modulation
TOD	Third-order dispersion
VCO	Voltage-controlled oscillator
WDM	Wavelength-division multiplexer
SM	Single mode
TL	Transform-limited
YB	Ytterbium
YDF	Ytterbium doped fiber
YLF	Yttrium lithium fluoride
YAG	Yttrium aluminum garnet

Chapter 1

Introduction

1.1 High power Yb-doped amplifier system

High-energy, high-peak-power pulses at 1-µm wavelength delivered from Ytterbium-doped (Yb-doped) amplifier systems are desired in many applications, including optical parametric chirped-pulse amplifier pumping [2], terahertz radiation generation and amplification [12] as well as free-electron lasers [3]. These amplifier systems include a wide variety of Yb-doped crystals, such as Yb: yttrium-aluminum (Yb: YAG) [13], Yb: KY(WO4)2 (Yb: KYW) [14] and Yb: yttrium lithium fluoride (Yb: YLF) [9]. The simple electronic structure of Yb^{3+} ion prevents laser losses due to up-conversion, concentration quenching, and excited-state absorption. The small quantum defect enhances the overall laser efficiency and reduces the thermal load [6]. Different Yb-doped gain materials feature a unique emission cross-section and laser saturation intensity, which depend on the local crystal fields surrounding the Yb^{3+} ion in the host lattice.

Room temperature (RT) Yb: YAG laser systems are becoming commonplace for producing high average power and high energy sub-ps optical pulses due to their quantum-limited emission efficiency, superior thermo-mechanical properties, and broadband emission spectrum. The long fluorescence lifetime and large emission cross-section of Yb: YAG enable a significant over-all gain [15]. The cryogenically cooling Yb: YAG solid-state amplifier can further scale up the average power due to the several advantages, such as the transition from a quasi-three-level to a four-level laser system, significant improvement of thermos-optic material properties, and a larger emission cross-section. However, the drawback of cooling Yb: YAG to liquid nitrogen temperature is a reduced emission bandwidth (from 8 nm to 1.5 nm) that cannot support sub-ps pulses operation anymore [15].

Cryogenically cooled Yb: yttrium lithium fluoride (Yb: YLF) has a gain bandwidth of several nanometers centered at 1018 nm or 995 nm, depending on the crystal orientation [15]. Besides, its gain profile has a flat shape, which can minimize the gain narrowing effect during amplification [16]. A considerable improvement in the thermos-optic properties of YLF at cryogenic temperatures and its weak and negative thermal lensing help to achieve high beam quality even in high-average power operation. Together with a longer excited-state lifetime, and a smaller quantum defect than Yb: YAG, cryogenically cooled Yb: YLF has the potential for realizing sub-ps laser sources featuring both high pulse energy and

high average power [17], [18]. The larger gain bandwidth of cryogenically cooled Yb: YLF is also advantageous for applying the chirped-pulse amplification (CPA) technique [11]. The summary of laser spectroscopic parameters for RT Yb: YAG, Cryo Yb: YAG, and Cryo Yb: YLF are listed in Table 1.1.

To operate an Yb-doped solid-state laser amplifier system reliably and efficiently, a suitable seed laser operating at 1-µm wavelength is essential. A Ti: sapphire laser can be used as the seeder for its broadband emission bandwidth covering the 1-µm spectral slot [9]. However, spectral filtering of its broad output spectrum leads to low efficiency and low pulse energy. Building an ultrafast seeding source based on Yb-doped crystals would be expensive and hard to maintain [19]. Therefore, a fiber-based seed source at 1-µm is desired for its low-cost and reliability, incorporating the advantage of a small footprint and alignment-free, turn-key operation.

Table 1.1: Spectroscopic and thermal parameters of Yb:YLF and Yb:YAG lasers

Gain medium	Yb:YAG At 300K	Yb:YAG At 80K	Yb:YLF At 300K	Yb: YLF At 80K
Pump cross-section $[\times 10^{-20} \, cm^2]$	0.8	1.5	0.4(//a) 1.05(//c)	2.4(//a) 6(//c)
Pumping wavelength [nm]	968.5/ 941.5	941.5	971.5	960
Amplification bandwidth [nm]	8	1.2	27 (//a) 36 (//c)	10 (//a) 4 (//c)
Central wavelength [nm]	~1030	~1030	1020	1018
Quantum defect [%]	6.8	8.6	4.6	5.7
Signal cross-section $[\times 10^{-20} \, cm^2]$	2.15	10	0.4 (//a) 0.75 (//c)	0.7 (//a) 1.25 (//c)
Fluorescence lifetime [ms]	0.94	0.94	2.08	1.99
Saturation fluence $[J/cm^2]$	9.5	2.05	23.5	14.1(//a) 7.9(//c)
Thermal conductivity [W/K.m]	11.2	46.1	5.3 (//a) 7.2 (//c)	26.6 (//a) 37.1 (//c)
Thermal expansion coefficient $[\times 10^{-6} \, /K]$	6.14	1.95	14.31 (//a) 10.05 (//c)	2.36 (//a) 3.18 (//c)

The reported values are taken from Ref [15], [20], [21], the thermal parameters are measured with the un-doped sample.

1.2 Fiber laser seed source at 1 µm

Yb-fiber lasers have superior performance in comparison with other existing solid-state counterparts at 1 µm. The large surface-to-volume ratio of fiber laser enables better thermal management and eliminates

the adverse effects of thermal lensing. The waveguide structure results in superior beam quality, stability and a small footprint. Fiber lasers benefit from the advanced development of telecom technology, and therefore, the cost of fiber laser components is relatively low. Besides, Yb-fibers exhibit a broader gain bandwidth than Yb-doped crystals thanks to the amorphous nature of the glass host making up the fiber core, allowing laser operation in the wavelength range between 980-1070 nm [22]. Due to the high gain of Yb fiber, they enable cascaded amplification or the implementation of master oscillator power amplifier (MOPA) concepts for power scaling [23], [24]. Nowadays, μJ-to-mJ pulse energies can be achieved from ultrafast Yb-fiber amplifier systems employing large-mode-area double-cladding gain fiber or rod-type gain fiber [25], [26]. Yb-fiber lasers are perfect seeding sources for high-power laser amplifier systems around 1 μm for their alignment-free laser structures and turn-key operation. Another important fact is the large emission bandwidth of Yb-doped fiber, which enables the customization of the seed pulse parameter in terms of pulse duration (from ps to sub 100 fs) [27], [28], the center wavelength (from 980 to 1070) [22] and repetition rate (from 100 Hz-12.5 GHz) [29], [30]. In this case, the laser parameters can be adjusted to match the specific parameter space of solid-state amplifiers based on the Yb-doped crystals. The high gain feature of Yb-doped fibers enables to further boost the seed pulse energy by a MOPA configuration. Therefore, powerful seed sources based on fiber lasers can relieve gain-narrowing in the follow-on amplifier chain. The fast development of fiber laser technology has been reviewed in [31]–[33].

Usually, the requirements on fiber seeding sources include high stability and highly stretched pulse with moderate pulse energy (>10 nJ) and low noise. These parameters cannot be achieved within one fiber oscillator. Therefore, an efficient fiber seeding source always consists of a fiber oscillator followed by several stages of fiber amplifiers. For some specific applications, techniques such as fiber-based nonlinear wavelength conversion and electronic feedback loop for active stabilization of lasers have to be considered as well. We will give a brief introduction to different techniques for expanding the parameter space of fiber laser source in the following. These fiber-optics techniques largely enhance the capability of fiber laser systems and result in an ultrafast fiber laser platform compatible with solid-state counterparts while keeping the advantages of the fiber waveguide structure.

1.2.1 Ultrafast fiber oscillator

Ultrafast fiber oscillators are the cornerstones of the ultrafast fiber laser system, defining the basic parameters of pulses, such as the spectral center wavelength, repetition rate, and pulse duration. In contrast to the ultrafast solid-state oscillators with free-space optical components, the fiber oscillator cavity is constructed by pieces of passive fiber spliced with ion-doped active fiber as the gain medium. The highly confined light in the fiber waveguide enhances its nonlinear interaction with the matter. The interplay between fiber nonlinearity and fiber dispersion enables a wide variety of pulse dynamics in the fiber oscillator cavity. Ultrafast fiber oscillators have been extensively exploited by using different mode-locking techniques. These techniques include both real saturable absorbers (e.g., the semiconductors, the carbon nanotubes, or two-dimension materials [22], [34]) and artificial saturable absorbers (SA) based on the nonlinear Kerr effect (e.g., the nonlinear polarization rotation technique (NPR) [35], [36], nonlinear optical loop mirror (NOLM) [37] or nonlinear amplifying loop mirror (NALM) [38]). While the real SAs usually feature a relatively long relaxing time, the artificial SAs based on the nonlinear Kerr effect exhibit

fast response characteristics. Therefore, they are beneficial to the generation of pulses with a shorter duration, lower intrinsic noise. Besides that, artificial SAs have a higher damage threshold and they are free from performance degradation, which is usually a problem for the real SAs [39].

Different mode-locking mechanisms (pulse shaping mechanisms) have also been extensively investigated. The first demonstration of mode-locking fiber laser is the generation of soliton pulse in a fiber cavity with all negative dispersion [40]. The balanced interaction between the nonlinear Kerr effect and negative dispersion renders and sustains a soliton formation in the cavity [41]. However, limited by the soliton area theorem $E_s = 2|\beta_2|/(|\gamma|\tau)$, the soliton pulses suffer from low pulse energy. The accumulation of excess nonlinear phase shift leads to consequently pulse deformation and soliton splitting, which is a crucial factor limiting the further performance improvement of fiber lasers. To achieve higher pulse energy, the other types of mode-locking mechanism have been proposed and demonstrated theoretically and experimentally, such as the dispersion management soliton (DMS) [42], similariton [43], dissipative soliton (DS) [36], dissipative-soliton-Resonance (DSR) pulse [44], and a new type of super high energy pulses generated from a Mamyshev oscillator [45]. The DMS mode-locking mechanism has advantage to achieve the lowest noise operation in close-to-zero net cavity dispersion region with a maximum nonlinear phase shift around π. In contrast, DS and DSR mode-locking mechanism enable the generation of pulses with higher pulse energy, and the tolerance of the nonlinear phase shift can be up to $10\ \pi$. Recently, a pulse train with even higher output energy is achieved by the Mamyshev oscillator, which delivers order-of-magnitude improvements in the pulse energy and shorter pulse duration with the nonlinear phase shift accumulated larger than $60\ \pi$. However, the Mamyshev oscillator is hard to mode lock without the help of an auxiliary cavity for the laser starting process [46]. The performance of single-mode (SM) ytterbium-doped fiber lasers based on the different mode-locking mechanisms are shown and compared in Table 1.2

Table 1.2: Performance of Yb-doped fiber lasers with different mode-locking mechanism

Mode-locking mechanism	Nonlinear phase	Best pulse energy	Best pulse duration
Soliton [41]	~0	<0.5 nJ	>100 fs
Stretched pulses [47]	<π	<3 nJ	>25 fs
Dissipative soliton [36]	<10π	<20 nJ	>70 fs
Similariton [48]	<10π	<15 nJ	>40 fs
Dissipative soliton resonance [44]	<10π	~137 nJ [49]	No found
Mamyshev oscillator[45]	>60π	~190 nJ [46]	~17 fs [50]

1.2.2 Linear/Nonlinear fiber amplifier

Fiber laser seeding source with high pulse energy is always appreciated since the powerful seeding signal will relieve the gain narrowing issue in the following solid-state laser amplifier system, which usually has a limited, much narrower gain bandwidth [11]. The energy of the pulses delivered directly from the fiber oscillator is usually less than 3 nJ and insufficient for that purpose. Therefore, the energy scaling of pulses in several stages of fiber amplifiers can be a solution. However, supposing no particular amplification scheme is used, in that case, the resulting nonlinear phase shift accumulated in fiber amplifier will

degrade the quality of pulses due to the tight confinement of high-peak-power pulses in fiber with a small core area. For the purpose of eliminating over accumulated nonlinear phase shift, pulses are commonly amplified in the chirped-pulse amplification (CPA) configuration, where the pulses from the oscillator are stretched, amplified and compressed in a sequence [51]. By using rod-type fiber [52], pulses with mJ energies have been demonstrated from fiber-rod CPA-systems [53], [54]. At the output of fiber-CPA systems, the pulse durations are typically longer than 200 fs due to a combination of effects: (a) Gain narrowing of the spectrum during amplification, (b) overall dispersion mismatching, and (c) nonlinear phase shifts due to SPM [6]. The large stretching in fiber-CPA mitigates the nonlinear effect of SPM. However, due to the waveguide-nature (i.e., confinement to small mode-areas and long propagation lengths), the effects of SPM can reappear in the CPA system for higher pulse energy. The resulting excess nonlinear phase-shifts lead to pulse-splitting and energy transfer into satellite pulses, limiting the quality of the output pulse [55]. To reach sub-100-fs pulses from fiber CPA systems, the operation at B-integrals < 1 rad and the meticulous optimization of overall third and fourth-order dispersion of the system are necessary. The latter is challenging due to the large stretching/ compression ratio required for fiber-CPA systems. By using large mode area photonic crystal fiber and dispersion-engineered fiber stretchers (typically non-PM), pulse durations as short as 75 fs have been reported at the output of a fiber-CPA system [56]. Nevertheless, CPA systems have their limitation due to the detrimental effects of self-focusing (whose threshold power is 4 MW) and the onset of thermal modal instability under high average power, which degrades the quality of output beam profile [57]. To further scale the output pulse energy while avoiding these detrimental effects, divided pulse amplification (DPA) and coherent beam combining are widely used and introduced into fiber CPA systems [25].

For energies in the range from nJ to µJ level, there also exist direct amplification schemes (i.e., that are not based on fiber-CPA) utilizing nonlinear effects to broaden the signal spectrum during amplification. The pulse can be compressed to a duration of less than 100 fs at the output. Self-similar amplification (also known as parabolic amplification) [58] is one of these nonlinear amplification schemes, 226-nJ pulses with a duration of 48 fs and 18 W average power have been obtained [59]. The self-similar amplifier was constructed from a PM 25/250 double-clad fiber that was bent to discriminate higher-order modes [60]. The finite gain-bandwidth prevents further energy scaling and pulse shortening of parabolic pulse amplification. Once the spectral bandwidth of the amplified pulse surpasses the emission band of Yb-doped fiber, the linear chirp of parabolic pulses is destroyed, leading to a compromised pulse quality. Another nonlinear amplification technique uses passive pulse-shaping before fiber-based amplification [61]. In this way, pulses with 780 fs and 49 µJ after grating-based compression have been demonstrated from a rod-type nonlinear amplifier (with accumulated B-integral of 12 rad during amplification).

Lately, the method of pre-chirp managed amplification (PCMA) was reported [62], [64], [65]. This technique and self-similar amplification offer the advantage of producing pulses with durations shorter than 100 fs. This is due to the spectral broadening originating from SPM during nonlinear amplification. The main benefits of PCMA include: (a) nonlinear effects during pulse propagation in fibers are desired and not mitigated. The spectral broadening due to SPM allows for reduced pulse durations as compared to the input pulse duration from an oscillator. (b) besides the generation of shorter pulse durations at the PCMA output, it also leads to high pulse qualities. And (c) only very compact compressors are needed for

both pre-chirp and final pulse compression. This results in very compact setups. Moreover, (d) the lengths of the fiber amplifiers in PCMA can be made very short. So, it applies to many types of gain fibers. Recently a new nonlinear amplification technique was proposed. Longitudinally evolving gain shaping is involved during the process of amplification [63]. The long length of the gain fiber, enabling the signal reabsorption, is crucial to construct such a nonlinear amplifier. As a result, high-energy, broad-band pulses at relatively long wavelength (>1050 nm) have been proved with 42-fs compressed pulse duration. Table 1.3 shows the best performance results based on different amplification schemes.

Table 1.3: Performance of different amplification schemes

Amplification scheme	B-integral	Best pulse energy	Best pulse duration
CPA [51]	<10 π	< 1 mJ	> 100 fs
DPA [25]	<10 π	< 12 mJ	> 100 fs
Parabolic Amp [58]	<50 π	< 300 nJ	> 50 fs
PCMA [62]	<100 π	< 1μJ	> 30 fs
GMN Amp[63]	>100 π	~107 nJ	-42 fs

1.2.3 Nonlinear wavelength shift based on fiber-optic method

Although the gain bandwidth of Yb-doped fiber is much broader than their solid-state counterparts (Yb-doped crystal), Yb-doped fiber laser systems are not broadly wavelength-tunable. The emission wavelength is limited within the range from 1010 nm to 1070 nm. While the pulses at the longer wavelength can be generated through signal reabsorption in longer gain fiber with lower pumping [63], the generation and amplification of pulses at the shorter wavelength is extremely difficult for the low-gain and strong ASE from the 1030-nm emission band. This limitation hampers their widespread usages as a versatile laser source for high power solid-state amplifier systems once the demanding wavelength of pulses is out of the emission band of Yb-doped fiber [66]. For example, the amplifier system based on cryogenic cooling Yb: YLF has 6 folds higher emission cross-section at 995 nm compared with the 1020 nm emission band [15]. Therefore, a seeding source that works at 995 nm wavelength is demanding for achieving higher output power from Yb: YLF based amplifier system. The typical emission cross-section of Yb-fiber is above 1000 nm, resulting in the difficulty of amplifying the pulse at such a relatively short wavelength.

Nonlinear wavelength conversion is widely adopted to overcome the wavelength limitation of the fiber laser. Solid-state optical parametric oscillator (OPO) synchronously pumped by an ultrafast source laser can generate widely tunable signal/idler pulses. Another attractive approach is to employ third-order nonlinearity inside an optical fiber to generate ultrafast pulses centered at a wavelength different from the input pulses. Fiber-optic methods are of particular interest because they are compatible with the rapid development of powerful ultrafast fiber lasers. Fiber-optic methods have been demonstrated for efficient wavelength conversion, including dispersive wave generation [72], [73], fiber OPO [68], [74]–[76], and soliton self-frequency shift (SSFS) [69], [77], [78], to name a few.

Dispersive wave generation typically produces positively chirped femtosecond pulses with limited wavelength tuning range for its phase-matching condition. Up to 100 nm wavelength turnable range can

be achieved by varying the input pulse peak power [72]. The further tuning of wavelength relies on utilizing several PCFs with different zero-dispersion wavelength [79]. Besides dispersive wave has poor energy scalability and relatively high noise level.

Fiber OPOs feature a certain wavelength tunability (up to ~180 nm) [74], but the allowed narrow phase-matching bandwidth given by fiber dispersion limits the generated pulse duration, resulting in sub-picosecond or picosecond pulses. Besides, fiber OPOs need fine cavity tuning to match the pump laser's repetition rate, and the long OPO cavity is sensitive to environmental disturbance.

Soliton self-frequency shift (SSFS) is widely adopted to generate transform-limited pulses, and the resulting Raman soliton can be as short as ~50 fs. A unique and attractive feature associated with SSFS is that this approach does not require specific phase matching, which is typically a necessity for other approaches such as dispersive wave generation and fiber optical parametric oscillator. The continuously red-shifted Raman soliton can be achieved by varying the input pulse energy. However, the pulse energy of Raman soliton has to satisfy the so-called soliton area theorem, resulting in pulse energy lower than 1nJ in single-mode fibers. As a result, large-mode-area (LMA) fibers (e.g., rod-type fibers or high-order mode (HOM) fibers) with negative group-velocity dispersion (GVD) can be used to generate high-energy (up to ~100 nJ) Raman soliton pulses tunable in a broad wavelength range [70], [80].

Recently, a new method to generate wavelength widely-tunable pulses is proposed, in which self-phase modulation (SPM) dominates the broadening of an input narrow optical spectrum, and the broadened spectrum comprises multiple isolated spectral lobes. Using proper bandpass filters to select the leftmost or the rightmost spectral lobe produces nearly transform-limited pulses with ~100 fs duration. Such SPM-enabled spectral selection (SESS) source exhibits excellent energy scalability and can deliver >100-nJ pulses with ~1-MW peak power [81].

Table 1.4: Generated pulse parameters based on different wavelength conversion schemes

Nonlinear wavelength conversion scheme	Typical Wavelength (μm)	Best pulse energy (nJ)	Shortest pulse duration (fs)
Dispersive wavelength	0.6-0.8 [67]	4	14
Fiber OPO	0.87-0.92 /1.2-1.3 [68]	250	350
SSFS in SM fiber	1.15-1.35 [69]	6.4	<50
SSFS in HOM fiber	1.05-1.6 [70]	80	50
SESS	0.82-1.21 [71]	33	50

Table 1.4 shows the best performance results in terms of pulse energy, pulse duration, and wavelength-tunable range with different fiber-optics nonlinear wavelength conversion schemes. To have a better comparison, Figure 1.1 from Ref. [33] plots the maximum pulse energy obtained by nonlinear fiber-optical wavelength conversion as a function of wavelength tuning range.
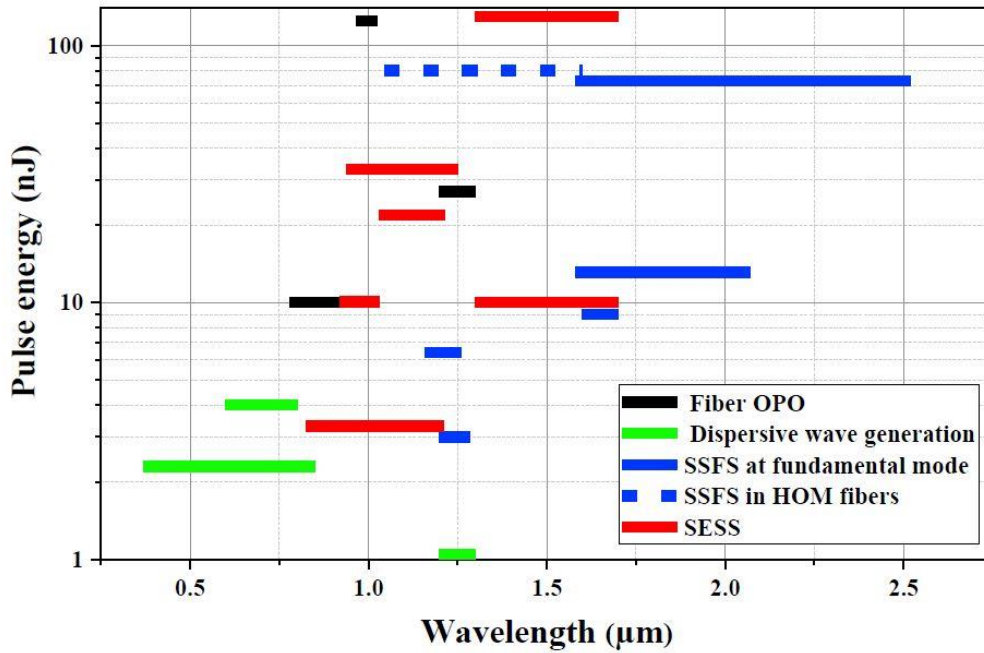
Figure 1.1: Maximum pulse energy versus wavelength tuning range for different nonlinear wavelength conversion schemes. [33]

1.2.4 Active stabilization of fiber laser systems
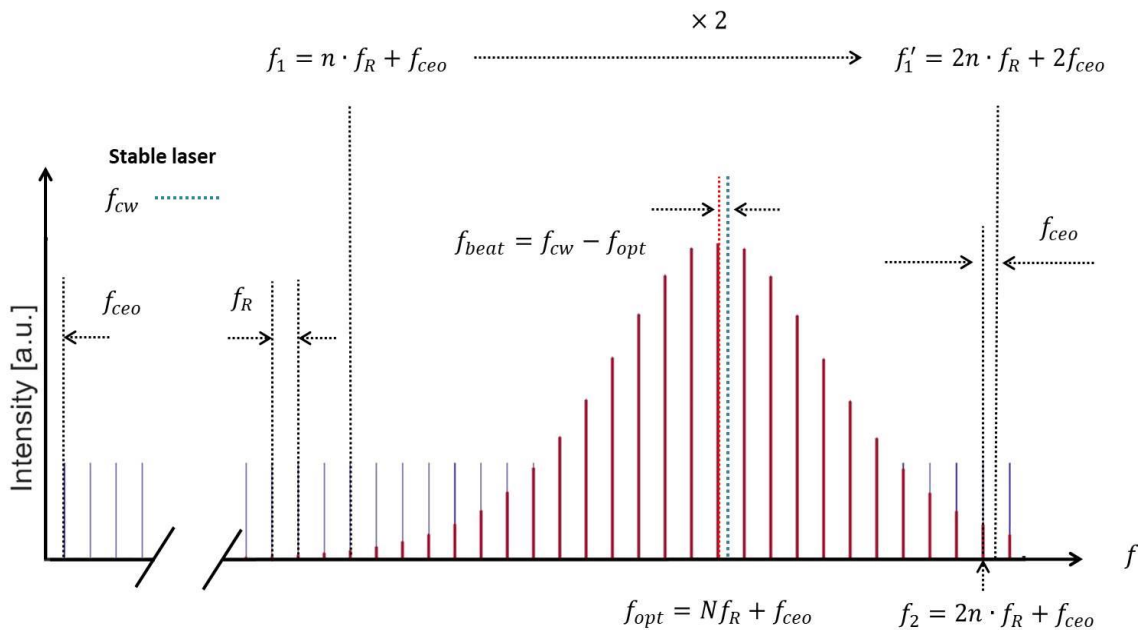
Figure 1.2: Typical optical spectrum of a mode-locked laser. f_{opt}: optical frequency; f_R: pulse repetition rate of the mode-locked laser; f_{ceo}: carrier-envelope-offset frequency; N: integer mode number. f_{cw}: optical frequency of stable laser.

The direct output from a mode-locked laser is a train of equally spaced pulse in the time domain and the optical spectrum is a frequency comb consisting of equally spaced narrow lines, as shown in Figure 1.2. The formation of the comb line can be described as [82]:

$$f_{opt} = Nf_R + f_{ceo} \tag{1-1}$$

where N is a large integer number (mode number), f_R is the repetition rate of pulse and f_{ceo} is the carrier-envelope offset frequency, which is an offset of the whole spectrum away from zero. The f_{ceo} is determined by the carrier-envelope phase shift due to the mismatch of group and phase velocity in a mode-locked laser. The repetition rate f_R is influenced by the round-trip time of the oscillating pulse in the laser cavity, which depends on the optical cavity length. The full stabilization of both the carrier-envelop offset frequency and the repetition rate leads to a frequency comb with a fixed position of each comb line [83]. This can be used as a frequency reference for the timing synchronization of other serve lasers [84], [85], or in the applications, such as ultra-low-noise microwave generation, astronomical spectrographs calibration and direct comb-based spectroscopy.

The full stabilization of a fiber laser system will also expand its capacity as a seeding laser for multiple channels of solid-state amplifier systems. It guarantees the intrinsic synchronization of different laser systems so that the time resolution is enhanced once these following laser systems have to operate together with precious time-controlling.

The common scheme to actively stabilize a mode-locked fiber laser is a method called f-2f self-referencing [50], [86]. The output spectrum of fiber laser is broadened in a piece of fiber to generate an octave-spanning supercontinuum. Its low-frequency part (f_1) gets frequency doubling, and the corresponding second harmonic signal beats with its high-frequency component (f_2) to acquire the signal of carrier-envelope offset frequency, which is then stabilized to an RF reference. At the same time, the repetition rate is fixed by locking one comb line (f_{opt}) to an ultra-stable laser (f_{cw}). Since the f_{ceo} and f_{opt} are locked simultaneously, the f_R or the time separation of the corresponding pulse train is stabilized.

1.3   Structure of this thesis

This thesis aims to investigate different parts of the ultrafast Yb-based fiber laser system in terms of the oscillator, fiber-optics nonlinear wavelength conversion, amplification of pulses at a short wavelength as well as laser noise and its stabilization. As a 1-µm seed laser platform for high-power Yb-based solid-state amplifier systems, efforts are put into customizing the output parameter of the fiber laser system, such as pulse energy, spectral center wavelength, laser stability, and its noise level. In this thesis, I discuss four essential elements in the construction of the ultrafast fiber laser platform:

- Chapter 2: Ultrafast polarization-maintaining Figure 9 fiber oscillator.
  Ultrafast fiber oscillators are the cornerstones of the ultrafast fiber laser system, which defines the basic parameters of the pulses, such as the spectral center wavelength, repetition rate, and pulse duration. In this chapter, we numerically and experimentally investigate the performance of a state-of-art ultrafast fiber oscillator constructed with a free-space reflection arm and an asymmetric nonlinear amplifying loop mirror (NALM) for mode-locking. As it shows low-noise characteristics and the potential to resist environmental perturbations, it can substitute the well-known mode-locked fiber laser based on the nonlinear-polarization-rotation (NPR) mechanism to provide pulses for the following applications.
- Chapter 3: Methods of nonlinear wavelength conversion and noise characteristics

Chapter 1: Introduction

The spectra of pulses delivered from the Yb-fiber laser system are limited by the gain bandwidth of Yb-doped fiber (40 nm). To expand the wavelength-tuning capacity of the Yb-fiber laser system, two types of fiber-optics nonlinear wavelength conversion schemes are investigated in terms of the energy scaling capacity of wavelength shifted pulse and the noise level. We demonstrated that the method of self-phase modulation (SPM) enabled a spectral selection (SESS) pulse that produced ten times more pulse energy than Raman soliton generated by soliton self-frequency shift (SSFS). And the relative timing jitter (RTJ) of the SESS pulse to the pump pulse is in the attosecond level.

- Chapter 4: Fiber seed sources for Cryo Yb:YLF amplifier system.

Two ultrafast fiber laser systems for seeding solid-state Yb: YLF amplifiers are presented in this chapter. The laser design strategies are explained as well as the corresponding simulation results. The experiments are carried out under the guide of simulation. Efforts are put on the generation and amplification of pulses at the shorter wavelength (1018 nm and 995 nm). For the first system at the wavelength of 1018 nm, 87-W, 4.9-µJ pulses are achieved with the MOPA structure. The second laser system, which takes advantage of the efficient SESS method for nonlinear wavelength shifting, is a wavelength-tunable (from 995 nm to 1030 nm) fiber laser source with moderate pulse energy (from 10 nJ to 30 nJ). It enables to seed different types of Yb based solid-state amplifier systems at around 1-µm wavelength.

- Chapter 5: Low-noise master fiber laser delivering 10-nJ, 60-fs pulses

10-nJ, 60-fs ultrafast fiber laser system with intensity noise as low as 0.008% is presented in this chapter, which is going to be a master seeding laser for different solid-state amplifier stages. The design strategies, and the corresponding simulation and experimental results, are shown in a sequence. PCMA is investigated in detail for the generation of the broadband parabolic pulse with a linear chirp. The noise reduction mechanism in the fiber amplifier chain is analyzed and proved by the experiment. In the final section of this chapter, I discuss the strategies to transform this laser into a frequency comb for further stabilization.

It should be noted that Chapter 2 focuses on Figure 9 oscillator, which is not used in the fiber laser systems of chapter 4 and chapter 5 recently. However, we can replace the corresponding NPR mode-locking fiber oscillator in these laser systems with Figure 9 oscillator to further improve the overall laser performance. The nonlinear wavelength conversion method discussed in chapter 3 is utilized in the laser system of chapter 4 for wavelength-tunable pulse generation.

Chapter 2

Ultrafast Polarization Maintaining Figure-9 Fiber Oscillator

In a master-oscillator-power-amplifier (MOPA) laser system, the ultrafast oscillator defines the fundamental parameters of seeding pulses, including the center wavelength, transform-limited pulse duration, repetition rate, and noise performance. Apart from the pulse energy, the basic parameters of the pulses are settled by the oscillator in a linear laser amplifier system. In this scenario, a stable oscillator is essential to support the subsequent laser system. Apart from being the seeding source [11], the ultrafast oscillator itself has versatile applications for self-reference frequency comb [87], optical sensing [88], or timing distribution and synchronization [89].

Ultrafast fiber oscillators offer several clear advantages over their solid-state counterparts, such as a compact structure, easy thermal management, alignment-free and turn-key operation, and excellent beam quality. Over the last decades, ultrafast fiber oscillators have been extensively exploited by using different mode-locking techniques. These techniques include real saturable absorbers (e.g., the semiconductors [90], the carbon nanotubes [91], and two dimension materials [92]) and artificial saturable absorbers based on the nonlinear Kerr effect (e.g., the nonlinear polarization rotation technique (NPR) [93], frequency-doubling crystal [94], nonlinear optical loop mirror (NOLM) [95] or nonlinear amplifying loop mirror (NALM) [96]). Different types of mode-locking mechanisms (pulse shaping mechanisms) have been extensively investigated as well. The first mode-locking fiber laser delivered soliton pulse from a negative-net-dispersion oscillator cavity [97]–[99]. The balanced interaction between the nonlinear Kerr effect and the negative dispersion renders and sustains soliton formation in the cavity. However, the soliton suffers from low pulse energy, limited by the soliton area theorem. The accumulation of excess nonlinear phase shift leads to consequently pulse deformation and wave breaking, which is the crucial fact limiting the further performance improvement of fiber lasers. To overcome this issue and to achieve higher pulse energy, the other types of mode-locking mechanisms have been proposed and demonstrated theoretically and experimentally, such as the dispersion-managed soliton (DMS) [100], [101], similariton [102]–[104], dissipative soliton (DS) [105]–[107], dissipative-soliton-Resonance (DSR) pulse [108]–[110], and a new type of super high energy pulses generated from a Mamyshev oscillator [111], [112]. Among them, the DMS mode-locking mechanism can deliver the

lowest noise pulses in close-to-zero net cavity dispersion region with a maximum nonlinear phase shift around π [113]–[115]. In contrast, DS and DSR mechanisms enable the generation of pulses directly from a fiber oscillator with considerable pulse energy. The tolerance of nonlinear phase shift without the issues of wave breaking and pulse splitting is around 10 π [106], [116]. Recently, an even higher energy pulse could be achieved by the Mamyshev oscillator, which enables order-of-magnitude improvements in the pulse energy and shorter pulse duration. The nonlinear phase shift accumulated in such a fiber oscillator cavity can be larger than 60 π [45], [117]. However, the Mamyshev oscillator is hard to start mode-locking. Therefore, an auxiliary cavity is necessary for the laser starting process [46].

Nowadays, the artificial SAs that are based on the nonlinear Kerr effect exhibit fast response characteristics compared to the real SAs, which usually have a picosecond-level relaxing time. The fast response of artificial SAs enables the generation of pulses with shorter pulse duration, lower intrinsic noise [118], [119]. The nonlinear polarization rotation (NPR) technique (artificial SAs) has been mainly used for decades because of its simple structure, large modulation depth, and high power handling ability [120]. However, non-PM fiber is usually utilized for NPR in this type of oscillator. Therefore, any environmental perturbations, such as mechanical vibration, variation of temperature and humidity, as well as air pressure on fiber, lead to a change of pulse polarization and interrupt the mode-locking state of the oscillator. These limitations prevent the application of NPR fiber lasers outside of a well-controlled specialized optical lab. Instead, fiber oscillators with nonlinear optical loop mirror (NOLM) or nonlinear amplifying loop mirror (NALM) have attracted much attention for their compact structures, all-polarization-maintaining configuration, and low noise characteristics [96], [121]–[124]. They are environmentally stable even under harsh conditions as might be present in industrial manufacturing halls, vehicles, and even satellites [125]. With dispersion management, NOLM/NALM lasers have achieved state-of-art noise performance [39], very suitable for seeding a MOPA high-power laser system.
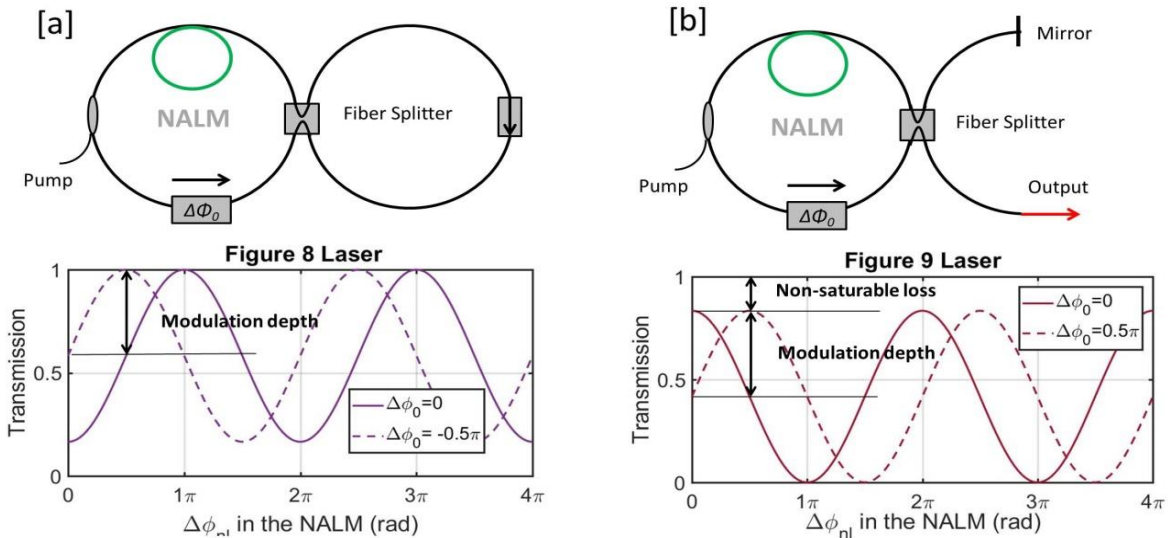
Figure 2.1: Schematic of two different laser configurations with a nonreciprocally biased NALM. (a) NALM fiber laser operates in its transmitted mode (Figure 8 laser); (b) NALM fiber laser operated in its reflected mode. For each configuration (top row), the theoretical cavity transmission is plotted (bottom row) without (solid line) and with (dash line) nonreciprocal phase bias, assuming an exemplary energy splitting ratio of 70:30.

Chapter 2: Ultrafast polarization maintaining Figure 9 fiber oscillator

The intensity-dependent transmission of NOLM (artificial saturable absorber effect) is caused by a differential nonlinear phase shift ($\Delta\varphi_{nl}$) between the two counter-propagating pulses in the Sagnac loop. The phase shift difference is due to the unbalanced pulse energy splitting ratio at the entrance of NOLM. To enhance the nonlinear phase shift difference, an asymmetrically placed amplifying fiber is inserted into NOLM, which is termed as the nonlinear amplifying loop mirror (NALM). With the NALM structure in fiber oscillators, the energy splitting ratio at the entrance of the Sagnac loop is not necessary to be asymmetrical anymore. There are two typical fiber oscillator structures (see Figure 2.1) with NOLM/NALM. When connecting the two fiber ports and forming a shape of "8", NOLM/NALM operates at the transmission mode (Figure 2.1(a)). The increase of $\Delta\varphi_{nl}$ in the loop enables the enhancement of the cavity transmission. However, the small deviation of $\Delta\varphi_{nl}$ from zero only leads to a slight change of the cavity transmission (see Figure 2.1(a), solid curve). The self-starting mode-locking operation is difficult due to this trivial intensity-dependent transmission change. To solve the problem of self-starting, a non-reciprocal phase bias (including a proper arrangement of Faraday rotators and waveplates) is inserted into the Figure-8 laser cavity, which shifts the cavity transmission curve to a position where this curve has a steeper slope when $\Delta\varphi_{nl}$ is small [126]. Apart from the Figure-8 laser structure, NOLM / NALM can operate at the reflection mode when combining one fiber port with an end mirror (Figure 2.1(b)). However, the reflection of NOLM/NALM leads to an intrinsic anti-saturable absorber effect, which means the cavity transmission decreases when $\Delta\varphi_{nl}$ increases (see Figure 2.1(b), solid curve). The mode-locking operation could only be achieved by assembling the non-reciprocal phase bias elements. The reflected NOLM/NALM laser structure is named as Figure-9 laser. Compared with the Figure-8 laser, the Figure-9 laser has advantages on a more compact laser design and the easy assembling of the stabilization-tuning elements in its reflected arm. However, there is a non-saturable loss of the Figure-9 laser due to the non-50:50 splitting ratio at the entrance of NOLM/NALM, as shown in the transmission curve (Figure 2.1(b)). The larger the splitting ratio at the NALM entrance deviates from 50:50, the higher the non-saturable loss is.

A modified version of the Figure-9 laser is investigated and constructed [124] (see Figure 2.2) to eliminate the non-saturable loss. This modified Figure-9 laser consists of a NALM and a free-space reflected arm. Its cavity transmission curve is the same as the Figure-8 laser (see Figure 2.1(a)) while keeping the flexible structure of the Figure-9 laser for the easily assembled actuators. The variation of the energy splitting ratio at the NALM's entrance leads to the change of the modulation depth of the cavity transmission curve. But the non-saturable loss is always zero. Such a laser structure enables further shortening of the fiber length in the NALM by raising the energy splitting ratio at the NALM entrance for compensation of the decrease of $\Delta\varphi_{nl}$ in the shorter fiber loop. However, the detailed investigations of this modified Figure-9 laser structure in the different mode-locking regimes are absent. Due to its degree of freedom to operate in a large parameter space, we investigated the influence of both its cavity transmission curve and the dispersion map on its mode-locking characteristics and pulse dynamics.

In this chapter, we numerically investigate the operation of the Yb-fiber based Figure-9 fiber oscillator working in the all-normal-dispersion (ANDi) regime and dispersion-managed mode-locking regime. The influence of the cavity transmission curve on pulse quality is discussed. The pulse build-up dynamic and the over-shooting problem in the laser cavity are analyzed as well. In the end, we experimentally obtained ~65 fs transform-limited pulses directly from the dispersion-managed NALM fiber oscillator.

2.1 Mode-locking mechanism of the Figure-9 laser
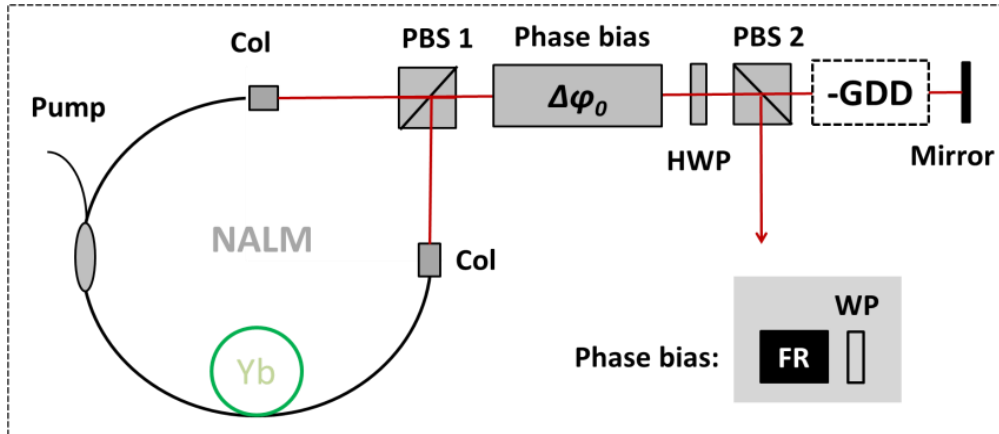
Figure 2.2: Schematic of modified Figure 9 fiber oscillator. FR: Faraday-Rotator（45° rotation） HWP: half-wave plate; WP: wave plate; PBS: polarization beam splitter; Col: collimator. The WP is placed with its optical axis 45° away from the p-polarization light transmitted from PBS 2. The phase of WP is half of $\Delta\varphi_0$, and the combination of FR and WP enables a nonreciprocal phase shift of $\Delta\varphi_0$ between CCW and CW pulse in the NALM. The rotation of HWP changes the energy splitting ratio between CCW and CW pulse at the entrance of NALM.

The modified polarization-maintaining Figure-9 fiber oscillator is shown in Figure 2.2, including a NALM and a free-space reflection arm. The intensity-dependence cavity transmission (T_c.) at the position of PBS2 is caused by a differential nonlinear phase shift between the two counter-propagating pulses in the asymmetry fiber loop. The differential phase shift results both from the difference of input pulse energy between clockwise (CW) and counter-clockwise (CCW) pulses at the NALM's entrance, and from the asymmetrically placed amplifying fiber. In our specific case, the NALM part includes a polarization beam splitter (PBS1), 0.4-m PM fiber, 0.4-m PM Yb-doped fiber and 0.6-m PM fiber in a sequence, while the reflection arm consists of the non-reciprocal phase bias element ($\Delta\varphi_0$), a half-wave plate (HWP), the second polarization beam splitter (PBS2), a dispersion management component (-GDD) and an end mirror (For all-normal-dispersion mode-locking, the dispersion management component is removed). The energy splitting ratio at the entrance of the NALM is controlled by rotating the HWP. The phase bias part includes a Faraday rotator (FR) and a wave plate (WP), which applies a non-reciprocal phase bias for the counter-propagating pulses when the optical axis of the WP is 45° away from the direction of the p-polarization light (the transmission light from PBS2). The value of the non-reciprocal phase bias is two times of the phase of the waveplate for the double passing of the reflection arm in one round trip. The cavity transmission without the phase bias component is strictly reciprocal for low pulse intensity, the same as the T_c of the Figure-8 laser (Figure 2.1(a), solid curve). A small deviation of $\Delta\varphi_{nl}$ from zero only leads to a slight change of T_c, making the mode-locking state hard to achieve. Compared with the NALM fiber laser using fiber splitter (Figure 2.1(b)), this modified version Figure-9 laser structure based on PBSs enables lower cavity loss even when introducing a large energy splitting ratio at the entrance of NALM. The decrease in overall loss makes mode-locking operation easier, and the laser can be operated

with lower noise. Besides, the free-space linear arm can easily include the tuning elements for further laser stabilization and dispersion management [96].

2.1.1 Calculation of the cavity transmission
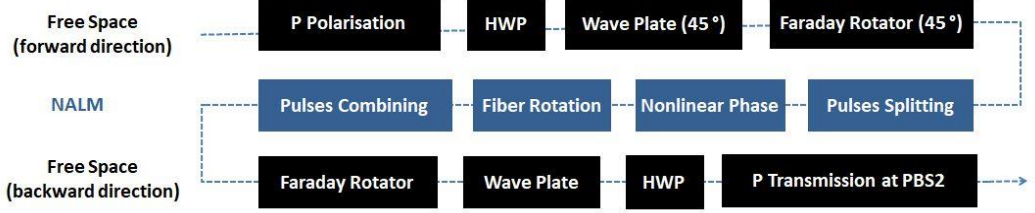
Figure 2.3: Calculation sequence of Figure 9 laser cavity transmission. The starting component is the p-polarization electric field transmitted from PBS2 in the direction to the fiber loop.

The cavity transmission (T_c) at PBS2 versus the differential nonlinear phase shift ($\Delta\varphi_{nl}$) of the counter-propagating pulses in the NALM can be calculated by the Jones matrix. The starting point of calculation is the transmitted p- polarization (p-pol) light from PBS2 in the direction to the fiber loop. The sequence of calculation is shown in Figure 2.3. The electric field at the starting point is written as

$$\text{E}_0 = \begin{bmatrix} E_p \\ E_s \end{bmatrix} = \begin{bmatrix} 1 \\ 0 \end{bmatrix} \tag{2-1}$$

and the Jones matrix of WP and its rotation is written as：

$$M_{WP}(\Delta\varphi_0/2) = \begin{bmatrix} e^{i\Delta\varphi_0/4} & 0 \\ 0 & e^{-i\Delta\varphi_0/4} \end{bmatrix} \tag{2-2}$$

$$M_R(\alpha) = \begin{bmatrix} \cos(\alpha) & \sin(\alpha) \\ -\sin(\alpha) & \cos(\alpha) \end{bmatrix} \tag{2-3}$$

In the equation 2-2, the $\Delta\varphi_0/2$ is the phase of the wave plate, HWP and QWP are described by setting $\Delta\varphi_0/2$ equal to π and $\pi/2$. In equation 2-3, α is the rotation angle of the wave plate optical axis away from the p-pol electric field. In the end, the rotating waveplate can be expressed as the multiplication of the inverse rotation matrix, the wave plate matrix, and the rotation matrix in a sequence. For example, the random-rotated HWP and the 45-degrees-rotated WP are described as equation 2-4 and 2-5, respectively:

$$M_{HWP}(\alpha) = M_R(\alpha)^{-1} \cdot M_{WP}(\pi) \cdot M_R(\alpha) \tag{2-4}$$

$$M_{WP\,45}(\Delta\varphi_0/2) = M_R(\pi/4)^{-1} \cdot M_{WP}(\Delta\varphi_0/2) \cdot M_R(\pi/4) \tag{2-5}$$

The 45° Faraday rotator is given by:

$$M_{FR} = \begin{bmatrix} \cos(\pi/4) & \sin(\pi/4) \\ -\sin(\pi/4) & \cos(\pi/4) \end{bmatrix} \tag{2-6}$$

The electric field after the first line of the optical component in Figure 2.3 can be calculated by multiplying the corresponding Jones matrices in a sequence:

$$E_{in} = M_{FR} \cdot M_{Wp45}(\Delta\varphi_0/2) \cdot M_{HWP}(\alpha) \cdot E_0 = \begin{bmatrix} E_p{}' \\ E_s{}' \end{bmatrix} = \begin{bmatrix} E_{ccw} \\ E_{cw} \end{bmatrix} \tag{2-7}$$

Then, the resulting electric field is sent into the fiber loop. The E_p component propagates in the counter-clockwise (CCW) direction and the E_s component in the clockwise direction (CW). We suppose that the differential nonlinear phase shift is $\Delta\varphi_{nl}$, and the dispersion in the fiber loop is neglected. The fiber loop enables the counter-propagating electric fields to accumulate a nonlinear phase difference of $\Delta\varphi_{nl}$, and its

Jones matrix is equal to the one of a wave plate. But it needs to note that the value of $\Delta\varphi_{nl}$, depends on the intensity of the counter-propagating electric field:

$$M_F(\Delta\varphi_{nl}) = \begin{bmatrix} e^{i\Delta\varphi_{nl}/2} & 0 \\ 0 & e^{-i\Delta\varphi_{nl}/2} \end{bmatrix} \tag{2-8}$$

At the point of pulse recombining in the PBS1, the E_{cw} becomes the E_p component of the recombing pulse, and the E_{ccw} is the E_s component due to the twist of the fiber loop. The Jones matrix of the twisting fiber could be written in the following way:

$$T_F = M_{HWP}\left(\frac{\pi}{4}\right) \cdot \begin{bmatrix} 1 & 0 \\ 0 & 0 \end{bmatrix} + M_{HWP}\left(-\frac{\pi}{4}\right) \cdot \begin{bmatrix} 0 & 0 \\ 0 & 1 \end{bmatrix} \tag{2-9}$$

After the fiber loop, the pulses recombine, and the recombining electric field is calculated by multiplying the E_{in} in the following way:

$$E_{out} = T_F \cdot M_F(\Delta\varphi_{nl}) \cdot E_{in} \tag{2-10}$$

Then, the pulses travel back to the linear arm with free-space optical components, but this time the electric field passes through them in the opposite direction. The Jones matrix of beam reflection from the loop mirror is described by:

$$R = \begin{bmatrix} 1 & 0 \\ 0 & -1 \end{bmatrix} \tag{2-11}$$

So that the backward electronic field at the position of PBS 2 can be calculated by:

$$E_{pbs2} = M_{HWP}(\alpha) \cdot M_{wp45}\left(\frac{\Delta\varphi_0}{2}\right) \cdot M_{FR} \cdot R \cdot E_{out} = \begin{bmatrix} E_t \\ E_r \end{bmatrix} \tag{2-12}$$

At the end of PBS2, the E_p component is kept oscillating inside this laser cavity (E_t), and the E_s component gets rejected (E_r) by the PBS2. By calculating the intensity of E_t versus the change of nonlinear phase difference ($\Delta\varphi_{nl}$), we obtain the cavity transmission curve (T_c). Its specific shape depends on the rotation of HWP (α), which determines the energy splitting ratio at the entrance of NALM, and the phase of WP ($\Delta\varphi_0/2$), which shifts the phase of the transmission curve by $\Delta\varphi_0$.

$$E_t = f_{(\Delta\varphi_0, \ a)}(\Delta\varphi_{nl}) \tag{2-13}$$

The cavity transmission curve (T_c) is:

$$T_c = |E_t|^2 \tag{2-14}$$

2.1.2 Characteristic of the cavity transmission curve

The energy splitting ratio between the CW and the CCW pulses at the entrance of NALM could be turned by rotating the HWP. The blue curve in Figure 2.4(a) is the energy ratio of Ep at the entrance of NALM, which travels through the fiber loop in the counter-clockwise (CCW) direction, and the red curve represents the Es in the clockwise (CW) direction. Figure 2.4(a) shows that the ratio between E_{ccw} and E_{cw} can be changed continually from 100:0 to 0:100 by rotating HWP from -22.5° to +22.5° (the angle of the HWP optical axis away from the direction of the p-pol light). By rotating the HWP, the energy splitting ratio of the counter-propagating pulses at the entrance of NALM can be turned to further adjust the $\Delta\varphi_{nl}$ value in the fiber loop.

Figure 2.4(b) shows the cavity transmission curve versus the differential nonlinear phase shift when the energy splitting ratio is fixed to be 50:50 (the ration of HWP is 0°). Without the non-reciprocal phase bias ($\Delta\varphi_0=0$), the transmission curve has its minimum value when $\Delta\varphi_{nl}$ equals to be zero (Figure 2.4(b), blue curve). At this point, the modulation of the laser intensity-dependent transmission is small when $\Delta\varphi_0$

slightly deviates from zero value. The Figure-9 fiber oscillator is hard to mode lock at this point. To avoid the difficulty in the laser starting, the non-reciprocal phase bias is assembled to shift this curve away from its minimum value at the point where $\Delta\varphi_{nl}=0$. The red curve in Figure 2.4(b) with the phase bias of -0.5π has a positive slope when $\Delta\varphi_{nl}$ is zero. In comparison with the blue curve, the cavity transmission increases faster when $\Delta\varphi_{nl}$ rises from zero. This feature plays the same role as an intensity-dependence saturable absorber for a mode-locking oscillator, because $\Delta\varphi_{nl}$ is proportional to the intensity of the electric field in the NALM. A pulse can build up from the noise background due to its higher cavity transmission compared with the CW lasing state. The correct choice of phase bias ($\Delta\varphi_0$) helps for mode-locking and even makes the laser self-start.
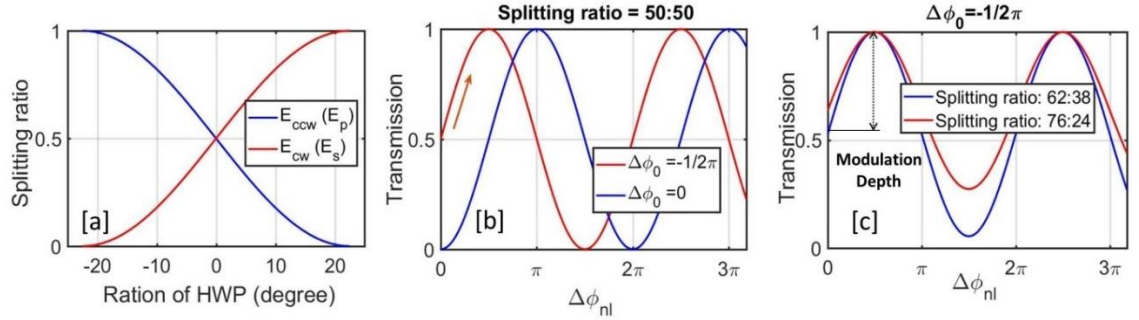
Figure 2.4: Calculated cavity transmission curve based on Jones matrix. (a) the energy splitting ratio between CW and CCW pulses at the entrance of NALM versus the rotation of HWP; (b) the cavity transmission curve at PBS2 versus the differential nonlinear phase shift when the energy splitting ratio is 50:50, and the non-reciprocal phase bias ($\Delta\varphi_0$) is varied; (c) the cavity transmission curve versus the differential nonlinear phase shift when the non-reciprocal phase bias is -0.5 π, and the energy splitting ratio is varied.

Apart from the non-reciprocal phase bias, the energy splitting ratio also influences the shape of the cavity transmission curve. Figure 2.4(c) shows the transmission curves with different pulse energy splitting ratios at the NALM's entrance (Rotation of HWP; α) while the phase bias is fixed at -0.5π. It is easy to tell that the change of the energy splitting ratio does not influence the tendency of these curves; however, the modulation depth decreases when the energy splitting ratio increases. In most cases, the equivalent saturable absorption corresponds to the first part of the transmission curve with a positive slope. The corresponding modulation depth of such an artificial SA is equal to the value of $1 - T_c(0)$. Figure 2.4(c) shows that the modulation depth depends on both the phase bias and the energy splitting ratio.

However, such a sinusoidal cavity transmission function is not a monotonic intensity dependence. Once the $\Delta\varphi_{n,max}$ is over the point with the highest transmission, the pulse enters the anti-saturable absorption region of SA. This phenomenon is referred to as the over-driving of SA. It may destroy the mode-locking state by continue wave (CW) breakthrough or lead to pulses splitting (double pulsing). In some cases, the anti-saturable absorption is utilized for the generation of DSR pulses. The influence of sinusoidal SA on pulse shaping will be discussed in the later sections.

As discussed above, the rotating of HWP in the cavity only changes the energy splitting ratio at the entrance of NALM and the modulation depth of the transmission curve. And by inserting 45°-rotating

$\Delta\varphi_0/2$-WP, the transmission curve gets a certain amount of phase shift ($\Delta\varphi_0$), which is twice of the phase value of the WP. However, during the experiment, we want to investigate the full parameter space of the Figure-9 fiber oscillator with a continually tunable phase bias. Changing the WP to satisfy different phase bias values is inconvenient. Instead, replacing the 45°-rotating WP with a free-rotating QWP can allow us to search for the desired value of phase bias. The free rotation of both QWP and HWP in the Figure-9 laser cavity enables the full possibility to shape the cavity transmission curve. But in this case, the solely rotating of HWP or QWP not only changes the modulation depth of T_c but also the phase shift ($\Delta\varphi_0$) of it. As shown in Figure 2.5 (a), when the rotation of HWP is fixed at 0°, rotating QWP leads to the change of both the phase of the curve and the energy splitting ratio at NALM's entrance. In general, fixing the rotation of QWP and tuning the HWP leads to a similar effect. But in a specific case, when the QWP is rotated to an angle such as 0° (Figure 2.5(b)) or 45° (Figure 2.5(c)), the rotation of HWP only leads to the change of phase (Figure 2.5 (b)) or the change of the modulation depth of the transmission curve (Figure 2.5 (c)).
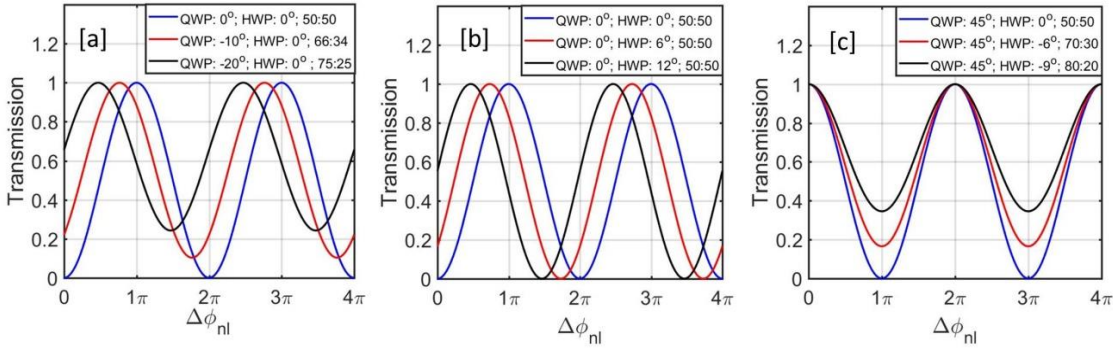
Figure 2.5: Cavity transmission curve by replacing 45°-rotated WP with free-rotated QWP. (a) The cavity transmission curve when the rotation of HWP is fixed to 0°, and the rotation of QWP is adjustable. In this case, both the modulation depth and the phase bias are changed by rotating the QWP. (b) The cavity transmission curve when the QWP is fixed to 0°, and the ration of HWP is changed. In this specific angle of QWP, the rotating of the HWP only shifts the phase bias. (c) The cavity transmission curve when the QWP is fixed to 45° and the rotation of HWP only leads to the change of modulation depth.

2.2   Pulse dynamics in the Figure-9 fiber laser

In the last section, we discuss the function of the phase bias components in the Figure 9 laser cavity and how to shape the cavity transmission curve. The intensity-dependent cavity transmission plays a role as a fast saturable absorber. The mode-locking operation can be acquired by setting the QWP and HWP in the cavity correctly. However, the interaction between the cavity transmission and the pulse dynamics is still unclear. In this section, we investigate the pulse dynamics in Figure 9 laser cavity in the all-normal dispersion regime and the dispersion-managed regime of the fiber laser cavity. Both the cavity dispersion and the cavity transmission curve can lead to versatile pulse dynamics.

2.2.1 Numerical model for Figure 9 oscillator simulation

The dynamics of counter-propagating pulses in fiber is modeled by nonlinear Schrodinger equations, written as [121]:

$$\frac{\partial A}{\partial z} + \frac{i}{2}\beta_2 \frac{\partial^2 A}{\partial T^2} - \frac{1}{6}\beta_3 \frac{\partial^3 A}{\partial T^3} + \frac{(\alpha - g(A))}{2} A = i\gamma(|A|^2 A) \tag{2-15}$$

where the A represents the complex electric field envelope, z is the distance, and $T = t - \beta_1 z$ is the time frame moving along with the pulse group velocity. The linear terms are located on the left-hand side, which includes the second- and third-order dispersion (β_2 and β_3), the linear optical loss (α), and the gain of Ytterbium-doped fiber (g). For this gain term, the saturation is considered as follows:

$$g = \frac{g_0}{1 + E/E_{sat}} \tag{2-16}$$

where E_{sat} is the saturation energy, E is the pulse energy, and g_0 is the wavelength dependence small-signal gain with Lorenz shape and 40-nm gain bandwidth centered at 1030 nm.

The right-hand side represents the self-phase modulation term. The symbol γ represents the nonlinear coefficient. Here the self-steepening and the Raman effects are neglected for simplicity. We solve the counter-propagating pulses, respectively, without considering the cross-phase modulation between them. Indeed, the pulses in the fiber loop are shorter than 10 ps; the interaction length between the bidirectional pulses is shorter than 2 mm, which is negligible concerning the fiber length. Also, we didn't consider the gain sharing between these two pulses. Due to the asymmetrical placement of gain fiber in the NALM, gain sharing is trivial. In this numerical analysis, we use the same configuration, as shown in Figure 2.2. All the fiber components are polarization-maintaining; the dispersion and nonlinear coefficient are listed in Table 2.1.

Table 2.1: Fiber and gratings parameters used in the simulation

Components	β_2 (ps²/km)	B_3 (ps³/km)	γ (W⁻¹· km⁻¹)	L (m)	g_0 (dB/m)
PMF 1	23	0.041	4.7	0.4	0
YDF	23	0.040	4.7	0.4	5
PMF 2	23	0.041	4.7	0.6	0
Gratings (-GDD)	-6.14e3	17.3	0	Var	0

*We adjust the gratings separation to simulate the laser working states at different net cavity dispersion regions
Var: Variable;
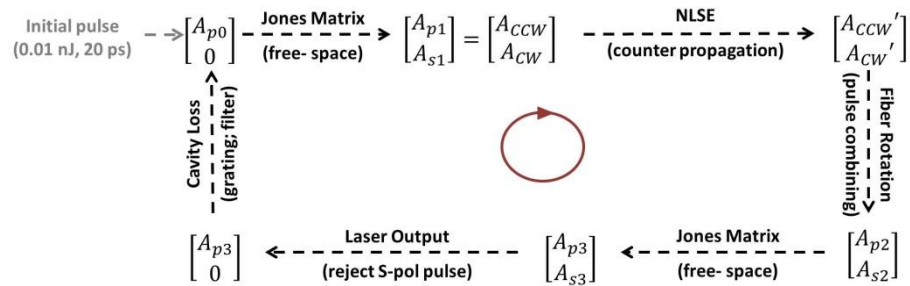
Figure 2.6: Numerical model for a pulse round trip in Figure 9 fiber oscillator. NLSE: nonlinear Schrodinger equation. A 0.01nJ, 20-ps, p-polarization Gaussian pulse is assumed as the initial condition to start the computing process of the first round trip. Jones matrices of free-space components are the same as Section 2.11.

A 0.01nJ, 20-ps, p-polarization Gaussian pulse instead of random white noise is set as the initial electronic field to accelerate the simulation process. The saturation energy E_{sat} in the gain fiber is adjusted to achieve a stable single-pulse steady state. The simulation sequence for one pulse round trip is shown in Figure 2.6. And the starting point of the simulation is p-pol light from PBS 2 in the direction to the NALM. The Gratings in Figure 2.6 with negative group delay dispersion are considered as the cavity loss and dispersion compensation element (-GDD) in Figure 2.2. When we check the pulse dynamics of the all-normal-dispersion laser, the dispersion compensation in the simulation model is removed. The electric field envelope resulting from the last round trip continuously feeds back in the next roundtrip until the resulting envelope converges to a steady state. Then, we break the feeding loop and stop the computing process.

2.2.2 Mode-locking in the all-normal dispersion regime
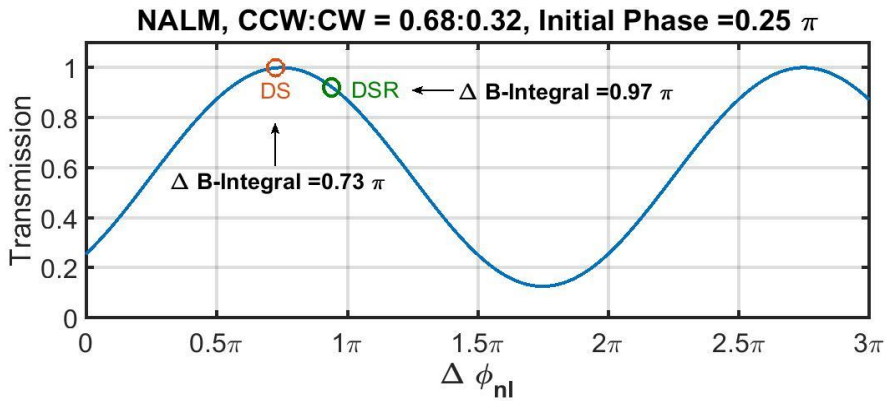
Figure 2.7: Cavity transmission curve in the simulation of all-normal dispersion Figure 9 laser. Blue curve: the cavity transmission versus the $\Delta\varphi_{nl}$ of counter-propagating pulses; Orange Dot: the pulse peak transmission when it is dissipative soliton mode-locking; Green dot: dissipative-soliton-resonance (DSR) mode-locking.

Oscillators delivering pulses with higher energy are always appreciated for the possibility to avoid complicated amplification processes. Traditional soliton is generated in a fiber laser cavity by balancing the negative cavity dispersion and the nonlinear Kerr effects. However, limited by the soliton area theorem, the pulse energy is usually below 0.1 nJ. In 2007, Chong et al. demonstrated a new type of soliton generated in the all-normal dispersion regime, enabling one order of magnitude improvement of pulse energy [36], [127]. Because the dissipative process is crucial for mode-locking, this type of soliton is named "dissipative solitons (DSs)." Besides DSs, Change et al. proposed another concept of soliton formation by solving the complex CGLE with specific parameters in the normal cavity dispersion region [44]. The energy of the so-called "dissipative soliton resonance" (DSR) pulse can be increased further since the peak power of the DSR pulse is clamped at a relatively low level.

All-normal-dispersion Figure-9 laser can generate high energy DS/DSR pulse in an environmentally stable structure. However, the pulse characteristics of all-normal-dispersion Figure-9 laser have not yet been discussed in the publications. In this section, we numerically investigate the pulse dynamic and characteristics in the all-normal-dispersion regime of the Figure-9 laser when the net dispersion of the

cavity is 0.032 ps². Two types of stable mode-locking pulses can be generated in different pumping conditions (different values of E_{sat} in the simulation). The DS pulse is generated by monotonic saturable absorption with lower pump power, and the DSR pulse is achieved by over-driving the cavity transmission curve (reaching the anti-saturable absorption region) with higher pump power. The DSR pulse enables considerable pulse energy due to its peak-power-clamping effect.

In the simulation, the linear cavity loss is set to be 80%, the phase bias is $1/4\pi$, and the energy splitting ratio between CCW and CW pulses is 68: 32. The setting of WP and HWP enables an artificial saturable absorber with a modulation depth of 70%, as shown in the blue curve of Figure 2.7. Reference [128] indicates that in the case where the net cavity dispersion is positive, substantially higher modulation depths are required to generate the steady-state pulses. Whereas, in the abnormal net dispersion region, the ~ 1.5% modulation depth is large enough to sustain a stable soliton pulse. In our case, the 70% modulation depth is sufficient to stabilize DS and DSR in the cavity with all-normal-dispersion without the need for additional spectral filtering to sustain the pulses.

By increasing the pump power, the DS steady-state can evolve into the DSR state. The reason for this transformation is that the pump power changes $\Delta\varphi_{nl,max}$ in the Signac loop so that the DS pulses working in the monotonic saturable absorption region slowly shift into the anti-saturable absorption region as shown in Figure 2.7. In the anti-SA region, the DSR pulses can be generated and sustained.

2.2.2.1 Dissipative Soliton (DS)
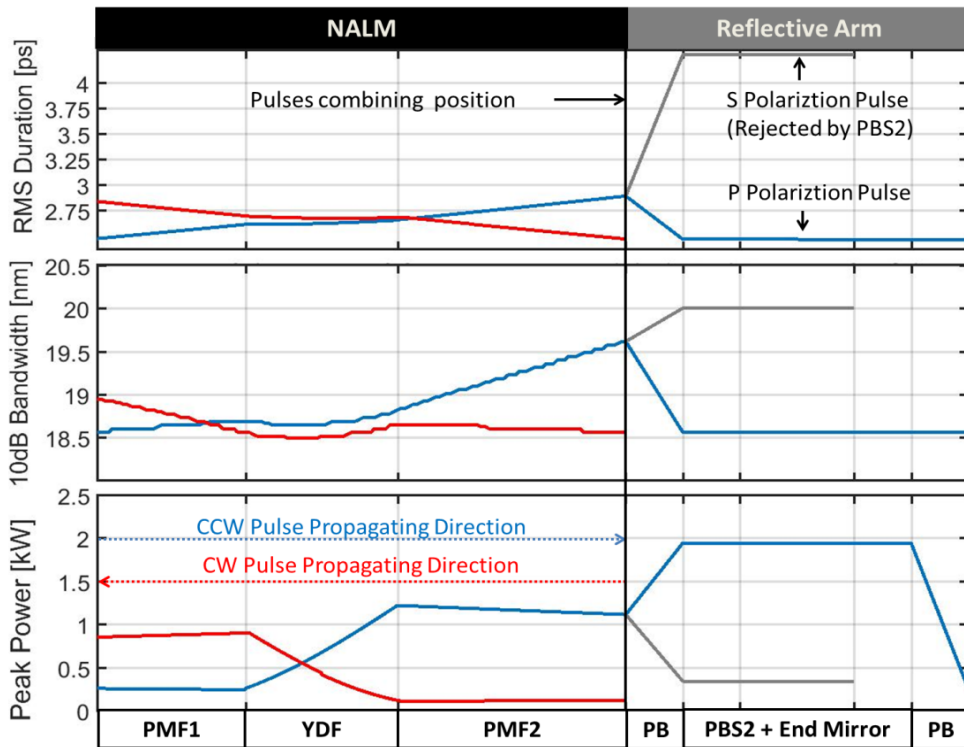
Figure 2.8: Pulse duration. spectral bandwidth and peak power evolution during one DS pulse round trip. At the combining point, CW pulse and CCW pulse combined by PBS1; PB: phase bias and HWP; Pulse split into two pulses in p-polarization and s-polarization after PB in the linear arm. S-polarization pulse is rejected from the cavity after PBS 2.

Chapter 2: Ultrafast polarization maintaining Figure 9 fiber oscillator

The orange dot in Figure 2.7 shows the ΔB-integral in the NALM and the corresponding transmission of pulses' peak intensity at the position of PBS2 when the oscillator reaches dissipative soliton steady-state. At DS state, the peak of pulses has the highest transmission, and the wings of pulses and small-signal noise are suppressed. This enables a monotonic saturable absorption effect imposed on the pulse. The intensity-dependent transmission shortens the pulse duration and results in a single pulse steady-state. Due to the highly chirped characteristic of pulses in the all-normal dispersion laser cavity, pulse shortening comes along with spectral filtering. The spectrum components corresponding to the pulse's edges in the temporal domain are suppressed and rejected from the oscillator cavity. Such a spectral dissipation process compensates for the combined influence from the normal dispersion and the nonlinear effect, which broadens the spectrum of pulses. Because the dissipative processes of gain and loss, as well as the dissipative process of spectral broadening and filtering, play a crucial role for pulse stabilization in the normal dispersion mode-locking regime, the pulses are named by "dissipative solitons (DSs)."

A stable dissipative soliton steady state could be observed when the saturated pulse energy (E_{sat}) is set to be around 1.5 nJ. Figure 2.8 shows the evolution of RMS pulse duration, 10-dB bandwidth, and peak power of dissipative soliton in one round trip. Both the pulse duration and the spectrum bandwidth of counter-propagating pulses are minimum at the entrance of NALM and grow monotonically in the fiber loop. At the end of the loop, the CW pulse and the CCW pulse combine into a vector pulse with both p- and s-polarization components. Then the combining pulse travels through phase bias components, which rotate the polarization state of the vector pulse. In the end, the resulting pulse component in the s-polarization is rejected from the cavity by PBS 2 while the p-polarization component transmits and is reflected by the end mirror into the NALM again. It needs to be noted that dissipative solitons keep their linear positive chirp for the whole round trip, and the shortest pulse in the cavity is located at the entrance of NALM. The breathing ratio of RMS pulse duration and spectral bandwidth is small for one pulse oscillating round trip.

The mode-locked pulses and spectrums at the end of the NALM are shown in Figure 2.9 (a) and (b) when E_{sat} is 1.5 nJ. Because the CCW pulse has larger initial pulse energy and is amplified earlier in the NALM, it accumulates a larger nonlinear phase shift than the CW pulse. The B-integral difference between the counter-propagating pulses in the NALM is 0.73 π. The transmission of pulse peak intensity at PBS2 (as shown in Figure 2.7 (orange dot)) is close to 100%, while the pulse wings have only 30% transmission.

Figure 2.9 (c) and (d) show the p- and s- polarization pulses and their spectrum components in the reflection arm when E_{sat} is 1.5 nJ. The p-pol pulse transmits through PBS2, and the s-pol pulse is rejected from the oscillator cavity. It is easy to tell that the s-pol pulse component with lower peak power, which is located at the edges of the vector pulse, gets rejected. Therefore, the transmission of PBS2 plays a role as a saturable absorber to shorten the pulse duration. Besides, PBS2 also serves as a bandpass filter, which rejects the spectral edges (spectrum of s-pol pulse), as shown in Figure 2.9 (d), and the center spectral component remains in the cavity. Such a spectrum dissipative process helps to stabilize pulse in the all-normal-dispersion regime. The numerically compressed pulses and their corresponding transform-limited (TL) shape are shown in Figure 2.10 (a) and (b), respectively. Compared with the s-pol pulse, the p-pol pulse after compression shows better quality with the Strehl ratio close to 1, while the s-pol pulse contains massive incompressible pedestals due to its more complicated spectral phase.

Figure 2.9: Pulses and spectra from ANDi Figure 9 laser delivering DS pulse. CCW and CW pulses (a) and their spectrums (b) at the end of NALM; p- and s-polarization pulse component (c) and their spectrum (d) at the position of PBS2 in the reflection arm.
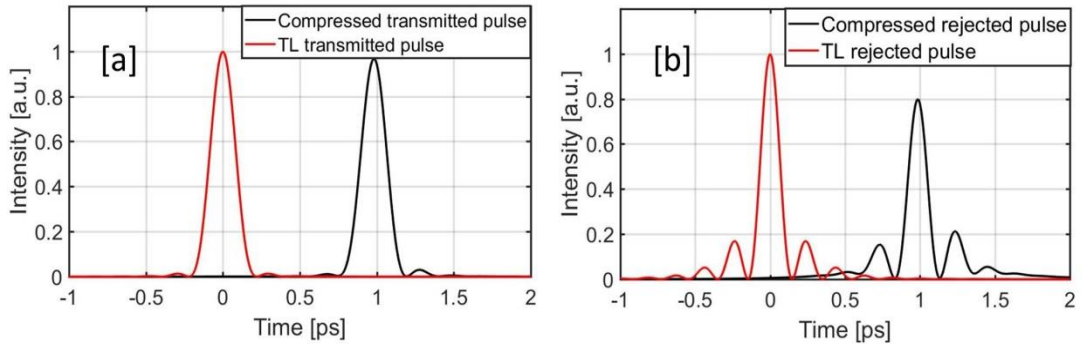
Figure 2.10: Compressed pulses and the corresponding TL pulses of dissipative soliton. (a) The numerically compressed transmitted pulse (black) and its transform limit (red); (b) the numerically compressed rejected pulse (black) and its transform limit (red) when the E_{sat} is 1.5 nJ.

We further record the peak power build-up process of p- and s-pol pulses before the oscillator reaches its steady state. As it shows in Figure 2.11, after about 50 round trips, the Figure-9 laser starts to deliver a stable DS pulse. The energy of the transmitted pulse (p-pol) is 6.78 nJ, while the rejected pulse (s-pol) has an energy of 1.08 nJ. There is an over-shooting of both the peak power and the 3-dB bandwidth of the transmitted pulse before the laser reaches its steady state. The over-shooting effect becomes more apparent when the pump power (E_{sat}) is increased in the simulation. By checking the pulse in the 16th

round trip in Figure 2.11 (the over-shooting pulse before reaching the steady state), we find that the $\Delta\varphi_{nl,max}$ of the counter-propagating pulses is larger than $0.75\,\pi$ in Figure 2.7, and the peak intensity of pulse reaches the over-driven region of the cavity transmission curve. However, this state is not stable, so that the pulse peak power drops back afterward due to the anti-saturable absorber effect. It finally reaches a steady state where the pulse peak has the highest cavity transmission.
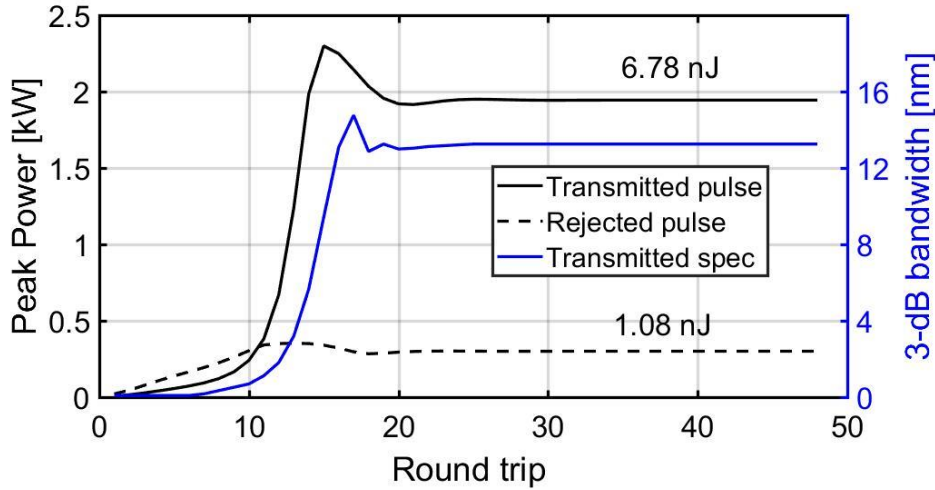
Figure 2.11: DS pulse peak power building up process before mode-locking. Black solid curve: the transmitted pulse from PBS2, black dash curve: the rejected pulse from PBS2; blue solid curve: the 3-dB spectrum band width of the transmitted pulse.

2.2.2.2 Dissipative-Soliton-Resonance (DSR)

As the cavity transmission of the Figure-9 laser shows a sinusoidal function in Figure 2.7, once the ΔB-integral between the bidirectional propagating pulses in the NALM is larger than 0.75π, the peak intensity of pulse enters the anti-saturable absorber region. In a fiber laser cavity with all-normal dispersion, the peak-power-clamping effect occurs due to the anti-saturable absorption [116]. When this effect is strong enough, both the pulse peak power and the pulse spectral 3-dB bandwidth are confined to a small value. At the same time, further increasing the pump power leads to longer pulse duration and higher pulse energy with constant peak power. To achieve the DSR mode-locking state, we increase the pump power by changing E_{sat} from 1.5 nJ to 10.5 nJ in the simulation. At the threshold value of 4.5 nJ, the flat-top DSR pulse is generated with fixed peak power.

Figure 2.12 (a) and (b) show the counter-propagating pulses and their spectra at the end of the NALM when the pump power (E_{sat}) is changed. As the pump power increases, the pulse evolves into the flat-top shape with clamping peak power at around 1.6 kW for the CCW pulse (1.2 kW for the CW pulse). The pulse duration grows along with higher pulse energy under higher pumping. At the same time, the corresponding 3-dB spectral bandwidth decreases. For all the pulse pairs shown in Figure 2.12 (a), the B-integral difference is around 0.95π, so that the pulse peak transmission is champed at the value of 90% (as shown in Figure 2.7: green dot). In this case, the cavity transmission (artificial SA) is no longer a monotonic intensity-dependent function. The over-driving SA effect satisfies the particular parameter space in complex CGLE for DSR generation in the normal net dispersion regime, resulting in a flat-top DSR pulse. DSR pulses have a rectangular spectral base with steep edges, as shown in Figure 2.12(b).

The spectral base part does not change with the pumping power. However, the spectral peak located at the center shrinks as pulse duration increases. The spectral peak corresponds to the flat-top part of pulses while the base spectral component corresponds to the edge of pulses.
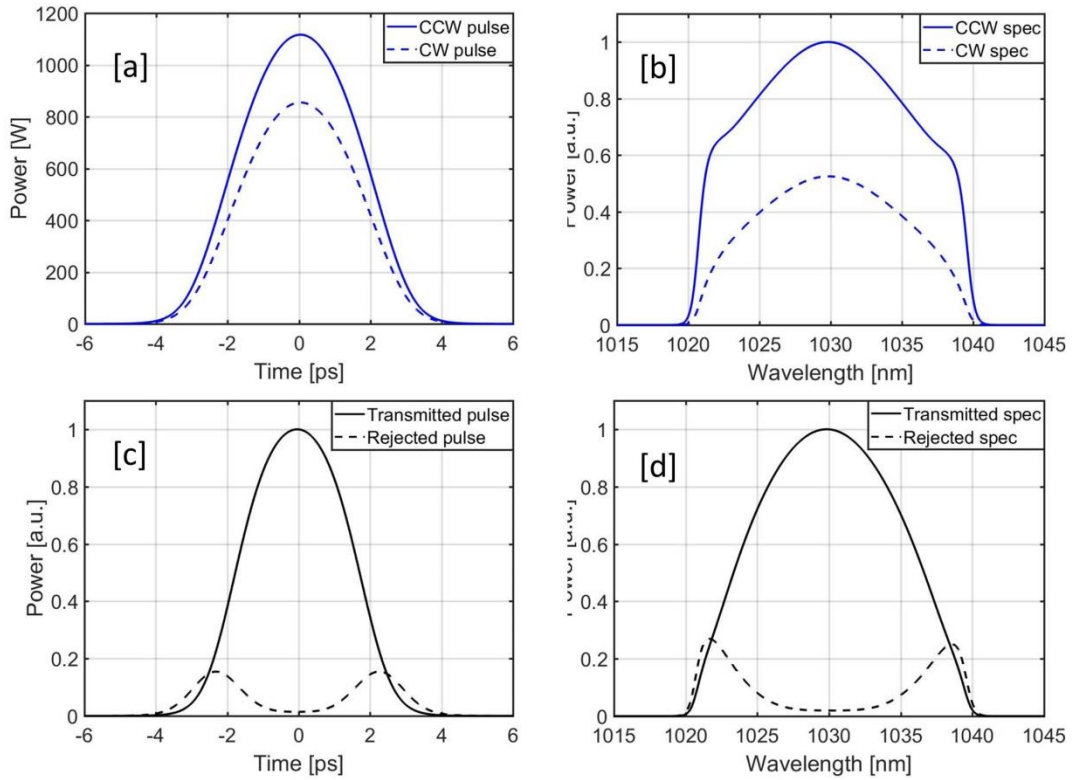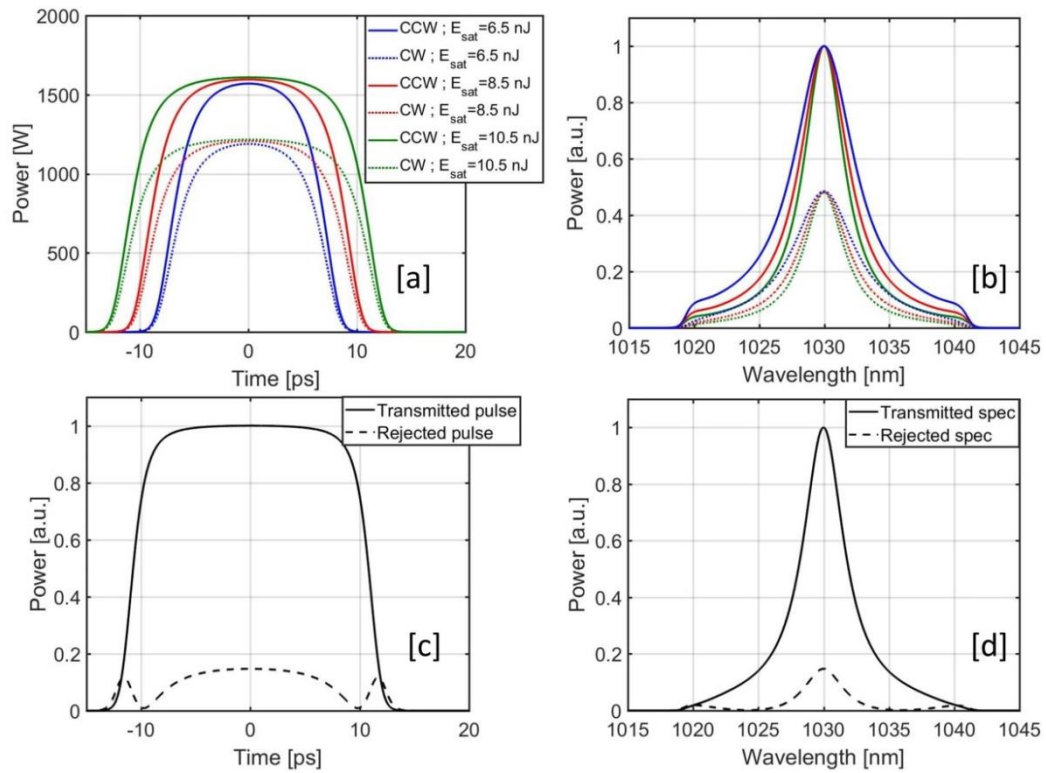

Figure 2.12: Pulses and spectra from ANDi Figure 9 laser delivering DSR pulse. CCW and CW pulse (a) and their spectrum (b) at the end of NALM under different pump power (different Esat); p- and s-polarization pulse components (c) and their spectrums (d) at the position of PBS2 in the reflection arm when E_{sat} is 10.5 nJ.

In the steady state of DSR pulse, the nonlinear phase shift is dramatically reduced by the peak-power-clamping effect, enabling the generation of enormous pulse energy directly from the oscillator. DSR pulse energy has been boosted up to uJ level by using double-cladding gain fiber in the nonlinear amplifier loop mirror [108]. Besides, the flat-top pulses are suitable for the following fiber amplifiers since their specific pulse shape can lead to less nonlinear phase shift accumulation in the fiber. Figure 2.12(c) and (d) show the transmitted pulse (p-polarization) and rejected pulse (s-polarization) in the reflection arm and their corresponding spectrums when E_{sat} is 10.5 nJ. Compared with pulses in Figure 2.12(a), the transmitted pulse also has a flat top, but its spectrum is in a Lorenz shape without the rectangle base. The temporal and spectral profiles of the rejected pulse are complicated due to the over-driving effect of the S.A.

The evolution of RMS pulse duration, 10-dB spectral bandwidth, and peak power of DSR pulse for one oscillator round trip are shown in Figure 2.13. Compared with the DS pulse shown in Figure 2.8, DSR has one order of magnitude longer pulse duration and narrower spectrum. Besides, the pulse duration is almost unchanged within the oscillator (blue curve), and the spectra of counter-propagating DSR pulses shrink in the NALM. In contrast, the spectra of DSs broaden in the fiber loop (Figure 2.8). Though the pulse energy and spectrum characteristics are quite different, the peak power evolution of

both types of pulses is similar. The pulse with the highest peak power is the transmitted pulse in the reflection arm.
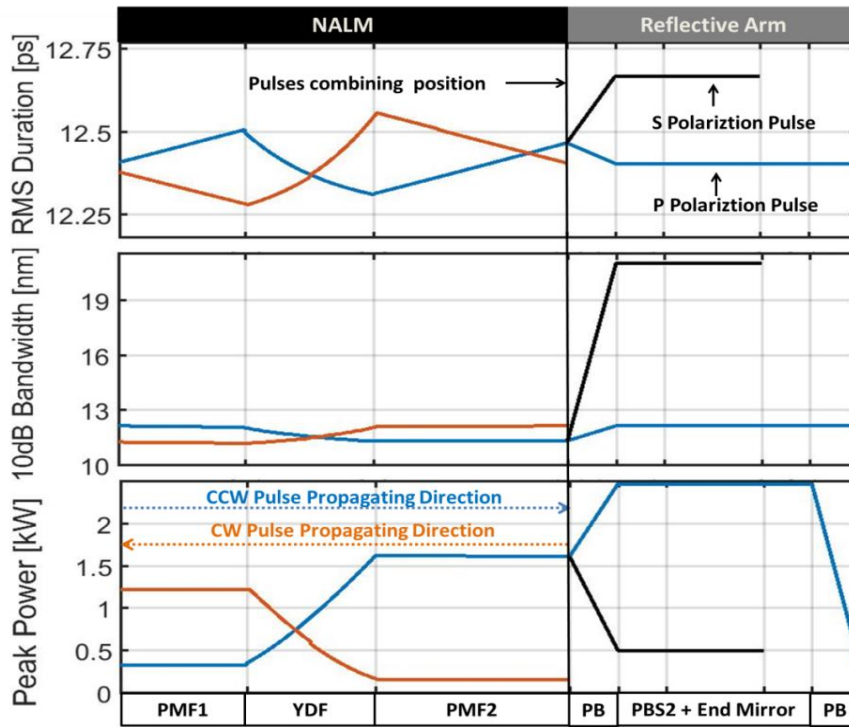
Figure 2.13: Pulse duration. spectral bandwidth and peak power evolution during a DSR pulse round trip. At the combining point, CW pulse and CCW pulse combine at PBS1; PB: phase bias and HWP; Pulse split into two pulses in p-polarization and s-polarization after PB in the reflection arm. S-polarization pulse is rejected from the cavity after PBS 2.
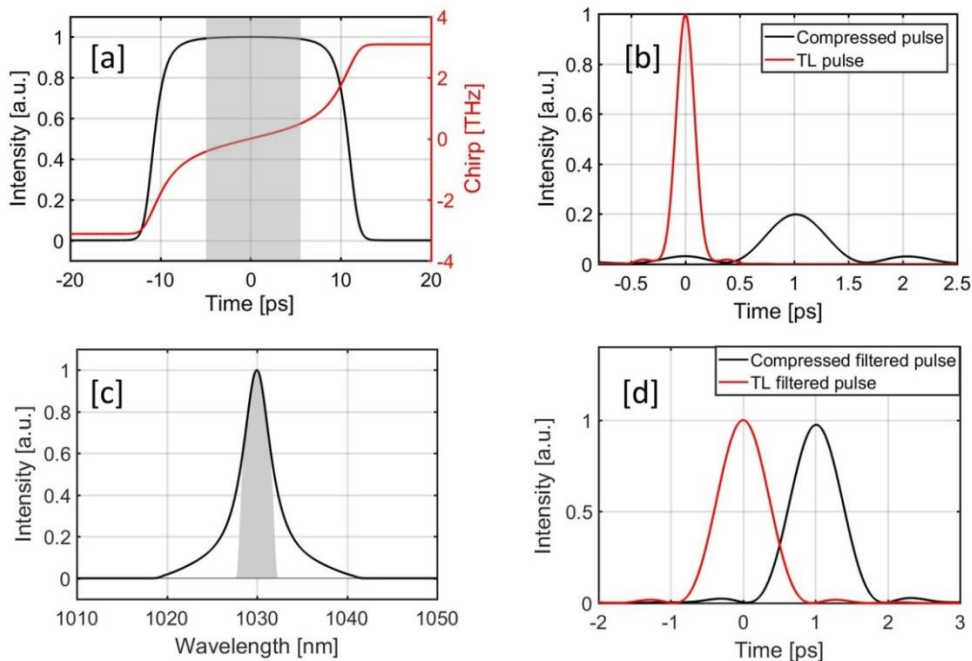
Figure 2.14: Compressed and the corresponding transform limited formation of DSR pulse. (a) The transmitted pulse (p-pol) at PBS2 and its corresponding instant frequency when E_{sat} is 10.5 nJ. (b) The

compressed transmitted pulse and the corresponding transform-limited pulse. (c) The spectrum of the transmitted pulse, the grey shadow is the filtered spectrum after a 4-nm bandpass filter. (d) The compressed filtered pulse and the corresponding transform-limited pulse.

The DSR pulse from the oscillator has a highly nonlinear chirp. It is impossible to compress the DSR pulses by a pair of gratings compressor. We take the transmitted pulse (p-pol pulses) in the reflected arm as an example (see Figure 2.14). The chirp of instantaneous frequency in the pulse center part is different from the chirp in the pulse edges, as shown in Figure 2.14 (a). When the pulse is numerically compressed by a Littrow grating pair with 1000 grooves, the Strehl-ratio of the compressed pulse is only 0.2 (see Figure 2.14 (b)). The incompressible pedestal is due to the highly nonlinear chirp crossing the whole pulse. When a 4-nm super-Gaussian bandpass filter is inserted to cut off the spectral edges, as shown in Figure 2.14 (c), we can achieve a filtered pulse with a nearly linear chirp (Figure 2.14 (a), the grey part). The compressed pulse after filtering and its transform limit formation are shown in Figure 2.14(d). Its Strehl-ratio is close to 1, indicating that the compressed pulse has a transform-limited formation. After filtering, the pulse lost 50% pulse energy, and the pulse duration decreases too.
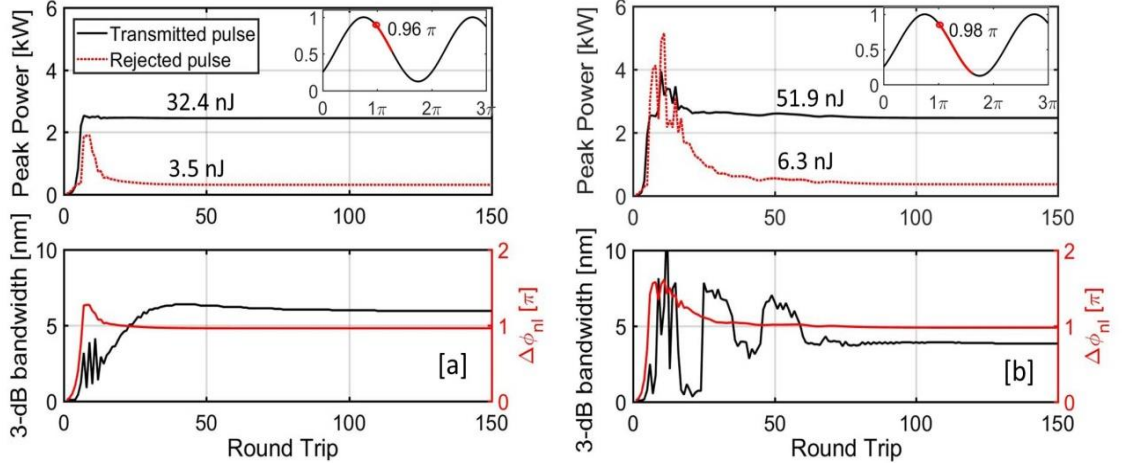
Figure 2.15: DSR pulse building up dynamic as a function of continual oscillating round trips. Top row: the peak power of both the transmitted pulse (black) and the rejected pulse (red) for each round trip; bottom row: the 3-dB spectral bandwidth of the transmitted pulse and the maximum $\Delta\varphi_{nl}$ in the NALM for each round trip. Inset: the cavity transmission curve (black) and the over-driving effect (red) before the laser is mode-locking; the red dot in the inset: the mode-locking point. (a) E_{sat}=6.5 nJ. (b) E_{sat}=10.5 nJ.

The peak power build-up process of the DSR pulses in the reflection arm is displayed in Figure 2.15 for two different pump powers. The black curve and the red curve in the top row show the peak power build-up process of the transmitted and the rejected pulse, respectively. Regardless of the difference in the pump power, the peak power of the transmitted (rejected) pulse is always stabilized at ~2.5kW (~0.5kW). Due to the peak-power-clamping effect, ΔB-integrals in the NALM at the steady state are also clamped at a fixed value (see Figure 2.15, inset: red dot). It is noteworthy that the fixed ΔB-integral corresponds to an overdriven region of the cavity transmission curve, which is a critical condition for the generation of DSR pulses in this cavity. The black curve in the bottom row shows the 3-dB spectral evolution of the transmitted pulse, and the red curve is the maximum differential nonlinear phase shift $\Delta\varphi_{nl}$ accumulated in each round trip. For both pump conditions, the maximum $\Delta\varphi_{nl}$ surpasses the monotonically increasing

region of the cavity transmission curve and finally stabilizes at a value of 0.98π. For the several initial roundtrips, $\Delta\varphi_{nl}$ is even larger than 1.3π. The corresponding cavity transmission curve has a negative slope, resulting in a strong anti-saturable absorption effect on the pulse peak intensity. This effect gradually shapes the transmitted pulse into the characteristic DSR pulse with a flat-top intensity profile.

Compared with the build-up process of the pulse peak power when pump power is lower in Figure 2.15(a), Figure 2.15(b) shows that the peak power of the rejected pulse reaches up to 5 kW for a short time before it drops to a steady-state of 0.5 kW for higher pumping. This over-shooting phenomenon of pulse's peak power becomes severe when the pump power is comparable higher. Under the condition of intense pumping, the maximum $\Delta\varphi_{nl}$ accumulated by the counter-propagating pulses in the NALM reaches deep into the anti-saturable absorber region of the cavity transmission curve (see Figure 2.15, inset: red curve). A large amount of power is dumped out from the cavity so that the rejected pulse energy grows up at the first several round trips. Then, the $\Delta\varphi_{nl}$ decreases gradually since the pulse evolves into a profile with a flat-top and longer pulse duration. This severe over-shooting issue might be a reason for breaking down in fiber-optic components during the laser starting process under high pump power.
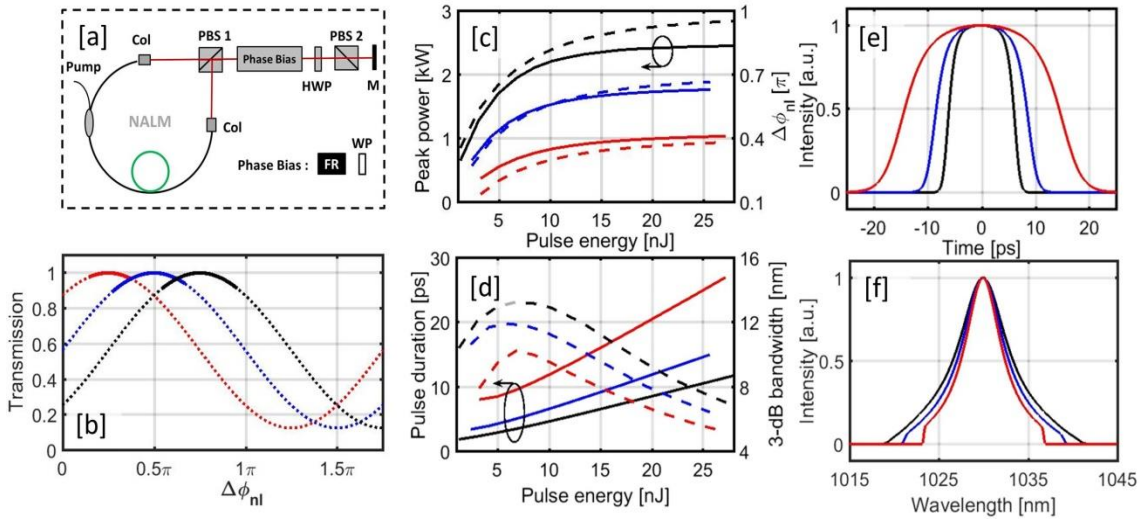
Figure 2.16: Pulse characteristics versus pulse energy in the ANDi Figure 9 laser with different phase bias. (a) the schematic of laser setup; (b) the cavity transmission curve with different phase bias (Black: 0.25 π; Blue: 0.5 π; Red: 0.75 π) but the same input energy splitting ratio at the entrance of NALM (68:32); (c) the peak power and the maximum $\Delta\varphi_{nl}$ in the NALM versus the mode-locking transmitted pulse's energy; solid curve: peak power; dash curve: the maximum $\Delta\varphi_{nl}$; (d) the FWHM pulse duration and the 3-dB spectral bandwidth versus the mode-locking transmitted pulse energy; solid curve: pulse duration; dash curve: 3-dB spectral bandwidth; (e) the profile of the mode-locking transmitted pulses with 28.5-nJ pulse energy; (f) the corresponding spectrum of the mode-locking transmitted pulses with 28.5-nJ pulse energy; (c-f) blue, red and black represent the output from Figure 9 laser with different cavity transmission curve, as shown in (b).

To further investigate the transition between DS and DSR pulse when the pump power increases, we carry out more simulation by scanning the pump power while fixing the other cavity parameters (fiber length, the energy splitting ratio of NALM, and the reciprocal phase shift). The peak pulse, 3-dB bandwidth and pulse duration of the transmitted pulse in the reflection arm, as well as the maximum $\Delta\varphi_{nl}$

(ΔB-integral) of the counter-propagating pulses in the NALM, are recorded for the laser build-up process. The laser configuration is shown again in Figure 2.16(a). The cavity transmission is shown as the black curve in Figure 2.6(b) when the corresponding phase bias between the counter propagating pulses is 0.25π and the energy splitting ratio is 68:32 at the entrance of NALM. The solid part of the transmission curve represents the range where the laser can mode lock. The black curve in Figure 2.16 (c) shows the pulse peak power and the ΔB-integral of counter-propagating pulse in the NALM versus the transmitted pulse energy (intra-cavity pulse). It is found that increasing pump power finally leads to peak power clamping and the saturation of ΔB-integral, a signature of DSR pulse generation. The smooth evolution of peak power into its clamping-state in Figure 2.16(c) indicates that the DS pulse gradually evolves into DSR pulse by adjusting pumping power. The black curve in Figure 2.16 (d) shows the corresponding pulse duration and 3-dB spectral bandwidth versus the pulse energy. The FWHM duration of the transmitted pulse in this laser cavity increases along with the pulse energy. However, the 3-dB spectral bandwidth rises along with the intra-cavity pulse energy for a relatively low pump power and decreases afterward as the pump power keeps increasing.

The values of the saturated peak power, pulse duration, 3-dB spectral bandwidth of the mode-locking intra-cavity pulse in the reflection arm also depend on the initial phase bias. We simulate the oscillator output using different phase bias values, as shown in Figure 2.16 (b) and record the pulse parameters versus the pulse energy. It is found that the large phase bias ($0.75\,\pi$, red curve) can lead to a DSR pulse with lower peak power and a smaller value of the saturated ΔB-integral (see Figure 2.16 (c), red curve). Besides, the cavity transmission with large phase bias results in a longer pulse duration and a narrower spectrum at the steady state. Figure 2.16 (e) and (f) show the pulses' profile and spectra when the intra-cavity pulse energies are 28.5 nJ. The longest pulse with a narrow spectrum is from the oscillator with $0.75\,\pi$ initial phase bias (red curve).

Apart from the initial phase bias, the variation of the energy splitting ratio at the entrance of NALM can also influence DS and DSR pulses' parameters. Figure 2.17(a) shows the transmission curve of NALM with different energy splitting ratios at its entrance when the phase bias is fixed at 0.5π. The pulses are stabilized when the ΔB-integral in the NALM is within the range of the solid curve in Figure 2.17(a). Again, Figure 2.17(b) shows the changes in peak power of pulse in the reflection arm and the ΔB-integrals in the NALM along with the intra-cavity pulse energy. It is found that pulses' peak power is clamped at a different level due to the change of energy splitting ratio, while the saturated ΔB-integrals are almost the same. Obviously, the more even energy splitting ratio enables the generation of DSR pulse with higher peak power. Figure 2.17 (c) shows the pulse duration and spectrum bandwidth change along with the intra-cavity pulse energy. The simulation result reveals that balancing the energy splitting ratio can achieve a shorter pulse duration and a broader spectrum. The typical spectrum and pulse are shown inset of Figure 2.17(a), corresponding to the blue dot in Figure 2.17(b).

Through Figure 2.16 and Figure 2.17, we prove that the change of phase bias and energy splitting ratio at the entrance of NALM influences the parameter of DS and DSR pulses. The higher peak power pulse with a shorter pulse duration and broader spectrum bandwidth is always enabled by a smaller phase bias and a more balanced energy splitting ratio.
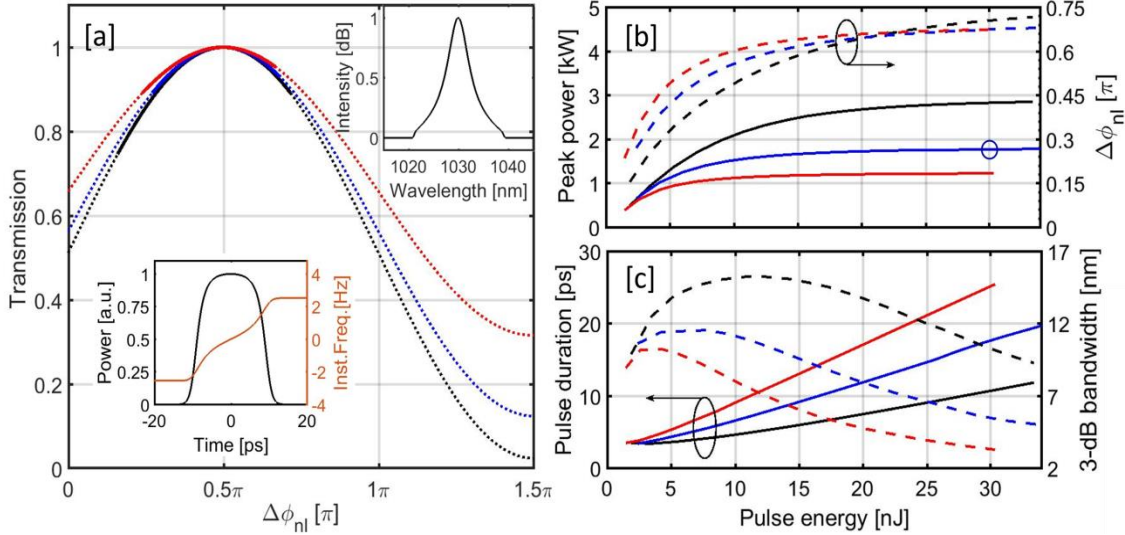
Figure 2.17: Pulse characteristics from ANDi Figure 9 laser with different energy splitting ratio. (a) the cavity transmission curve with different energy splitting ratio at the entrance of NALM, and the initial phase bias is 0.5π; black: 58: 42; blue: 68: 32; red: 78: 22. (b) When the laser is mode-locking, the change of peak power of the intra-cavity pulse and ΔB-integral in the NALM along with the intra-cavity pulse energy; solid curve: peak power; dash curve: ΔB-integral. (c) The pulse duration and spectrum bandwidth of intra-cavity pulse changes with its pulse energy; solid curve: pulse duration; dash curve: spectral bandwidth.

2.2.3 Mode-locking in dispersion management regime

Short pulse duration and low noise operation (f_{ceo} phase noise [39], intensity noise [129], [130], and timing jitter [131], [132]) are other essential aspects for the fiber lasers. Low-noise fiber laser has versatile usages such as optical frequency combs [125] and timing distribution system [84]. The dispersion management NALM laser is proved to have a state-of-art noise performance for its mode-locking mechanism [39]. In this section, we investigate the dispersion management of the Figure-9 laser based on Yb-doped fiber. The characteristics of stretched pulse mode-locking are investigated numerically and experimentally. The pulse dynamics of dispersion management mode-locking, and the dynamic of the pulse building process, are shown in the simulation. We also pursue the possibility to generate an ultrashort transform-limited pulse directly out from the laser cavity experimentally, which will favor the applications like self-reference frequency comb and nonlinear microscopy [133].

2.2.3.1 Pulse dynamics in one oscillating round trip

The dispersion management Figure-9 laser structure is shown in Figure 2.18. The NALM part includes a polarization beam splitter (PBS1), 0.4-m polarization-maintaining fiber (PMF1), 0.4-m Yb-doped fiber (YDF), and 0.6-m PMF2 in a sequence. The reflection arm consists of the phase bias (PB), a 50-nm bandpass filter, an intra-cavity pulse compressor (GP, transmission grating pair), the second polarization beam splitter (PBS2), a QWP and the end mirror. Compared with the all-normal-dispersion Figure-9 laser, a pair of gratings is inserted into this cavity in a double-pass configuration. The polarization beam splitter is put after the gratings, exactly in the middle of abnormal GDD components. The QWP in front of the

end mirror is used for coupling out part of the intra-cavity pulse (Port 2, p-pol), while Port 1 is the output for the rejected pulse (s-pol). The 50-nm bandpass filter is inserted into the cavity for center wavelength stabilization. The grating distance is turned numerically to achieve -63-fs2 net cavity GDD. The HWP and QWP are set so that the transmission curve has a phase shift of 0.33π, and the energy splitting ratio between the counter-clockwise and the clockwise pulses is 58:42. The gain of Yb fiber is adjusted to achieve a steady-state in the simulation when the transmission of pulse peak power in the reflection arm is highest when the ΔB-integral in the NALM is 0.66 π. The stable dispersion-management pulse is generated in this cavity after 80 round trips. The pulse evolution dynamics at the steady state for one oscillator round trip is shown in Figure 2.19.
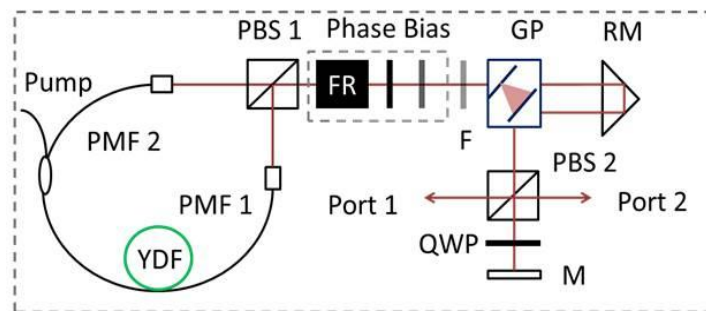
Figure 2.18: Schematic of Yb-based dispersion-managed Figure 9 oscillator. FR: Faraday-Rotator; HWP: half wave plate; QWP: quarter wave plate; PBS: polarization beam splitter; Col: collimator; GP: the grating pair; RM: roof mirror; PMF: polarization maintaining fiber; YDF: ytterbium doped fiber; Phase Bias is consisted by a FR, a QWP and a HWP in a sequence. F: 50-nm bandpass filter centered at 1030 nm.
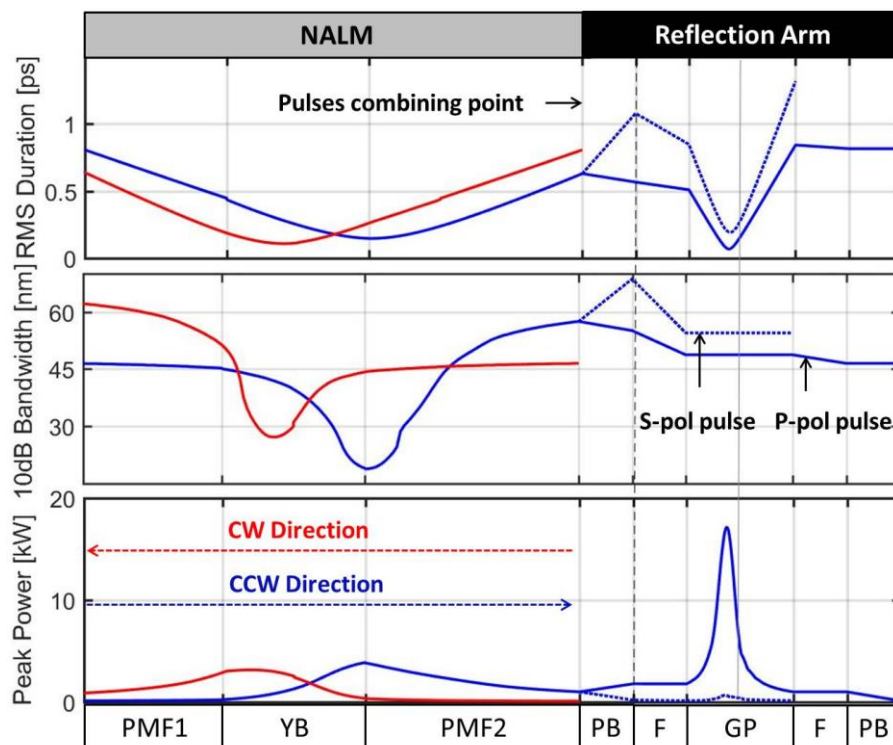
Figure 2.19: Pulse duration. 10-dB spectrum bandwidth and peak power evolution during one oscillator round trip for the stretched pulse mode-locking at close-to-zero net cavity dispersion region. At the

combining point, CW pulse and CCW pulse combine at PBS1; PB: FR, QWP and HWP; Pulse split into two pulses in p-polarization and s-polarization after PB in the linear arm. S-polarization pulse is rejected from the cavity after PBS 2. PBS2 is located in the center of grating pair.

It is found that the DM pulse is compressed to its transform-limited (TL) formation twice for one round trip. The first chirp-free pulse exists in the fiber loop with normal GDD, and the second one appears near the center of abnormal GDD components. The breathing rate of pulse duration and spectral bandwidth in the NALM are ~8 and ~3, respectively. The pulses in the reflection arm have ~50 nm 10-dB spectral bandwidth. The highest peak power of the pulse inside the fiber loop is ~ 4 kW. In this regime, the lowest noise performance of fiber laser can be achieved because of the suppressing the ASE quantum noise by generating a broader mode-locking spectrum [134]. Besides, the all-PM-fiber configuration and sinusoidal transmission function of NALM lasers further reduce the laser noise level [135]. All these facts make dispersion-managed figure 9 a promising fiber oscillator for the ultra-low noise operation.
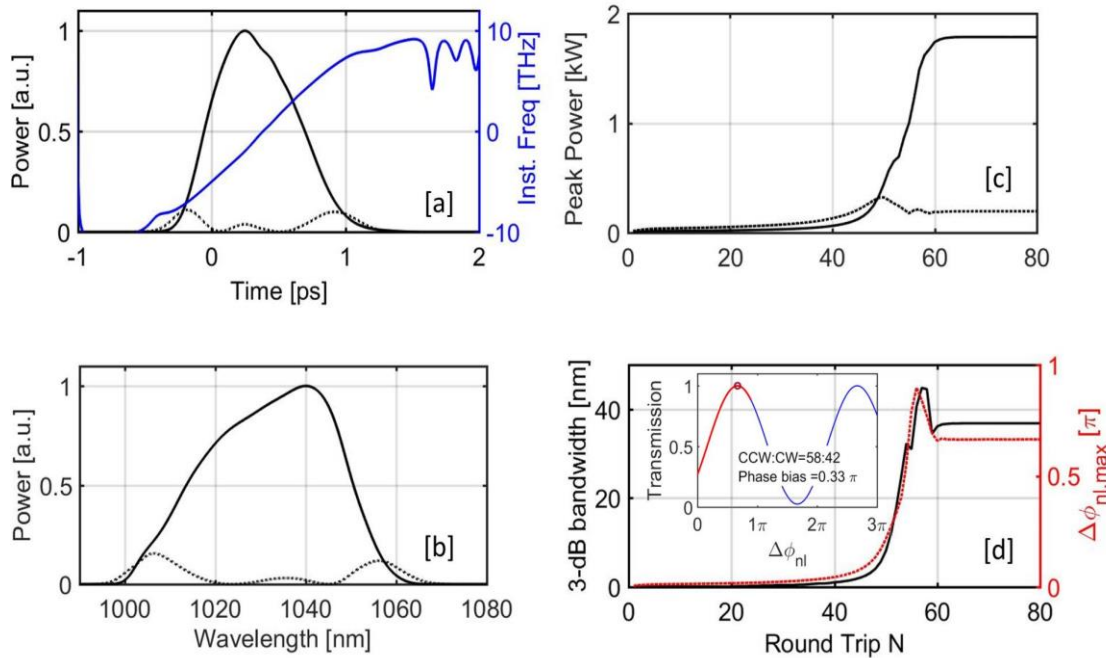
Figure 2.20: Pulses, spectra and peak power characteristics of the stretched pulse. (a) the profile of p-pol (solid curve) and s-pol (dot curve) pulses and the instant frequency of p-pol pulse (blue curve) (b) the corresponding spectrum of p-pol and s-pol pulses; (c) the peak power of p-pol and s-pol pulses building up process before mode-locking. (d) the 3-dB bandwidth of p-pol pulse and the ΔB-integral of the counter-propagating pulse in the NALM for each round trip before mode-locking; inset: the cavity transmission curve (blue)，the range of pulse peak transmission before mode-locking (red), the pulse peak transmission when it is mode-locked (red dot).

The corresponding temporal profiles of p-pol and s-pol pulses and their spectra in front of the bandpass filter (marked with the black dash line in Figure 2.19) are shown in Figure 2.20. The p-pol pulse (the intra-cavity pulse) has a clean temporal profile with a highly linear chirp. The s-pol pulse at the temporal edge of the combined vector pulse is dumped out by the PBS2. Because the p-pol and s-pol pulses are positively linearly chirped, their spectra shapes are similar to their temporal profiles. In the

stretched pulse mode-locking regime, the spectrum of the intra-cavity pulse (p-pol) is ultra-broad (see Figure 2.20(b)), covering 1000-1060 nm, corresponding to TL pulse duration of ~60 fs. The peak power build-up dynamic of p-pol and s-pol pulses before reaching the steady state are shown in Figure 2.20(c), indicating that the stable mode-locking is established roughly after 80 round trips by using the 20-ps Gaussian pulse with 0.01-nJ as the initial field. The over-shooting phenomenon of the peak power is not apparent in the stretched pulse mode-locking regime, for the peak power of both p-pol and s-pol pulses slowly builds up along each round trip. However, the 3-dB spectrum of intra-cavity pulse and the ΔB-integral in the NALM, however, show an over-shooting before the oscillator reaches the steady-state, as shown in Figure 2.20(d). The over-shooting ΔB-integral drives the oscillator into an anti-saturable absorber region (see Figure 2.20(d), inset: red part). Afterward, the feedback process of the oscillator pulls back the value ΔB-integral and finally stabilizes the laser at the point with the highest cavity transmission (see Figure 2.20(d), inset: red dot). Slightly changing the cavity net GDD from abnormal to normal does not influence the pulse dynamic. However, if the absolute value of the cavity net GDD exceeds the corresponding threshold, a similariton or a soliton can be generated in the dispersion-management NALM laser.

Figure 2.21: Pulse duration. 10-dB spectrum bandwidth and peak power evolution during one oscillator round trip for the soliton mode-locking at anomalous net cavity dispersion region (-6300 fs^2). At the combining point, CW pulse and CCW pulse combine at PBS1; PB: FR, QWP and HWP; Pulse split into two pulses in p-polarization and s-polarization after PB in the linear arm. S-polarization pulse is rejected from the cavity after PBS 2. PBS2 is located in the center of the grating pair.

Figure 2.21 shows the soliton pulse evolution dynamics for one round trip in the steady-state (the net dispersion is -6300 fs^2). Like the DM pulse, the soliton pulse is chirp-free at two fixed positions in the cavity, but the breathing ratios of pulse duration and spectral bandwidth are much smaller in the soliton

regime, with the value of ~3 and ~2, respectively. The pulse is shortest at the position close to the exit of the NALM. The ΔB-integral of counter-propagating pulses is 0.25π at the steady-state, lower than the one in the stretched pulse mode-locking regime.

The temporal profile of pulses (p-pol and s-pol) and their spectra before the bandpass filter are shown in Figure 2.22 (a) and (b). Since the soliton pulse accumulates less ΔB-integral in the NALM (see Figure 2.22(d), inset: red dot), the transmission for the intra-cavity pulse (p-pol) is lower and the rejection is higher (s-pol). The rejected pulse (s-pol) is in the same shape as the intra-cavity pulse (p-pol) due to the nearly zero intensity-dependent modulation for the constant phase across the soliton temporal profile (see Figure 2.22(d), inset: red curve). The build-up process of pulse peak power displays an oscillating pattern before entering the steady state, as shown in Figure 2.22 (c). This pattern is not observed in other mode-locking regimes in our simulations. The 3-dB spectrum bandwidth of p-pol pulse and ΔB-integral in the NALM for each round trip are shown in Figure 2.22(d). They all show the modulation pattern when the laser is approaching its steady state. In the soliton pulse regime, the over-shooting phenomenon is absent because of its relatively low pulse energy.

Figure 2.22: Pulses, spectrums and peak power characteristics of soliton mode-locking. (a) The temporal profile of p-pol (solid curve) and s-pol (dot curve) pulses (b) the corresponding spectrum of p-pol and s-pol pulses; (c) the peak power of p-pol and s-pol pulses building up process before mode-locking. (d) the 3-dB bandwidth of p-pol pulse and the ΔB-integral of the counter-propagating pulse in the NALM for each round trip before mode-locking; inset: the cavity transmission curve (blue)，the range of pulse peak transmission before mode-locking (red), the pulse peak transmission when it is mode-locked (red dot).

Figure 2.23 shows the similariton pulse dynamics in a round trip (the cavity net dispersion is 6300 fs²). The similariton oscillates in the cavity with a positive chirp all the time. The pulse duration is compressed to its minimum by the grating pair and then is stretched by the fiber in the NALM. The breathing ratios of pulse duration and spectral bandwidth are 6 and 1, respectively. The pulses and their spectra before entering the bandpass filter are shown in Figure 2.24. The intra-cavity pulse evolves into a parabolic

profile, accumulating linear chirp in the fiber loop. The corresponding spectrum of similariton (p-pol pulse) is much broader than the spectrum of soliton pulse. There is a moderate overshooting of peak power of p-pol pulse before reaching the steady state, as shown in Figure 2.24(c). The peak power rises to 2.3 kW, then slowly drops back into the steady-state at 1.8-kW. However, the evolution of its 3-dB bandwidth and the ΔB-integral in the NALM shows no apparent overshooting effect (see Figure 2.24(d)). The corresponding pulse peak transmission for each round trip is marked in red on the cavity transmission curve (Figure 2.24(d), inset), and the final steady-state is marked with the red dot in the curve. It is found that the transmission of pulse increases along each round trip and finally is stabilized at the position when the transmission is highest.
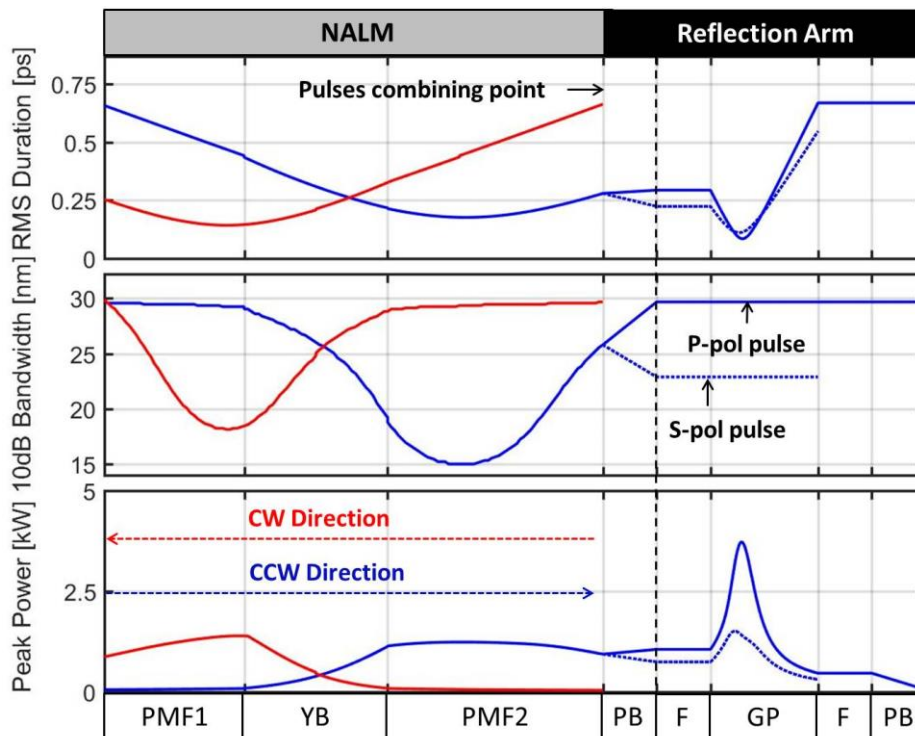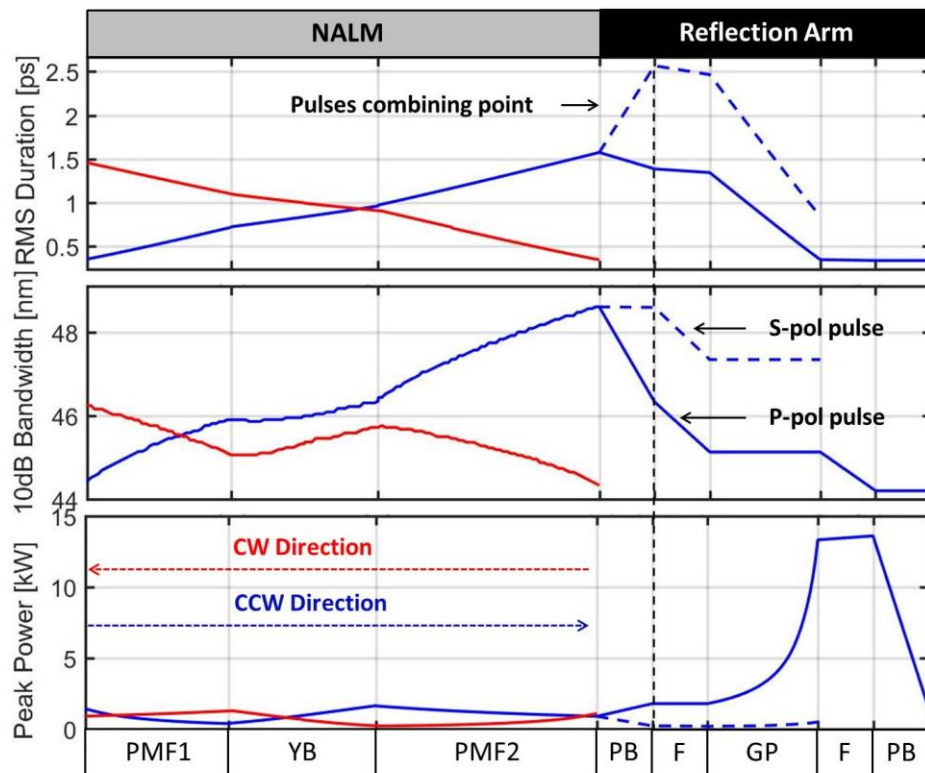

Figure 2.23: Pulse duration. 10 dB spectrum bandwidth and peak power evolution during one oscillator round trip for the similariton mode-locking at normal net cavity dispersion region (6300 fs^2). At the combining point, CW pulse and CCW pulse combine at PBS1; PB: FR, QWP and HWP; Pulse split into two pulses in p-polarization and s-polarization after PB in the linear arm. S-polarization pulse is rejected from the cavity after PBS 2. PBS2 is located in the center of the grating pair.

In this section, we numerically investigate three types of pulses dynamics in the dispersion-managed Figure 9 laser. Compared with soliton and similariton, the stretched pulse mode-locking regime enables the highest pulse quality and the broadest spectrum bandwidth. According to Ref [136], it also shows the lowest noise level with moderate pulse energy. However, in the close-to-zero net dispersion region, the saturable absorber with more considerable modulation depth is necessary in order to stabilize the pulse [128]. Figure 9 has the advantage of tunable cavity transmission curve and environmentally stable operation, enabling the mode-locking operation with a specific cavity transmission function by rotating the wave-plates under the guide of simulation.
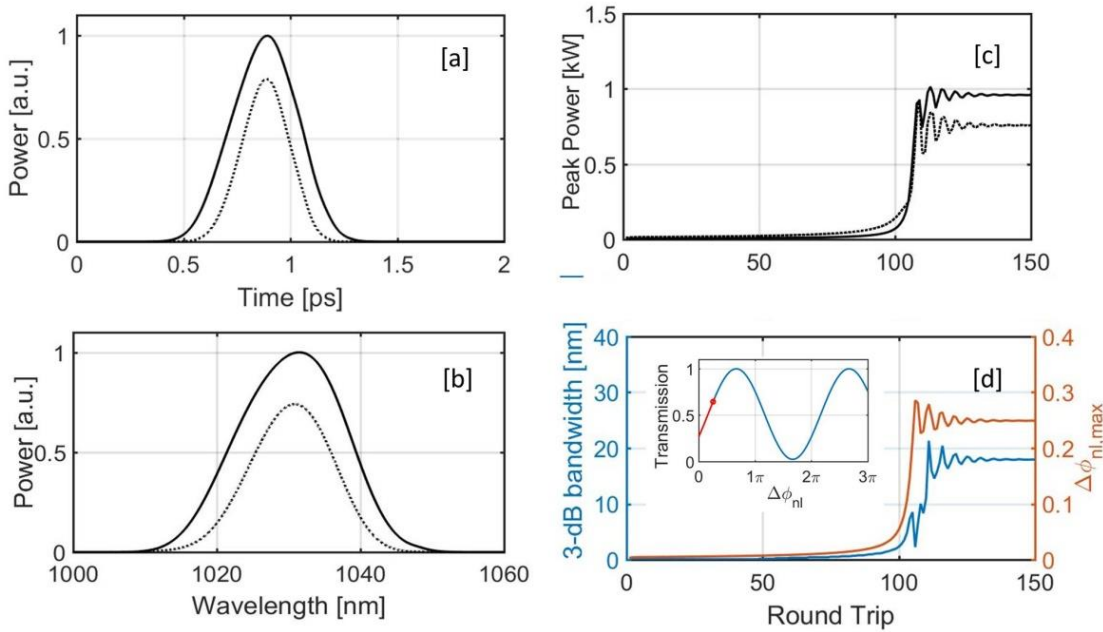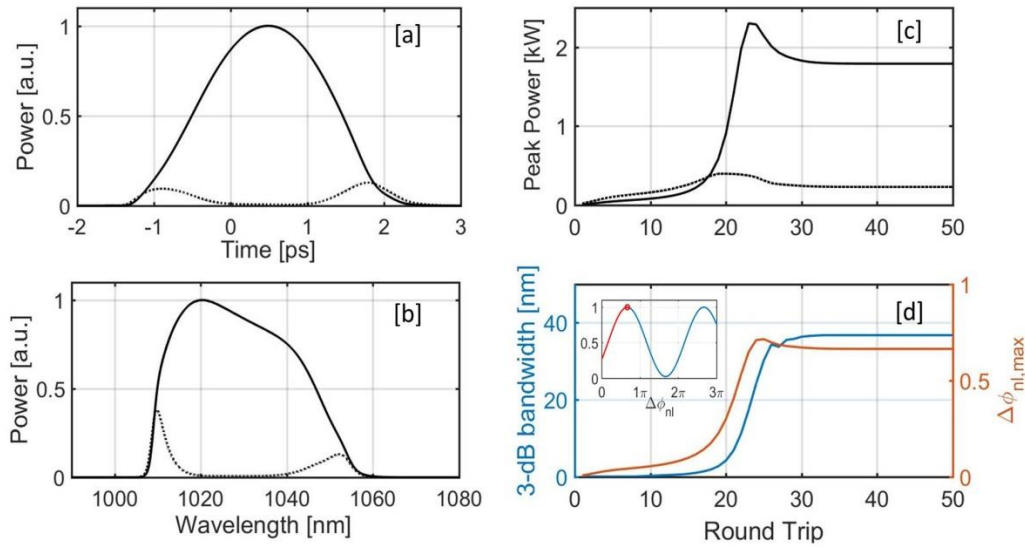
Figure 2.24: Pulses, spectra, and peak power characteristics of the similariton. (a) The temporal profile of p-pol (solid curve) and s-pol (dot curve) pulses (b) the corresponding spectrum of p-pol and s-pol pulses; (c) the peak power of p-pol and s-pol pulses building up process before mode-locking. (d) the 3-dB bandwidth of p-pol pulse and the ΔB-integral of the counter-propagating pulse in the NALM for each round trip before mode-locking; inset: the cavity transmission curve (blue)，the range of pulse peak transmission before mode-locking (red), the pulse peak transmission when it is mode-locked (red dot).

2.2.3.2 Shortest pulse delivering directly from the NALM laser

Ultrafast fiber oscillators directly delivering high-peak-power, transform-limited (TL) pulses are essential for a variety of applications, such as broadband coherent anti-Stokes Raman microscopy (B-CARS) [75] as well as seeding of broadband parametric amplifiers [137]. All-polarization maintaining NALM laser has state-of-art noise performance, which favors frequency comb generation. However, to achieve an ultrashort pulse with enough energy for the supercontinuum generation in the f-2f self-referencing method, the pulse has to be amplified and compressed out of the laser cavity, making the laser system complicated. By checking the dynamic of stretched-pulse mode-locking in Figure 2.19, we find that there is a shortest pulse inside the negative dispersion component with the broadest spectral bandwidth. But the specific position of this shortest pulse is related to the NALM structure and the net dispersion. In this section, we numerically and experimentally investigate how to get the shortest pulse directly out of the NALM laser cavity by controlling the dispersion and NALM's transmission.

Figure 2.25 (a) shows a schematic of the experimental setup, including the NALM and the free-space reflection arm. The NALM includes a polarization beam splitter (PBS1), 0.4-m polarization-maintaining fiber (PMF1), 0.4-m Yb-doped fiber (YDF) and 0.6-m PMF2 in a sequence. The reflection arm includes the phase bias (PB), an intra-cavity pulse compressor (GP, transmission grating pair), another polarization beam splitter (PBS2) and the end mirror. A band-pass filter (FWHM 50 nm) is inserted after the GP. The stretched-pulse mode-locking regime results in two fixed positions in the cavity, where the pulse reaches its transform-limited duration. They are located close to the center of the dispersion sections with

opposite sign [138]. In order to utilize this property, we place PBS2 (the output ports) at the position between the GP and the end mirror, hence at the center of the area with negative dispersion. The typical transmittance of the NALM at the position of PBS2 is displayed in Figure 2.25 (b). Its shape depends on the setting of the components responsible for the phase bias, including the Faraday rotator (FR), a quarter-wave plate (QWP) and a half-wave plate (HWP).
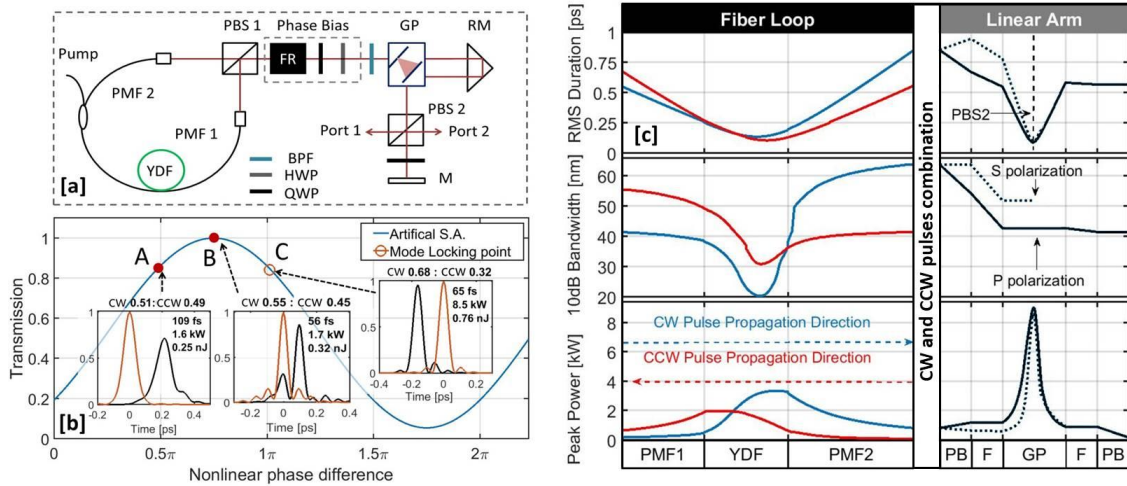
Figure 2.25: Simulation results of stretched-pulse mode-locking with TL pulse output. (a) The structure of the oscillator; FR: Faraday-Rotator; BPF: band-pass filter; GP: grating pair; RM: roof-mirror; M: mirror; (b) The transmittance of NALM at PBS2; x-axis: nonlinear phase difference between the counter propagating pulses in the NALM; A, B and C: three characteristic mode-locked steady-states with different energy splitting ratios at the input of the NALM. Inset: the output pulse (black) and the corresponding TL pulse (red) from Port 1 at these steady-states; (c) RMS pulse duration, 10 dB spectral bandwidth and peak power during one round trip for steady-state C, The fiber loop: counterclockwise (CCW; Red curve) and clockwise (CW; Blue curve) propagating pulses; The linear arm: p-polarized (solid curve) and s-polarized (dashed curve) component of the resulting pulse; PB: phase bias, F: band-pass filter

To generate TL pulses at Port 1 in the simulation, we slightly change the energy splitting ratio between the CW and the CCW pulse at the input of the NALM as well as the net dispersion while keeping the gain and nonreciprocal phase bias constant. The cavity loss is set to be 80%. Stable mode-locking can always be achieved around the highest transmittance shown in Figure 2.25(b). When the net dispersion is around +0.16 ps^2 and the nonreciprocal phase shift is around 0.25π, three characteristic steady-states are marked on the curve (A, B, and C shown Figure 2.25(b)) with different values of the B-integral accumulated by the counter-propagating pulses. Among them, the steady-state C is achieved through slightly overdriving the transmittance of the NALM. The resulting pulses directly emitted from Port 1 (rejected pulse from the cavity, s polarized) are clean, TL pulses with 8.5 kW peak power, while the steady-states A and B result in pulses with much lower peak power and huge pedestals. Furthermore, the round-trip pulse dynamics for steady-state C is shown in Figure 2.25(c). The breathing ratios of the RMS pulse duration and the 10-dB bandwidth are found to be ~8.5 and ~3, respectively. The shortest pulse (65 fs) shows up exactly at the center of the area with negative dispersion (GP) under these conditions.
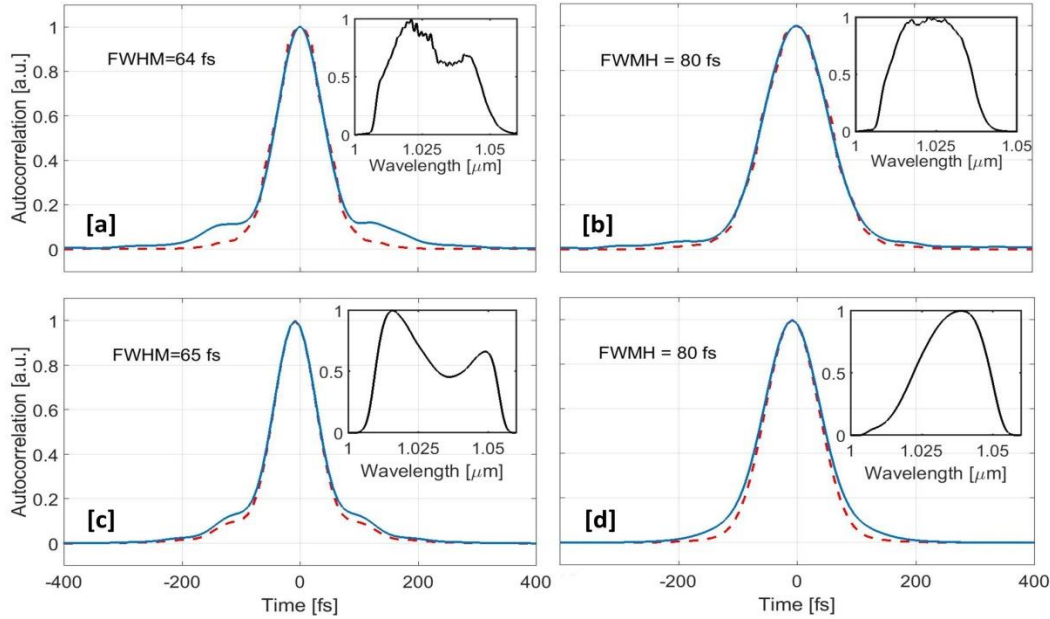
Figure 2.26: Autocorrelation (blue) of output pulses and the correlated AC of TL pulses (red). Pulses from Port 1 (a), (c) and Port 2 (b), (d). Insets: the corresponding spectra; (a), (b) the measured pulses in the experiment; (c), (d) the pulses resulting from the simulation.

Guided by simulations, we construct the experimental setup, as shown in Figure 2.25(a). Another QWP is inserted in front of the end mirror in order to couple out a portion of the transmitted pulse (Port 2, p-polarized). By adjusting the net dispersion and the angles of the wave plates, TL pulses are generated from both output ports simultaneously in accordance with the numerical results (as shown in Figure 2.25 (c): transform-limited p- and s-polarized component at the position of PBS2). The autocorrelation (AC) traces of these pulses from Port 1 and Port 2 are shown in Figure 2.26 (a) and (b), respectively. The corresponding pulse durations are 64 fs and 80 fs. However, the intra-cavity pulse from Port 2 features a longer pulse duration due to its narrower spectral bandwidth. Considering the rejected pulse from Port 1 has pulse energy around 1 nJ, the peak power is evaluated to be more than 10kW. The numerical AC traces and spectra of the pulses for the steady-state C in Figure 2.25 (b) are shown in Figure 2.26 (c), (d) for comparison. The perfect fitting between the numerical and experimental results prove our assumption that clean TL pulses are generated in the stretched-pulse regime by overdriving the transmittance of the NALM.

In conclusion, we demonstrate a modified dispersion-managed Figure-9 fiber laser, generating 64-fs TL pulses with more than 10 kW peak power directly from the cavity. Overdriving of the NALM transmittance helps to shape the rejected output pulses, enabling clean TL pulse generation. Pulses with these characteristics directly delivered from the oscillator will facilitate compact supercontinuum sources without external amplification and pulse compression.

2.3 Summary of the chapter

In this chapter, we numerically investigate the pulse dynamics of a Figure-9 fiber laser in the all-normal-dispersion and the dispersion-managed regime. The details of the numerical model used for the

simulations are outlined and discussed. Two unique pulses (dissipative soliton and dissipative soliton resonance) can be achieved in all-normal-dispersion NALM lasers. Among them, the flat-top DSR pulse can be generated through an anti-saturated effect of the cavity transmission, with its pulse characteristics being influenced by modifying the transmission curve. Three different mode-locking states (stretched-pulse, soliton, and similariton) are achieved in a dispersion-managed NALM laser cavity. The pulse dynamics in conjunction with the pulse build-up process are investigated. A pronounced over-shooting peak power is revealed during the pulse build-up in the similariton, DS and DSR mode-locking regime.

In addition, we experimentally demonstrated the shortest pulse delivered directly from a Figure-9 laser in the experiment. The 65-fs pulse with around 10kW peak power is achieved by precise management of the cavity parameters in a unique cavity structure. We believe that pulses with these characteristics directly delivered from the oscillator benefit construction of compact supercontinuum sources without external amplification and pulse compression.

Chapter 3

Nonlinear Wavelength Conversion and Its Noise Characteristics

Ultrafast fiber lasers have attracted substantial attention as an alternative to bulk solid-state lasers due to their compact structure, turn-key operation, and good beam profile with the waveguide medium. However, fiber lasers are not broadly wavelength-tunable. The emission wavelength range of fiber lasers is limited by the available gain media, which are glass fibers doped with laser-active rare-earth ions, including Nd-doped (900-950 nm), Yb-doped (1000-1100 nm), Er-doped (1500-1600 nm) and Tm/Ho-doped (1700-2100 nm) fiber. The limited tuning range of fiber lasers due to their finite gain bandwidth and the huge wavelength gaps between them hamper their widespread usages as a versatile laser source for microscopy [139], spectroscopy[140], [141] and high power solid-state amplifier system [6]. Apart from that, generating a wavelength-tunable pulse are of importance for many applications, including implementation of high-power mid-infrared (mid-IR) frequency combs [142], [143], coherent Raman scattering microscopy [144], [145], coherent control of molecules, multimodal multiphoton microscopy imaging [146], and two-color pump-probe investigations.

Nonlinear wavelength conversion is widely adopted to overcome the wavelength limitation of fiber lasers. Solid-state optical parametric oscillator (OPO) synchronously pumped by an ultrafast source laser can generate widely tunable signal/idler pulses [147]. Another attractive approach is to employ third-order nonlinearity inside an optical fiber to generate ultrafast pulses centered at a wavelength different from the input pulses. Fiber-optic methods are of particular interest because they are compatible with the rapid development of powerful ultrafast fiber lasers [31], [148], which holds promise for implementing ultrafast two-color sources in an all-fiber format.

Fiber-optic methods have been demonstrated for efficient wavelength conversion, including dispersive wave generation [72], [73], fiber OPO [149], [150] and soliton self-frequency shift (SSFS) [151], to name a few. Dispersive wave generation normally produces positively chirped pulses with poor energy scalability and has a limited wavelength tuning range. Although fiber OPOs feature a certain wavelength tunability (up to ~180 nm) [68], [74], the allowed narrow phase matching bandwidth given by fiber dispersion limits the generated pulse duration. Besides, fiber OPOs need fine cavity tuning to match the repetition rate of the pump laser, and the long OPO cavity is sensitive to environmental disturbance.

Soliton self-frequency shift (SSFS) is widely adopted to generate transform-limited pulses and the resulting Raman soliton can be as short as ~50 fs. A unique and attractive feature associated with SSFS is that this approach does not require specific phase matching, which is typically a necessity for other approaches such as dispersive wave generation and fiber optical parametric oscillator. As a result, large-mode-area (LMA) fibers (e.g., rod-type fibers or high-order mode fibers) with negative group-velocity dispersion (GVD) can be used to generate high-energy (up to ~100 nJ) Raman soliton pulses tunable in a broad wavelength range [70], [80]. Recently, we demonstrated a new method to generate wavelength widely tunable pulses, in which self-phase modulation (SPM) dominates the broadening of an input narrow optical spectrum and the broadened spectrum comprises multiple isolated spectral lobes. Using proper bandpass filters to select the leftmost or the rightmost spectral lobe produces nearly transform-limited pulses with ~100 fs duration [71], [81]. Such SPM-enabled spectral selection (SESS) source exhibits excellent energy scalability and can deliver >100-nJ pulses with ~1-MW peak power [81]. We have applied SESS sources to multiphoton microscopy imaging [152] and the generation of mid-IR pulses via difference-frequency generation (DFG) [153].

Both SFSS and SESS pulses provide the possibility of broadband wavelength conversion without a specific phase matching condition. However, their noise characteristics, e.g., their relative timing jitter with respect to the source laser, are still unclear. In this chapter, we investigate these two types of nonlinear wavelength conversion approaches numerically and experimentally. The timing jitter and the intensity noise are investigated in both approaches. Finally, we propose a highly synchronized wavelength-tunable two-color source based on the SESS method with the relative timing jitter between the two colors in 100-as-level [154].

3.1   Noise of Raman soliton

When a femtosecond pulse propagates inside an optical fiber with abnormal dispersion, the interplay between the dispersion and nonlinearity of the waveguide produces optical solitons. In particular, the ideal periodic evolution of a higher-order soliton is perturbed by third- and higher-order dispersions (HOD) to the extent that it breaks into its fundamental components, a phenomenon known as soliton fission [155]. These fundamental solitons experience the intra-pulse Raman scattering, resulting in a Raman soliton self-frequency shift (SSFS) [156], [157]; that is, the Raman soliton redshifts continuously during propagation while maintaining its transform-limited hyperbolic secant profile. Capable of providing wavelength-tunable femtosecond pulses at desired wavelengths that cannot be directly obtained from mode-locked ultrafast lasers. The amount of self-frequency shift depends on many parameters, such as fiber nonlinearity and GVD, input pulse duration and energy, and fiber length.

In general, for the SSFS wavelength conversion method, the amount of wavelength shift can be readily tuned by varying the input energy of the excitation pulse. Therefore, any input-energy fluctuations result in center-wavelength fluctuations of the derived pulse (e.g., Raman soliton), which is in turn translated by fiber dispersion into relative timing jitter (RTJ) between the derived pulse and the excitation pulse [158]. Besides, the intensity noise of the excitation pulse directly contributes to the intensity noise of Raman soliton. The noise transfer function is still unclear due to the complicated noise coupling

processing during the process of supercontinuum generation. In this section, we numerically investigate the influence of excitation pulse energy fluctuation on the parameters of Raman soliton.

3.1.1 Numerical model for Raman soliton generation

Accurate modeling of Raman soliton evolution necessitates numerically solving the generalized nonlinear Schrödinger equation (GNLSE) that considers nonlinear effects, including self-phase modulation, self-steepening, and Raman scattering. It is written in its normalized form as:

$$\frac{\partial A}{\partial z} + \frac{i}{2}\beta_2\frac{\partial^2 A}{\partial T^2} - \frac{1}{6}\beta_3\frac{\partial^3 A}{\partial T^3} + \frac{i}{24}\beta_4\frac{\partial^4 A}{\partial T^4} + \frac{a}{2}A = i\gamma(|A|^2A + \frac{i}{\omega_0}\frac{\partial}{\partial T}(|A|^2A) - T_R A\frac{\partial|A|^2}{\partial T}) \tag{3-1}$$

where A represents the complex electric field envelope, z is the propagation distance in fiber, and T=t-β_1z. The linear terms are in the left part of the equation, including the second-, third- and fourth-order dispersions, as well as the optical linear loss. The right part represents the nonlinear terms, including self-phase modulation (SPM), self-steepening, stimulated Raman scattering (SRS). The symbols γ and ω_0 represent the nonlinear coefficient and the center angular frequency. The symbol T_R is a parameter corresponding to the Raman response time, and in our case, T_R is set to be 5 fs. In the simulation, we solved the GNLSE by the adaptive split-step Fourier method [159].

Table 3.1 Parameters of PCFs used in simulations

PCF (type)	d	AFR	ZDF (μm)	MFD(μm)	γ (W$^{-1}\cdot$ km^{-1})	β_2 (ps^2/km)	β_3 (ps^2/km)
NL-3.2-945	3.3	0.48	0.945	2.8	23	-11.4	0.0725
NL-3.7-975	4.18	0.68	0.975	3.1	18	-7.2	0.0768

MFD: mode field diameter, ZDF: zero-dispersion wavelength, γ: nonlinear parameter, d: fiber core diameter, and *AFR*: air filling ratio in the cladding.
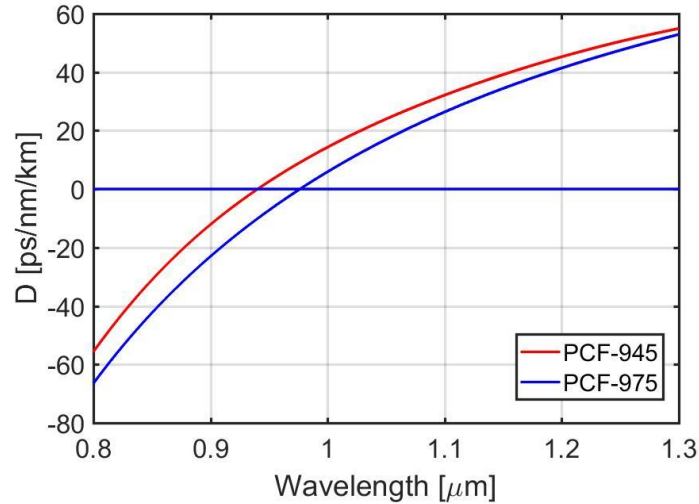
Figure 3.1: Calculated fiber dispersion curve of PCF-945 (red) and PCF-975 (blue). Calculation of the fiber dispersion is based on the effective refractive index model from [160].

To be consistent with the following experiments, an optical pulse centered at 1.030 μm with 200 fs pulse duration is launched into two different PCFs—NL-3.2-945, NL-3.7-975—all commercially available from NKT Photonics. Table 3.1 lists the parameters for these two PCFs. The dispersion curves

of these PCFs are shown in Figure 3.1, which is calculated based on the effective refractive index model [160]. Both PCFs has abnormal dispersion above 1µm, but the dispersion of PCF-945 has larger absolute value in this wavelength region.

3.1.2 Simulation results of RS noise characteristics
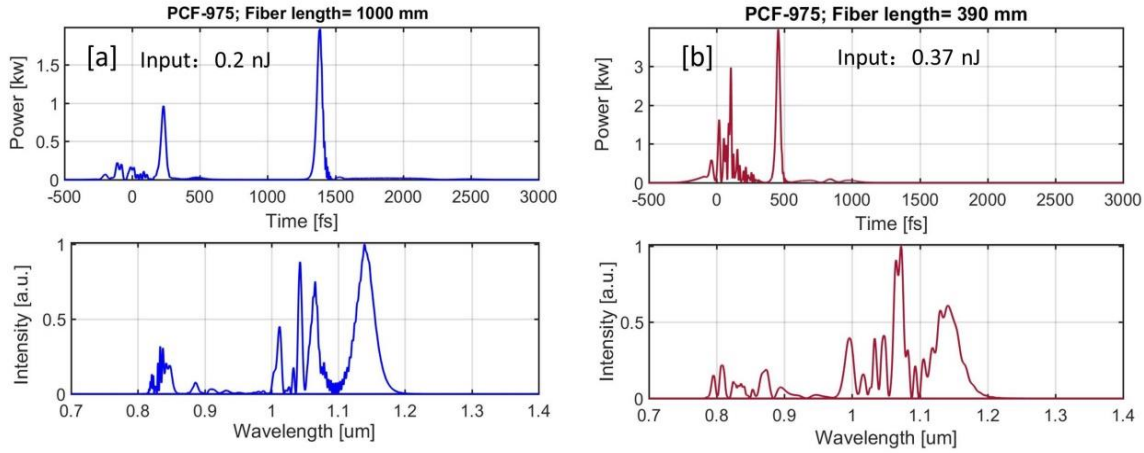
Figure 3.2: Raman soliton output in time domain (top) and frequency domain (bottom row) from PCFs. (a) 1-m PCF-975 when 0.2-nJ, 200-fs pulse is launched into it. (b) 0.39-m PCF-975 when 0.37-nJ, 200-fs pulse is launched into it.
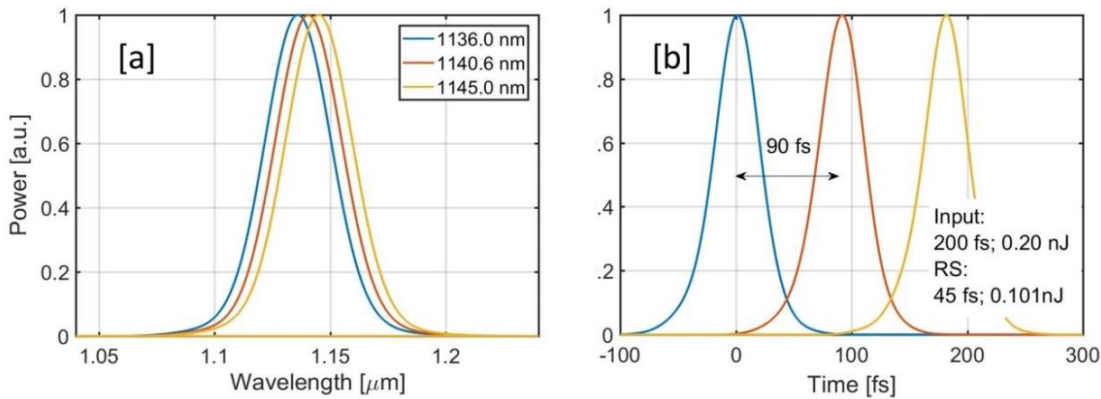
Figure 3.3: Simulation results for propagating a 200-fs pulse (at 1030 nm) through 1.0-m PCF-975. (a) Raman soliton spectra and (b) Raman soliton pulses corresponding to different excitation pulse energies: 0.19 nJ (blue), 0.20 nJ (red), and 0.21 nJ (yellow).

We first numerically investigate the RTJ of Raman soliton pulses generated by launching a 200-fs Gaussian pulse at 1030 nm into PCF-975. As Figure 3.2 (a) shows, propagation of 0.2-nJ input pulses in 1-m PCF-975 results in a Raman soliton centered at 1140-nm wavelength. Filtering this isolated spectral lobe leads to a 45-fs Raman soliton pulse with 0.1-nJ pulse energy (see Figure 3.3(b), red curve). A slight change of input pulse energy by 0.01 nJ causes a temporal shift as large as 90 fs [see Figure 3.3(b)]. The large temporal shift is because 0.01-nJ energy change of the excitation pulse causes center–wavelength fluctuations of the resulting Raman soliton (see Figure 3.3(a)), and then translates into the RTJ between the Raman soliton and the excitation pulse by dispersion of 1-m PCF-975. The 90-fs temporal shift is

twice the length of the 45-fs pulse, which will degrade time resolution for spectroscopy experiments or result in a large signal noise for the parametric process such as the mid-IR DFG frequency comb generation. The approach of using a shorter piece of fiber while pumping the PCF with more pulse energy could reduce the RTJ to some extent for the decrease of the accumulated fiber dispersion[158].
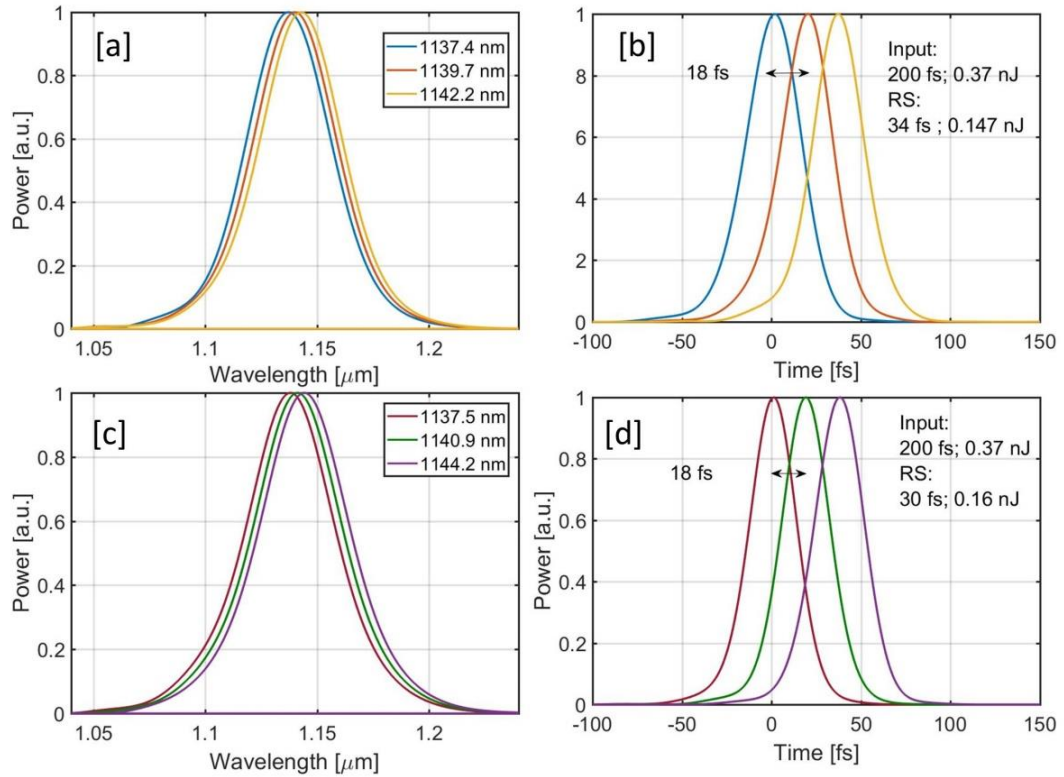
Figure 3.4: Simulation results for sending a 200-fs pulse in PCFs for Raman soliton generation. (a-b) 1-m PCF-975 and (c-d) 0.75-m PCF-945. (a,c) Raman soliton spectra and (b,d) Raman soliton pulses corresponding to different excitation pulse energies: 0.19 nJ (blue), 0.20 nJ (red), and 0.21 nJ (yellow).The relative intensity noise (RIN) of Raman soltion
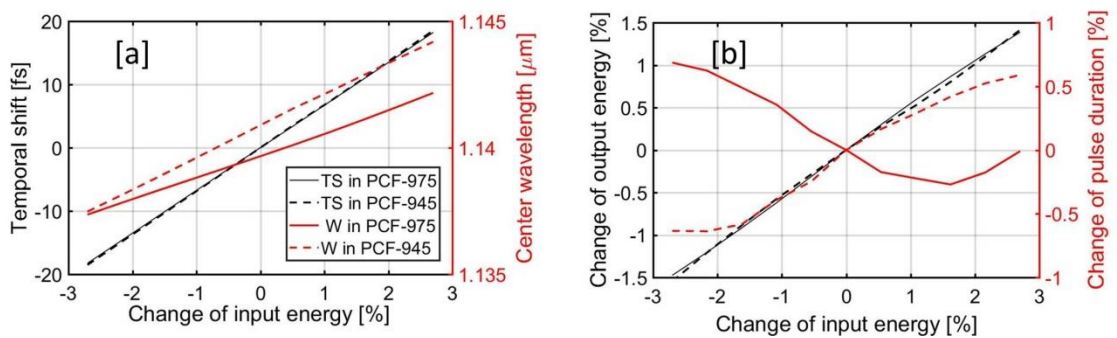
Figure 3.5: Change of Raman soliton parameters as a function of change of input signal's power. (a) Relative timing shift of Raman soliton at 1140 nm and the correlated center wavelength shift in PCF-975 (solid curve) and in PCF-945 (dash curve) when the input excitation pulse is varied in terms of pulse energy. (b) Change of pulse energy of Raman soliton at 1140 nm and its pulse duration in PCF-975 (solid curve) and in PCF-945 (dash curve) when the input excitation pulse is varied in terms of pulse energy.

For example, by increasing the excitation pulse energy to 0.37 nJ and cutting back the fiber to 0.39 m, a similar isolated Raman soliton at1140-nm wavelength is generated. The direct output from the fiber is

shown in Figure 3.2 (b) in both the time and the frequency domain. Filtering its spectrum generates a 34-fs Raman soliton pulse with 0.15-nJ pulse energy (see Figure 3.4 (b), red curve). A slight change of input pulse energy by 0.01 nJ causes a temporal shift of 18 fs [see Figure 3.4 (b)]. The reduction of RTJ is about 4 times by simply shortening the fiber length. However, the temporal shift of 18 fs is still a large value compared with the 34-fs pulse duration. It is worth noting that we cannot use a shorter fiber length for the generation of 1140-nm Raman soliton, because further increasing the excitation pulse energy leads to the formation of multiple solitons with their spectra merged in the frequency domain, which cannot be separated by a bandpass filter.

We then numerically investigate the RTJ of Raman soliton pulses in PCF-945 with a different dispersion profile. The PCF-945 has a larger anomalous dispersion above 1μm, so the fiber length needed for the same wavelength shifting is much shorter than PCF-975 when the excitation pulse energy is the same. For example, we keep the input pulse energy in 0.37nJ, 0.28-m PCF-945 is long enough to achieve the same wavelength shifting to 1140 nm. The soliton profile and its spectrum are shown in Figure 3.4 (c,d). Compared with the Raman soliton generated in PCF-975 with the same excitation pulse, the resulting pulse energy of Raman soliton generated in PCF-945 is larger while its pulse duration is shorter. However, the slight change of the input pulse energy by 0.01 nJ leads to the temporal shift of 18 fs, the same as the case in PCF-975 (see Figure 3.4 (b)). Apart from that, the shift of the center wavelength due to the change of input pulse energy is slightly larger in PCF-945.

The wavelength and temporal shift versus the fluctuation of input energy in PCF-975 and PCF-945 are further checked in Figure 3.5(a). The temporal shift of Raman solitons stays the same in these two cases, and the wavelength shift of soliton pulse in PCF-945 is slightly larger. We calculate the temporal shift as a function of the relative energy change. The temporal shifting slope for the Raman soliton is 6.83 fs per 1% input-energy change. Besides, the change of pulse energy of RS and its pulse duration in both PCFs are shown in Figure 3.5(b). The fluctuation of the output pulse energy as a function of the input is the same for both cases, which is 0.63% for 1% change of input pulse energy. This result reveals that the intensity noise of RS is smaller than the excitation pulse. The changes in pulse duration in both fibers have a slight difference. However, the fluctuations of pulse duration in both cases are less than 1%, even when the input pulse energy changes by 3%.

In the end, we found that the 1140-nm Raman solitons generated in both fibers are similar in their parameters when the input pulse energy is the same. The intensity noise of Raman soliton is lower than the noise of the excitation pulse, while the RTJ of Raman solitons generated from both fibers is comparable large. An approach to deduce RTJ is by cutting the fiber length while increasing the excitation pulse energy. However, Raman soliton requires a relatively large amount of negative GDD to achieve red-shifted Raman soliton with an isolated spectrum, so that the fiber length cannot be shortened further. The large intrinsic RTJ of Raman soliton is unavoidable by its wavelength conversion mechanism.

3.2 Noise of SPM-enabled spectral selection (SESS)

SPM-enabled spectral selection (SESS) is a method to generate wavelength tunable pulses, in which self-phase modulation (SPM) dominates the broadening of an input narrow optical spectrum in a piece of fiber with small normal dispersion value. The typical broadened spectrum comprises multiple isolated spectral

lobes. Selection of the leftmost or the rightmost spectral lobe with a proper bandpass filter produces nearly transform-limited pulses with ~100 fs duration [71]. The center wavelengths of the rightmost and leftmost spectral components are tunable by increasing or decreasing the energy of excitation pulses.

In contrast to the formation of Raman soliton, to form well isolated spectral lobes and increase the amount of wavelength shift, SESS prefers minimized group-delay dispersion (GDD) achieved by shortening the fiber length to several cm [146]. Since GDD translates the variation of the excitation pulse to the RTJ, SESS pulses should exhibit less RTJ than Raman soliton. In this section, we numerical investigate the intensity noise and the relative timing jitter (RTJ) of SESS pulses caused by the fluctuation of the excitation pulse energy.

3.2.1 Numerical model for SESS pulse generation
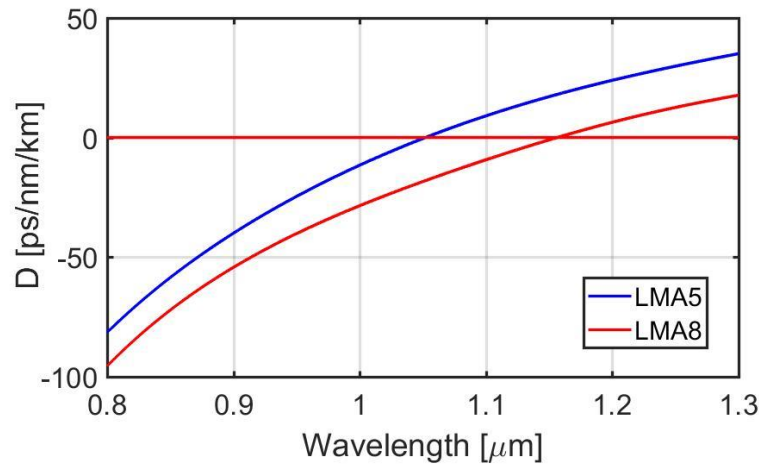
Figure 3.6: Calculated fiber dispersion curve of large mode-area PCF LMA8 (red) and LMA5 (blue). The dispersion curves of LMA fiber are presented in the data sheet on the website of NKT Photonics.

Table 3.2: Parameters of LMA fibers used in simulations

PCF (type)	d	ZDF (µm)	MFD(µm)	γ (W$^{-1}\cdot$ km^{-1})	β_2 (fs^2/µm)	β_3 (fs^2/µm)	β_4 (fs^3/µm)
LMA-8	8.6	1.156	7.3	3.79	0.0126	0.0494	-0.1037
LMA-5	5.0	1.052	4.7	9.14	0.0026	0.0667	-0.0993

MFD: mode field diameter, ZDF: zero-dispersion wavelength, γ: nonlinear parameter, d: fiber core diameter

The same method as modeling the Raman soliton generation, the accurate simulation results are achieved by solving the generalized nonlinear Schrödinger equation (Equation 3-1) that takes into account nonlinear effects, including self-phase modulation, self-steepening, and Raman scattering. Two types of commercially available fibers (LMA-5 and LMA-8) from NKT Photonics are investigated in the simulation. Both the fibers have slight normal dispersion below the wavelength of 1.05 µm and 1.15 µm, respectively, as shown in Figure 3.6, which benefits the SPM-dominated spectral broadening process. Table 3.2 lists the parameters for these two LMA fibers. To be consistent with the following experiments, an optical pulse centered at 1.030 µm with 200 fs pulse duration is launched into the fibers.

3.2.2 Simulation results of SESS noise characteristics

The simulation is first carried out in a piece of LMA-5 fiber with an input of 200-fs Gaussian pulse at 1030 nm. As Figure 3.7 (a) shows, propagation of 31.5-nJ input pulses in 24.5-mm LMA-5 results in the rightmost spectral lobe center at 1140 nm. Filtering this isolated spectral lobe by a long pass filter (cut off at 1115 nm) leads to a 65.6-fs SESS pulse with 9.27-nJ pulse energy (see Figure 3.8(b), red curve). A slight change of input pulse energy by 1 nJ causes a temporal shift of ~ 1.2 fs [see Figure 3.8(b)], which is at least 10 times lower than the temporal shift of Raman soliton. The 1-nJ energy change of the excitation pulse causes center–wavelength fluctuations of the resulting SESS pulse (see Figure 3.8(a)). However, the change of center wavelength cannot translate into the RTJ between the SESS pulse and the excitation pulse efficiently because of the small dispersion of 24.5-mm LMA-5. Compared with the SESS pulse duration of 65 fs, the temporal shift of 1.2 fs induced by the intensity fluctuation of excitation pulse are negligible, and the SESS pulse is highly synchronized with the excitation pulse.
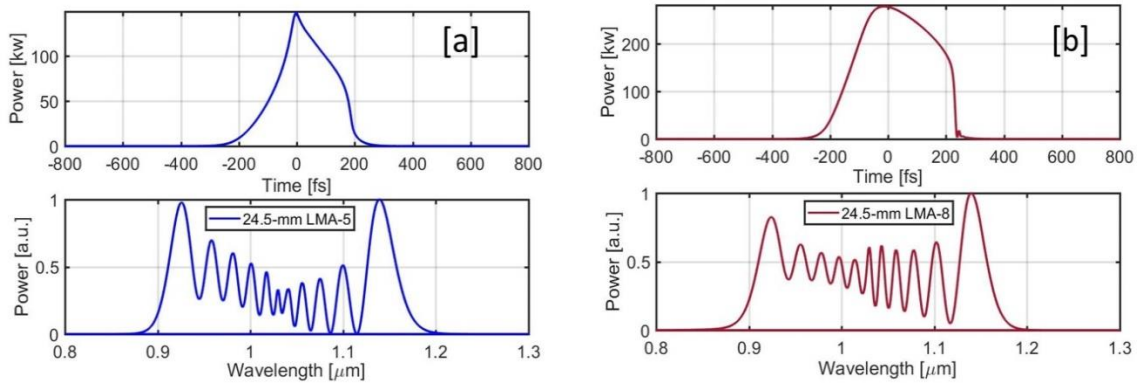
Figure 3.7: SPM output in time domain (top row) and frequency domain (bottom row) from LMA fibers. (a) The output in both time domain (top row) and frequency domain (bottom row) from 85-mm LMA-8 when 31.5-nJ, 200-fs pulse is launched into it. (b) The output in both time domain (top row) and frequency domain (bottom row) from 24.5-mm LMA-5 when 31.5-nJ, 200-fs pulse is launched into it.
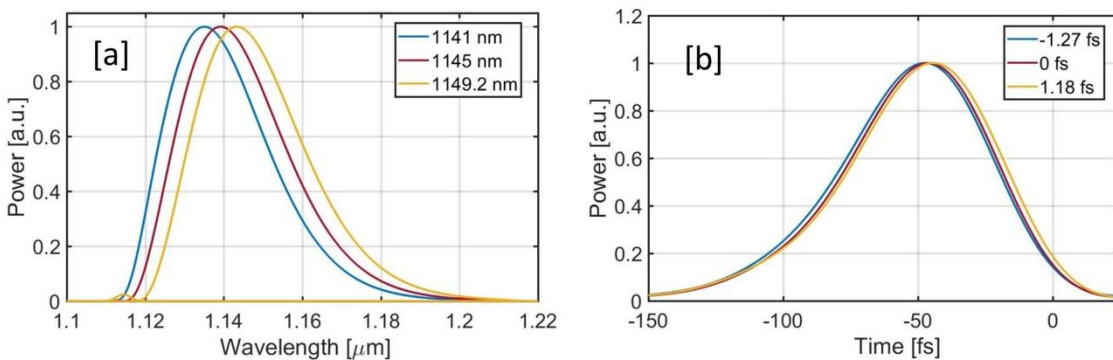
Figure 3.8: Simulation results for sending a 200-fs pulse for SESS pulse generation in 24.5-mm LMA-5. (a) SESS spectra and (b) SESS pulses corresponding to different excitation pulse energies: 30.5 nJ (blue), 31.5 nJ (red), and 32.5 nJ (yellow).

We then change the fiber to LMA-8 in the simulation with the same input pulse (200-fs Gaussian pulse at 1030 nm). Due to the lower nonlinear parameter of LMA-8, the pulse energy launched into fiber

must be enhanced if we keep the fiber length the same. As Figure 3.7 (b) shows, propagation of 91.5-nJ input pulses in 24.5-mm LMA-8 results in the rightmost spectral lobe center at the same wavelength of 1140 nm. Filtering this isolated spectral lobe by a long pass filter (cut off at 1117 nm) leads to a 68.8-fs SESS pulse with 22.19-nJ pulse energy (see Figure 3.8(b), red curve). With the same fiber length, the SESS pulse has two times of pulse energy than the one generated in LMA-5. The center-wavelength shift and temporal shift of pulse are shown in Figure 3.9 when the injected pulse energy changes by 1nJ. It is found that 1-nJ change of pulse energy only results in ~0.3 fs temporal shift, which is 5 times lower than the shifting in LMA-5. Besides, the change of the SESS spectrum is milder.
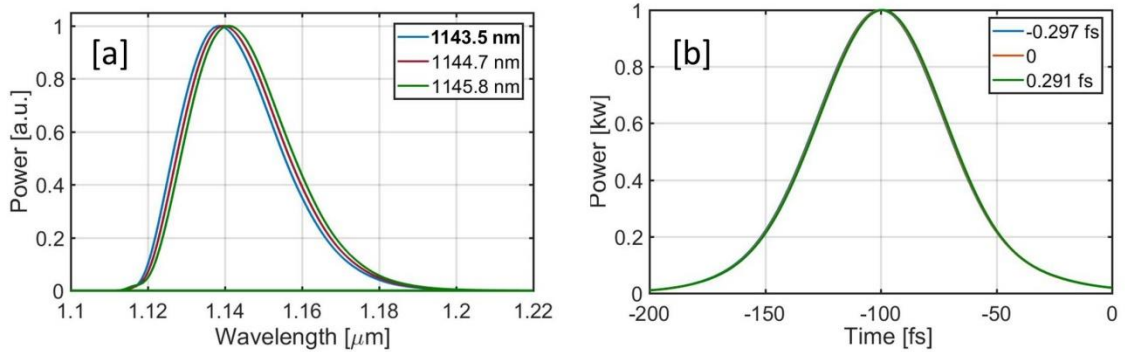
Figure 3.9: Simulation results for sending a 200-fs pulse for SESS pulse generation in 24.5-mm LMA-8. (a) SESS spectra and (b) SESS pulses corresponding to different excitation pulse energies: 90.5 nJ (blue), 91.5 nJ (red), and 92.5 nJ (green).
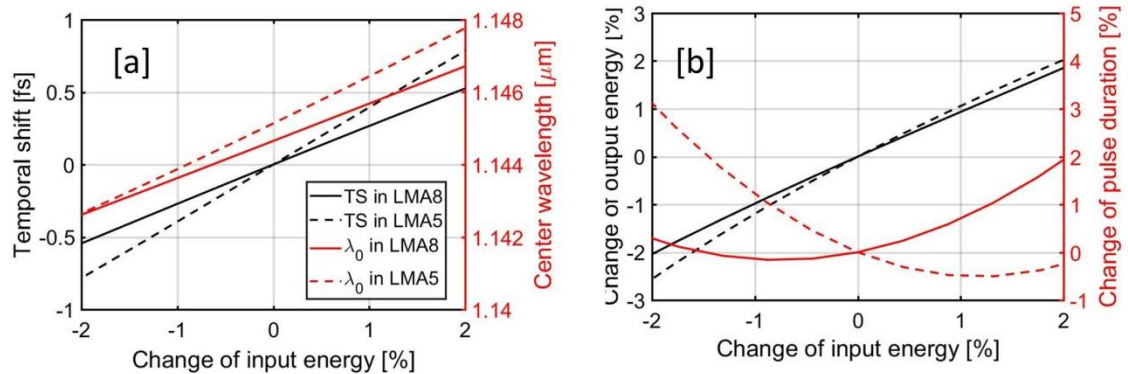
Figure 3.10: Change of SESS pulse parameters as a function of change of input signal's power. (a) Relative timing shift of SESS pulse at 1140 nm and the corresponding center wavelength shift in 24.5-mm LMA-8 (solid curve) and in 24.5-mm LMA-5(dash curve) when the input excitation pulse is varied in terms of pulse energy. (b) Change of SESS pulse energy at 1140 nm, its pulse duration in LMA-8 (solid curve) and in LMA-5 (dash curve) when the input excitation pulse is varied in terms of pulse energy.

For a fair comparison in these two cases, we investigate the influence of input power fluctuation on the output in terms of the pulse energy, center-wavelength, timing jitter, and pulse duration. As Figure 3.10(a) shows, the slopes of the temporal shift versus the change of input power are 0.386 fs/ 1% for LMA-5, and 0.273 fs / 1% for LMA-8, although the shifts of center-wavelength due to the input power fluctuation are similar in both cases. The main reason for the differential temporal shift is that 1140-nm

SESS pulse accumulated less GDD during the spectrum broadening process in LMA-8. The changes of SSES pulse energy and pulse duration versus the input power fluctuation are shown in Figure 3.10(b). The slopes of output energy fluctuation are ~1.15 % / 1% for LMA-5 and ~0.98% /1% for LMA-8. Compared with Raman soliton (see Figure 3.5), the temporal shift of SESS pulse due to input intensity fluctuation is one-order of magnitude lower, while the intensity fluctuation of the SESS pulse with a slope of ~1.15%/ 1% is slightly larger than Raman soliton with a slope of 0.63%/ 1%. From the simulation result, we conclude that the SESS pulse and its excitation pulse consist of a highly synchronized two-color source with a relative timing jitter in the attosecond-level. In the next section, we experimentally verify our prediction.

3.3 Two-color source synchronized at 100- as-precision based on SESS pulse

In this section, we both theoretically and experimentally compare the RTJ performance of SESS and SSFS. Our results show that the RTJ between a SESS pulse and its excitation pulse can be as low as 100-as, at least one order of magnitude less than can be achieved from SSFS. SESS pulse and its excitation pulse center at different wavelengths such that they constitute a femtosecond two-color source.

3.3.1 Simulation results
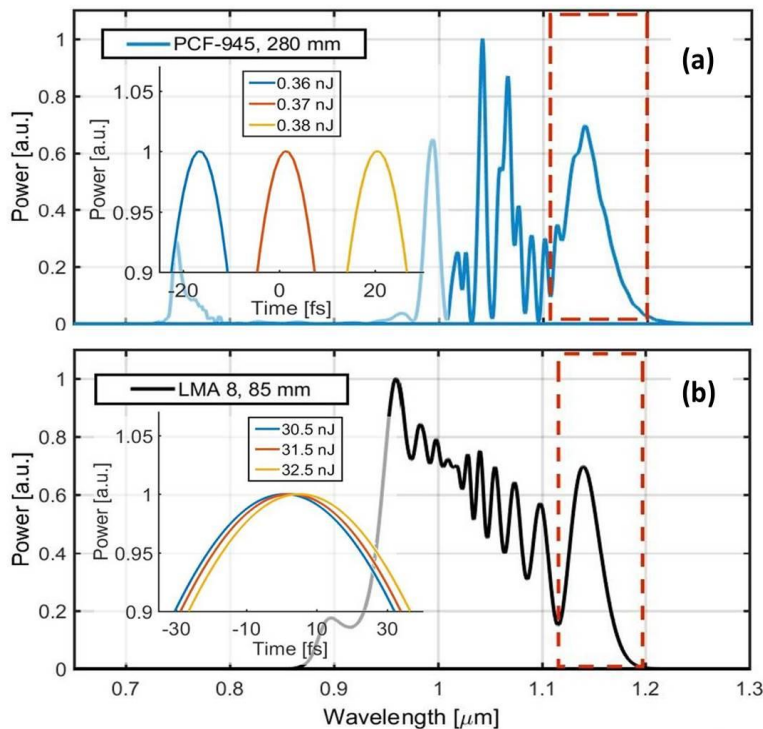
Figure 3.11: (a) Raman soliton generated from 280-mm PCF-945. (b) SESS pulses from 85-mm LMA8. The parameters are carefully chosen such that both spectra generate isolated spectral lobe peaking at 1140 nm. Insets show the temporal shift due to the energy variation of the excitation pulse.

For comparison with the experiment result, we first numerically investigate the RTJ of both Raman soliton pulses generated from 280-mm PCF-945 and SESS pulses generated from 85-mm LMA-8, and both of them derived from the same Yb-fiber laser that produces 200-fs Gaussian pulses at 1030 nm. For PCF-945, the fiber length of 280 mm is as short as possible to generate an isolated Raman-soliton spectrum at 1140 nm. The SESS source is implemented using a LMA-8 fiber of 85-mm long to generate high-energy SESS pulses at the same wavelength. In an ideal case, the length of LMA-8 could be cut shorter, at the same time injecting more pulse energy to achieve the same wavelength conversion. However, for the convenient of the experiment, we choose a relative longer fiber length to reduce the injection pulse energy, which helps to avoid the possible damage at the fiber end face. The parameters of both fibers are list in Table 3.1 and Table 3.2.

As Figure 3.11(a) shows, propagation of 0.37-nJ input pulses in 28-cm PCF-945 results in a Raman soliton spectrum peaking at 1140 nm. Filtering this isolated spectral lobe leads to Raman soliton pulses with 0.16-nJ pulse energy. A slight change of input pulse energy by 0.01 nJ causes a temporal shift as large as 18 fs [inset of Figure 3.11(a)]. In contrast, 31.5-nJ excitation pulses are required in 8.5-cm LMA8 such that the rightmost spectral lobe peaks at 1140 nm [Figure 3.11(b)]; filtering this spectral lobe with 50-nm bandpass filter also generates femtosecond pulses with 4.96-nJ pulse energy, much stronger than the Raman soliton pulse. Varying the excitation pulse energy by 1 nJ results in only 1.5-fs temporal shift [inset of Figure 3.11(b)].
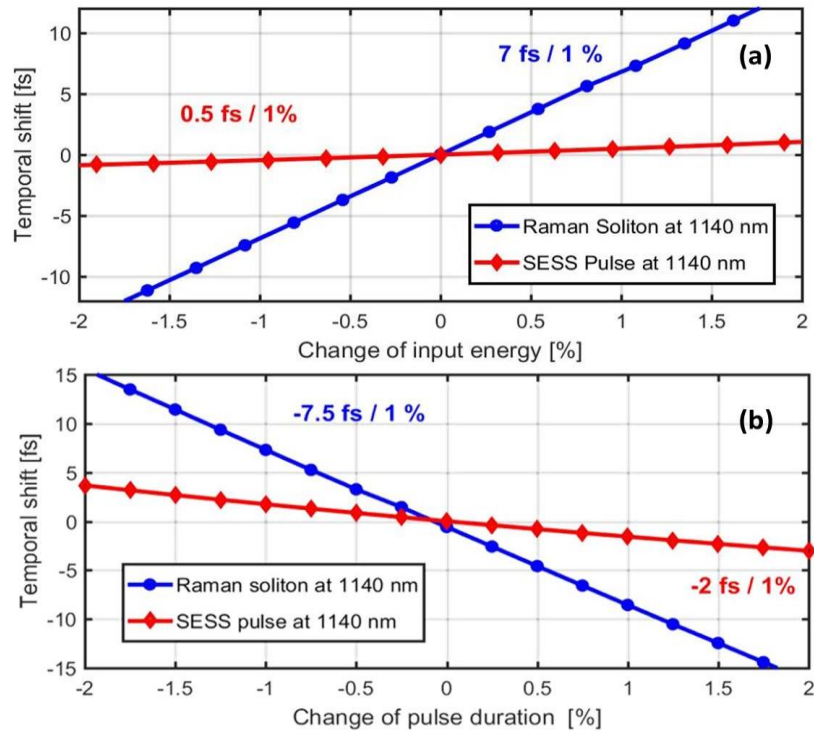
Figure 3.12: Relative timing shift of Raman soliton (blue curves) and SESS pulse (red curves) both at 1140 nm when the input excitation pulse is varied; in terms of (a) pulse energy and (b) duration change.

To make a fair comparison, we calculate the temporal shift as a function of relative energy change, as shown in Figure 3.12(a). The slope for the Raman soliton source and SESS source is 7 fs and 0.5 fs per 1% input-energy change, respectively, indicating that SESS sources exhibit significantly lower RTJ compared

with Raman soliton sources. Besides energy fluctuations, variation of the excitation-pulse duration affects the RTJ as well. Figure 3.12(b) show the dependence of temporal shift versus pulse duration change. In this simulation, the input pulse energy is fixed at 0.37 nJ (31.5 nJ) for SSFS (SESS). A 1% change of the excitation pulse duration causes -7.5 fs (-2 fs) temporal shift of the Raman soliton (SESS) pulse. The results in Figure 3.12 illustrate that the noise transfer effect is weaker in the process of SESS pulse generation. The eventual RTJ between a SESS pulse and its excitation pulse arises from the combined effects of all the parameter fluctuations of the excitation pulse, which can only be experimentally determined.

3.3.2 Experimental setup
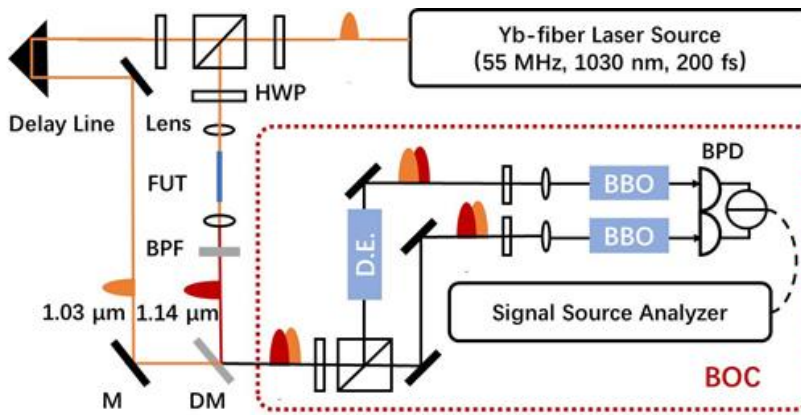
Figure 3.13: Schematic experimental setup. PBS: polarization beam splitter. HWP: half-wave plate, FUT: PCF-945/LMA8, BPF: bandpass filter with 50-nm bandwidth, DM: dichroic mirror, D.E., delay element, BBO: beta-BaB2O4 crystal, BPD: balanced photodetector, and M: mirror.

Guided by the simulation results, we carry out a detailed experimental study. Figure 3.13 illustrates the experimental setup. The home-built 55 MHz Yb-fiber laser source delivers 200-fs pulses centered at 1.03 μm with up to 8-W average power [146]. The laser output is split into two replicas: one is coupled into 28-cm PCF-945 (or 8.5-cm LMA8) to obtain 0.15-nJ Raman soliton pulses (or 3.3-nJ SESS pulses) at 1140 nm when the incident power coupled into PCF-945 is 21 mW (or LMA8, 1.8 W). The other replica is used as reference. We built a two-color balanced optical cross-correlator (BOC) to measure the RTJ between the generated pulses at 1140 nm and the reference pulses at 1030 nm [158].

More specifically, at the fiber output, a dichroic mirror (DM) is used to spatially combine the wavelength conversion pulse and the reference pulse before sending them into a balanced optical cross-correlator (BOC) [161] to measure their RTJ. The power of the input pulse pair is first separated into two branches by a PBS. In each branch, the pulse pair is focused into a 10 mm Type-I phase-matched beta-BaB2O4 (BBO) crystal (cutting angle: 21.9°) for sum–frequency generation (SFG). A delay element (DE) that consists of two half-inch cubes made of N-SF1 glass is inserted into one branch to provide a 150 fs delay offset. The two SFG signals are then filtered out by bandpass filters (centered at 555 nm, bandwidth 40 nm) and, finally, detected by a balanced photodetector (BPD). BOC converts the timing fluctuations between the two pulses to voltage fluctuations at BPD output. BOCs have been widely used in ultra-low

timing jitter characterization [162], timing error detection in timing distribution systems [161], [163], and pulse synthesis from independent mode-locked lasers [164], [165].

3.3.3 Experiment results

To evaluate the RTJ from our experiment, we first characterize the relative intensity noise (RIN) of our Yb-fiber laser [blue curve in Figure 3.14(a)]. The integrated RIN [I-RIN, black curve in Figure 3.14 (a)] from 100 Hz to the Nyquist frequency of 27.5 MHz is 0.27%. Based on the RIN of the excitation pulse and the slope displayed in Figure 3.12 (a), the RTJ introduced by excitation pulse intensity noise is estimated to be ~1.9 fs for the Raman soliton source and ~135 as for the SESS source. Figure 3.14 (b) presents the RTJ measured by the BOC. The blue curve shows the RTJ power spectral density (PSD) of the Raman soliton source (30 fs in duration) with an integrated-RTJ (I-RTJ) of 2.65 fs. In contrast, the SESS source (100 fs in duration) has much lower measured RTJ [red curve in Figure 3.14(b)]; the integrated RTJ (I-RTJ) is 160 as. These experimental results show that SESS produces wavelength tunable pulses with ~17 times smaller RTJ and >20 times (3.3 nJ versus 0.15 nJ) larger pulse energy in comparison with a Raman soliton source.
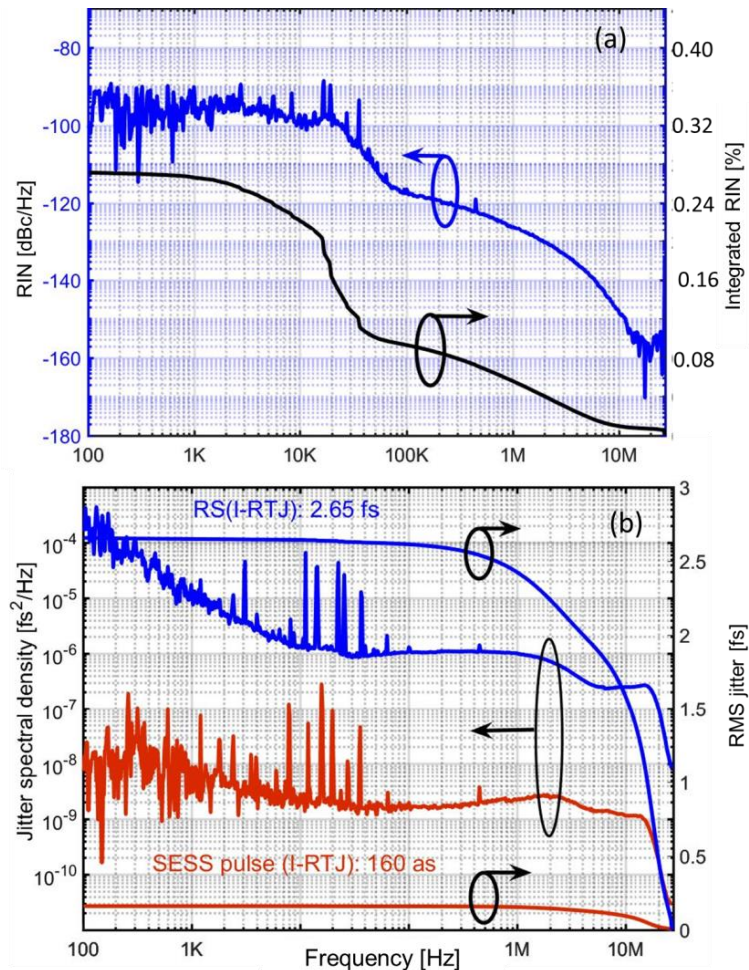
Figure 3.14: RIN measurement (blue curve) of the source laser at 1030 nm. Black curve: integrated RIN. (b) RTJ of Raman soliton source (blue curve) and SESS source (red curve) both at 1140 nm. I-RTJ: integrated RTJ.
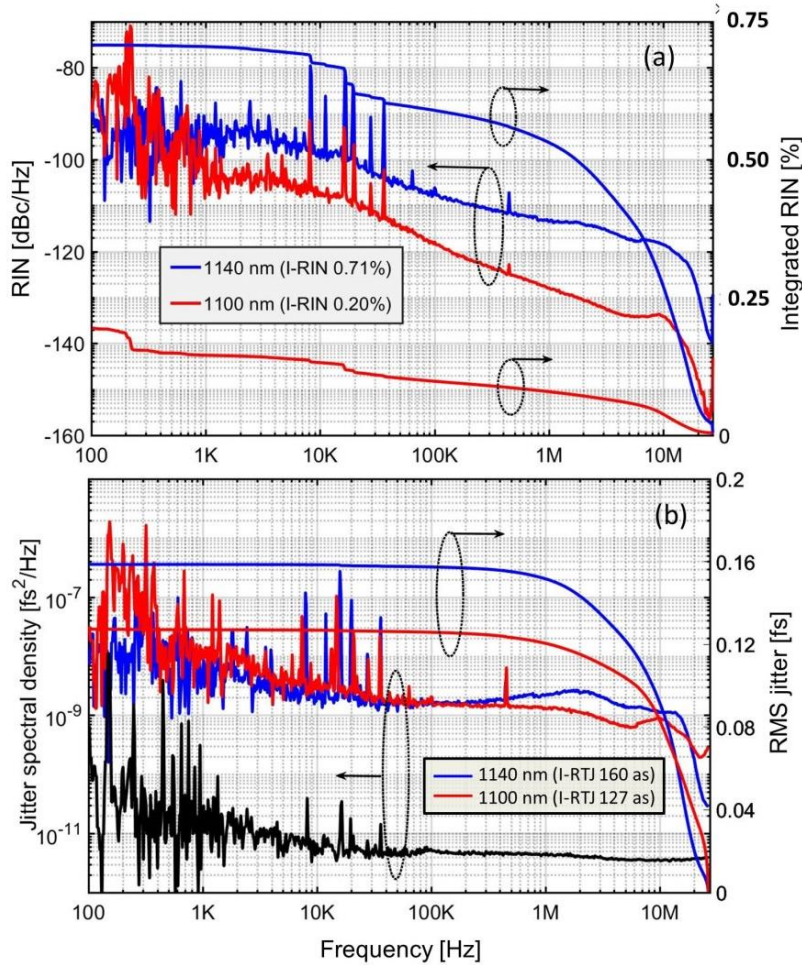
Figure 3.15: RIN and RTJ measurement of SESS pulses. (a) RIN measurement of two SESS pulses at 1140 nm (blue curve) and 1100 nm (red curve). (b) RTJ of the SESS pulses at 1140 nm (blue curve) and 1100 nm (red curve). Black curve: instrument noise floor.

The peak wavelength of the pulses can be tuned by varying the excitation pulse energy. By decreasing the incident power coupled into the optical fiber from 1.8 W to 1.2 W, the rightmost spectral lobe shifts from 1140 nm to 1100 nm. Both RIN and RTJ of SESS pulses are recorded and compared at these two wavelengths. Figure 3.15(a) shows the PSD of RIN from 100 Hz to the Nyquist frequency of 27.5 MHz. The I-RIN in this frequency range is 0.71% and 0.20%, respectively. It is noteworthy that the RIN of a SESS pulse highly depends on the relation between the bandwidth of the rightmost spectral lobe and the bandwidth of the bandpass filter. As we couple more power into fiber LMA8, the rightmost spectral lobe shifts towards longer wavelength and meanwhile becomes broader. The rightmost spectral lobe peaking at 1140 nm has nearly twice the bandwidth of the one peaking at 1100 nm and its 10-dB bandwidth is well beyond 50 nm. As we use the bandpass filter of 50-nm bandwidth to filter the SESS pulse, a larger portion of the 1140-nm spectral lobe is blocked by the filter compared with the 1100-nm spectral lobe. Consequently, the SESS pulse at 1140 nm is more sensitive to the RIN of the source laser than the 1110-nm SESS pulse and therefore exhibits a much larger RIN. Figure 3.15(b) plots the RTJ of the filtered pulses at 1140 nm (blue curve) and 1100 nm (red curve). The instrument noise floor is also shown as the black curve. The I-RTJ from 100 Hz to 27.5 MHz is 160 as and 127 as corresponding to the filtered

pulses at 1140 nm and 1100 nm, respectively. Such a 100-as precision RTJ ensures a tight synchronization between the SESS pulse and the excitation pulse. To the best of our knowledge, this represents the lowest RTJ ever reported from a two-color source derived from an ultrafast laser.

To further prove that the SESS pulse is highly synchronized with the excitation pulse, we measure the RIN of the sum frequency generation (SFG) pulses generated by mixing the SESS pulses at 1140 nm and the excitation pulses at 1030 nm. The signal is detected from one arm of the BOC. For comparison, we also carried out the same measurement for the Raman soliton pulse centered at 1140 nm. Figure 3.16 presents the RIN of the SFG pulses. Due to the limited detection bandwidth of balanced photo-detection in our BOC setup, we only record the measurement from 100 Hz to 1 MHz. The RTJ of two pulses in the process of SFG mainly contribute to the power fluctuation of the SFG pulses. A huge decrease (more than 50%) of RIN noise of SFG pulses is observed when SESS pulses instead of Raman soliton pulses are used for SFG. The SESS pulses have much lower RTJ in the frequency region larger than 1 MHz, and therefore the SFG pulses generated by the SESS-enabled two-color source should have much lower I-RIN when integrated from 100 Hz to 27.5 MHz.
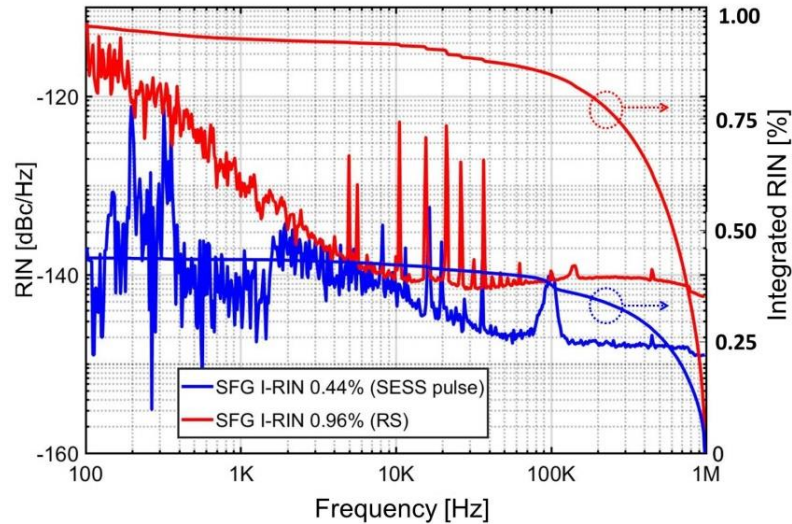
Figure 3.16: RIN measurement of SFG pulses generated by pump laser pulses at 1030 nm and signal pulses at 1140 nm. The signal pulses are derived from the pump pulses via SESS (blue curve) or SSFS (red curve).

In conclusion, we both numerically and experimentally investigate the RTJ performance of SSFS and SESS. We show that the SESS pulse is tightly synchronized to the excitation pulse with the RTJ at ~100-as precision, at least 10 times lower than can be achieved from SSFS. A SESS source and its excitation laser source form a tightly synchronized two-color source that opens avenues to many applications. Recently, we study the power scalability of high repetition-rate DFG and show that high power longwave mid-IR frequency combs can be implemented via DFG in which the signal pulse has the energy comparable with the pump pulse [166]. We believe that the energetic tunable pulses produced by SESS are suitable to be used as the signal pulse. Together with the excitation pulse as the pump pulse, such a tightly synchronized two-color source will facilitate the development of high-power, low-noise mid-IR frequency combs tunable in 6-18 μm.

3.4   Summary of the chapter

This chapter numerically and experimentally investigate the nonlinear wavelength conversion method, including Soliton self-frequency shift (SFSS) and SPM-enabled spectral selection (SESS), in different fibers. First, in the simulation, their relative timing jitter to the excitation pulse is investigated. Then we conduct the experiment to compare the relative timing jitter (RTJ) of RS and SESS pulse and conclude that the SESS pulse highly synchronizes to its excitation pulse with an RTJ in the attosecond level. Furthermore, combining the SESS pulse with the source laser demonstrates a highly synchronization wavelength-tunable two-color source with the relative timing jitter at 100-as-level.

Chapter 4

Fiber Seed Source for Cryo Yb:YLF Amplifier System

High-energy pulses at high average power with sub-picosecond (sub-ps) duration at 1 μm wavelength are desired in many applications, such as soft x-ray generation [1], optical parametric chirped-pulse amplifier pumping [2], terahertz radiation generation and amplification, as well as high-brightness photoinjectors for laser wakefield acceleration or free-electron lasers [3]. Room temperature (RT) Yb: yttrium aluminum garnet (Yb:YAG) laser systems are becoming commonplace for producing high average power and high energy sub-ps optical pulses due to their quantum-limited emission efficiency, strong thermo-mechanical properties and broadband emission spectrum. The long fluorescence lifetime (τ: 940 μs) and large emission cross-section (σ_{em}: $2.15 \times 10^{-10} cm^2$) of Yb: YAG enables a large overall gain [15]. The cryogenically cooling Yb:YAG can further scale up the average power due to the several advantages under cryogenic temperature, such as the transition from quasi-3-level to a four-level laser system, improved thermos-optic effects and a larger emission cross-section [167]. However, the drawbacks of cooling Yb:YAG to liquid nitrogen temperatures is a reduced emission bandwidth (from 8 nm to 1.5 nm) that cannot deliver sub-ps pulses, as shown in
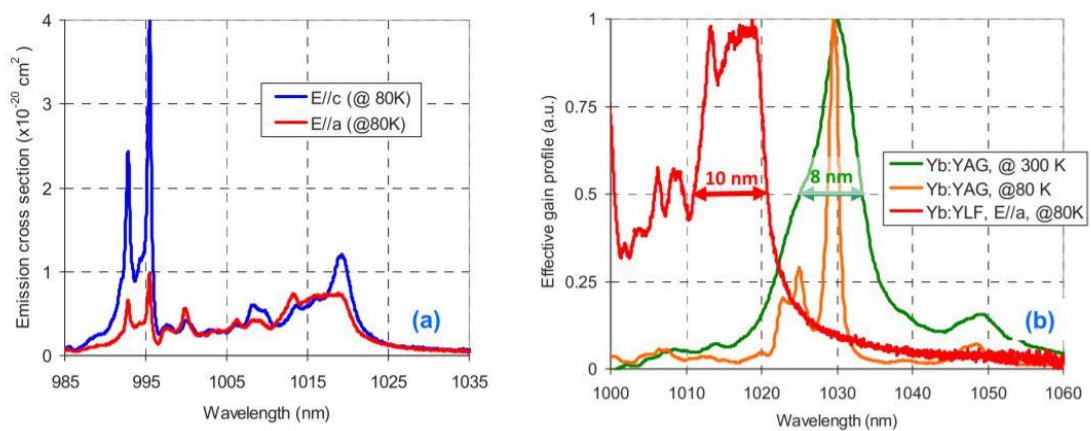
Figure 4.1: Measured emission cross section of Yb:YLF at 80K for E//a and E//c polarizations. (b) Comparison of effective gain cross section of Yb:YLF (E//a, 80K) with room temperature (RT:300K)

Chapter 4: Fiber seed source for cryo Yb:YLF amplifier system

In contrast, cryogenically cooled Yb: yttrium lithium fluoride (Yb:YLF) has a gain bandwidth of several nanometers centered at 1018 nm （10 nm for E//a , 2.5 nm for E//c）, enough to support sub-500 fs (sub-800 fs) pulse operation for E//a axis (E//c axis) [15]. Besides, its gain profile has a flat shape, which can minimize the gain narrowing effect during amplification. A considerable improvement in the thermos-optic properties of YLF at cryogenic temperatures and its weak and negative thermal lensing helps to achieve high beam quality even in high-average power operation. Together with a high saturation fluence, a longer excited-state lifetime, and a smaller quantum defect than Yb:YAG, cryogenically cooled Yb:YLF has the potential for realizing sub-ps laser sources featuring both high pulse energy and high average power [18]. The larger gain bandwidth of cryogenically cooled Yb:YLF is also advantageous for the application of the chirped-pulse amplification (CPA) technique. However, a seed laser operating at 1018 nm central wavelength and with a large stretching factor is required to permit efficient and damage-free energy extraction in the subsequent 200 mJ-class amplifiers under construction [17]. In a previous implementation of a cryogenic Yb:YLF CPA laser system, a Ti:sapphire laser was used as the seeder to reach 100 W at 10 kHz [9]. However, the low seeding pulse energy (~1 nJ) at the wavelength of 1018 nm required numerous passes in subsequent amplifiers with unfavorable consequences on stability and spectral narrowing due to the large gain required to achieve 10 mJ level pulse energy.

Apart from the broadband luminescence (10 nm) of cryogenically cooled Yb:YLF for E//a axis, Cryo YLF has an even larger emission cross-section ($\sim4.6\times10^{-20}$ cm^2) of the 995 nm laser transition with a long upper laser level lifetime (~2 ms) for E//c axis [168]. Consequently, the gain product of Yb: YLF is as high as 8.95×10^{-23} cm^{2}s, which is 6 times larger than the broadband laser transition at 1018 nm for E//a. Recently, high-power cryogenically cooled Yb:YLF laser system working at 995 nm laser transition has largely been investigated in both continue wave and Q-switch modes operation. However, due to the lack of mode-locking seed source delivering enough pulse energy at the wavelength of 995 nm, the power scaling capability of cryo Yb:YLF amplifier for 995 nm mode-locking pulses has not yet been demonstrated so far.

A high-energy mode-locking seeding source with tunable wavelength (from 995 nm to 1020 nm) and bandwidth (3 nm~10 nm) will facilitate the investigation and implementation of a several-hundred mJ cryogenically cooled Yb:YLF amplifier chain by mitigating amplified spontaneous emission (ASE) and gain-narrowing in the onwards amplifier chain. Such a multi-functional wavelength-tunable fiber seed source allows the cryo Yb:YLF amplifier system either to work at the sub-500 fs pulse mode at 1020 nm for E//a axis or ps-pulse mode at 995 nm for E//c axis. Usually, μJ to-mJ pulse energy can be achieved in an ultrafast Yb-fiber amplifier system employing large-mode-area double cladding gain fiber or rod-type gain fiber [169]. However, all these high-energy sub-ps sources operate at 1030 nm. Indeed, Yb-fiber exhibits a broad gain bandwidth, allowing laser operation in the wavelength range between 980 and 1070 nm [22].

To date, the reported high-power Yb-fiber lasers at around 1018 nm produce either continuous waves [170] or pulses of several picoseconds in duration [171]. Sub-ps high power sources at 1018 nm specially

designed for seeding cryogenic cooling YLF have never been reported before. For the fiber laser operating at the wavelength of 995 nm, there is barely any report. Apart from the lack of a seed source range from 995 nm to 1018 nm, the amplifying pulse at this wavelength range in a Yb-doped fiber front end is another challenge because Yb-fiber lasers operate as three-level systems for the signal wavelength below 1030 nm [172]. Consequently, the relatively small emission cross-section and high absorption cross-section require high inversion pumping and short gain fiber length to prevent signal reabsorption that decreases the slope efficiency of the Yb-fiber amplifier system. Additionally, the ASE around 1030 nm competes with the signal at the shorter wavelength for up-level population. To suppress the ASE at 1030 nm and efficiently amplify the signal from 995 nm to 1020 nm, high inversion pumping or specialty gain fibers are necessary. During the amplification, spectral broadening and wavelength shifting should also be carefully controlled.

In this chapter, we first experimentally demonstrate a high-power fiber-based system specifically designed to seed a high-energy Yb:YLF amplifier system at the wavelength of 1018 nm with 2.5-nm spectral bandwidth. With a repetition rate of 17.88 MHz, the fiber-based master-oscillator power amplifier (MOPA) front end employs the CPA technique and produces 87-W, 4.9-μJ pulses centered at 1018 nm with 1-ns stretched duration. The amplification is achieved by two stages of specially designed fiber amplifiers that suppress the ASE at 1030 nm [11]. Then, we demonstrate a compact wavelength-tunable fiber seed source (from 995 nm to 1018 nm) with moderate pulse energy (10 to 30 nJ) for the further investigation of sub-500 fs pulse amplification at 1020 nm as well as the high-energy pulse amplification at 995 nm.

4.1   Linear Fiber MOPA system at 1018 nm
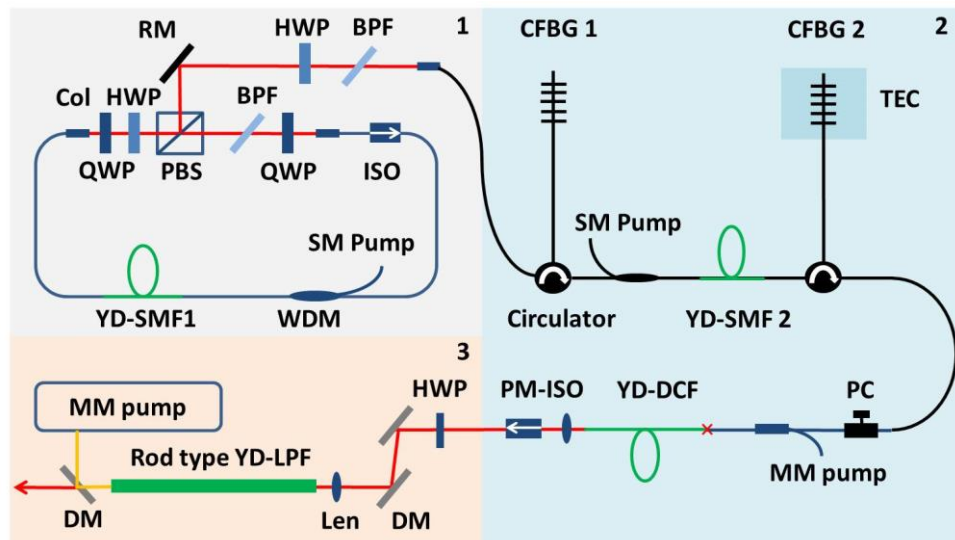
Figure 4.2: Schematic of 1018-nm MOPA system. It includes three parts: Yb-fiber oscillator (Part 1), two stages of pulse stretcher and preamplifier (Part 2), and rod-type Yb-fiber power amplifier (Part 3). HWP, half-wave plate; QWP, quarter-wave plate; BPF, bandpass filter; PBS, polarization beamsplitter; RM, reflecting mirror; Col, collimator; WDM, wavelength division multiplexer; SM, single mode; MM, multimode; CFBG, chirped fiber Bragg grating; PC, polarization controller; PM-ISO, polarization sensitive isolator; DM, dichroic mirror; YD, ytterbium-doped; SMF, single mode fiber; DCF, double-clad

fiber; LPF, large-pitch fiber. Non-PM fiber, PM fiber, and Yb-doped fiber are denoted by the blue line, black line, and green line, respectively.

In this section, we experimentally demonstrate the first fiber front-end laser system developed for E//c-cut cryo Yb:YLF amplifier system, delivering highly-chirped pulse at the wavelength of 1018 nm with 2.4 nm bandwidth. By stretching the pulse to 1 ns in several stages of chirped fiber Bragg gratings (CFBG), a linear fiber MOPA system is constructed, delivering 87-W and 4.9-µJ pulse.

Figure 4.2 shows the experimental setup consisting of three parts: an Yb-fiber oscillator, two stages of fiber stretchers with preamplifiers, and a rod-type power amplifier. Part 1 is a 17.88- MHz all-normal-dispersion (ANDi) oscillator at 1020 nm mode-locked by nonlinear polarization evolution in combination with an intracavity bandpass filter (BPF) [48]. Part 2 includes two PM circulators connected to two PM chirped fiber Bragg gratings (CFBGs), which stretch the laser pulse to ~1 ns duration therefore alleviating nonlinear effects in subsequent amplifier stages. Part 3 is the power amplifier consisting on a 1.2-m Yb-doped rod-type large-pitch fiber (LPF) [169], which can produce 100 W, high quality µJ pulses configured in pre-chirp managed amplification [65].

4.1.1 ANDi fiber oscillator at 1020 nm (Part 1)

To seeding pulse centered around 1020 nm for following amplification, a 17.88 MHz all-normal-dispersion (ANDi) oscillator at 1020 nm mode-locked by nonlinear polarization evolution in combination with an intracavity bandpass filter (BPF). The BPF has 4-nm transmission bandwidth, and the center wavelength can be tuned by tilting its incident angle. The passive fiber is 10 and 0.5 m long before and after the 0.4-m gain fiber (Coractive Yb 401), respectively. This ANDi laser relies on the narrow bandpass filter for wavelength selection and energy dissipation to achieve stable mode-locking at the target wavelength. The shortest and longest center wavelength achieved by the ANDi laser is usually limited by the pump power, the cavity length, and the emission spectrum of the gain fiber inside the cavity [173]. The longest wavelength ever reported for ANDi mode-locked fiber lasers is 1070 nm, while the shortest is 1024 nm. Further blue shifting the center wavelength is extremely challenging because low gain and large gain dispersion may prevent mode-locking.
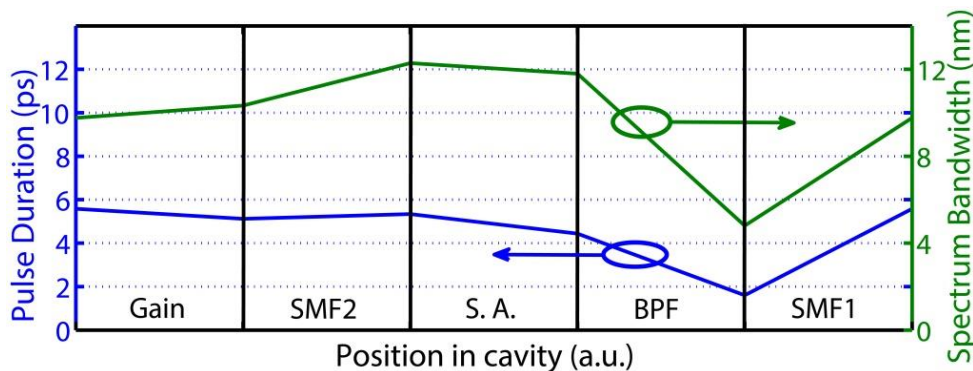
Figure 4.3: Simulation of spectral bandwidth (Green) and pulse duration (Blue) for one laser round-trip. GAIN: 0.4-m high doping Yb-fiber, SMF2: 0.5-m single mode fiber, S.A.: saturable absorber, BPF: narrow bandpass filter at 1020 nm with 4-nm bandwidth, SMF1: 10-m single mode fiber.

Chapter 4: Fiber seed source for cryo Yb:YLF amplifier system

We first carry out numerical simulation to investigate the mode-locking of this Yb-fiber oscillator at ~1018 nm. The intracavity pulse built up is modeled by the generalized nonlinear Schrödinger equation incorporating a simplified saturable absorber model, in which the transmittance of the effective saturable absorber is given by $T=1-l_0/[1+P(t)/P_{sat}]$. l_0 is the unsaturated loss, $P(t)$ the instantaneous pulse power, and P_{sat} the saturation power [43]. The Yb-fiber gain has a Lorenz line shape centered at 1030 nm with 40-nm bandwidth. A 4-nm bandwidth filter (super-Gaussian shape) with a tunable central wavelength selects the target mode-locking wavelength in the cavity. By shifting the central wavelength of the filter to 1020 nm, the oscillator reaches a stable mode-locking state. The evolution of pulse duration and spectral bandwidth inside the cavity is shown in Fig. 2, revealing the features of similariton evolution as a result of the narrow bandpass filter and large passive fiber length [48]. Both the pulse duration and the spectral bandwidth breathe during a round trip.
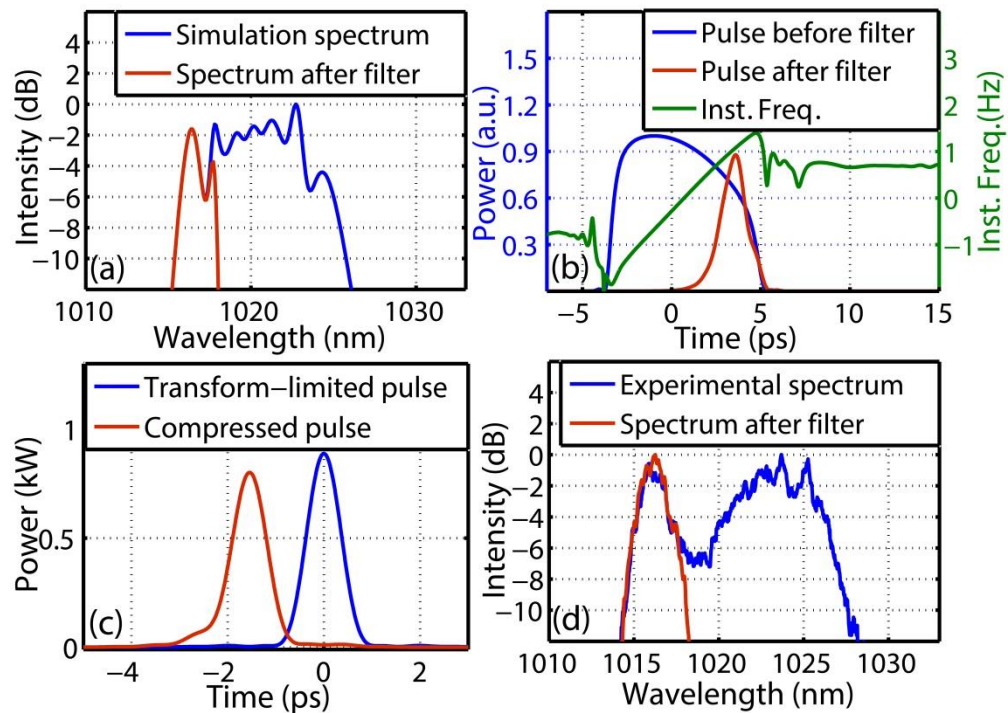
Figure 4.4: Simulation and experimental results of fiber oscillator in 1018-nm laser system. (a) Simulation of oscillator output spectrum (blue curve) and spectrum after filter (red curve) with 2.5 nm bandwidth at 1016. (b) Simulation of Output pulse (blue curve) with nonlinear chirp (green curve) and filtered pulse (red curve). (c) Simulation of transform-limited pulse (blue curve) and compressed pulse (red curve) after spectral filtering. (d) Measured output spectrum of oscillator (blue curve), spectrum after BPF with 2 nm bandwidth at 1016 nm (red curve) in experiment. Inst. Freq.: instantaneous frequency.

Figure 4.4(a-c) presents the simulation results on the spectral and temporal properties of the Yb-fiber oscillator. The laser output spectrum (blue curve in Figure 4.4(a)) centers at 1020 nm with 10-nm bandwidth and covers the key spectral component around 1018 nm. Further tuning the spectrum to shorter wavelength leads to failure of mode-locking because the increased wavelength mismatch with the Yb-fiber peak gain reduces the round-trip gain to a value that cannot compensate for the intra-cavity loss. Figure 4.4(b) shows the temporal profile of the output pulse (blue curve) with positive chirp (green curve).

73

The asymmetric pulse shape is due to the gain dispersion, which destroys the symmetry of the similariton pulse and its linear chirp [174]. Another super-Gaussian bandpass filter placed outside the cavity selects a 2.5 nm wide spectral band centered at 1016 nm (red curve in Figure 4.4(a)). We intentionally pick the wavelength slightly shorter than 1018 nm such that it shifts to longer wavelength in the subsequent fiber components due to nonlinear propagation. The corresponding filtered pulse is shown as the red curve in Figure 4.4(b). Although the whole output pulse exhibits strong nonlinear chirp, the pulse given by the filtered spectrum is located at the tail of the overall pulse and is almost linearly chirped. Numerical compression of the pulse after filtering by a pair of transmission gratings (groove density: 1000 lines/mm) is compared with the transform-limited pulse in Figure 4.4(c) demonstrating the feasibility of good pulse compression.

Guided by the simulations, we construct the Yb-fiber oscillator. The blue curve in Figure 4.4(d) shows the experimentally achieved broadband oscillator output, which covers 1015-1025 nm with a 2-nm spectral lobe centered at 1016 nm. A comparison between Figure 4.4(a) and Figure 4.4(d) shows that the numerical simulation agrees qualitatively with the experimental results. We use a bandpass filter to select the spectral lobe at 1016 nm (red curve in Figure 4.4(d)) and then free-space couple it into the subsequent polarization maintaining (PM) fiber that belongs to Part 2 of our setup.

4.1.2 CFBG stretcher and pre-amplification of 1018 pulse (Part 2)
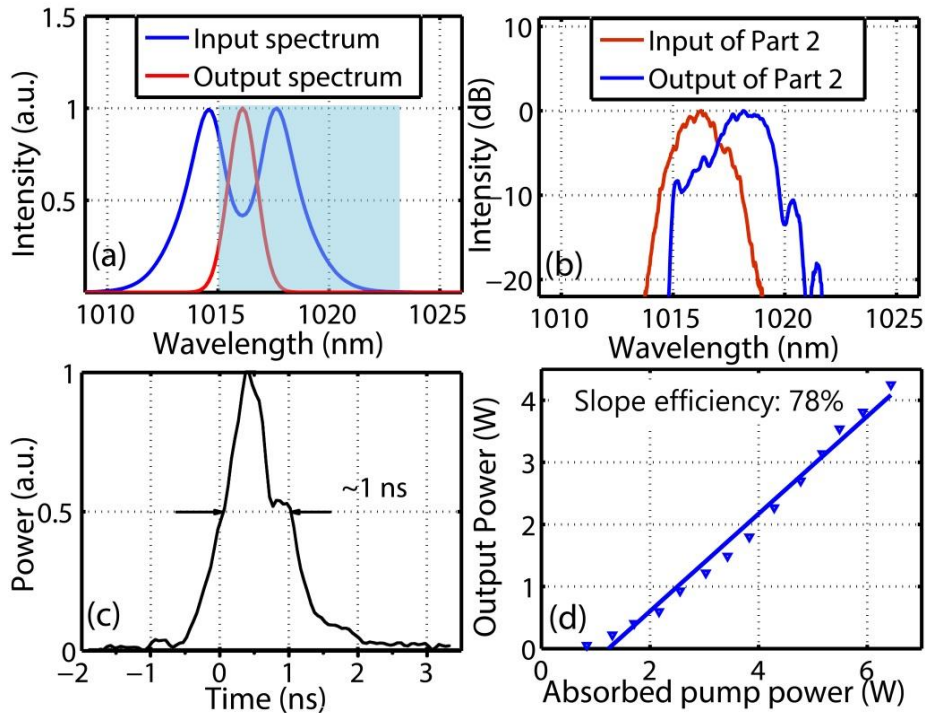
Figure 4.5: Simulation and experimental results of fiber pre-amplifier in 1018-nm laser system. (a) Simulation of 800-fs, 1-nJ transform-limited Gaussian pulse propagating through 0.8-m passive fiber. Red curve: input spectrum, blue curve: output spectrum, blue shadow: reflection bandwidth of the CFBG. (b) Measured spectra at the input (red curve) and output (blue curve) of Part 2. (c) Measured pulse after two stages of CFBGs. (d) Measured output power versus absorbed pump power in the flattened absorption Yb-fiber amplifier.

Chapter 4: Fiber seed source for cryo Yb:YLF amplifier system

Part 2 includes two PM fiber-pigtailed circulators connected to two PM chirped fiber Bragg gratings (CFBGs) with 7.5-nm reflection bandwidth centered at 1019 nm. These CFBGs are designed to compensate for the dispersion of a 1760 lines/mm grating-pair compressor operated at 61-degree incidence angle. The dispersion curve of the grating compressor is shown in Figure 4.6.
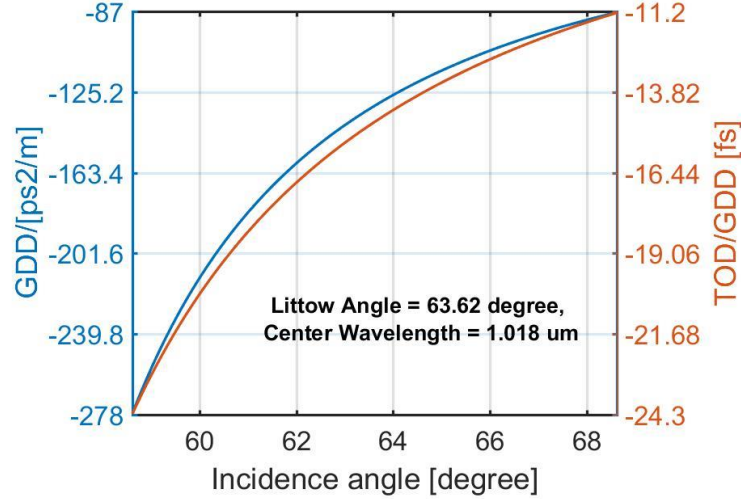
Figure 4.6: GDD (blue) and the ratio of TOD versus GDD (orange) of 1760 grooves grating pair. For our case, the incidence angle is fixed at 61 degree so that the GDD is -182 ps^2/m and TOD/GDD is -18.3 fs for this grating compressor.

The first CFBG has a chirp rate of -306 ps/nm, corresponding to GDD value of 168.2 ps^2 at 1018 nm and the second one -100 ps/nm with GDD value of 55 ps^2. The TOD/GDD is the same in these two pieces of CFBG with the value of -18.3 fs. Considering that the nonlinear length is about 0.2 m for a 1-nJ transform-limited Gaussian pulse with 2-nm spectrum bandwidth, we expect that the spectrum of the input pulse broadens in the passive fiber prior to the first CFBG. Relying on both this spectral broadening and the CFBG filtering, the target wavelength around 1018 nm can be readily achieved. This is confirmed by the simulation in which we numerically propagate 1-nJ, 800-fs transform-limited Gaussian pulse (corresponding to 2-nm bandwidth) in 0.8-m passive fiber. As Figure 4.5(a) shows, the initial Gaussian spectrum (red curve) evolves into two spectral lobes mainly due to self-phase modulation. The spectral lobe on the longer side peaks at ~1018 nm and is selected by the CFBGs. The simulation results are confirmed by the measured output spectrum from Part 2 (blue curve in Figure 4.5(b)) that is red-shifted compared with the input spectrum (red curve in Fig. 4(b)). During the experiment, we adjust the passive fiber length and fine tuning the input pulse energy to achieve the output spectrum with 2.5 nm bandwidth centered at 1018 nm. The bandwidth is 0.5 nm larger than the emission spectrum of Cryogenic YLF (2 nm) for E//c axis at 1018 nm, which pre-compensates for the gain narrowing in the cryogenic Yb:YLF amplifier. The two stages of CFBGs stretch the pulse to ~1 ns duration (Figure 4.5(c), measured using a 20-GHz bandwidth photodiode attached to a 4-GHz bandwidth oscilloscope) therefore alleviating nonlinear effects in subsequent amplifier stages. A pre-amplifier based on a 3-m long, low doping gain fiber (Nufern PM-YSF-LO) is inserted between the two circulators to compensate the losses introduced

by the circulators and CFBGs. There is no noticeable wavelength shifting in this amplifier stage owing to the high level of inversion in the gain fiber [175].

The second amplifier that is spliced directly to the port 3 of circulator 2 is constructed from 1-m flattened absorption Yb-doped double-clad fiber (Coractive DCF-YB-8/128P-FA). Usually, Yb-doped fiber lasers exploit the quasi-four-level system between 1030 and 1100 nm [176]. For wavelength below 1030 nm, Yb-fiber operates as a three-level system, making amplification of sub-ps pulses at 1018 nm difficult due to the low emission cross section and high absorption cross section at shorter wavelength. Fortunately, the flattened absorption Yb-fiber is specially designed to suppress ASE at 1030 nm and provides higher gain at 1018 nm than 1030 nm [177]. As a result, the Yb-fiber amplifier efficiently amplifies the signal wavelength to 4-W average power with a very high slope efficiency of 78% at a wavelength of 1018 nm (Figure 4.5(d)) and negligible ASE. Although the Yb-fiber is non-PM, adjusting the polarization controller at the combiner input results in 18-dB polarization extinction ratio.

The maximum output from Part 2 is 4 W corresponding to 223-nJ pulse energy. This energy level is sufficient for seeding a 10-mJ class cryogenically cooled YLF amplifier and subsequent 100-mJ class amplifiers. Indeed, more power extracted from the fiber front end leads to less gain needed for the following 100-mJ-level cryogenic YLF amplifiers. Since the cryogenically cooled gain crystal has a relatively narrow gain spectrum of only 2 nm compared with Yb-doped fiber amplifiers with 40 nm bandwidth, increasing the seed power directly from the fiber can mitigate the gain narrowing effect in subsequent amplifier stages and, therefore, allows to obtain sub-ps duration pulses in the final amplifier stage [16]. Because the pulse is stretched to ~1 ns, further amplification to higher pulse energy levels can be readily achieved.

4.1.3 Power amplifier based on rod-type LPF (Part 3)

To demonstrate the possibility of further amplification, Part 3 is constructed, which is a power amplifier using a 1.2-m long Yb-doped, rod-type large pitch fiber (LPF) for further energy boosting [169]. The special design of large core diameter (80 µm) and robust single mode operation allows for high energy extraction with diffraction-limited beam quality. It is noteworthy that the unique double cladding structure of rod-type LPF with the small clad-to-core area ratio is critical for achieving a relatively high slope efficiency to amplify wavelength shorter than 1030 nm with negligible ASE [178].

Figure 4.7(a) shows the output spectra versus average power of the amplified pulses. The signal spectra remain unchanged suggesting a linear amplification. Broadband ASE peaking at 1030 nm grows with the increased pump power, yet remains 26 dB below the signal spectral peak even at the highest average power of 87 W. The slope efficiency of the LPF amplifier is 49% (Figure 4.7(b)), which is higher than that achieved from other rod-type LPF laser systems working at the same wavelength around 1018 nm [179]. Inset of Figure 4.7(b) shows the excellent spatial profile of the 87-W amplified pulses, corresponding to a pulse energy of 4.9 uJ. Due to the limited input signal power level of rod type fiber amplifier, we restrict the final power output to below 100 W in order to avoid the onset of harmful parasitic oscillation at the ASE peak.

At this end, we report a high-power 17.88 MHz Yb-fiber MOPA system operating at 1018 nm with 87-W average power. The ASE at 1030 nm is efficiently suppressed during amplification using specially

designed flattened absorption fiber and rod-type LPF. It is the first powerful fiber front end designed especially for 100 mJ, sub-ps duration cryogenic Yb:YLF amplifier chain with its output spectrum precisely matching the gain of Yb:YLF crystals (2-nm bandwidth at the center wavelength of 1018 nm for E//c axis), and the bandwidth is slightly larger to compensate for the gain narrowing effect. The 4.9-µJ pulse energy is the highest pulse energy at 1018 nm achieved by fiber laser systems. At 1-ns stretched pulse duration, linear amplification to mJ pulse energy is feasible [25]. Since the main scope of this work is to develop a suitable frontend seeding source for cryogenic Yb:YLF amplifier chain, we leave the amplified pulses uncompressed. Indeed, they can be compressed using a pair of transmission gratings (groove density: 1700 lines/mm). We recently implemented a 1018-nm frontend with the similar design and seeded a 190-mJ-level cryo Yb:YLF amplifier chain. The amplified pulses were compressed to 1.2 ps while the transform-limited duration is 800 fs. Such a deviation can be mitigated by incorporating temperature gradient to fine tune the dispersion property of the CFBG stretcher.
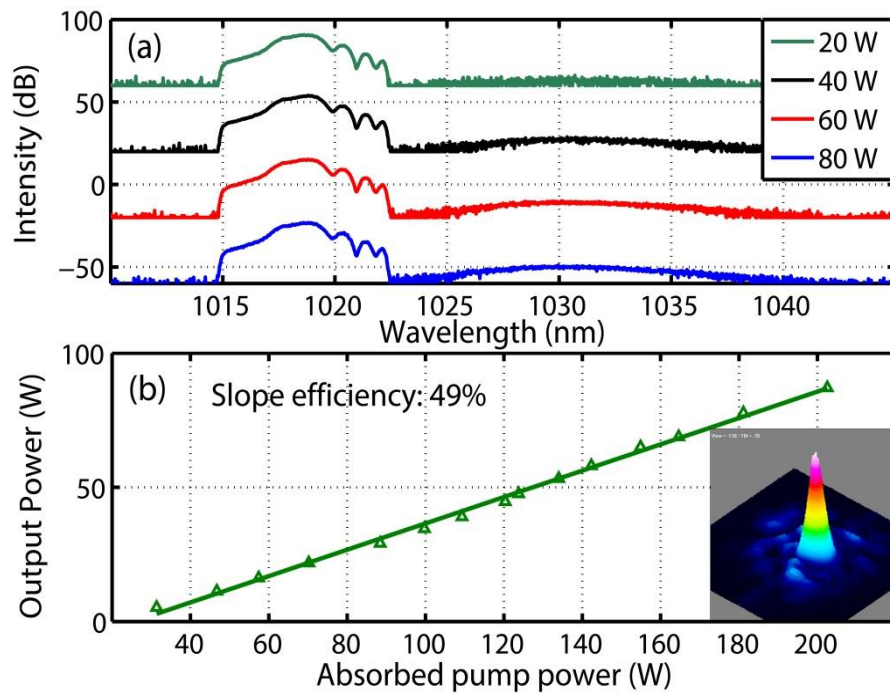
Figure 4.7: Experimental results of rod-type power amplifier in 1018-nm laser system. (a) Output power versus absorbed pump power of rod type LPF amplifier and spatial profile (inset). (b) Output spectra of rod-type LPF amplifier at 1018 nm for increasing pump powers.

4.2 Wavelength-tunable Fiber MOPA system

The emission cross-section of cryogenic Yb: YLF covers the 980-1040 nm range, with two strong and distinct emission peaks centered around 995 and 1020 nm [15]. Since the gain spectrum of cryogenic Yb: YLF crystal and Yb-doped fiber overlap around the wavelength of 1020 nm, it is straightforward to construct a seed source based on a fiber laser at the wavelength of 1020 nm. In the last section, we designed a compact fiber-based master-oscillator-power-amplifier (MOPA) seed source operating at 1018 nm that delivers 4.9-uJ pulses with 2.5-nm spectral bandwidth, supporting sub-ps pulse operation. However, the emission band around 995 nm is 5-6 folds stronger, and it is broad enough to allow

amplification of sub-500-fs pulses. Moreover, the 995 nm emission shows a smaller quantum defect, potentially minimizing the thermal load on the crystal. All these facts could facilitate the development of high peak and average power ultrafast laser amplifier systems around 995 nm based on cryogenic Yb: YLF. However, the required broadband seed pulses centered at 995 nm are hard to realize due to the lack of a gain medium directly covering this wavelength range. Though Ti:Sapphire lasers offer broadband pulses, spectral filtering at 995 nm leads to pulses with low energy and low efficiency. Building an ultrafast seeding source directly based on cryogenic Yb: YLF crystals would be expensive and hard to maintain [10]. Therefore, a fiber-based seed source at 995 nm is desired. The basic idea to achieve 995 nm seeding is to utilize the nonlinearity of the gain fiber for amplification and wavelength shifting with relatively high efficiency.

In this section, we demonstrate a wavelength-tunable (from 995 nm to 1020 nm) fiber-based system specifically designed to optimally seed a high energy cryogenic Yb: YLF amplifier chain. Only single-mode diodes are used for pumping, which enables a small laser footprint. The fiber-based seed laser operating at a repetition rate of 1.47 MHz produces wavelength-tunable pulses in the range from 995 to 1020 nm with >10 nJ pulse energy and ~4-nm bandwidth, ideally matching the emission spectrum of cryogenic Yb: YLF crystals. Wavelength tunability is achieved by simply changing the pump power, which makes it easy to operate. The output wavelength is adjustable to fit the emission band of the subsequent amplifiers, either around 1020 nm or 995 nm. As far as we know, this is the first demonstration of a fiber laser system specifically designed for efficient seeding of cryogenic Yb: YLF amplifier systems.
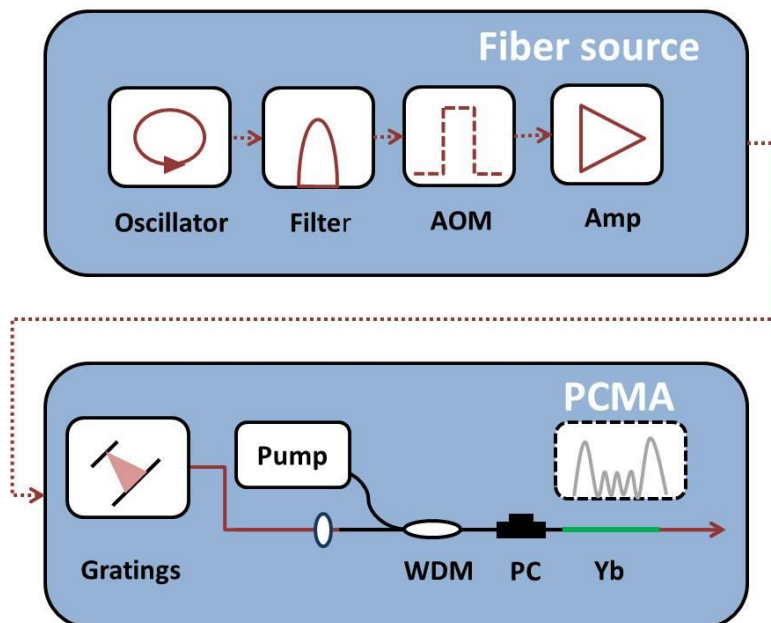
Figure 4.8: Schematic of the wavelength-tunable seed laser setup. Fiber source includes a 22-MHz fiber oscillator, a 4-nm Gaussian bandpass filter, an Acousto-Optic Modulator (AOM) for pulse picking and the fiber-based pre-amplifier. The pre-chirp managed amplifier (PCMA) includes a grating pair, and a nonlinear fiber amplifier with single mode highly doped Yb fiber (Yb-406, Coractive) pumped by a single mode diode at 976 nm through a wavelength division multiplexer (WDM). An in-line polarization controller (PC) is put in front of gain fiber. The sketch of typical output spectrum from the PCMA is shown above Yb fiber.

Chapter 4: Fiber seed source for cryo Yb:YLF amplifier system

The seed laser setup consists of a fiber source (Part 1) and a pre-chirp-managed nonlinear amplifier (PCMA) (Part 2). The fiber source contains a 22-MHz Yb-doped fiber oscillator, a 4-nm Gaussian bandpass filter, an inline Acousto-Optic Modulator (AOM) for pulse picking followed by a single-stage preamplifier. It delivers a 1.47-MHz chirped Gaussian pulse at the wavelength of 1030 nm with 4-nm bandwidth. The PCMA consists of a pair of transmission gratings for pre-chirp management, an inline polarization controller (PC), and a commercial highly doped Yb fiber pumped through a WDM. By overcompensation of the injected pulse to a tunable negative chirp as well as adjusting the PC, we can fully control the seeding pulse's parameters (duration, energy, polarization) in the highly-Yb-doped fiber for spectral broadening and amplification. The broadband wavelength-tunable pulse is generated in this stage of the amplifier. But there is a trade-off between nonlinear spectral broadening and the amplification of the spectral components within the Yb fiber's emission band. If the shift of the spectral components to the edge is too fast, the pulse could not be amplified due to a lack of signal inside the gain bandwidth of the Yb fiber. Hence, during the experiments, the system parameters are optimized such that spectral broadening mainly occurs in the last section of the gain fiber, enabling extraction of high energy broadband pulse. The spectral broadening is controlled by carefully choosing the fiber length and adjusting the seed pulse duration with the help of a grating pair.

4.2.1 1.5-MHz fiber source at 1030 nm (Part 1)

The detailed schematic of the fiber source is shown in Figure 4.9. The 22-MHz fiber oscillator works on an all-normal-dispersion (ANDi) regime. It is mode-locked by nonlinear polarization evolution in combination with an intracavity bandpass filter (BPF). The BPF has 10-nm transmission bandwidth with the center wavelength of 1030 nm. The passive fiber is 7.9 m and 0.5 m long before and after the 0.4-m gain fiber (Coractive Yb 401), respectively. This ANDi laser relies on the bandpass filter for wavelength selection and energy dissipation to achieve stable mode-locking at the target wavelength. The output pulse centered at 1030 nm with 10-nm bandwidth is highly chirped. The direct output pulse duration is stretched to ~10 ps due to the long fiber cavity length. Considering the limited rising time (10 ns) of the following Acousto-optic modulator (AOM), we intend to construct the oscillator with a low repetition rate (22 MHz) for clean pulse picking afterward.
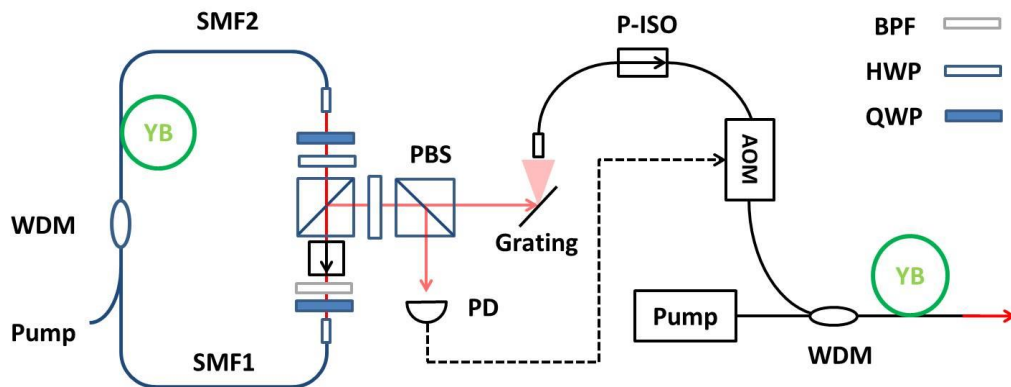
Figure 4.9: Schematic of the fiber laser source in wavelength-tunable seed laser. It includes a 22-MHz fiber oscillator, a 4-nm Gaussian bandpass filter, an Acousto-Optic Modulator (AOM) for pulse picking and the fiber-based pre-amplifier in a sequence. The 4-nm Gaussian bandpass filter is constructed with a

300 grooves refection grating and a collimator with focus length of 5mm. By rotating the angle of grating, the center wavelength of Gaussian bandpass filter could be changed. The partial output from oscillator is sent into a photo detector (PD) for repetition rate detection. And the signal of oscillator repetition rate is used as trigger signal for pulse picker (AOM). The in-line AOM with a rising time of 10 ns (G&H) enables to decrease the repetition rate from 22MHz to 1.5 MHz with an insertion loss of 2.5 dB.

The direct output from the rejection port of the PBS is sent into a 4-nm bandwidth Gaussian filter for pulse shaping. The clean Gaussian pulse with a linear chirp is generated by removing the spectral edge, which contains a large amount of incompressible high-order phase. Apart from that, by acquiring a perfect Gaussian input pulse in the experiment, we could directly compare the simulation result of PCMA (input signal is Gaussian pulse) with the experimental result afterward. Such a filter is constructed by a 300 grooves reflection golden grating and a collimator with 5-mm focus length. By adjusting the reflective angle of the grating, the center wavelength of this filter could be turned. The spectrum and the autocorrelation (AC) trace of the filtered pulses are shown in Figure 4.10. The pulse has an AC duration of 6.1 ps, corresponding to a pulse duration of 4.3 ps. Such a long pulse enables the direct pre-amplification afterward without the need for a complicated CPA system. We also compress the filtered pulse by transmitted grating pairs with 1000 grooves (Light Smyth). The AC trace of the compressed pulse with a duration of 580 fs is close to the AC of the corresponding transform-limited pulse (As shown in Figure 4.9), proving that the filtered pulse has a compressible linear chirp.
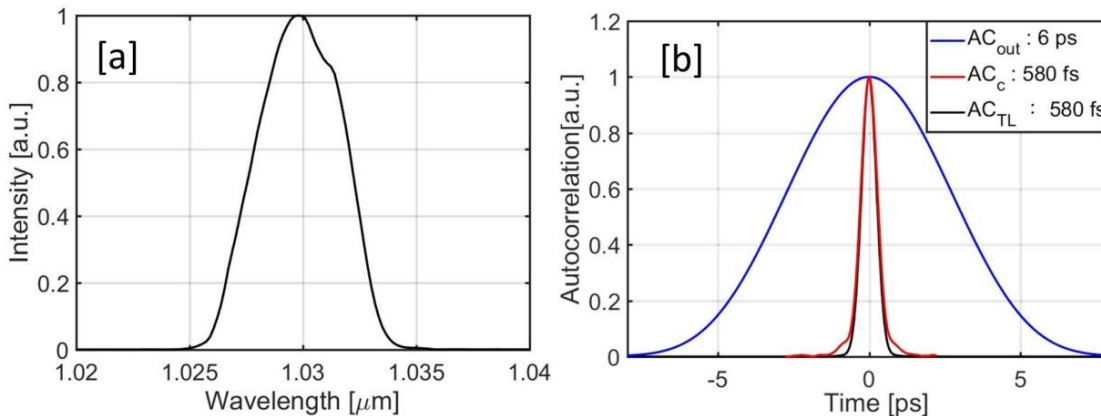
Figure 4.10: Experimental results of fiber laser source in wavelength-tunable seed laser. (a) The output spectrum from the fiber source after filtering. (b) The autocorrelation trace of filtered pulse (Blue curve), the pulse after compression (Red curve), and the transform limited pulse (Black curve).

Partial output from the oscillator is sent to a photodetector for repetition rate measurement; its output voltage is used as the trigger signal to drive the pulse pick. The in-line AOM is used as a pulse picker to decrease the repetition rate from 22 MHz to 1.47 MHz with an insertion loss of 2.5 dB. Since this wavelength-tunable fiber laser source is designed to fit the demand of the following cryo Yb:YLF amplifiers, decreasing the repetition rate leads to higher pulse energy in the end while eliminating the beam pointing issue in the PCMA. Besides, the resulting low average power enables the implementation of a single-mode diode as the pumping source for the whole fiber laser system, leading to a smaller footprint and higher stability. To compensate for the loss induced by a Gaussian bandpass filter and AOM,

we implement a stage of pre-amplifier with 0.5-m high-doping Yb fiber (Yb 401 PM, Coractive), where the pulse energy rises to 3 nJ without apparent spectrum broadening.

To this end, we achieve a stable fiber laser source delivering a 4.3-ps linear-chirped pulse with a 4-nm Gaussian spectrum centered at 1030 nm. The pulse energy and repetition rate could be tuned by increasing the pumping of the pre-amplifier and controlling the AOM, respectively. As a seed source for the following PCMA, we keep the fiber source running at 1.47 MHz with 3 nJ pulse energy to eliminate the potential beam pointing issue due to the free space to fiber coupling in the PCMA.

4.2.2 Pre-chirp management fiber amplifier (Part 2)
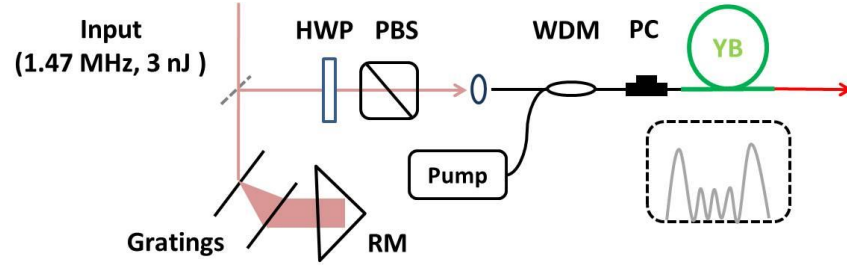
Figure 4.11: Schematic of Pre-chirp management amplifier (PCMA) in wavelength-tunable seed laser. The PCMA consists of a pair of transmission gratings for pre-chirp management, an in-line polarization controller (PC), and a commercial highly-doped Yb fiber (YB 406, Coractive) pumped through a WDM.

The schematic structure of the pre-chirp management amplifier (PCMA) is shown in Figure 4.11, including a pair of transmission grating for pre-chirp management and a stage of fiber amplifier with highly doped Yb fiber (Yb 406, Coractive). A single-mode diode at the wavelength of 976 nm pumps PCMA through a WDM. Since the highly doped Yb fiber could not be manufactured in a PM structure, this amplifier stage is constructed with non-PM fiber. In addition, an in-line fiber polarizer is placed in front of the gain fiber to control the nonlinear shift accumulated.

4.2.2.1 The simulation model for fiber amplifier

We first carry out numerical simulation to investigate both the fiber and the pulse parameter space for sufficient power amplification and wavelength shifting in PCMA. Accurate modeling of PCMA necessitates numerically solving the generalized nonlinear Schrödinger equation (GNLSE) that takes into account nonlinear effects, including self-phase modulation, self-steepening, and Raman scattering and the fiber gain [62], [180]. It is written in its normalized form as:

$$\frac{\partial A}{\partial z} + \frac{i}{2}\beta_2\frac{\partial^2 A}{\partial T^2} - \frac{1}{6}\beta_3\frac{\partial^3 A}{\partial T^3} - \int_0^\infty g(\omega)\,\tilde{A}(\omega)e^{-i\omega T}d\omega \tag{4-1}$$

$$= i\gamma(1 + \frac{i}{\omega_0}\frac{\partial}{\partial T})(A(t,z)\int_0^\infty R(t')|A(z,T-t')|^2 dt')$$

where A represents the complex electric field envelope, z is the propagation distance in fiber and T=t-β_1z. The linear terms are located in the left part of the equation, including the second- (β_2), and third-order (β_3) dispersions, as well as the fiber gain $g(\omega)$. The right part represents the nonlinear terms, including self-phase modulation (SPM), self-steepening, stimulated Raman scattering (SRS). The symbols γ and ω_0

represents the nonlinear coefficient and the center angular frequency. R(t) is a parameter corresponding to both the instantaneous electronic and delayed molecular response of silica molecules, in our case, R(t) is defined as following, where f_R, τ_1, and τ_2 are 0.18, 12.2 fs, and 32 fs, respectively.

$$R(t) = (1 - f_R)\delta(t) + f_R \frac{\tau_1{}^2 + \tau_2{}^2}{\tau_1{}^2 \cdot \tau_2{}^2} e^{-\frac{t}{\tau_2}} \sin(\frac{t}{\tau_1}) \tag{4-2}$$

In the simulation, we solved the GNLSE by adaptive split-step Fourier method implemented using the fourth-order Runge-Kutta method in the interaction picture [159]. We calculate the corresponding gain term $g(\omega)$ for each split-step based on the steady-state propagation rate equation that treats the Yb-fiber as a two-level system [175]. In the simulation of Yb fiber gain, we focus on the co-propagating model that the pump and signal propagate in the same direction. The amplified spontaneous emission (ASE) term is neglected in the simulation [62].

$$\frac{\partial N_2(t,z)}{\partial t} = [R_{12}(\omega,z) + W_{12}(\omega,z)]N_1(t,z) - \left[R_{21}(\omega,z) + W_{21}(\omega,z) + \frac{1}{\tau_{21}}\right]N_2(t,z) \tag{4-3}$$

$$\frac{\partial N_1(t,z)}{\partial t} = \left[R_{21}(\omega,z) + W_{21}(\omega,z) + \frac{1}{\tau_{21}}\right]N_2(t,z) - [R_{12}(\omega,z) + W_{12}(\omega,z)]N_1(t,z)$$

$$\frac{\partial P_p(\omega,z)}{\partial z} = \Gamma_p(\omega)[\sigma_e(\omega)N_2(z) - \sigma_a(\omega)N_1(z)]\rho P_p(\omega,z)$$

$$\frac{\partial P_s(\omega,z)}{\partial z} = \Gamma_s(\omega)[\sigma_e(\omega)N_2(z) - \sigma_a(\omega)N_1(z)]\rho P_s(\omega,z)$$

In Equation 4-3, ρ represents the ion density per unit volume. N_2 and N_1 account for the ratio of the ion in the upper and ground laser transition level, respectively. The sum of N_2 and N_1 is equal to 1. P_s and P_p are the pump and signal power at the position of z for the laser frequency of ω. Γp (Γs) is the modal overlap factor between the pump (signal) and the ion distribution. For a single-mode step-index fiber with its fundamental mode approximated by a Gaussian, the overlap of the optical mode and ion distribution becomes

$$\Gamma(\omega) = 1 - \exp(-\frac{2a^2}{w(\omega)^2}) \tag{4-4}$$

In Equation 4-4, a is the ion dopant radius or core radius, and w is the mode field radius at $1/e^2$ power intensity. The mode field radius is approximated by the Whitely mode:

$$\frac{w}{a} = 0.65 + 1.619V^{-3/2} + 2.879V^{-6} \tag{4-5}$$

Equation 4-5 is of considerable practical value, and it is accurate to with 1% when the V parameter in the range from 1.2 to 2.4 [181]. V parameter is the normalized frequency, which is defined as follows in Equation 4-6, where a is the core radius, and $n_c(n_1)$ is the cladding (core) refractive index.

$$V = \frac{2\pi}{\lambda} a(n_1^2 - n_c^2)^{0.5} = \frac{2\pi}{\lambda} a \cdot NA \tag{4-6}$$

In Equation 4-3, the wavelength-dependent emission cross-section and absorption cross-section are σ_e and σ_a, adapted from Figure 2 in Ref [175]. τ_{21} is the characteristic fluorescence lifetime. The spontaneous decay rate from the upper state to the ground state is $1/\tau_{21}$. The stimulated absorption and emission rate of the signal, as well as the absorption and emission rate of the pump for a fiber core-area A are W_{12}, W_{12}, P_{12}, and P_{21}, respectively.

$$W_{12} = \frac{\Gamma_s(\omega)\sigma_a P_s}{h v_s A}, \ W_{21} = \frac{\Gamma_s(\omega)\sigma_e P_s}{h v_s A} \tag{4-7}$$

$$R_{12} = \frac{\Gamma_p(\omega)\sigma_a P_p}{h v_p A}, \ R_{21} = \frac{\Gamma_p(\omega)\sigma_e P_p}{h v_p A}$$

If the amplifier reaches its steady state, we assume that $\partial N_2(t,z)/\partial t = 0$. By solving the rate equation 4-3 in each step with the input $P_p(\omega, z)$ and $P_s(\omega, z)$, we could acquire the output $P_p(\omega, z + \Delta z)$ and $P_s(\omega, z + \Delta z)$ at the steady state. Consequently, the wavelength-dependent gain parameter of each step in Equation 4-1 could be solved as following.

$$g(\omega, z) = \frac{1}{2\Delta z}\log\left(\frac{P_s(\omega, z + \Delta z)}{P_s(\omega, z)}\right) \tag{4-8}$$

Table 4.1 lists the key simulation parameters.

Table 4.1: Amplifier parameters used in the simulation

Parameters	Value
λ_p (μm)	0.976
λ_0 (μm)	1.03
D_{core} (μm)	3.8
NA	0.16
τ_{21} (ms)	1.0
ρ (m^{-3})	20×10^{25}
β_2 (fs^2/μm)	0.020
β_3 (fs^3/μm)	0.040
γ (W$^{-1} \cdot$ km^{-1})	8.7
D_{MFD} @1.03μm (μm)	5.2

4.2.2.2 Simulation results of PCMA

Following the experimental results in Section 4.2.1, a 4.3-ps positive chirped Gaussian pulse centered at 1030 nm with 4-nm spectral bandwidth is launched into the PCMA. The seeding pulse train has a repetition rate of 1.5 MHz with 3.75-mW average power corresponding to 2.5-nJ pulse energy. The amplifier is constructed with 0.16-m highly doping Yb fiber (YB 406, Coactive) with the ion density of $20 \times [\![10]\!]^{\wedge}25$ pumped by a 976-nm diode. The pre-chirp of the pulse is tunable by a diffraction-grating pair with 1000 grooves, operating at 31° incident angle. It introduces a negative group-delay dispersion (GDD) of -6140 fs^2/mm and a third-order dispersion of 1730 fs^3/mm.

Figure 4.12 shows the input and output signal of PCMA when the pump power is fixed at 350 mW, and the pre-chirp GDD on the pulse is -0.147 ps2. Under this specific application condition, the leftmost output spectral lobe shifts to 995 nm with a bandwidth of ~5 nm (see Figure 4.14 (b)). Filtering this part results in a ~40-nJ nearly transform-limited pulse with RMS pulse duration of 323 fs (see Figure 4.14(a)). The pulse duration of input and output signal stays the same (1.18 ps) due to the short fiber length; however, the temporal pulse profile converts into a triangle shape. The almost pure self-phase modulation (SPM) dominates the amplification process, leading to very clean spectral lobes on both sides.
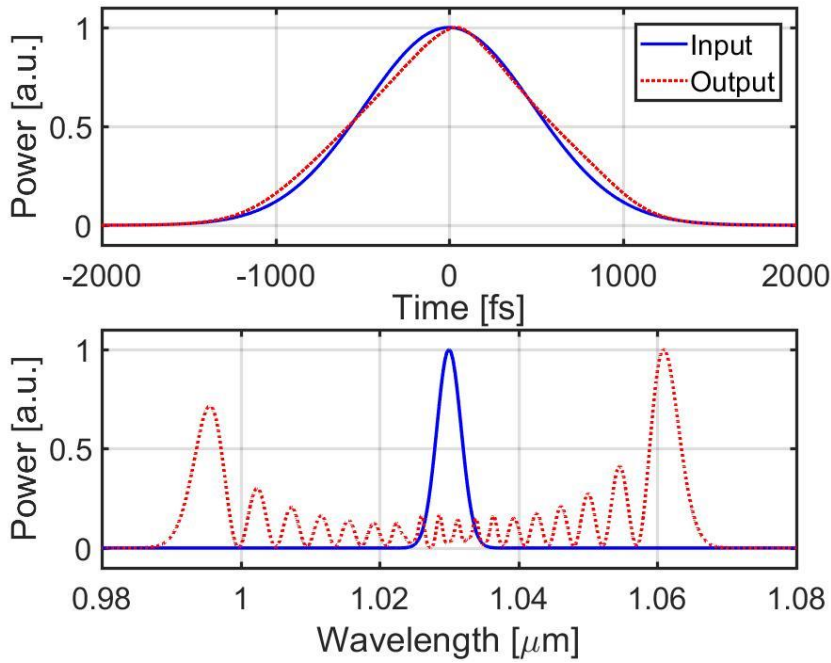
Figure 4.12: Simulation results of input and output pulse (top) and their spectrum (botton) from PCMA. PCMA is constructed with 0.16-m highly doping Yb fiber. The input pulse with pre-chirped GDD of -0.147 ps^2 is amplified under 350-mW pump power.
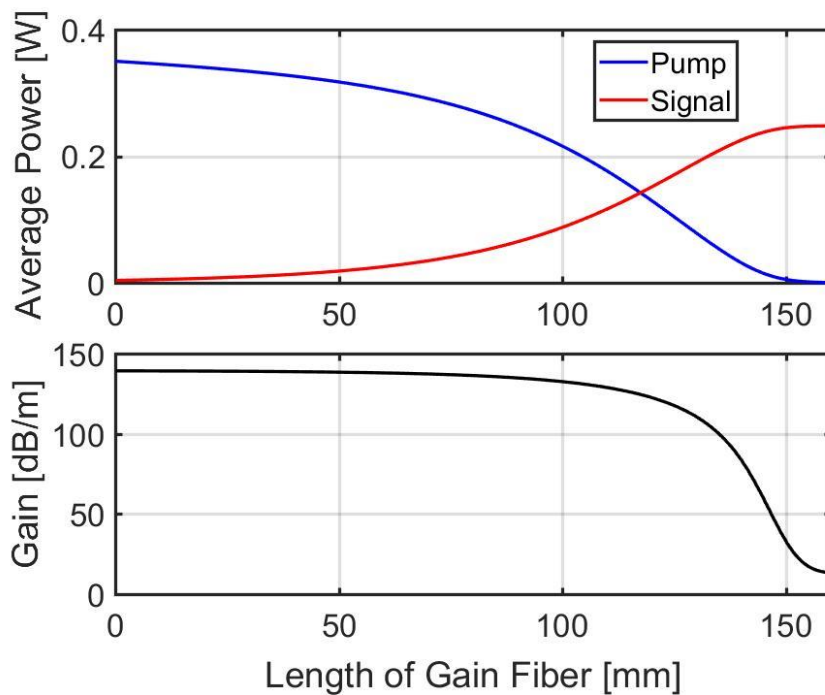
Figure 4.13: Top low: Pump (blue) and signal power as a function of Yb-fiber length. (b) Fiber gain as a function of Yb fiber length. The input power of signal is 3.75 mW corresponding to 2.5 nJ pulse energy. Under 350 mW pump power, the output power of signal is 248 mw, corresponding to 165 nJ pulse energy.

The top row in Figure 4.13 shows the absorption of the pump (blue) and amplification of signal (red) as a function of Yb-fiber length. For 160-mm Yb fiber, the pump is almost completely absorbed, and the

signal power reaches the maximum of 248 mW, corresponding to 165-nJ pulse energy. The bottom row in Figure 4.13 plots the corresponding fiber gain as a function of fiber length. The gain parameter starts from ~140 dB/m and ends at ~20 dB/m due to gain saturation. Under the condition of saturated amplification, the input signal's low-frequency noise is inhibited by the lifetime of gain medium [182], so the output signal is less sensitive to the fluctuation of the input, resulting in lower noise.

Figure 4.14 (d) shows the spectrogram of the output signal, which simultaneously visualizes the output signal in the temporal and spectral domains. It is constructed using a short-time Fourier transform. The duration of the time window, which continually samples the pulse in the time domain, will jointly define the temporal and spectral resolution of the resulting spectrogram plot. The corresponding spectrum and pulse are shown in Figure 4.14 (b) and (c). Although the spectrogram pattern indicates that the pulse has a highly nonlinear chirp due to SPM, a clean near transform-limited pulse can always be achieved by filtering the leftmost or rightmost spectral lobe.
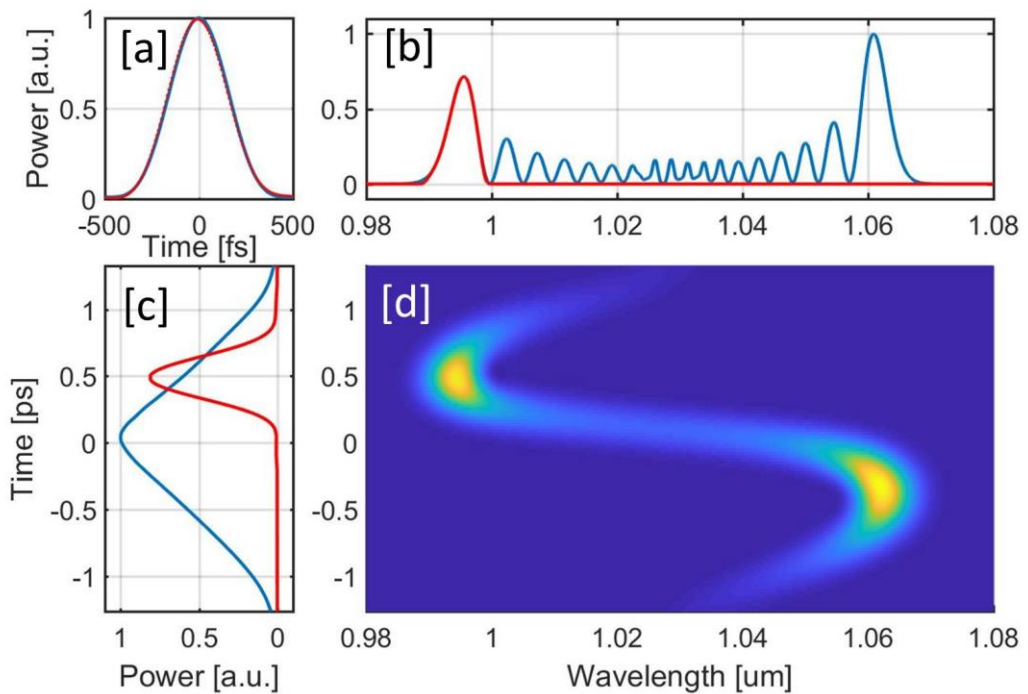
Figure 4.14: Simulation results of output pulse's spectrogram from PCMA. (a) The filtered pulse at the wavelength of 995 nm (red) and the corresponding transform-limited pulse (blue). (b) The spectrum of output signal (blue) and the filtered spectral lobe (red). (c) The temporal profile of output signal (blue) and the temporal profile of the filtered pulse (red). (d) The spectrogram of the whole output signal. While the whole pulse is highly nonlinear chirped, the filtered pulse at the leftmost lobe is transform-limited.

By just varying the pump power and keeping the parameters of the input signal the same, we can continually shift the wavelength of the leftmost spectral lobe, as shown in Figure 4.15 (a). When the pump decreases to 100 mW, a ~4-nm spectral lobe at the wavelength of 1017 nm is achieved, perfectly matching the broad emission band of cryo Yb:YLF at around 1020 for E//a axis. The pulse energy and RMS pulse duration as a function of the center wavelength of the filtered spectral lobe are shown in Figure 4.15(b). It is noteworthy that as the pumping decreasing, the filtered pulse goes on redshift with lower pulse energy and narrower spectral bandwidth. While the spectral lobe at 1017 nm has pulse energy

of ~11 nJ, which could be amplified further by using the same amplifier system discussed in Section 4.1.2., the spectral lobe at 995 nm is powerful enough to seed the solid-state amplifier chain. Since the amplification of pulse at 995 nm in the Yb fiber amplifier suffers from the very low efficiency and high ASE noise nm resulting from the much larger fiber gain at 1030, the nonlinear amplification method discussed in this section is the most favorable way to acquire powerful 995-nm mode-locking pulses.
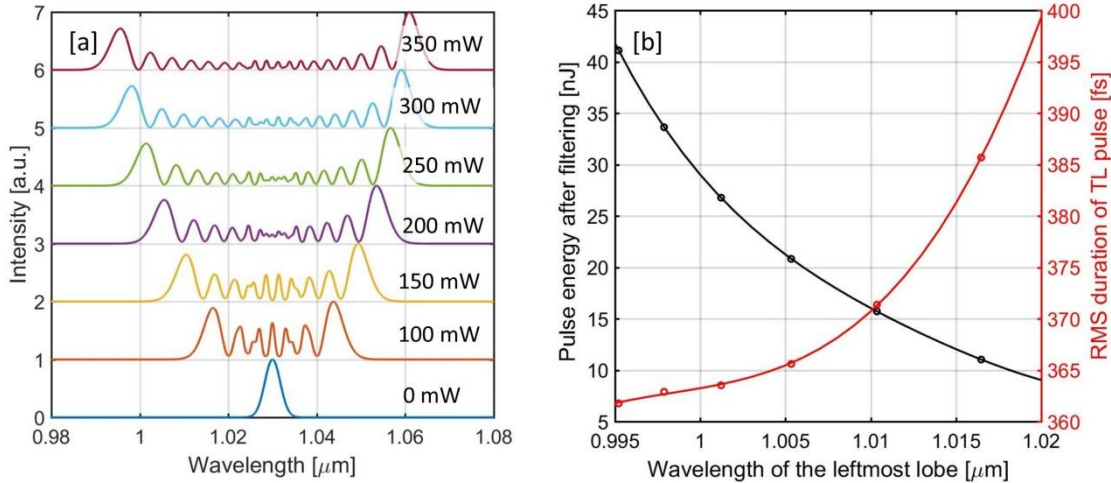
Figure 4.15: Simulation results of PCMA output parameters under different pump power. (a) The spectrums of output signal when varying the pumping power from 350 mW to 100 mW. The wavelength of the leftmost spectral lobe continually shifts from 995 nm to 1017 nm. (b) Pulse energy (black) and transform-limited pulse duration (red) of the filtered signal as a function of the center wavelength of the leftmost spectral lobe.

Table 4.2: Filtered pulse parameters in the simulation

Pump power	Input (pulse duration)	Leftmost spectral lobe	Output (pulse energy)	Ouput (pulse duration)
30 mW	*580 fs*	*1015 nm*	*2.67 nJ*	*227 fs*
50 mW	*780 fs*	*1015 nm*	*4.83 nJ*	*265 fs*
100 mW	*1100 fs*	*1015 nm*	*10.65 nJ*	*333 fs*

Launching high-peak-power and high-energy pulse into a piece of PCF will lead to a similar result. However, such a method requires expensive PCF and is not suitable for long-term running due to beam pointing issues and potential fiber end-face damage. They are a direct consequence from the free-space to fiber coupling under high power. Besides, high-peak-power and high-energy pulses are usually acquired by complicated CPA fiber laser system demanding long fiber stretcher and large optical beam path of the gratings compressor, which further influence the stability of such a laser system. In comparison, our cost-efficient laser system based on PCMA with a small laser footprint enables a long-term operation, so that it is much more suitable as a seed laser source for high power amplifier laser system.

Apart from the varying pump power, we can also acquire different output spectra by controlling the pulse pre-chirp. The spectral bandwidth of the leftmost lobe is highly correlated to the input pulse duration in such a way that if the input pulse is stretched longer, the resulting spectral lobe becomes

narrower. Take the 1015-nm spectral lobe as an example; the input and output parameters of the signal are shown in Table 4.2. As the input pulse is stretched longer, we have to increase the pump power for the leftmost lobe shifting to the same wavelength of 1015 nm. As a consequence, the filtered output pulse becomes longer with higher pulse energy. Figure 4.16 shows the corresponding output spectra for the three cases listed in Table 4.2.
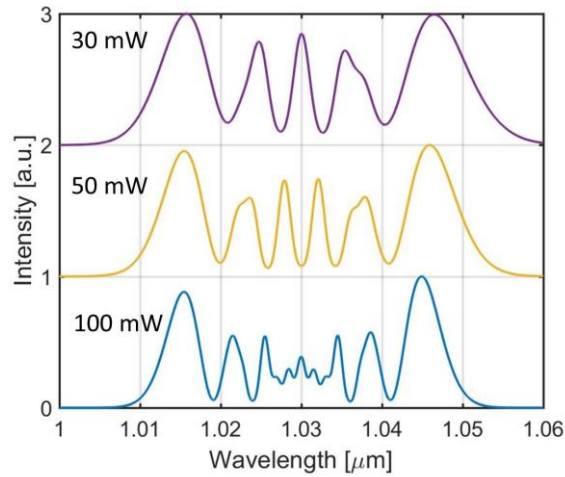
Figure 4.16: Simulation results of PCMA output spectra with different input pulse pre-chirp. At the same time, the pump power is adjusted in a way that the wavelength shift of the leftmost lobe is fixed at 1015nm with different pre-chirp value of input pulse.

4.2.2.3 The experimental results of PCMA
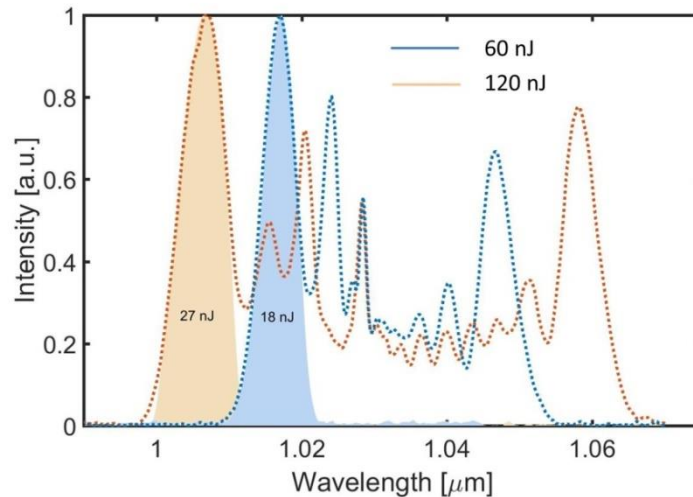
Figure 4.17: Output spectrum of PCMA with 130-mm gain fiber length. The wavelength of the leftmost spectral lobe is tunable by changing pump power.

Guided by the simulations, we construct the pre chirp management amplifier. In the experiment, we splice a WDM with 0.7-m pigtail length with the gain fiber. The end-face of gain fiber for output is cut with 8° Brewster angle to eliminate the back reflection. The input pulse is pre-chirped into ~1 ps. The

blue curve and orange curve in Figure 4.17 are the output spectrum from 130-mm gain fiber under different pump conditions.

When the output signal is amplified to 60 nJ, the leftmost spectral lobe is shifted to 1018 nm with ~5 nm bandwidth, containing 18 nJ pulse energy. The resulting pulse AC trace at this wavelength is shown in Figure 4.17(a). The filtered pulse at 1018 nm has an AC duration of 623 fs (yellow), slightly larger than its transform limit (blue, 361 fs). By further increasing the pump power, the leftmost spectral lobe undergoes a continually blue shift and finally reaches the wavelength of 1005 nm. The 1005-nm spectral lobe contains pulse energy of 27 nJ out of the 120-nJ output. Figure 4.18 (b) shows the measured AC trace of both filtered pulse and its TL pulse. The filtered pulse at 1005 nm has an AC duration of 520 fs (yellow) while the AC trace of its TL pulse is 361 fs. Compared with the pulse at 1018 nm, the 1005-nm filtered pulse has a similar TL pulse duration but contains a smaller chirp. Figure 4.19 shows the power of the filtered pulse at 1018 nm taken by every 1s for 15 mins. The standard deviation was 0.08 mW for 26.4-mW output power. The periodic change of power is due to the temperature change of the lab. By covering the laser with a temperature isolated box, we can further stabilize the output power.
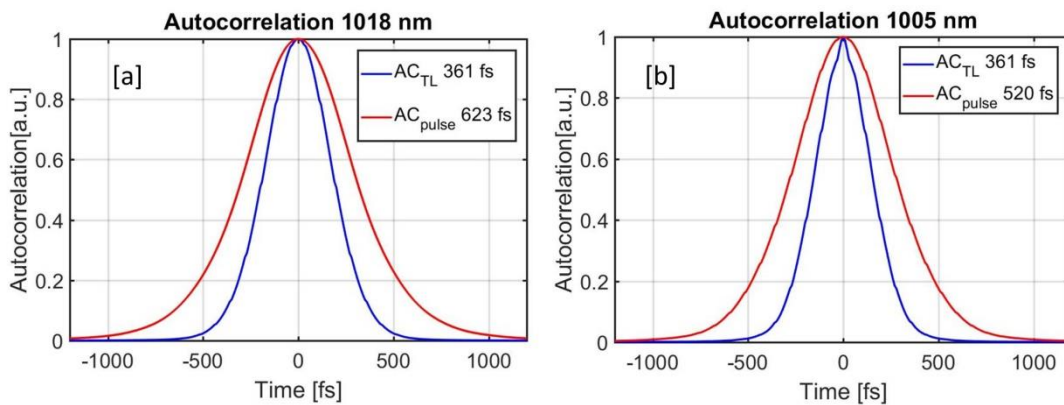
Figure 4.18: Autocorrelation (AC) traces of the filtered pulse (red); at 1018 nm (a) and 1005 nm (b). And the AC traces of their correlated transform-limited pulse (blue).
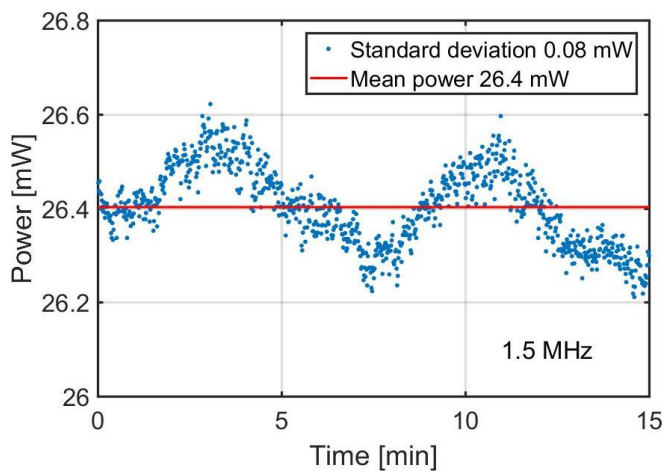
Figure 4.19: Output power measurement of filtered pulse at 1018 nm. The measurement is taken by every one second and lasts for 15 mins. The standard deviation of output power is 0.335%. The period pattern in output power is due to the temperature change in the lab.
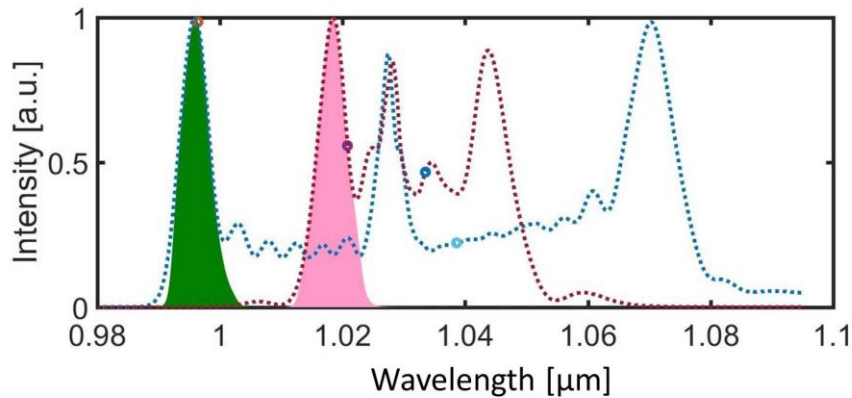
Figure 4.20: Output spectrum of PCMA with 180-mm gain fiber length. The wavelength of the leftmost spectral lobe is tunable by changing pump power.

With 130-mm gain fiber length, the further blue shifting is inhibited due to the gain saturation and corresponding limited nonlinear phase shift accumulated in such a short piece of gain fiber. Shortening the input pulse duration through less pre-chirp will increase the nonlinear phase shift, resulting in less output pulse energy and a broader spectrum. Considering that 995-nm gain spectrum of cryo Yb:YLF is narrowband (~ 4nm), the combined effect of broad-spectrum and less pulse energy at the wavelength of 995 nm leads to a limited seeding pulse energy within the efficient gain bandwidth of following solid-state amplifier system. Instead of tuning the pre-chirp value, we increase the gain fiber length to 180 mm for further wavelength shifting.
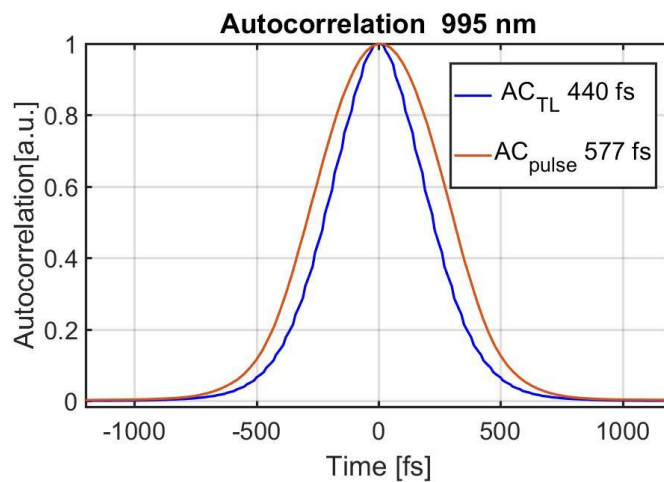
Figure 4.21: Autocorrelation (AC) traces of the filtered pulse (red) at the wavelength of 995 nm. And the AC traces of its transform-limited pulse (blue).

Figure 4.20 shows the output spectrum from PCMA with 180-mm gain fiber; the 1.0-ps chirped input pulse has 1-nJ pulse energy is sent into the amplifier. At the pump power of 160 mW, the output power is 51 mW corresponding to 34 nJ pulse energy, and the leftmost spectral lobe is shifted to 1018 nm with 9.1-nJ pulse energy. Further increasing the pump power leads to the blue shift of this spectral lobe. When the pump power reaches 490 mW, the output is 135 mW, and the 995-nm spectral lobe contains 13 nJ pulse energy. The autocorrelation trace of the 995-nm pulse is shown in Figure 4.21. The filtered pulse has an

AC duration of 577 fs, corresponding to a Gaussian pulse duration of 410 fs, while its transform limit pulse duration is 312 fs.
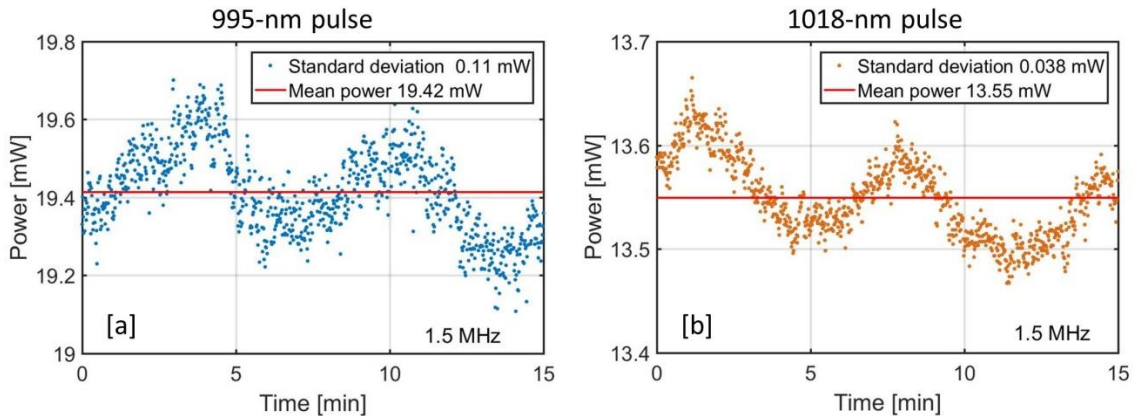
Figure 4.22: Output power measurement of filtered pulse at 995 nm (a) and 1018 nm (b) from PCMA with 180-mm gain fiber. The measurement is taken by every one second and lasts for 15 mins. The standard deviation of output power is 0.11 mW for 995-nm pulse and 0.038 mW for 1018-nm pulse. The period modulation of output power is due to the temperature change in the lab.

For the amplifier with 180-mm gain fiber, the output power stability of 995-nm pulse and 1020-nm filtered pulses are also measured and illustrated in Figure 4.22. The powers of the filtered pulses are taken by every 1s for 15 mins. The standard deviation of output power was 0.11 mW (0.038 mW) for 995-nm pulse (1018-nm pulse) with an average power of 19.42 mW (13.55 mW). The periodic change of power is due to the temperature change of the lab. It is noteworthy that the power deviation of the 1018-nm pulse is smaller than the 995-nm pulse due to the less nonlinear phase shift accumulated in the amplifier. Although the periodic power modulation exists, the maximum power change for 995-nm pulse (1018-nm pulse) is about 2% (~0.7%), indicating that this wavelength-tunable fiber seed source is very stable. Covering this laser with an isolated box will further reduce the output power fluctuation.

4.3   Summary of the chapter

In this chapter, we construct two fiber seed lasers specifically designed to seed a high-energy cryo Yb:YLF amplifier system. For the first one, we experimentally demonstrate a high-power fiber-based at the wavelength of 1018 nm with 2.5-nm spectral bandwidth. With a repetition rate of 17.88 MHz, the fiber-based master-oscillator power amplifier (MOPA) front end employs the CPA technique and produces 87-W, 4.9-μJ pulses centered at 1018 nm with 1-ns stretched duration. The amplification is achieved by two stages of specially designed fiber amplifiers that suppress the ASE at 1030 nm.

For the second one, we numerically and experimentally demonstrate a compact wavelength-tunable fiber seed source (from 995 nm to 1018 nm) with moderate pulse energy (10 to 30 nJ) and high stability. This wavelength-tunable source is designed to further investigate sub-500 fs pulse amplification at 1020 nm and the high-energy pulse amplification at 995 nm of cryo Yb:YLF amplifier system.

Chapter 5

Low-noise Master Fiber Laser delivering 10-nJ, 60-fs Pulse

Applications of ultra-short pulsed lasers for multi-photon or photo-electron spectroscopy, rely on the existence of very compact and robust laser sources. Such laser sources can generate ultrashort pulses with durations shorter than 100 fs, Watt-level powers at high-repetition rates and diffraction-limited beam quality. For nonlinear bio-optical imaging in which photo-induced damage is caused by pulse energy rather than average power, Watt-level outputs from the ultra-short pulse laser source will improve the signal-to-noise ratio and reduce data acquisition time. Ytterbium-based Kerr-lens mode-locked lasers can provide sub-100 fs pulses at Watt-level average powers [183]. However, it is Ytterbium-doped fiber-lasers that, due to all-optical wave-guiding, exhibit superior robustness - making them suitable for the most demanding laser applications, including space applications that involve rocket launches [125]. All-fiber, ultrashort pulse systems are typically set up in a master oscillator power amplifier (MOPA) configuration: The fiber oscillator generates pulse energies around 1 nJ that are amplified to higher pulse energies. The MOPA configuration has the additional benefit that fiber-coupled optical modulators (having limited power handling capability) can be sandwiched in a fully fiber-integrated way between the oscillator and the power amplifier, and thus, greatly enhance the versatility and applicability of such fiber MOPA systems.

Besides inherent robustness, the light propagation in an optical waveguide also facilitates the occurrence of nonlinear effects. Specifically, self-phase modulation (SPM) is of relevance for ultrashort pulse amplification. SPM enables spectral broadening that allows the compression to even shorter pulse durations. However, without any special measures, the interplay of SPM, group-velocity dispersion and gain results in severe deterioration of the pulse quality at the output of the fiber amplifier. Chirped-pulse amplification (CPA) is commonly employed in fiber systems to mitigate nonlinear effects during amplification [51]. In this scheme, the peak intensity is significantly lowered during amplification by stretching the pulse prior to amplification. Fiber-amplification systems based on CPA offer the highest output energies. By using standard single-mode fiber in an all-fiber configuration, pulses with durations

of 120 fs and energies of 6 nJ have been obtained after free-space grating-based compression. By using rod-type fiber, pulses with mJ energies have been demonstrated from fiber-rod CPA-systems [53]. At the output of fiber-CPA systems, the pulse durations are typically longer than 100 fs due to a combination of effects: (a) Gain narrowing of the spectrum during amplification, (b) overall dispersion mismatching, and (c) nonlinear phase shifts due to SPM. Particularly, the large stretching in fiber-CPA mitigates the nonlinear effect of SPM. Due to the waveguide-nature (i.e., confinement to small mode-areas and long propagation lengths), the effects of SPM start reappearing in CPA: At large nonlinear phase-shifts, pulse-splitting and energy transfer into satellite pulses impose limitations on the quality of the output pulse. To reach sub-100-fs pulses from fiber CPA systems, both the operation at B-integrals < 1 rad and the meticulous optimization of overall third as well as fourth-order dispersion of the system are necessary. The latter is challenging due to the large stretching/ compression ratio required for fiber-CPA systems. By using large mode area photonic crystal fiber and dispersion-engineered fiber stretchers (typically non-PM), pulse durations as short as 75 fs have been reported at the output of a fiber-CPA system [56]. However, for CPA-systems based on standard single-mode fibers, B-integrals > 1 rad are easily reached at low pulse-energies (~nJ) due to mode-areas as small as < 40 μm^2.

For energies in the range nJ…μJ, there also exist direct amplification schemes (i.e., that are not based on fiber-CPA) utilizing nonlinear effects. These methods include self-similar amplification (also known as parabolic amplification) [58], [59]. Pulses with a duration of 48 fs and energies of 226 nJ and 18 W average power have been obtained [59]. The self-similar amplifier was constructed from a PM 25/250 double-clad fiber that was bent to discriminate higher-order modes [60]. Another nonlinear amplification technique uses passive pulse-shaping prior to fiber-based amplification [61]. In this way, pulses with 780 fs and 49 μJ after grating-based compression have been demonstrated from a rod-type nonlinear amplifier (with accumulated B-integral of 12 rad during amplification).

Lately, the method of pre-chirp managed amplification (PCMA) was reported [62], [65]. This technique and self-similar amplification offer the advantage of producing pulses with durations shorter than 100 fs. This is due to the spectral broadening originating from SPM during nonlinear amplification. The main benefits of PCMA include: (a) nonlinear effects during pulse propagation in fibers are desired and not mitigated. The spectral broadening due to SPM allows for reduced pulse durations as compared to the input pulse duration from an oscillator. In fiber-CPA, this is typically not the case. Also, fiber CPA suffers from degradation of the pulse contrast due to pulse splitting at B-integrals > 1 rad. PCMA uses pulses that are not strongly chirped before amplification. Thus, the formation and action of 'temporal phase-gratings' due to SPM of modulated strongly chirped pulses – which causes pulse contrast degradation in nonlinear fiber-CPA – does not impose limitations on operation at high B-integrals. Also, (b) besides the generation of shorter pulse durations at the PCMA output, it also leads to high pulse qualities. And, (c) only very compact compressors are needed for both pre-chirp and final pulse compression. This results in very compact setups. Moreover, (d) the lengths of the fiber amplifiers in PCMA can be made very short. So, it applies to many types of gain fibers. Specifically, the short fiber-lengths of PCMA correspond to high doping levels enabling higher small-signal-gain coefficients at smaller wavelengths. PCMA enables amplification at lower wavelengths (< 1020 nm), making the spectra compatible with the gain center of some of the most widely used high-energy solid-state amplifiers, e.g., Yb:YAG or Yb:YLF. Differently, self-similar amplification relies on the nonlinear evolution of the pulse

into a final parabolic shape over several meters. As a result of the lower inversion levels, amplification will be favored at longer wavelengths, e.g., see [59]. PCMA can be operated with highly doped fiber as short as < 1 m. Thus, it can also be employed to >100 W fiber-rod amplifiers [65].

In this chapter, we first develop design strategies for a PCMA configuration that is solely based on (standard) polarization-maintaining (PM), core-pumped single-mode fiber. The average power scaling of PCMA was demonstrated by using free-space coupling into a rod-type fiber. Here, the goal is to design a practical, robust PCMA front-end configuration that can be used to seed high-energy power amplifiers. The use of PM single-mode fiber offers not only the potential of all-fiber configuration and robustness but also makes it compatible with the use of fiber-pigtailed optical modulators. We propose and demonstrate a two-stage amplification for PCMA to mitigate the impact of input fluctuations or system deterioration, enabling robust long-term operation. We present design strategies resulting in pulses exhibiting sub-100-fs durations and high pulse qualities as well as a low noise output. Emphasis is placed on tailoring the spectral evolution through the system. As shown in the following, this results in improved pulse qualities and very smooth output spectra even at accumulated nonlinear phase shifts as high as B > 40 rad. Then, we analyze the noise reduction effect in this two-stage amplifier. 0.008% relative intensity noise (RIN) is achieved after the amplification.

Some strategies to further reduce the noise of this master laser system are also discussed in this chapter. Our target is to transfer this master laser into an ultra-low noise frequency comb for multiple applications in the AXSIS project ongoing in our group. These applications include the seed source for several solid-state high power laser systems, the probe pulse for THz EO sampling, the reference standard for frequency and phase locking, to name a few. Since all of them need synchronization, the most convenient way is to use the same seeding source, which we discuss in this chapter with low-noise operation.

5.1 Simulation results of pre-chirp managed amplifier

In this section, we present a design of a PCMA configuration that is solely based on (standard) PM core-pumped single-mode fiber. The power and energy of this configuration are set by the PM, highly doped, core-pumped (standard) single-mode fiber that is employed as the fiber amplifier. The modeling parameters are oriented towards the experimental configuration in Section 5.2. Specifically, the available output power (or energy) is determined by the power of the multiplexed single-mode pump diodes.

Ultrashort pulse amplification in fibers is governed by the interplay of fiber dispersion, nonlinear effects, and gain. In general, this interplay does not lead to compressible pulses at the output of a direct amplification scheme. Conversely, PCMA corresponds to a beneficial operation regime of the nonlinear pulse amplification. In PCMA, a small chirp is imposed on the pulse before amplification. In this way, the amplified pulse can be compressed to shorter pulse-durations and with very high pulse quality. In this section, the pulse quality is measured in terms of Strehl-ratio, which is ratio between the pulse peak-power after compression and the peak-power of TL pulse. Depending on the parameters of the nonlinear evolution, the pre-chirp required for PCMA may be positive or negative. Due to the nonlinear dynamics, the operation region of PCMA can – to the best of our knowledge - only be designed numerically by solving the generalized nonlinear Schrödinger equation. To obtain accurate results, the numerical model

must include the spectral gain profile of the Ytterbium-doped fiber and other parameters of the pulse amplification. These include inversion distribution and fractional mode power of pump and signal in core [180]. Due to the nonlinear nature of PCMA, the power levels define PCMA's operation point. Especially for high gain (> 20..30 dB) fiber amplifiers, this can be challenging as input power fluctuations can affect not only the noise performance of the amplifier but also the pulse parameters at the output. To mitigate such effects, we develop an amplification scheme that employs two amplifier stages. Each of these core-pumped amplifiers is saturated. The two Ytterbium fiber-amplifiers are made of polarization-maintaining (PM) single-mode fiber. For this experimental demonstration, the goal is a 10 nJ output for repetition rates around 70 MHz. A "mini" CPA configuration is employed by stretching the pulse with approximately 6 m of PM980 fiber. The pulse-energy is low in this stage so that the detrimental effects of SPM are avoided. After the first amplifier, the pulses are compressed using a grating pair in a double-pass configuration. The stretching that is followed by compression enables the use of either positive or negative pre-chirp for PCMA. The distance between the gratings is adjusted in such a way that it introduces the required pre-chirp for the second PCMA amplifier. The sign and amount of pre-chirp depend on the power level. Note, that this is a distinct feature of PCMA compared to self-similar amplification. In self-similar amplification, the corresponding parabolic pulses always possess an up-chirp during amplification. In PCMA, the pre-chirp can be a down-chirp. In the case of initial down-chirp, the joint action of SPM and the down-chirp result in spectral compression in the initial stage of the amplification of PCMA [184]. The parameters of the PCMA configuration are displayed in Table 5.1. In the following, we calculated the required pre-chirp by characterizing the resulting output pulse.

Table 5.1: Parameters of PCMA configuration for the simulation

Parameter	Value
Input pulse:	
Power (input)	(as shown in Figures)
Linear pre-chirp	(as shown in Figures)
TOD	0.0015 ps^3 (based on estimate of joint action of 6 meters of fiber and the pre-chirp gratings prior the PCMA amplifier)
Repetition rate (f_{rep})	70 MHz
λ center	1032 nm
Δλ (input)	10 nm
Spectral shape	Super Gaussian (M=3)
Fiber amplifier:	(which is based on gain fiber Nufern PM-YSF-LO)
Passive fiber before gain fiber (WDM pigtails)	3.0 m PM980 fiber with MFD = 6.2 μm, n_2, $\beta^{(2)}$, $\beta^{(3)}$ same as gain fiber below
Gain fiber Length	3.2 m
MFD	6.5 μm @ 1060 nm
n_2	$2.6 * 10^{-20}\,m^2/W$
$\beta^{(2)}$	23 fs^2/ mm
$\beta^{(3)}$	46 fs^3/ mm
Doping concentration	$0.83 * 10^{25}$ ion density / m^3
Pump power	1 W @ 980 nm (co-directional pumping through WDM)
Cross-sections:	R. Paschotta et al, IEEE Journal of quantum electronics, Vol.33, p 1049 (1997).
pump loss	adjusted in such a way to match the experimental slope efficiency of 75%
Grating compressor:	

Groove density	1000 lpmm
AOI	31° (with respect to normal of grating surface)

Figure 5.1 shows the result of the numerical simulation of the PCMA configuration with parameters of Table 1. Figure 5.1(a) and (b) show the pulse-quality in terms of the Strehl-ratio and the pulse peak-power, respectively. Here, the Strehl-ratio is defined as the ratio of peak power of the best-compressed pulse to peak-power of the transform-limited pulse. The data of Figure 5.1 is calculated as a function of both input power and the amount of pre-chirp (shown in terms of the initial GDD), TOD is fixed at 0.0015 ps3). At every data point in Figure 5.1, the pulse is numerically compressed to the highest peak-power. For this, we assume a grating compressor (with parameters of Table 1). As can be seen in Figure 5.1(a), there are two optimal regions (that are highlighted via the blue and black dot) where the pulse-quality after compression is highest. However, the output pulse's peak-power in the region marked with the blue dot is higher than that of the region with the black dot, as shown in Figure 5.1(b). Around this region ("blue dot"), the regions of highest peak power and highest pulse quality overlap, but not completely. Also, it can be seen in Figure 5.1 that the amount of pre-chirp has a substantial impact on the peak-power of the compressed output pulse. The input pulse energy (or input power) also has an impact – however, it is not as pronounced.
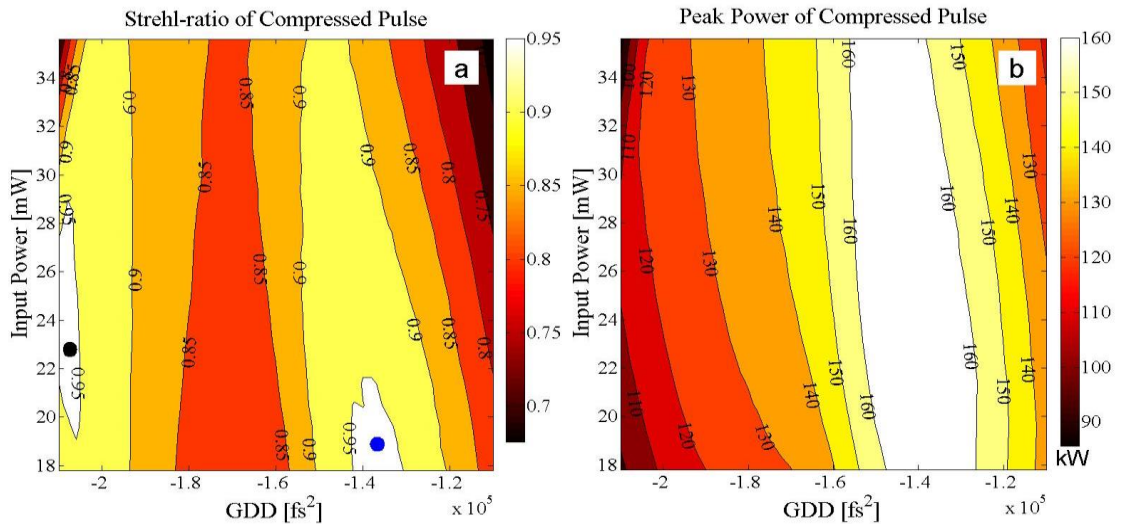
Figure 5.1: Simulation: (a) Output pulse quality and (b) pulse peak-power as a function of the pre-chirp´s GDD and the input power of the PCMA configuration.

In the following, we analyze the power-dependence for a single pre-chirp value in more detail. Figure 5.2(a) shows a cross-section of Figure 5.1. Essentially, this mimics the situation in a real experiment: the pre-chirp is set to a suitable value, and then the input power into the PCMA is varied. The pre-chirping GDD is set to -0.144 ps^2. As can be seen in Figure 5.2(a), even for a large variation of input energy, the output parameters of the pulse, namely Strehl-ratio and pulse-peak power, stay close to constant (within approx. 2%). As can be seen in Figure 5.2(c), the output power levels also remain almost constant due to the operation of the amplifier in saturation. At the same time, the B-integral (i.e., the amount of accumulated nonlinear phase-shifts) is larger than 40 rad and increases with input power by approximately 20%. Note, the B-integral shown in Figure 5.2 is only that of the final PCMA amplifier,

and additional amplifiers may cause additional contributions to the B-integral. In comparison, conventional CPA-systems require operation with B-integrals below 1 rad to ensure good pulse quality at the output. Figure 5.2(b) shows that the compressed pulse duration remains the same (within approx. 3%). Note, for each input power level, the grating distance of the compressor is adjusted for best compression.

For the case of a constant compressor, Figure 5.3 shows the output pulse's characteristic parameters for the different input powers (otherwise, the situation is similar to Figure 5.2). The grating distance of the final compressor is optimized for an input power of 26 mW. It can be seen that in this case, there is a significant change in the output pulse's characteristics with input power. This clearly demonstrates the nonlinear dependency and sensitivity of the operation point of PCMA.
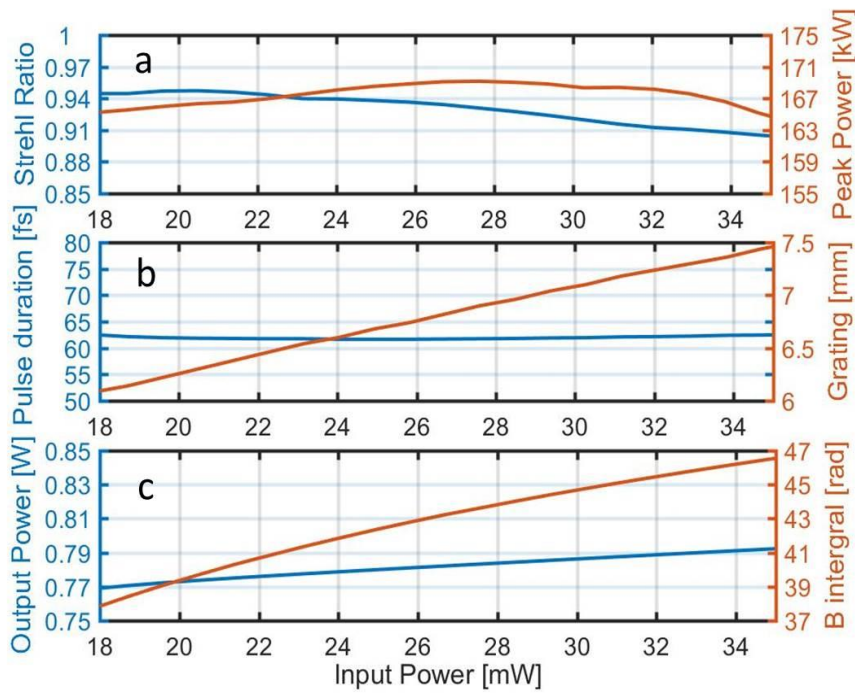
Figure 5.2: Simulation of output pulse parameters as a function of input power with a fixed pre-chirp. Simulation of (a) output peak-power and Strehl-ratio (b) output pulse duration and compressor grating separation, and (c) output power and B-integral as a function of input power at fixed pre-chirp and adapted compression at output.

In the following, we exemplarily show the pulse shapes and spectra at the PCMA's output. For an input power of 22 mW and pre-chirp GDD value of -0.144 ps^2, Figure 5.4 shows the input and output pulse, the input and output spectrum, and the compressed pulse and the corresponding transform-limited pulse from the output of the PCMA amplifier. It can be seen from Figure 5.4(a) that the interplay of dispersion, nonlinear effects, and gain during pulse propagation in the PCMA results in a parabolic pulse shape before compression. This can be regarded as one of the main reasons for the excellent pulse quality at the output: the SPM results in a parabolic phase that can be removed by the final compressor. The asymmetry of the input pulse is due to TOD. Also, it can be seen from Figure 5.4(b), that there is significant spectral broadening. This enables reduced pulse durations at the PCMA's output. Figure 5.4(c) shows that the compressed pulse at the output is very close to the transform limit, i.e., resulting in a Strehl-ratio close to 1.
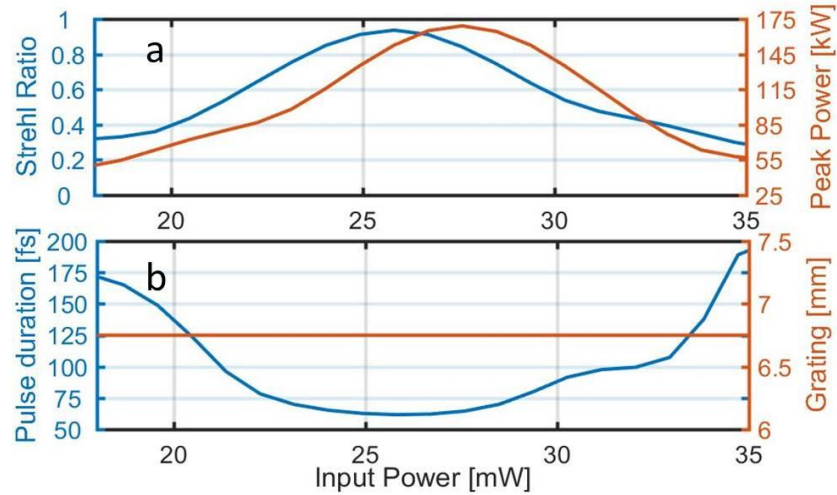
Figure 5.3: Simulation of output parameters versus input power with a fixed pre-chirp and compressor. Simulation of (a) output peak-power and Strehl-ratio, and (b) output pulse duration and compressor grating separation as a function of the input power at fixed pre-chirp as well as constant compression at output (optimized for input power of 26 mW)
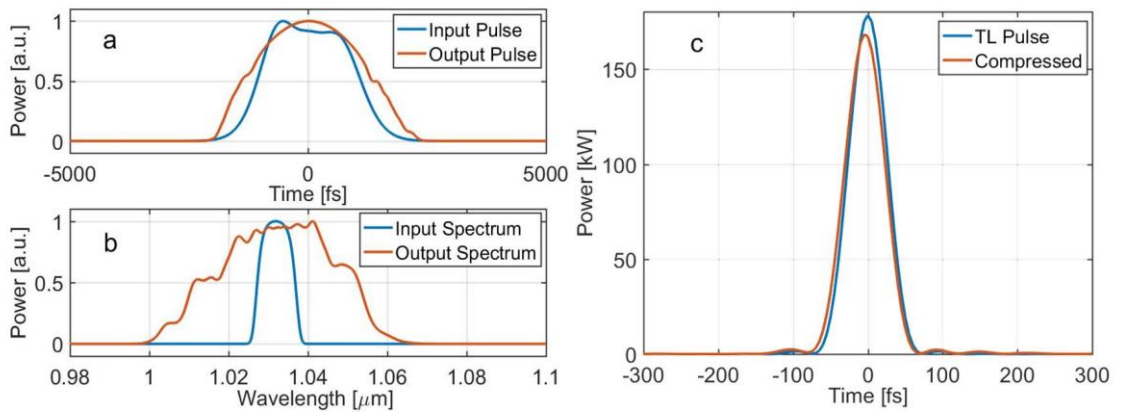
Figure 5.4: Simulation results of PCMA output when fixing the input signal parameters. (a) Input and output pulse, (b) input and output spectrum, (c) the best compressed pulse of output and the corresponding transfer limited pulse for pre-chirp's GDD of -1.44×105 fs^2 and input power of 22 mW.

5.2 Experiment results of 60-fs, 10-nJ master fiber laser

5.2.1 Experimental setup

Figure 5.5 shows the schematic of the experimental setup. It consists of an ultra-short pulsed oscillator and two amplification stages. The setup essentially implements the parameter configuration of Section 5.1. The oscillator is based on a Ytterbium-doped fiber oscillator, which is mode-locked by nonlinear-polarization rotation. The 0.4-m Yb-doped gain fiber is used as the gain medium (Coractive YB 401). The other fibers (of the pigtails and WDM) are Corning Hi 1060 with a total length of 1.8 m. Dispersion management is achieved by a pair of dielectric transmission gratings (1000 grooves). Different mode-locking states - including soliton, stretched pulse, and similariton - were tested by adjusting the grating-

separation in the intra-cavity grating compressor. The similariton type is chosen for the following demonstration. Note, the similariton shows all positive chirp during one pulse round-trip in the oscillator. In the experiment, we find that the similariton state provided the highest pulse energy and the best initiation of mode-locking. The perpendicular grating separation is set to ~7 mm. The characteristic parameters at the oscillator's output are 0.4-nJ energy, 40-nm spectral bandwidth (3dB) nm, and 100-fs compressed pulse duration. The repetition rate is set to exactly 70 MHz by using the variable section in the oscillator, which includes a PBS, QWP, end mirror, and an optical delay stage.

The 1st amplification stage ("mini" CPA configuration): The output of the oscillator passes through a bandpass filter with a bandwidth of 20 nm at full width at half maximum (FWHM). A HWP is set so that the polarization of the light is aligned to the slow axis of the PM fiber. The total length of passive fiber before the gain fiber is ~6 m. The gain fiber is Coractive PM-YB 501, with a length of 0.6 m. The input and output powers at the fiber amplifier are 4 mW and 186 mW, respectively. The PM Ytterbium-doped fiber is core-pumped.
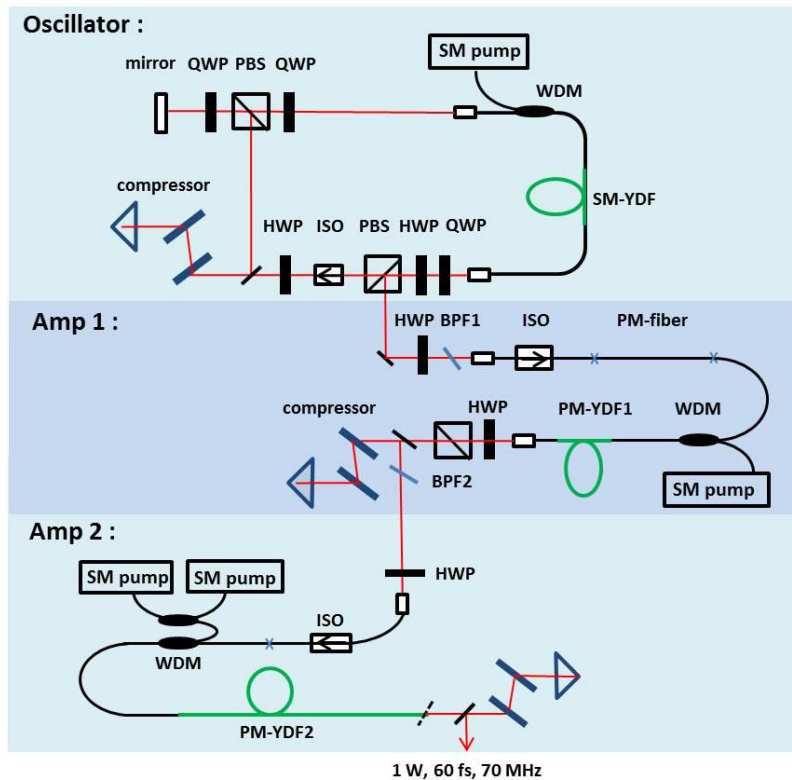
Figure 5.5: Schematic of the experimental setup for 10-nJ, 60-fs laser system. QWP: quarter wave-plate, HWP: half-wave plate, PBS: polarization beam splitter, ISO: optical isolator, WDM: wavelength division multiplexer, YDFA: Ytterbium doped fiber, SM: single mode non-polarization maintaining, PM: polarization maintaining, BPF: band-pass filter, SM pump: single-mode fiber pigtailed pump diode at 975 nm.

The 2nd amplification stage (PCMA amplifier): The pre-chirp of the pulse is adjusted by a grating compressor consisting of (1000 grooves) dielectric transmission gratings. To control the input power of the PCMA, a HWP and a PBS are placed before the grating compressor. The compressor's perpendicular grating separation and efficiency are 62 mm and 87%, respectively. The spectrum of the pulse is filtered

by a second bandpass filter BPF2 with a bandwidth of 10 nm before entering the second core-pumped polarization-maintaining fiber. The bandpass filter clips the uncompressible phase in the wings of the spectrum and facilitates evolution into a parabolic output spectrum. By slightly tuning the angle of BPF2, we can change the center wavelength of the input spectrum of the second amplifier to match it to the center of the gain spectrum [61]. The input and output powers at the fiber amplifier are 26 mW and 820 mW, respectively. The PM Ytterbium-doped fiber is 3.2 m Nufern PM-YSF-LO, which is core-pumped. There is about 3-m passive of PM 980 before the gain fiber (pigtails of the WDM and the inline fiber isolator). The output pulse is compressed by a pair of dielectric transmission gratings with a groove density of 1000 lpmm in a double-pass configuration.

5.2.2 Experimental results

The goal of the experiment is to prove the predictions of the simulation and to verify the general design guidelines of Section 5.1. To obtain a clean compressed pulse at the output of PCMA, we follow the guideline of simulation and set the grating compressor in such a way that the pre-chirp corresponds to a GDD of -0.144 ps^2. By turning the input power to the level of 26 mW, PCMA works on a saturated state and delivers a total output power of 820 mW, corresponding to a pulse energy of 12 nJ. The compressor's perpendicular grating separation and efficiency are ~7 mm and 89%, respectively. Behind the compressor, the average power is 734 mW. Thus, the energy of the compressed pulses is above 10 nJ. The autocorrelation trace of compressed pulse and the transfer limit pulse from PCMA output are shown in Fig. 6, which corresponds to a high-quality pulse with a duration of 63 fs. This is in good agreement with the simulation (note the same input and output power as well as GDD; however, the 10 nm super-Gaussian input spectrum, which is close to the experimentally observed spectral shape).
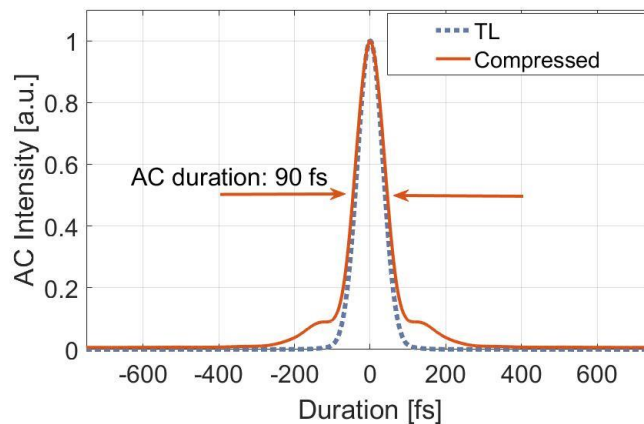
Figure 5.6: Autocorrelation at the PCMA output.

Control of spectral evolution through the amplifier is key to accomplish the best system performance. Specifically, it enables the generation of a smooth output spectrum of common shape. Figure 5.7 shows the spectral evolution through the amplifier chain (corresponding to the output pulse shown in Figure 5.6). The oscillator is mode-locked at the close-zero-dispersion region, which facilitates the generation of a broad output spectrum, as shown in Figure 5.7(a). Also, in this case, the oscillator should exhibit low timing jitter noise [62]. However, such a broadband spectrum will undergo strong gain narrowing during

amplification [16], and the spectrum edge will accumulate nonlinear phase that is not compressible. To achieve pulses with better quality, a bandpass filter with a bandwidth of 20 nm is inserted between the oscillator and the first amplifier. The first amplifier following the oscillator is a "mini" CPA system. The input and output spectra of the 1st amplifier show similar shapes, as shown in Figure 5.7 (b) and (c). The gain of the Yb-doped fiber shows a limited bandwidth and a certain gain-peak location (depending on the actual inversion level). Thus, some narrowing of the spectrum is visible. Another bandpass filter is inserted between the first amp and the second amplifier to further reduce the spectrum's bandwidth to 10 nm. This removes the un-compressible phase due to SPM and/or the limited gain of the first amplifier. Furthermore, it produces a clean spectrum with close to parabolic shape at the input of the PCMA system. By tuning the second bandpass filter's angle, we can match the input spectrum's center to the gain center of the second amplifier. Note, simulations have shown that the bandwidth of the spectrum at the input of the PCMA does not have a strong impact on the generation of output pulses with sub-100 fs durations. In principle, filters with narrower passband could be used. However, in this case, further adjustments may be needed to obtain the best operation point of the PCMA. As shown in Figure 4, the experimental spectrum is in excellent agreement with the prediction. Note, the spectrum is smoother as compared to other PCMA systems.
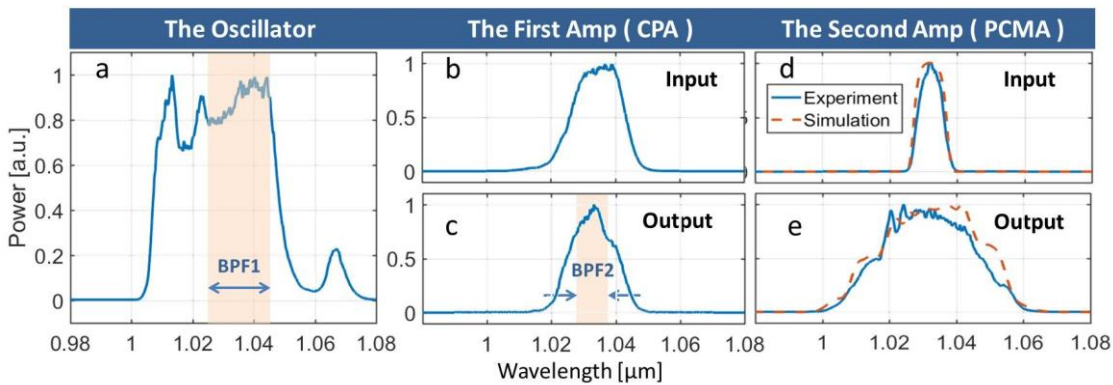
Figure 5.7: Experimental results of the spectra of 10-nJ, 60-fs laser system. Spectra of the pulse: (a) at the output of the oscillator, (b) after passage through BPF1, (c) after the first fiber-amplifier, (d) after passage through BPF2, (e) after the second fiber-amplifier.

5.2.3 Intensity noise reduction in fiber amplifier chain

During the experiment, we also investigate the relative amplitude noise transfer function in the Yb-doped fiber amplifier chain. Usually, in the condition of saturated amplification, the relative intensity noise (RIN) transfer function (in the frequency domain) exhibits a high-pass filtering behavior for the signal noise and a low-pass filtering behavior for pump noise, as shown in Fig.1 of [182]. The reason behind this phenomenon is the population of the upper laser level can only adapt to the pump (signal) power fluctuation below the corner frequency ω_{eff}, so that low-frequency pump modulation will transfer to the output power. In contrast, the low-frequency signal modulation will change the gain in fiber when the amplifier is saturated, resulting in a less influence of output power fluctuation. In fact, the corner frequency can be calculated in the analytic model developed for telecom amplifiers without considering amplified spontaneous emission (ASE) [185]. The corner frequency can be expressed as follow:

$$\omega_{eff} = P_s^0(L) \cdot B_s + P_p^0(L) \cdot B_p + 1/\tau \tag{5-1}$$

where τ is the fluorescence lifetime and $P_s^0(L)$ and $P_p^0(L)$ are the average signal and pump power at the end of the fiber given in the number of photons per second. The coupling factors $B_s = \Gamma_s(\sigma_{12}(\omega_s) + \sigma_{21}(\omega_s))/A$ and $B_p = \Gamma_p(\sigma_{12}(\omega_p) + (\sigma_{21}(\omega_p))/A$ depend on the overlap with the doped region Γ, the emission σ_{21} and absorption σ_{12} cross-section of signal and pump, as well as the mode area A. Apart from the corner frequency, the RIN reduction function of signal in a fiber amplifier can be written as:

$$m_s' = m_s \frac{\sqrt{\omega^2 + (\omega_{eff} + B_s[P_s^0(0) - P_s^0(L)])^2}}{\sqrt{\omega^2 + \omega_{eff}^2}} \tag{5-2}$$

The m_s and ω are the signal modulation index and modulation frequency defined via $P_s = P_s^0(1 + m_s \cdot \sin(\omega t))$. For high-frequency modulation, m_s' is close to the value of m_s, which means the gain medium cannot reduce the high-frequency noise from signal. When the modulation frequency is low (close to 0), and the residual pump power is negligible, the low-frequency noise reduction index can be written as:

$$m_s' = \frac{m_s}{P_s^0(L)} \cdot \left(P_s^0(0) + \frac{1}{\tau B_s} + P_p^0(L)\frac{B_p}{B_s}\right) \tag{5-3}$$

Under the condition of saturated amplification, the third term is negligible. The second term in Equation 5-3 is low gain approximation of the saturation power of this fiber amplifier. As long as the power of the input signal is much larger than the saturation power, this equation can be rewritten as:

$$\frac{m_s'}{m_s} = \frac{P_s^0(0)}{P_s^0(L)} + \frac{1}{\tau B_s} \cdot \frac{1}{P_s^0(L)} \approx \frac{P_s^0(0)}{P_s^0(L)} \tag{5-4}$$

In this end, the noise reduction index of the low-frequency RIN in fiber amplifier is indeed the inverse number of fiber gain. Maximizing the fiber gain and minimizing the residual pump will lead to the highest noise reduction of low-frequency signal RIN. However, the RIN reduction function of pump is an inverse version of the signal's RIN reduction function [185]. It can be written as:

$$\frac{m_p'}{m_p} = \frac{B_s(P_p^0(0) - P_p^0(L))}{\sqrt{\omega^2 + \omega_{eff}^2}} \tag{5-5}$$

Reference [182] also adds the low-frequency RIN reduction index of the pump under the condition of saturated amplification, which is:

$$\frac{m_p'}{m_p} = \left(1 - \frac{P_s^0(0)}{P_s^0(L)} + \frac{N_2/\tau}{P_s^0(L)}\right) \approx 1 - \frac{P_s^0(0)}{P_s^0(L)} \tag{5-6}$$

If the term N_2/τ, which corresponds to spontaneous emission is low enough, the low-frequency noise reduction index of pump and signal can be described as:

$$\frac{m_p'}{m_p} = 1 - \frac{m_s'}{m_s} \tag{5-7}$$

When the low-frequency RIN of the signal is minimized, the noise transfer of the pump's low-frequency intensity noise is highest. If the fiber gain is not high enough, the pump's noise transfer function is not that efficient. It is noteworthy that Equation 5-3, 5-4, 5-6, and 5-7 are achieved with the large output

power approximation when the amplifier is saturated. Then, we estimate the operation condition of the two-stage amplifiers in our laser system. The estimated and experimental parameters of the amplifiers are list in Table 5.2. By incorporating these parameters into the formula 5-2 and 5-5, we can achieve the noise transfer functions for both pump and signal over full frequency range, as shown in Figure 5.8.

These two amplifiers have different corner frequencies, and the signal noise frequency under the value of 13.3 kHz (80.2 kHz) is suppressed in the first (second) amplifier. Besides, for the first one, the noise suppression index of the signal is -8 dB. The number drops to -4.5 dB in the second amplifier due to a large residual pump. On the other hand, the noise suppression of the pump at low frequency is nearly zero for the first one, and the second one has a value of -0.5 dB. Both amplifiers can suppress low-frequency signal-noise efficiently. However, the output signal becomes more sensitive to the low-frequency pump noise. Thinking of the pump noise of the first AMP transfers into the input signal noise in the second AMP, this is suppressed further in the second stage. So the final limitation of the low-frequency noise suppression in this two-stage amplifiers chain is the pump noise in the last stage amplifier [186], [187], while the high-frequency noise of this fiber laser system is limited by the oscillator.

Table 5.2: Parameters of fiber amplifiers

	The first AMP (Yb 401-PM)	The second AMP (PM-YSF-LO)
Mode field diameter (μm)	6	6.5
Overlaping Γ_p	0.664	0.668
Overlaping Γ_s	0.604	0.608
Fluorescence (ms)	0.9	1.4
λ_{signal} (nm)	1030	1030
λ_{pump} (nm)	976	976
$\sigma_{12}(\lambda_{pump})$ (m^2)	25.7×10^{-25}	25.7×10^{-25}
$\sigma_{21}(\lambda_{pump})$ (m^2)	24.7×10^{-25}	24.7×10^{-25}
$\sigma_{12}(\lambda_{signal})$ (m^2)	5.98×10^{-26}	5.98×10^{-26}
$\sigma_{21}(\lambda_{signal})$ (m^2)	6.4×10^{-25}	6.4×10^{-25}
Saturation power (mW)	14.3	10.7
Input signal $P_s^0(0)$ (mW)	5	26
Output signal $P_s^0(L)$ (mW)	150	820
Residual pump $P_p^0(L)$ (mW)	1	50
Corner frequency ω_{eff} (kHz)	13.3	80.2
Gain (dB)	14.8	15

Since PCMA (the second AMP) is a highly nonlinear fiber amplifier, intensity noise of input signal can be transferred into phase noise of the output efficiently, even though the intensity noise is suppressed due to saturated amplification. In order to achieve low-noise operation in terms of intensity noise and phase noise, the pump for the first AMP and second AMP should be very stable. In the experiment, we

intend to choose the signal-mode pumps for their better wavelength stabilization by utilizing the fiber Brag gratings (FBGs).

In the experiment, we have characterized the intensity noise level in the frequency range 10 Hz to 20 MHz of the output signal from the oscillator, the 1st amp, and the 2nd amplifier (using photo-detector Thorlabs DET36A). The noise spectrum and the accumulated noise are displayed in Figure 5.9. The integrated noise level reduces in every stage, particularly for lower frequencies. This is in good agreement with the fact that the amplifiers are saturated. The lifetime of Ytterbium is about 1 ms, suppressing noise frequencies in the band < 10 kHz. The noise suppression is far more efficient in the first AMP, which fits with our estimation in Figure 5.8. The low-intensity noise from the output of the first amplifier ensures good performance of the overall system.
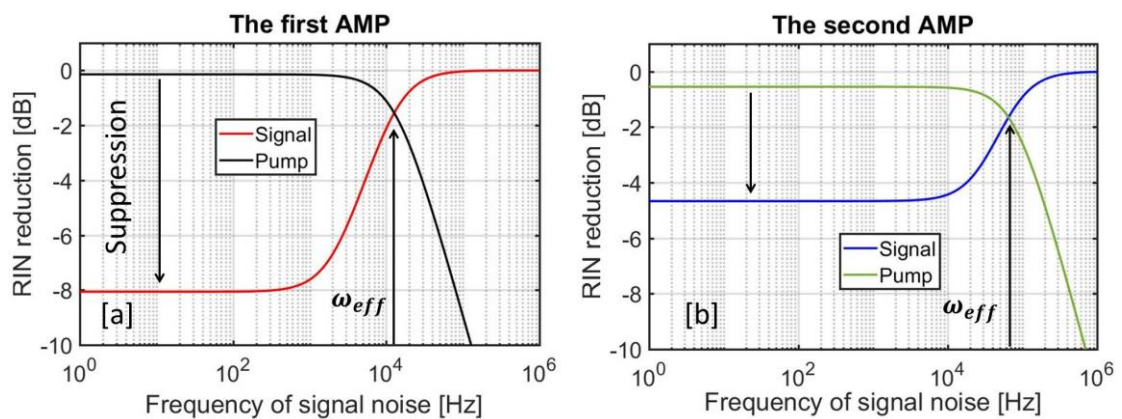
Figure 5.8: Intensity noise reduction functions versus noise frequency of signal and pump. (a) The first amplifier; (b) the second amplifier.
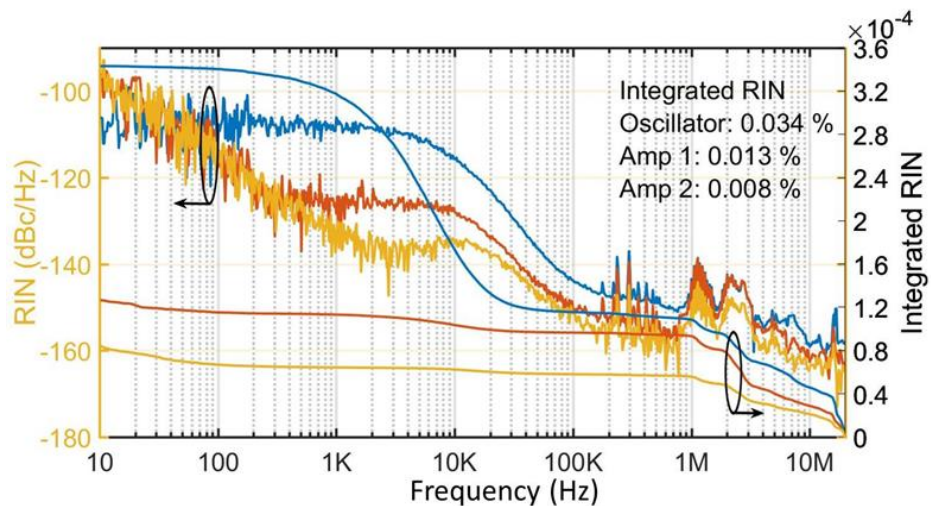
Figure 5.9: Noise spectra (a) after the oscillator, (b) after the first amplifier, (c) after the second amplifier.

The noise suppression in the second AMP is trivial in the frequency range below 100 kHz. This can be explained by the following facts.

a) The signal-noise reduction index is much smaller than the first AMP in the low-frequency range, as shown in Figure 5.8.

b) Further noise reduction is limited by the pump noise, which is in the same noise level as the output signal noise from the first AMP. (Both AMPs are pumped by the same type of diodes mounted on the same pump drivers.

c) The nonlinear processes in PCMA (the second AMP) enhance the signal's noise.

Apart from the low-frequency RIN, the high-frequency noise (above 1MHz) is also suppressed by every amplifier stage. Since the gain dynamic in fiber cannot explain this phenomenon, we assume that the spectrum broadening and filtering play a crucial role in the suppression of the high-frequency intensity noise.

5.3   Design of attenuators for the laser stabilization
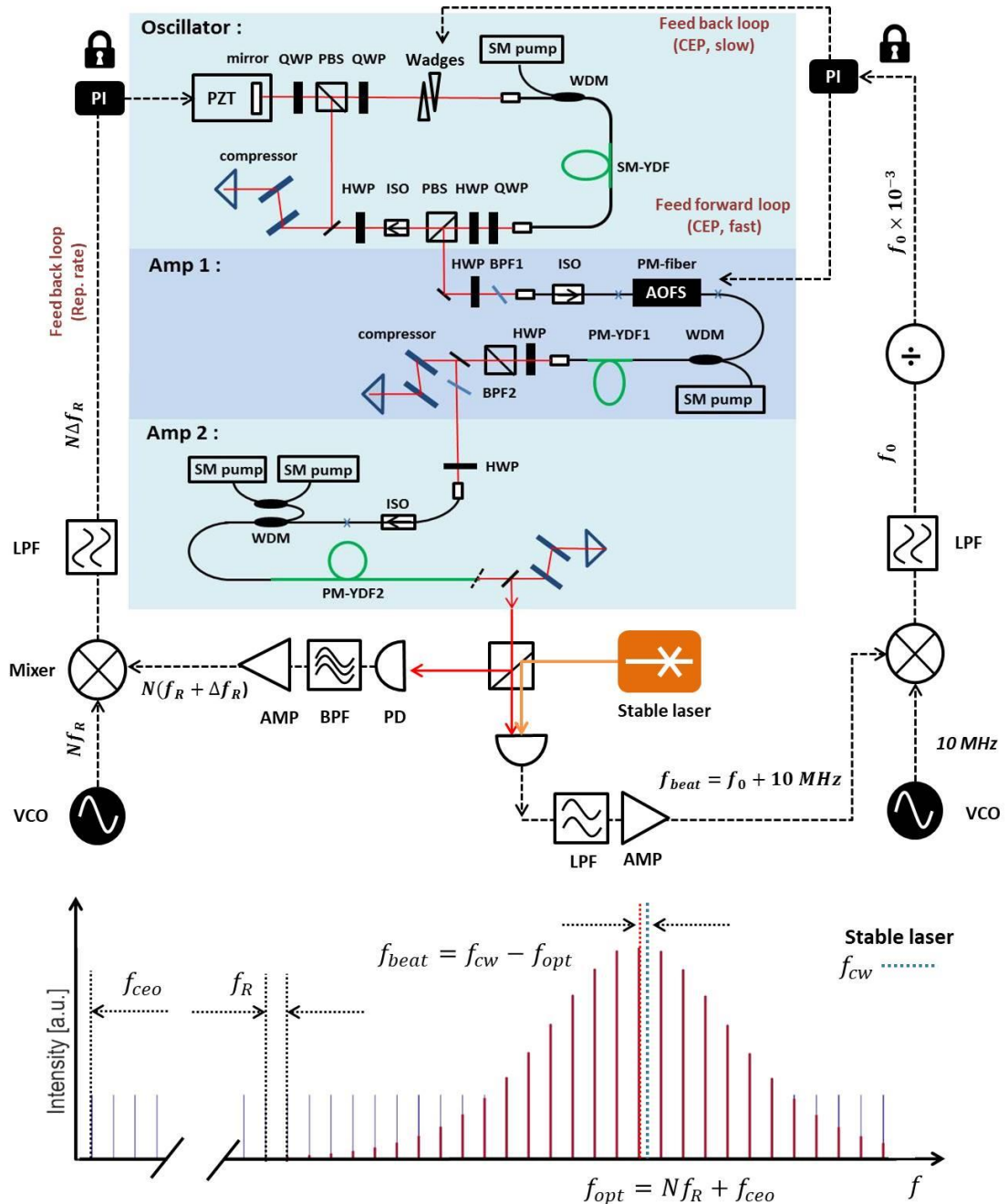
Figure 5.10: Schematic of frequency comb. It includes the master oscillator shown in Figure 5.5, three attenuators for repetition rate and fceo locking, and the electronic loops for feed-back and feed-forward control.

As discussed before, our target of building this maser laser is to transfer it into an ultra-stable frequency comb for the multiply applications, which requires the synchronization. To lock the laser's repetition rate and carrier-envelope phase (CEP), we modify this laser setup, as shown in Figure 5.10. On the top of the laser, three attenuators are assembled, including a fast piezo (PZT) for the repetition rate locking, an acoustic-optic frequency shifter (AOFS) for feed-forward CEP locking and a pair of wedges for the feed-back CEP locking.
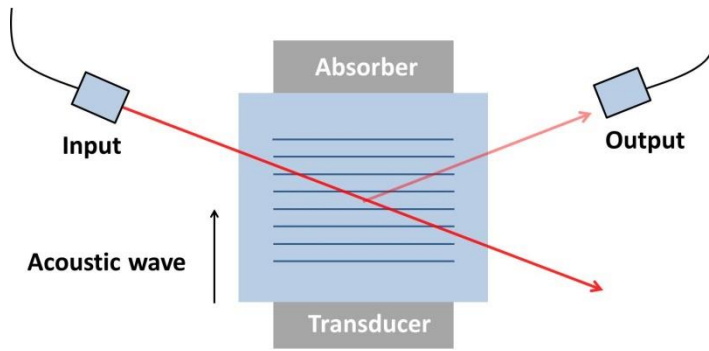
Figure 5.11: Schematic of acoustic-optic frequency shift. (which type ?)

The in-line AOFS is inserted between the oscillator and the first amplifier with a PM-fiber pigtail. The CEP locking technique based on AOFS is named the feed-forward method. It removes the cross-talking with the repetition rate by assembling the attenuator outside of the oscillator cavity [188], [189]. Besides, the feed-forward method has a much larger modulation bandwidth (up to several 100 kHz), which is only limited by the travel time of the acoustic wave from the actuator to the interaction zone with the optical beam. The 100 kHz-level modulation bandwidth is sufficient to eliminate all conceivable CEP noise. Remarkable low residual phase jitters have been reported through the feed-forward method [190], [191]. However, the drawbacks are also visible. For example, the significant insertion loss (>2.5 dB), limited modulation range (<1 MHz), and spatial chirp at the output of AOFS limit the application of this method. The spatial chirp is due to the wavelength-dependent diffracted angle of the Bragg grating introduced by the acoustic wave in the crystal. We use the AOFS with PM fiber pigtail to address this problem so that the mode-cleaning in fiber removes the spatial chirp. During the locking procedure, the frequency of the acoustic wave is modulated by an error signal from the feed-forward loop shown in Figure 5.10, so the first-order diffracted angle of acoustic Bragg grating changes as well. This effect further influences the power coupling efficiency from the first-order output to the fiber pigtail, leading to an enhancement of signal intensity noise. To compensate for the insertion loss and suppress the intensity noise introduced by AOFS, we put the AOFS before the first amplifier, which is a saturated CPA system. It can suppress the low-frequency (below 10 kHz) intensity noise of the signal during amplification without worrying about the phase noise transferred from the corresponding intensity noise. The last problem of AOFS is the limited modulation range around its center frequency (<1 MHz). Once the value of the error signal is larger than its modulation range, which is often the case for a long-term operation, the feed-forward locking loop will not more have any function.

To address the problem, we use a pair of home-designed wedges mounted on a PZT stage, which is controlled by a slow feed-back loop, in the oscillator for the compensation of CEP long-term drift [192], [193]. The wedge pair is constructed with two conversely oriented wedge prisms made from two different optical materials. It is designed to maximize the CEP modulation upon changing its insertion into the beam while keeping a constant group delay (GD). In this way, we can remove its influence on the repetition rate during CEP locking procedure. Apart from that, we have to consider the efficiency of CEP modulation and the corresponding side effects. In an ideal case, this feed-back method based on wedges has enough CEP modulation range and less influence on other laser parameters for maintaining a long-term operation.

Chapter 5: Low-noise master fiber laser delivering 10-nJ, 60-fs pulse

The configuration of the wedges is shown in Figure 5.12. The pair of wedges includes two prisms with different materials and different apex angles. They are optical contact, and the gap is filled with index matching fluid. The laser beam passes through with a Brewster incident angle so that the reflection of p-pol laser components in the first surface is zero. Certainly, the incident angle at the output surface of the wedge pair is no longer a Brewster angle, but we can minimize the reflection at the output by choosing these two materials with similar indices of refraction.
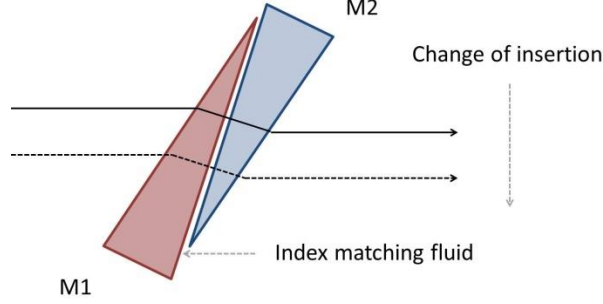
Figure 5.12: Schematic of the wedge pairs. Two materials are optical contact with index matching fluid. The input beam has a Brewster incident angle for the first material. No AR-coating.

The CEP shift per passage through the wedges can be computed as [192]:

$$\Delta\varphi_{CE} = \frac{2\pi}{\lambda}[(n_{g,2} - n_2)d_2 + (n_{g,1} - n_1)d_1] \tag{5-8}$$

where n_1 and n_2 are the indices of refraction, and d_1 and d_2 are the material paths in the two wedge prisms. The group delay introduced by these wedges can be calculated as:

$$GD = \frac{(n_{g,2} - n_2)d_2 + (n_{g,1} - n_1)d_1}{c} \tag{5-9}$$

where the n_g is the group index $n_g = n - \lambda\partial n/\partial\lambda$ of the corresponding material at the center wavelength of λ. Change of the prisms pair insertion results in the Δd_1 change of material path in prism1 and Δd_2 in prism2. If Δd_1 and Δd_2 satisfy the formula as following, the GD will keep constant.

$$\frac{\Delta d_2}{\Delta d_1} = -\frac{n_{g,1} - n_1}{n_{g,2} - n_2} \tag{5-10}$$

Under the small apex angle approximation, $\Delta d_2/\Delta d_1 \sim = -a_2/a_1$, where a1 and a2 are the apex angles of the prisms. If we fix the angle of prism1, the apex angle of prism2 can be calculated based on the corresponding material information of prisms. As discussed above, the two materials should have a very similar indices of refraction at the center wavelength to avoid reflection at the end face. At the same time, due to the challenge of manufacturing, the apex angles of the prisms should not be too small. Guided by these two principles, we search for the optimized material combination to maximize the efficiency of CEP modulation, at the same time, fewer side effects.

Table 5.3 lists the parameters of different wedge pairs. The parameter $\eta = \Delta\varphi_{cep}/\Delta d_1$ is defined as follow:

$$\eta = \frac{2\pi}{\lambda}\left[(n_{g,2} - n_2)\frac{tan\alpha_2}{tan\alpha_1} - (n_{g,1} - n_1)\right] \tag{5-11}$$

which represents the efficiency of the paired prisms to control CEP. $\Delta\theta/\Delta\lambda$ is the angular dispersion of the prisms' output. Δd is the change of the prims' insertion length for CEP shifting over one free spectral range (FSR, 2π). Δx and GDD are the change of output beam's position and group delay dispersion introduced for the variation of CEP over one FSR. The apex angle of the first prism is fixed at 3 degrees, and the apex angle of the second one is calculated to satisfy the condition of a constant GD (Equation 5-10).

Table 5.3: Calculated parameters of different wedge pairs

(Apex angle of prism1 is 3°; Center wavelength is 1030 nm)

Prism 1	Prism 2	n1	n2	Apex2 (degree)	$\Delta\varphi_{cep}/\Delta d_1$ rad/mm	$\Delta\theta/\Delta\lambda$ μrad/nm	Δd mm/FSR	Δx μm/FSR	GDD fs^2/FSR
N-BK10	N-PK51	1.49	1.52	2.84	24.49	-13.67	2.18	2.15	-0.90
N-PK51	N-BK10	1.52	1.49	3.17	-25.88	-9.31	-2.05	-2.19	-0.90
N-FK5	N-PK51	1.48	1.52	2.78	20.83	-12.83	2.58	4.49	-1.43
N-PK51	N-FK5	1.52	1.48	3.24	-22.49	-9.36	-2.36	-4.59	-1.43
N-SF6	N-LASF31A	1.77	1.86	2.73	51.87	-33.00	0.96	4.30	5.97
N-LASF31A	N-SF6	1.86	1.77	3.30	-56.99	-24.48	-0.85	-4.50	5.97
N-BK10	N-SF6	1.49	1.77	1.87	-41.38	-12.77	-1.29	-22.70	9.15
N-SF6	N-BK10	1.77	1.49	4.82	66.50	-31.86	0.75	25.69	9.15
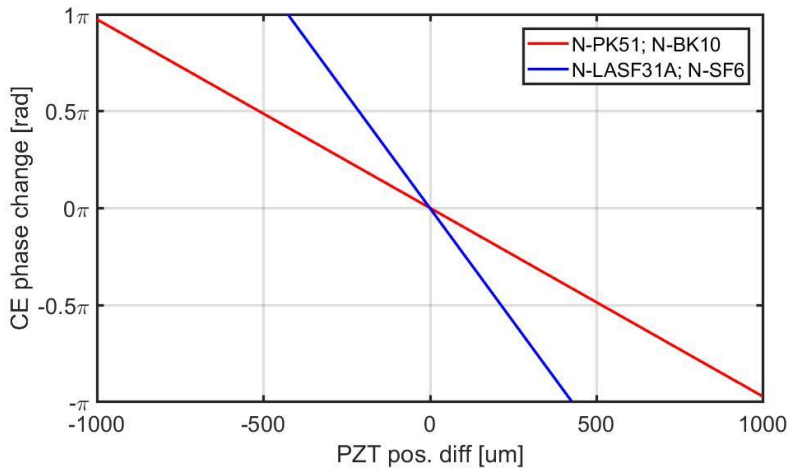
Figure 5.13: Change of carrier-envelope offset frequency versus the insertion length of wedge pairs.

For every material pair, we flip the sequence and calculate the pair's parameters again. It is found that when the first prism has a larger refractive index than the second one in the pair, the CEP compensator achieves better qualities in terms of angular dispersion and CEP shifting efficiency. Besides, the refractive index difference between these two materials in the pair should keep small, as discussed before. The N-BK10 and N-SF6 pair has a large refractive index difference of 0.27, which leads to a significant position shift of the output beam. Among all the pairs, the pair with N-PK51 and N-BK10, and the pair

with N-LASF31A and N-SF6 stand out with better performance. The N-LASF31A and N-SF6 prisms pair have a higher CEP shifting efficiency; however, it still suffers from large angular dispersion and GDD variation. The pair with N-PK51 and N-BK10 enables smaller output beam walking per FSR and minimum angler dispersion with relatively lower CEP modulation efficiency. Figure 5.13 shows the modulation of carrier-envelope phase versus the insertion length of the pair. The blue curve has a much steeper slope than the orange one, resulting in a higher modulation efficiency.
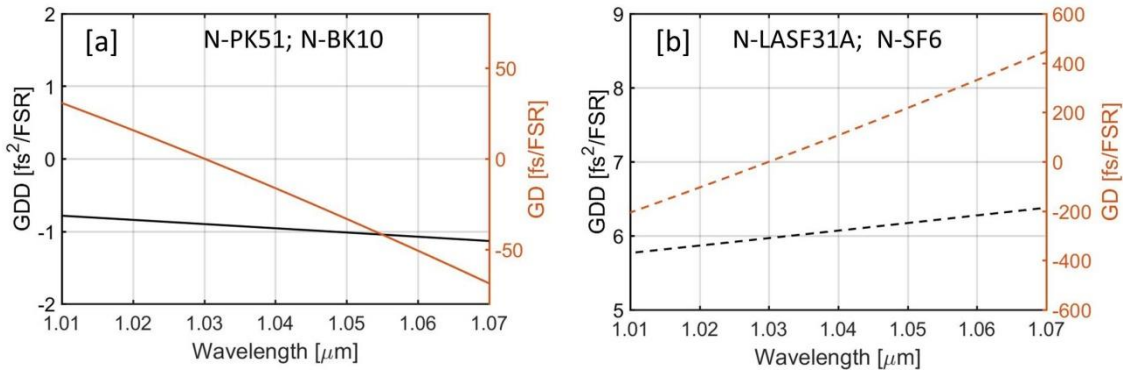
Figure 5.14: Variation of GDD and GD per FSR versus the center wavelength of pulses. (a):N-PK51 and N-BK10 pair; (b) N-LASF31A and N-SF6 pair.

Figure 5.14 shows the variation of GD and GDD per FSR as a function of the pulse's center wavelength when the parameters of the paired prisms are fixed in terms of materials, apex angles, and the Brewster incident angle. It is found that when the center wavelength of the pulse is fixed at 1030 nm, the GD values in both cases are nearly zero. However, the GD deviates from zero as soon as the center wavelength of pulse shifts away from 1030 nm. In the case with N-LASF31A and N-SF6, the deviation is far more extensive than the other one. This results in significant timing jitter during CEP modulation once the mode-locking spectrum shift. In the other case, as shown in Figure 5.14 (a), the deviation of GD is 3 times smaller. Considering the side effects of N-LASF31A and N-SF6 pair, we assume that the prism pair with N-PK51 and N-BK10 is a better solution for the CEP feed-back locking loop. The combination of the fast feed-forward loop based on AOFS and the slow feedback loop based on the specially designed wedges pair constitutes an ultra-robust and stable CEP locking method.

5.4   Summary of the chapter

In this chapter, we design and build a low-noise 10-nJ, 60-fs master laser system based on PCMA. The detailed simulation results of PCMA are given first as a guideline for the experiment. Then, the noise transfer functions during amplification are analyzed by the analytic model developed for telecom amplifiers and proved by the experiment. The ultra-low RIN with a value of 0.008% is achieved from the PCMA output. Finally, we discuss the methods to transfer this master laser into a stable frequency comb. The detailed design of the attenuators for CEP locking is given in the last part.

Chapter 6

Conclusion and Outlook

The works in this thesis focus on the development of a reliable ultrashort fiber platform with the merit of turn-key operation to seed high power amplifier systems at 1 µm. We investigate several parts of the Yb-doped fiber laser system, including all polarization-maintaining Fiber 9 fiber oscillators, nonlinear wavelength conversion methods in fiber, the linear and nonlinear fiber amplification methods for both short-wavelength pulses and broadband pulses as well as the noise performances for fiber amplifier chain.

For the oscillator, efforts were put on the investigation of pulse dynamic of all-polarization-maintaining Figure 9 fiber laser in both all normal dispersion regime and dispersion management regime. Different pulse mode-locking mechanisms are revealed as well as the building up process of the corresponding pulses in the simulation. In the experiment, we have achieved 65-fs transform-limited pulses directly from the dispersion management Figure 9 oscillator with close to 10-kW peak power. To our knowledge, this is the first demonstration of the shortest pulses delivered directly from a NALM-based fiber laser. We intend to use this type of dispersion-managed all-PM Figure 9 oscillator to replace the other oscillator in our ultrafast fiber laser systems in Chapter 4 and Chapter 5 for its merit of stability and low-noise operation.

For the nonlinear wavelength conversion method, we investigated both the soliton self-frequency shift (SSFS) and the SPM-enabled spectral selection (SESS) method. The parameters of the induced wavelength-shifted pulse through these methods were compared in terms of pulse energy, relative intensity noise (RIN), and the corresponding timing jitter. For the first time, we demonstrate experimentally that the attosecond-level timing jitter of SESS pulse is ten times lower than Raman soliton generated through SSFS. SESS pulses combined with the source laser pulses can constitute a tightly synchronized two-color laser source. The SESS method, with its merits of high pulse energy and low timing jitter, actually overcomes the wavelength limitation of Yb-doped amplifier and largely expands the parameter space of the Yb-doped fiber laser system. It is successfully used in Chapter 4 for 13-nJ pulse generation at the center wavelength of 995 nm.

In Chapter 4 and Chapter 5, the customized ultrashort fiber laser systems were introduced. Amplification methods (linear and nonlinear amplification) suitable for short-wavelength pulses (below 1020 nm) are discussed in Chapter 4. For the first time, the specialized fiber seed sources for cryogenic

Chapter 6: Conclusion and outlook

cooling Yb: YLF amplifiers are designed and demonstrated in the experiment. They provide the widely tunable pulses in terms of center wavelength (from 995 nm to 1020 nm) and pulse energy (up to µJ) to fit the specific parameter space of Yb: YLF crystals. In Chapter 5, we propose a low-noise (RIN 0.008%) master fiber laser system that delivers a 60-fs pulse with 10-nJ pulse energy. Its output pulse has a smooth spectrum covering the wavelength range from 1010 to 1050 nm, which can be a common seeding source for different solid-state amplifiers based on Yb-doped crystals (Yb: YAG, Yb: YLF, and Yb: KYW) and provide the synchronization among them. The attenuators for further active stabilizing this master laser are designed and installed in the laser system. Our target for the future development is to transfer the maser fiber laser system in Chapter 5 into a multi-functional platform by employing the environmentally stable oscillator (Chapter 2), nonlinear wavelength shift method (Chapter 3) and the linear/ nonlinear amplification schemes (Chapter 4) in this fiber laser system. This platform will offer low-noise wavelength-tunable pulses with up to µJ pulse energy in an all-PM fiber laser structure.

Bibliography

[1] F. Krausz and M. Ivanov, "Attosecond physics," *Rev. Mod. Phys.*, vol. 81, no. 1, pp. 163–234, Feb. 2009, doi: 10.1103/RevModPhys.81.163.

[2] S. Witte and K. S. E. Eikema, "Ultrafast Optical Parametric Chirped-Pulse Amplification," *IEEE J. Sel. Top. Quantum Electron.*, vol. 18, no. 1, pp. 296–307, Jan. 2012, doi: 10.1109/JSTQE.2011.2118370.

[3] C. Hernandez-Garcia, P. G. O'Shea, and M. L. Stutzman, "Electron sources for accelerators," *Phys. Today*, vol. 61, no. 2, pp. 44–49, Feb. 2008, doi: 10.1063/1.2883909.

[4] P. Russbueldt, T. Mans, G. Rotarius, J. Weitenberg, H. D. Hoffmann, and R. Poprawe, "400W Yb:YAG Innoslab fs-Amplifier," *Opt. Express*, vol. 17, no. 15, p. 12230, Jul. 2009, doi: 10.1364/OE.17.012230.

[5] O. Pronin *et al.*, "High-power 200 fs Kerr-lens mode-locked Yb:YAG thin-disk oscillator," *Opt. Lett.*, vol. 36, no. 24, p. 4746, Dec. 2011, doi: 10.1364/OL.36.004746.

[6] W. F. Krupke, "Ytterbium solid-state lasers. The first decade," *IEEE J. Sel. Top. Quantum Electron.*, vol. 6, no. 6, pp. 1287–1296, Nov. 2000, doi: 10.1109/2944.902180.

[7] L. E. Zapata, D. J. Ripin, and T. Y. Fan, "Power scaling of cryogenic Yb:LiYF_4 lasers," *Opt. Lett.*, vol. 35, no. 11, p. 1854, Jun. 2010, doi: 10.1364/OL.35.001854.

[8] T. Y. Fan *et al.*, "Cryogenic Yb$^{3+\$}$-Doped Solid-State Lasers," *IEEE J. Sel. Top. Quantum Electron.*, vol. 13, no. 3, pp. 448–459, May 2007, doi: 10.1109/JSTQE.2007.896602.

[9] D. E. Miller, L. E. Zapata, D. J. Ripin, and T. Y. Fan, "Sub-picosecond pulses at 100 W average power from a Yb:YLF chirped-pulse amplification system," *Opt. Lett.*, vol. 37, no. 13, p. 2700, Jul. 2012, doi: 10.1364/OL.37.002700.

[10] U. Demirbas, J. Thesinga, H. Cankaya, M. Kellert, F. X. Kärtner, and M. Pergament, "High-power passively mode-locked cryogenic Yb:YLF laser," *Opt. Lett.*, vol. 45, no. 7, p. 2050, Apr. 2020, doi: 10.1364/OL.390291.

[11] Y. Hua *et al.*, "87-W 1018-nm Yb-fiber ultrafast seeding source for cryogenic Yb: yttrium lithium fluoride amplifier," *Opt. Lett.*, vol. 43, no. 8, pp. 1686–1689, 2018.

[12] D. Zhang *et al.*, "Segmented terahertz electron accelerator and manipulator (STEAM)," *Nat. Photonics*, vol. 12, no. 6, pp. 336–342, 2018.

[13] P. Lacovara, H. K. Choi, C. A. Wang, R. L. Aggarwal, and T. Y. Fan, "Room-temperature diode-pumped Yb:YAG laser," *Opt. Lett.*, vol. 16, no. 14, p. 1089, Jul. 1991, doi: 10.1364/OL.16.001089.

[14] A. A. Lagatsky, C. T. A. Brown, and W. Sibbett, "Highly efficient and low threshold diode-pumped Kerr-lens mode-locked Yb:KYW laser," *Opt. Express*, vol. 12, no. 17, p. 3928, 2004, doi: 10.1364/OPEX.12.003928.

[15] U. Demirbas, H. Cankaya, J. Thesinga, F. X. Kärtner, and M. Pergament, "Efficient, diode-pumped, high-power (>300W) cryogenic Yb:YLF laser with broad-tunability (995-10205 nm): investigation of E//a-axis for lasing," *Opt. Express*, vol. 27, no. 25, p. 36562, Dec. 2019, doi: 10.1364/OE.27.036562.

[16] P. Raybaut, F. Balembois, F. Druon, and P. Georges, "Numerical and experimental study of gain narrowing in ytterbium-based regenerative amplifiers," *IEEE J. Quantum Electron.*, vol. 41, no. 3, pp. 415–425, Mar. 2005, doi: 10.1109/JQE.2004.841930.

Bibliography

[17] M. Hemmer, L. E. Zapata, Y. Hua, and F. X. Kärtner, "Addressing spectral narrowing in cryogenic Yb: YAG: a 10 mJ cryogenic Yb: YLF regenerative amplifier," in *Advanced Solid State Lasers*, 2016, pp. ATh4A–3.

[18] H. Cankaya *et al.*, "190-mJ cryogenically-cooled Yb: YLF amplifier system at 1019.7 nm," *OSA Contin.*, vol. 2, no. 12, pp. 3547–3553, 2019.

[19] C. J. Saraceno *et al.*, "Toward Millijoule-Level High-Power Ultrafast Thin-Disk Oscillators," *IEEE J. Sel. Top. Quantum Electron.*, vol. 21, no. 1, pp. 106–123, Jan. 2015, doi: 10.1109/JSTQE.2014.2341588.

[20] D. C. Brown *et al.*, "The Application of Cryogenic Laser Physics to the Development of High Average Power Ultra-Short Pulse Lasers," *Appl. Sci.*, vol. 6, no. 1, Art. no. 1, Jan. 2016, doi: 10.3390/app6010023.

[21] R. L. Aggarwal, D. J. Ripin, J. R. Ochoa, and T. Y. Fan, "Measurement of thermo-optic properties of Y3Al5O12, Lu3Al5O12, YAIO3, LiYF4, LiLuF4, BaY2F8, KGd(WO4)2, and KY(WO4)2 laser crystals in the 80–300K temperature range," *J. Appl. Phys.*, vol. 98, no. 10, p. 103514, Nov. 2005, doi: 10.1063/1.2128696.

[22] O. G. Okhotnikov, L. Gomes, N. Xiang, T. Jouhti, and A. B. Grudinin, "Mode-locked ytterbium fiber laser tunable in the 980–1070-nm spectral range," *Opt. Lett.*, vol. 28, no. 17, pp. 1522–1524, Sep. 2003, doi: 10.1364/OL.28.001522.

[23] Y. Jeong *et al.*, "Power Scaling of Single-Frequency Ytterbium-Doped Fiber Master-Oscillator Power-Amplifier Sources up to 500 W," *IEEE J. Sel. Top. Quantum Electron.*, vol. 13, no. 3, pp. 546–551, May 2007, doi: 10.1109/JSTQE.2007.896639.

[24] K. K. Chen *et al.*, "Polarisation maintaining 100W Yb-fiber MOPA producing µJ pulses tunable in duration from 1 to 21 ps," *Opt. Express*, vol. 18, no. 14, p. 14385, Jul. 2010, doi: 10.1364/OE.18.014385.

[25] M. Kienel, M. Müller, A. Klenke, J. Limpert, and A. Tünnermann, "12 mJ kW-class ultrafast fiber laser system using multidimensional coherent pulse addition," *Opt. Lett.*, vol. 41, no. 14, p. 3343, Jul. 2016, doi: 10.1364/OL.41.003343.

[26] J. S. Feehan, J. H. V. Price, T. J. Butcher, W. S. Brocklesby, J. G. Frey, and D. J. Richardson, "Efficient high-harmonic generation from a stable and compact ultrafast Yb-fiber laser producing 100 µJ, 350 fs pulses based on bendable photonic crystal fiber," *Appl. Phys. B*, vol. 123, no. 1, p. 43, Jan. 2017, doi: 10.1007/s00340-016-6620-8.

[27] L. A. Gomes, L. Orsila, T. Jouhti, and O. G. Okhotnikov, "Picosecond SESAM-based ytterbium mode-locked fiber lasers," *IEEE J. Sel. Top. Quantum Electron.*, vol. 10, no. 1, pp. 129–136, Jan. 2004, doi: 10.1109/JSTQE.2003.822918.

[28] F. Ilday, J. Buckley, L. Kuznetsova, and F. Wise, "Generation of 36-femtosecond pulses from a ytterbium fiber laser," *Opt. Express*, vol. 11, no. 26, p. 3550, Dec. 2003, doi: 10.1364/OE.11.003550.

[29] W. Wang *et al.*, "Gain-guided soliton: Scaling repetition rate of passively modelocked Yb-doped fiber lasers to 125 GHz," *Opt. Express*, vol. 27, no. 8, p. 10438, Apr. 2019, doi: 10.1364/OE.27.010438.

[30] P. Wan, L.-M. Yang, and J. Liu, "All fiber-based Yb-doped high energy, high power femtosecond fiber lasers," *Opt. Express*, vol. 21, no. 24, p. 29854, Dec. 2013, doi: 10.1364/OE.21.029854.

[31] M. N. Zervas and C. A. Codemard, "High Power Fiber Lasers: A Review," *IEEE J. Sel. Top. Quantum Electron.*, vol. 20, no. 5, pp. 219–241, Sep. 2014, doi: 10.1109/JSTQE.2014.2321279.

[32] J. Limpert *et al.*, "The Rising Power of Fiber Lasers and Amplifiers," *IEEE J. Sel. Top. Quantum Electron.*, vol. 13, no. 3, pp. 537–545, May 2007, doi: 10.1109/JSTQE.2007.897182.

[33] G. Chang and Z. Wei, "Ultrafast Fiber Lasers: An Expanding Versatile Toolbox," *iScience*, vol. 23, no. 5, p. 101101, May 2020, doi: 10.1016/j.isci.2020.101101.

[34] B. Fu, Y. Hua, X. Xiao, H. Zhu, Z. Sun, and C. Yang, "Broadband graphene saturable absorber for pulsed fiber lasers at 1, 1.5, and 2 µm," *IEEE J. Sel. Top. Quantum Electron.*, vol. 20, no. 5, pp. 411–415, 2014.

Bibliography

[35] M. E. Fermann, M. L. Stock, M. J. Andrejco, and Y. Silberberg, "Passive mode locking by using nonlinear polarization evolution in a polarization-maintaining erbium-doped fiber," *Opt. Lett.*, vol. 18, no. 11, p. 894, Jun. 1993, doi: 10.1364/OL.18.000894.

[36] A. Chong, W. H. Renninger, and F. W. Wise, "All-normal-dispersion femtosecond fiber laser with pulse energy above 20nJ," *Opt. Lett.*, vol. 32, no. 16, p. 2408, Aug. 2007, doi: 10.1364/OL.32.002408.

[37] N. J. Doran and D. Wood, "Nonlinear-optical loop mirror," *Opt. Lett.*, vol. 13, no. 1, p. 56, Jan. 1988, doi: 10.1364/OL.13.000056.

[38] M. E. Fermann, F. Haberl, M. Hofer, and H. Hochreiter, "Nonlinear amplifying loop mirror," *Opt. Lett.*, vol. 15, no. 13, p. 752, Jul. 1990, doi: 10.1364/OL.15.000752.

[39] N. Raabe *et al.*, "Excess carrier-envelope phase noise generation in saturable absorbers," *Opt. Lett.*, vol. 42, no. 6, p. 1068, Mar. 2017, doi: 10.1364/OL.42.001068.

[40] L. F. Mollenauer and R. H. Stolen, "The Soliton Laser," *Opt. News*, vol. 10, no. 6, p. 20_2, Nov. 1984, doi: 10.1364/ON.10.6.0020_2.

[41] A. Isomäki and O. G. Okhotnikov, "All-fiber ytterbium soliton mode-locked laser with dispersion control by solid-core photonic bandgap fiber," *Opt. Express*, vol. 14, no. 10, p. 4368, 2006, doi: 10.1364/OE.14.004368.

[42] K. Tamura, E. P. Ippen, H. A. Haus, and L. E. Nelson, "77-fs pulse generation from a stretched-pulse mode-locked all-fiber ring laser," *Opt. Lett.*, vol. 18, no. 13, p. 1080, Jul. 1993, doi: 10.1364/OL.18.001080.

[43] F. Ö. Ilday, J. R. Buckley, W. G. Clark, and F. W. Wise, "Self-Similar Evolution of Parabolic Pulses in a Laser," *Phys. Rev. Lett.*, vol. 92, no. 21, p. 213902, May 2004, doi: 10.1103/PhysRevLett.92.213902.

[44] W. Chang, A. Ankiewicz, J. M. Soto-Crespo, and N. Akhmediev, "Dissipative soliton resonances," *Phys. Rev. A*, vol. 78, no. 2, p. 023830, Aug. 2008, doi: 10.1103/PhysRevA.78.023830.

[45] Z. Liu, Z. M. Ziegler, L. G. Wright, and F. W. Wise, "Megawatt peak power from a Mamyshev oscillator," *Optica*, vol. 4, no. 6, p. 649, Jun. 2017, doi: 10.1364/OPTICA.4.000649.

[46] P. Sidorenko, W. Fu, L. G. Wright, M. Olivier, and F. W. Wise, "Self-seeded, multi-megawatt, Mamyshev oscillator," *Opt. Lett.*, vol. 43, no. 11, p. 2672, Jun. 2018, doi: 10.1364/OL.43.002672.

[47] Y. Lan, Y. Song, M. Hu, B. Liu, L. Chai, and C. Wang, "Enhanced spectral breathing for sub-25 fs pulse generation in a Yb-fiber laser," *Opt. Lett.*, vol. 38, no. 8, p. 1292, Apr. 2013, doi: 10.1364/OL.38.001292.

[48] W. H. Renninger, A. Chong, and F. W. Wise, "Self-similar pulse evolution in an all-normal-dispersion laser," *Phys. Rev. A*, vol. 82, no. 2, p. 021805, Aug. 2010, doi: 10.1103/PhysRevA.82.021805.

[49] J.-H. Cai, S.-P. Chen, and J. Hou, "1.1-kW Peak-Power Dissipative Soliton Resonance in a Mode-Locked Yb-Fiber Laser," *IEEE Photonics Technol. Lett.*, vol. 29, no. 24, pp. 2191–2194, Dec. 2017, doi: 10.1109/LPT.2017.2768487.

[50] C. Ma, A. Khanolkar, Y. Zang, and A. Chong, "Ultrabroadband, few-cycle pulses directly from a Mamyshev fiber oscillator," *Photonics Res.*, vol. 8, no. 1, p. 65, Jan. 2020, doi: 10.1364/PRJ.8.000065.

[51] P. Maine, D. Strickland, P. Bado, M. Pessot, and G. Mourou, "Generation of ultrahigh peak power pulses by chirped pulse amplification," *IEEE J. Quantum Electron.*, vol. 24, no. 2, pp. 398–403, Feb. 1988, doi: 10.1109/3.137.

[52] J. Limpert *et al.*, "High-power rod-type photonic crystal fiber laser," *Opt. Express*, vol. 13, no. 4, p. 1055, 2005, doi: 10.1364/OPEX.13.001055.

[53] F. Röser *et al.*, "Millijoule pulse energy high repetition rate femtosecond fiber chirped-pulse amplification system," *Opt. Lett.*, vol. 32, no. 24, p. 3495, Dec. 2007, doi: 10.1364/OL.32.003495.

[54] A. Klenke *et al.*, "Coherently-combined two channel femtosecond fiber CPA system producing 3 mJ pulse energy," *Opt. Express*, vol. 19, no. 24, p. 24280, Nov. 2011, doi: 10.1364/OE.19.024280.

[55] D. N. Schimpf, E. Seise, and J. Limpert, "The impact of spectral modulations on the contrast of pulses of nonlinear chirped-pulse amplification systems," p. 11, 2008.

Bibliography

[56] T. R. Schibli *et al.*, "Optical frequency comb with submillihertz linewidth and more than 10 W average power," *Nat. Photonics*, vol. 2, no. 6, pp. 355–359, Jun. 2008, doi: 10.1038/nphoton.2008.79.

[57] C. Jauregui, C. Stihler, and J. Limpert, "Transverse mode instability," *Adv. Opt. Photonics*, vol. 12, no. 2, p. 429, Jun. 2020, doi: 10.1364/AOP.385184.

[58] M. E. Fermann, V. I. Kruglov, B. C. Thomsen, J. M. Dudley, and J. D. Harvey, "Self-Similar Propagation and Amplification of Parabolic Pulses in Optical Fibers," *Phys. Rev. Lett.*, vol. 84, no. 26, pp. 6010–6013, Jun. 2000, doi: 10.1103/PhysRevLett.84.6010.

[59] Y. Deng, C.-Y. Chien, B. G. Fidric, and J. D. Kafka, "Generation of sub-50 fs pulses from a high-power Yb-doped fiber amplifier," *Opt. Lett.*, vol. 34, no. 22, pp. 3469–3471, Nov. 2009, doi: 10.1364/OL.34.003469.

[60] J. M. Fini, "Intuitive modeling of bend distortion in large-mode-area fibers," *Opt. Lett.*, vol. 32, no. 12, p. 1632, Jun. 2007, doi: 10.1364/OL.32.001632.

[61] S. Pierrot and F. Salin, "Amplification and compression of temporally shaped picosecond pulses in Yb-doped rod-type fibers," *Opt. Express*, vol. 21, no. 17, p. 20484, Aug. 2013, doi: 10.1364/OE.21.020484.

[62] H.-W. Chen, J. Lim, S.-W. Huang, D. N. Schimpf, F. X. Kärtner, and G. Chang, "Optimization of femtosecond Yb-doped fiber amplifiers for high-quality pulse compression," *Opt. Express*, vol. 20, no. 27, p. 28672, Dec. 2012, doi: 10.1364/OE.20.028672.

[63] P. Sidorenko, W. Fu, and F. Wise, "Nonlinear ultrafast fiber amplifiers beyond the gain-narrowing limit," *Optica*, vol. 6, no. 10, p. 1328, Oct. 2019, doi: 10.1364/OPTICA.6.001328.

[64] Y. Hua, G. Chang, F. X. Kärtner, and D. N. Schimpf, "Pre-chirp managed, core-pumped nonlinear PM fiber amplifier delivering sub-100-fs and high energy (10 nJ) pulses with low noise," *Opt. Express*, vol. 26, no. 5, pp. 6427–6438, 2018.

[65] W. Liu *et al.*, "Pre-chirp managed nonlinear amplification in fibers delivering 100 W, 60 fs pulses," *Opt. Lett.*, vol. 40, no. 2, p. 151, Jan. 2015, doi: 10.1364/OL.40.000151.

[66] O. de Vries *et al.*, "Highly customized 1010 nm, ns-pulsed Yb-doped fiber amplifier as a key tool for on-demand single-photon generation," *Opt. Express*, vol. 28, no. 12, p. 17362, Jun. 2020, doi: 10.1364/OE.394519.

[67] M.-C. Chan, C.-H. Lien, J.-Y. Lu, and B.-H. Lyu, "High power NIR fiber-optic femtosecond Cherenkov radiation and its application on nonlinear light microscopy," *Opt. Express*, vol. 22, no. 8, p. 9498, Apr. 2014, doi: 10.1364/OE.22.009498.

[68] T. Gottschall, T. Meyer, M. Schmitt, J. Popp, J. Limpert, and A. Tünnermann, "Four-wave-mixing-based optical parametric oscillator delivering energetic, tunable, chirped femtosecond pulses for non-linear biomedical applications," *Opt. Express*, vol. 23, no. 18, p. 23968, Sep. 2015, doi: 10.1364/OE.23.023968.

[69] J. Lim, H.-W. Chen, S. Xu, Z. Yang, G. Chang, and F. X. Kärtner, "3 GHz, watt-level femtosecond Raman soliton source," *Opt. Lett.*, vol. 39, no. 7, p. 2060, Apr. 2014, doi: 10.1364/OL.39.002060.

[70] L. Rishøj, B. Tai, P. Kristensen, and S. Ramachandran, "Soliton self-mode conversion: revisiting Raman scattering of ultrashort pulses," *Optica*, vol. 6, no. 3, p. 304, Mar. 2019, doi: 10.1364/OPTICA.6.000304.

[71] W. Liu, C. Li, Z. Zhang, F. X. Kärtner, and G. Chang, "Self-phase modulation enabled, wavelength-tunable ultrafast fiber laser sources: an energy scalable approach," *Opt. Express*, vol. 24, no. 14, p. 15328, Jul. 2016, doi: 10.1364/OE.24.015328.

[72] G. Chang, L.-J. Chen, and F. X. Kärtner, "Highly efficient Cherenkov radiation in photonic crystal fibers for broadband visible wavelength generation," *Opt. Lett.*, vol. 35, no. 14, p. 2361, Jul. 2010, doi: 10.1364/OL.35.002361.

[73] H. Tu, J. Lægsgaard, R. Zhang, S. Tong, Y. Liu, and S. A. Boppart, "Bright broadband coherent fiber sources emitting strongly blue-shifted resonant dispersive wave pulses," *Opt. Express*, vol. 21, no. 20, p. 23188, Oct. 2013, doi: 10.1364/OE.21.023188.

Bibliography

[74] M. Brinkmann, S. Janfrüchte, T. Hellwig, S. Dobner, and C. Fallnich, "Electronically and rapidly tunable fiber-integrable optical parametric oscillator for nonlinear microscopy," *Opt. Lett.*, vol. 41, no. 10, p. 2193, May 2016, doi: 10.1364/OL.41.002193.

[75] T. Gottschall *et al.*, "Fiber-based optical parametric oscillator for high resolution coherent anti-Stokes Raman scattering (CARS) microscopy," *Opt. Express*, vol. 22, no. 18, p. 21921, Sep. 2014, doi: 10.1364/OE.22.021921.

[76] M. Brinkmann, A. Fast, T. Hellwig, I. Pence, C. L. Evans, and C. Fallnich, "Portable all-fiber dual-output widely tunable light source for coherent Raman imaging," *Biomed. Opt. Express*, vol. 10, no. 9, p. 4437, Sep. 2019, doi: 10.1364/BOE.10.004437.

[77] P. Cadroas *et al.*, "All-fiber femtosecond laser providing 9 nJ, 50 MHz pulses at 1650 nm for three-photon microscopy," *J. Opt.*, vol. 19, no. 6, p. 065506, Jun. 2017, doi: 10.1088/2040-8986/aa6f72.

[78] B. Li, M. Wang, K. Charan, M. Li, and C. Xu, "Investigation of the long wavelength limit of soliton self-frequency shift in a silica fiber," *Opt. Express*, vol. 26, no. 15, p. 19637, Jul. 2018, doi: 10.1364/OE.26.019637.

[79] X. Liu, A. S. Svane, J. Lægsgaard, H. Tu, S. A. Boppart, and D. Turchinovich, "Progress in Cherenkov femtosecond fiber lasers," *J. Phys. Appl. Phys.*, vol. 49, no. 2, p. 023001, Jan. 2016, doi: 10.1088/0022-3727/49/2/023001.

[80] L. Rishøj, F. Deng, B. Tai, J.-X. Cheng, and S. Ramachandran, "Jitter-free, dual-wavelength, ultrashort-pulse, energetic fiber sources using soliton self-mode conversion," *Opt. Express*, vol. 28, no. 3, p. 4333, Feb. 2020, doi: 10.1364/OE.384395.

[81] H.-Y. Chung, W. Liu, Q. Cao, L. Song, F. X. Kärtner, and G. Chang, "Megawatt peak power tunable femtosecond source based on self-phase modulation enabled spectral selection," *Opt. Express*, vol. 26, no. 3, p. 3684, Feb. 2018, doi: 10.1364/OE.26.003684.

[82] J. Ye and S. T. Cundiff, *Femtosecond Optical Frequency Comb: Principle, Operation and Applications*. Springer Science & Business Media, 2005.

[83] S. T. Cundiff and J. Ye, "*Colloquium* : Femtosecond optical frequency combs," *Rev. Mod. Phys.*, vol. 75, no. 1, pp. 325–342, Mar. 2003, doi: 10.1103/RevModPhys.75.325.

[84] M. Xin *et al.*, "Attosecond precision multi-kilometer laser-microwave network," *Light Sci. Appl.*, vol. 6, no. 1, pp. e16187–e16187, Jan. 2017, doi: 10.1038/lsa.2016.187.

[85] T. Yasui, S. Yokoyama, H. Inaba, K. Minoshima, T. Nagatsuma, and T. Araki, "Terahertz Frequency Metrology Based on Frequency Comb," *IEEE J. Sel. Top. Quantum Electron.*, vol. 17, no. 1, pp. 191–201, Jan. 2011, doi: 10.1109/JSTQE.2010.2047099.

[86] A. Rolland *et al.*, "Ultra-broadband dual-branch optical frequency comb with 10^{-18} instability," *Optica*, vol. 5, no. 9, p. 1070, Sep. 2018, doi: 10.1364/OPTICA.5.001070.

[87] A. Ruehl, A. Marcinkevicius, M. E. Fermann, and I. Hartl, "80 W, 120 fs Yb-fiber frequency comb," *Opt. Lett.*, vol. 35, no. 18, p. 3015, Sep. 2010, doi: 10.1364/OL.35.003015.

[88] O. Frazão, J. L. Santos, F. M. Araújo, and L. A. Ferreira, "Optical sensing with photonic crystal fibers," *Laser Photonics Rev.*, vol. 2, no. 6, pp. 449–459, 2008, doi: 10.1002/lpor.200810034.

[89] J. Kim *et al.*, "Large-Scale Timing Distribution and RF-Synchronization for FEL Facilities," p. 4, 2004.

[90] U. Keller *et al.*, "Semiconductor saturable absorber mirrors (SESAM's) for femtosecond to nanosecond pulse generation in solid-state lasers," *IEEE J. Sel. Top. Quantum Electron.*, vol. 2, no. 3, pp. 435–453, Sep. 1996, doi: 10.1109/2944.571743.

[91] Z. Sun, T. Hasan, F. Wang, A. G. Rozhin, I. H. White, and A. C. Ferrari, "Ultrafast stretched-pulse fiber laser mode-locked by carbon nanotubes," *Nano Res.*, vol. 3, no. 6, pp. 404–411, Jun. 2010, doi: 10.1007/s12274-010-1045-x.

[92] W. Liu *et al.*, "70-fs mode-locked erbium-doped fiber laser with topological insulator," *Sci. Rep.*, vol. 6, no. 1, p. 19997, Dec. 2016, doi: 10.1038/srep19997.

Bibliography

[93] V. J. Matsas, D. J. Richardson, T. P. Newson, and D. N. Payne, "Characterization of a self-starting, passively mode-locked fiber ring laser that exploits nonlinear polarization evolution," *Opt. Lett.*, vol. 18, no. 5, p. 358, Mar. 1993, doi: 10.1364/OL.18.000358.

[94] K. Stankov, "Mode locking by a frequency-doubling crystal: generation of transform-limited ultrashort light pulses," *Opt. Lett.*, vol. 14, no. 7, p. 359, Apr. 1989, doi: 10.1364/OL.14.000359.

[95] L. M. Zhao, A. C. Bartnik, Q. Q. Tai, and F. W. Wise, "Generation of 8 nJ pulses from a dissipative-soliton fiber laser with a nonlinear optical loop mirror," *Opt. Lett.*, vol. 38, no. 11, p. 1942, Jun. 2013, doi: 10.1364/OL.38.001942.

[96] N. Kuse, J. Jiang, C.-C. Lee, T. R. Schibli, and M. E. Fermann, "All polarization-maintaining Er fiber-based optical frequency combs with nonlinear amplifying loop mirror," *Opt. Express*, vol. 24, no. 3, p. 3095, Feb. 2016, doi: 10.1364/OE.24.003095.

[97] M. E. Fermann, K. Sugden, and I. Bennion, "High-power soliton fiber laser based on pulse width control with chirped fiber Bragg gratings," *Opt. Lett.*, vol. 20, no. 2, p. 172, Jan. 1995, doi: 10.1364/OL.20.000172.

[98] L. F. Mollenauer, R. H. Stolen, and J. P. Gordon, "Experimental Observation of Picosecond Pulse Narrowing and Solitons in Optical Fibers," *Phys. Rev. Lett.*, vol. 45, no. 13, pp. 1095–1098, Sep. 1980, doi: 10.1103/PhysRevLett.45.1095.

[99] M. Brotons-Gisbert *et al.*, "Comprehensive Theoretical and Experimental Study of Short- and Long-Term Stability in a Passively Mode-Locked Solitonic Fiber Laser," *J. Light. Technol.*, vol. 33, no. 19, pp. 4039–4049, Oct. 2015, doi: 10.1109/JLT.2015.2455153.

[100] Y. Chen *et al.*, "Dispersion-managed mode locking," *J. Opt. Soc. Am. B*, vol. 16, no. 11, p. 1999, Nov. 1999, doi: 10.1364/JOSAB.16.001999.

[101] Y. Chen and H. A. Haus, "Dispersion-managed solitons in the net positive dispersion regime," *J. Opt. Soc. Am. B*, vol. 16, no. 1, p. 24, Jan. 1999, doi: 10.1364/JOSAB.16.000024.

[102] C. K. Nielsen *et al.*, "Self-starting self-similar all-polarization maintaining Yb-doped fiber laser," *Opt. Express*, vol. 13, no. 23, p. 9346, 2005, doi: 10.1364/OPEX.13.009346.

[103] B. Nie, D. Pestov, F. W. Wise, and M. Dantus, "Generation of 42-fs and 10-nJ pulses from a fiber laser with self-similar evolution in the gain segment," *Opt. Express*, vol. 19, no. 13, p. 12074, Jun. 2011, doi: 10.1364/OE.19.012074.

[104] B. Oktem, C. Ülgüdür, and F. Ö. Ilday, "Soliton–similariton fibre laser," *Nat. Photonics*, vol. 4, no. 5, pp. 307–311, May 2010, doi: 10.1038/nphoton.2010.33.

[105] P. Grelu and N. Akhmediev, "Dissipative solitons for mode-locked lasers," *Nat. Photonics*, vol. 6, no. 2, pp. 84–92, Feb. 2012, doi: 10.1038/nphoton.2011.345.

[106] W. H. Renninger, A. Chong, and F. W. Wise, "Dissipative solitons in normal-dispersion fiber lasers," *Phys. Rev. A*, vol. 77, no. 2, p. 023814, Feb. 2008, doi: 10.1103/PhysRevA.77.023814.

[107] A. Chong, W. H. Renninger, and F. W. Wise, "Properties of normal-dispersion femtosecond fiber lasers," *J. Opt. Soc. Am. B*, vol. 25, no. 2, p. 140, Feb. 2008, doi: 10.1364/JOSAB.25.000140.

[108] G. Semaan, F. B. Braham, J. Fourmont, M. Salhi, F. Bahloul, and F. Sanchez, "10 µJ dissipative soliton resonance square pulse in a dual amplifier figure-of-eight double-clad Er:Yb mode-locked fiber laser," *Opt. Lett.*, vol. 41, no. 20, p. 4767, Oct. 2016, doi: 10.1364/OL.41.004767.

[109] X. Wu, D. Y. Tang, H. Zhang, and L. M. Zhao, "Dissipative soliton resonance in an all-normaldispersion erbium-doped fiber laser," *Opt. Express*, vol. 17, no. 7, p. 5580, Mar. 2009, doi: 10.1364/OE.17.005580.

[110] X. Liu, "Pulse evolution without wave breaking in a strongly dissipative-dispersive laser system," *Phys. Rev. A*, vol. 81, no. 5, p. 053819, May 2010, doi: 10.1103/PhysRevA.81.053819.

[111] W. Liu *et al.*, "Femtosecond Mamyshev oscillator with 10-MW-level peak power," *Optica*, vol. 6, no. 2, p. 194, Feb. 2019, doi: 10.1364/OPTICA.6.000194.

Bibliography

[112]   K. Regelskis, J. Želudevičius, K. Viskontas, and G. Račiukaitis, "Ytterbium-doped fiber ultrashort pulse generator based on self-phase modulation and alternating spectral filtering," *Opt. Lett.*, vol. 40, no. 22, p. 5255, Nov. 2015, doi: 10.1364/OL.40.005255.

[113]   H. A. Haus and A. Mecozzi, "Noise of mode-locked lasers," *IEEE J. Quantum Electron.*, vol. 29, no. 3, pp. 983–996, Mar. 1993, doi: 10.1109/3.206583.

[114]   S. Namiki and H. A. Haus, "Noise of the stretched pulse fiber laser. I. Theory," *IEEE J. Quantum Electron.*, vol. 33, no. 5, pp. 649–659, May 1997, doi: 10.1109/3.572138.

[115]   C. X. Yu, S. Namiki, and H. A. Haus, "Noise of the stretched pulse fiber laser. II. Experiments," *IEEE J. Quantum Electron.*, vol. 33, no. 5, pp. 660–668, May 1997, doi: 10.1109/3.572139.

[116]   L. Zhao *et al.*, "Route to Larger Pulse Energy in Ultrafast Fiber Lasers," *IEEE J. Sel. Top. Quantum Electron.*, vol. 24, no. 3, pp. 1–9, May 2018, doi: 10.1109/JSTQE.2017.2771739.

[117]   T. North and M. Rochette, "Regenerative self-pulsating sources of large bandwidths," *Opt. Lett.*, vol. 39, no. 1, p. 174, Jan. 2014, doi: 10.1364/OL.39.000174.

[118]   F. X. Kurtner, J. A. der Au, and U. Keller, "Mode-locking with slow and fast saturable absorbers-what's the difference?," *IEEE J. Sel. Top. Quantum Electron.*, vol. 4, no. 2, pp. 159–168, Mar. 1998, doi: 10.1109/2944.686719.

[119]   K. Viskontas, K. Regelskis, and N. Rusteika, "Slow and fast optical degradation of the SESAM for fiber laser mode-locking at 1 μm," *Lith. J. Phys.*, vol. 54, no. 3, Art. no. 3, Oct. 2014, doi: 10.3952/physics.v54i3.2951.

[120]   M. Salhi, H. Leblond, and F. Sanchez, "Theoretical study of the erbium-doped fiber laser passively mode-locked by nonlinear polarization rotation," *Phys. Rev. A*, vol. 67, no. 1, p. 013802, Jan. 2003, doi: 10.1103/PhysRevA.67.013802.

[121]   N. Nishizawa, H. Suga, and M. Yamanaka, "Investigation of dispersion-managed, polarization-maintaining Er-doped figure-nine ultrashort-pulse fiber laser," *Opt. Express*, vol. 27, no. 14, p. 19218, Jul. 2019, doi: 10.1364/OE.27.019218.

[122]   D. Kim, D. Kwon, B. Lee, and J. Kim, "Polarization-maintaining nonlinear-amplifying-loop-mirror mode-locked fiber laser based on a 3 × 3 coupler," *Opt. Lett.*, vol. 44, no. 5, p. 1068, Mar. 2019, doi: 10.1364/OL.44.001068.

[123]   A. S. Mayer *et al.*, "Flexible all-PM NALM Yb:fiber laser design for frequency comb applications: operation regimes and their noise properties," *Opt. Express*, vol. 28, no. 13, p. 18946, Jun. 2020, doi: 10.1364/OE.394543.

[124]   W. Hänsel *et al.*, "All polarization-maintaining fiber laser architecture for robust femtosecond pulse generation," *Appl. Phys. B*, vol. 123, no. 1, p. 41, Jan. 2017, doi: 10.1007/s00340-016-6598-2.

[125]   M. Lezius *et al.*, "Space-borne frequency comb metrology," *Optica*, vol. 3, no. 12, p. 1381, Dec. 2016, doi: 10.1364/OPTICA.3.001381.

[126]   Hong Lin, D. K. Donald, and W. V. Sorin, "Optimizing polarization states in a figure-8 laser using a nonreciprocal phase shifter," *J. Light. Technol.*, vol. 12, no. 7, pp. 1121–1128, Jul. 1994, doi: 10.1109/50.301803.

[127]   W. H. Renninger, A. Chong, and F. W. Wise, "Pulse Shaping and Evolution in Normal-Dispersion Mode-Locked Fiber Lasers," *IEEE J. Sel. Top. Quantum Electron.*, vol. 18, no. 1, pp. 389–398, Jan. 2012, doi: 10.1109/JSTQE.2011.2157462.

[128]   J. Jeon, J. Lee, and J. H. Lee, "Numerical study on the minimum modulation depth of a saturable absorber for stable fiber laser mode locking," *J. Opt. Soc. Am. B*, vol. 32, no. 1, p. 31, Jan. 2015, doi: 10.1364/JOSAB.32.000031.

Bibliography

[129]   D. Kim *et al.*, "Intensity noise suppression in mode-locked fiber lasers by double optical bandpass filtering," *Opt. Lett.*, vol. 42, no. 20, p. 4095, Oct. 2017, doi: 10.1364/OL.42.004095.

[130]   I. L. Budunoğlu, C. Ülgüdür, B. Oktem, and F. Ö. Ilday, "Intensity noise of mode-locked fiber lasers," *Opt. Lett.*, vol. 34, no. 16, p. 2516, Aug. 2009, doi: 10.1364/OL.34.002516.

[131]   P. Qin *et al.*, "Reduction of timing jitter and intensity noise in normal-dispersion passively mode-locked fiber lasers by narrow band-pass filtering," *Opt. Express*, vol. 22, no. 23, p. 28276, Nov. 2014, doi: 10.1364/OE.22.028276.

[132]   Y. Song, C. Kim, K. Jung, H. Kim, and J. Kim, "Timing jitter optimization of mode-locked Yb-fiber lasers toward the attosecond regime," *Opt. Express*, vol. 19, no. 15, p. 14518, Jul. 2011, doi: 10.1364/OE.19.014518.

[133]   C. Xu and F. W. Wise, "Recent advances in fibre lasers for nonlinear microscopy," *Nat. Photonics*, vol. 7, no. 11, pp. 875–882, Nov. 2013, doi: 10.1038/nphoton.2013.284.

[134]   R. Paschotta, "Noise of mode-locked lasers (Part II): timing jitter and other fluctuations," *Appl. Phys. B*, vol. 79, no. 2, pp. 163–173, Jul. 2004, doi: 10.1007/s00340-004-1548-9.

[135]   C. X. Yu, H. A. Haus, and E. P. Ippen, "Soliton squeezing at the gigahertz rate in a Sagnac loop," *Opt. Lett.*, vol. 26, no. 10, p. 669, May 2001, doi: 10.1364/OL.26.000669.

[136]   J. Kim and Y. Song, "Ultralow-noise mode-locked fiber lasers and frequency combs: principles, status, and applications," *Adv. Opt. Photonics*, vol. 8, no. 3, p. 465, Sep. 2016, doi: 10.1364/AOP.8.000465.

[137]   G. Cerullo, M. Nisoli, S. Stagira, and S. De Silvestri, "Sub-8-fs pulses from an ultrabroadband optical parametric amplifier in the visible," *Opt. Lett.*, vol. 23, no. 16, p. 1283, Aug. 1998, doi: 10.1364/OL.23.001283.

[138]   B. G. Bale, S. Boscolo, and S. K. Turitsyn, "Dissipative dispersion-managed solitons in mode-locked lasers," *Opt. Lett.*, vol. 34, no. 21, p. 3286, Nov. 2009, doi: 10.1364/OL.34.003286.

[139]   N. G. Horton *et al.*, "In vivo three-photon microscopy of subcortical structures within an intact mouse brain," *Nat. Photonics*, vol. 7, no. 3, pp. 205–209, Mar. 2013, doi: 10.1038/nphoton.2012.336.

[140]   D. Grassani *et al.*, "Mid infrared gas spectroscopy using efficient fiber laser driven photonic chip-based supercontinuum," *Nat. Commun.*, vol. 10, no. 1, p. 1553, Dec. 2019, doi: 10.1038/s41467-019-09590-3.

[141]   I. Coddington, N. Newbury, and W. Swann, "Dual-comb spectroscopy," *Optica*, vol. 3, no. 4, p. 414, Apr. 2016, doi: 10.1364/OPTICA.3.000414.

[142]   A. Schliesser, N. Picqué, and T. W. Hänsch, "Mid-infrared frequency combs," *Nat. Photonics*, vol. 6, no. 7, pp. 440–449, Jul. 2012, doi: 10.1038/nphoton.2012.142.

[143]   G. Soboń, T. Martynkien, P. Mergo, L. Rutkowski, and A. Foltynowicz, "High-power frequency comb source tunable from 27 to 42 µm based on difference frequency generation pumped by an Yb-doped fiber laser," *Opt. Lett.*, vol. 42, no. 9, p. 1748, May 2017, doi: 10.1364/OL.42.001748.

[144]   J.-X. Cheng and X. S. Xie, *Coherent Raman Scattering Microscopy*. CRC Press, 2016.

[145]   C. Zhang, D. Zhang, and J.-X. Cheng, "Coherent Raman Scattering Microscopy in Biology and Medicine," *Annu. Rev. Biomed. Eng.*, vol. 17, no. 1, pp. 415–445, 2015, doi: 10.1146/annurev-bioeng-071114-040554.

[146]   W. Liu, S.-H. Chia, H.-Y. Chung, R. Greinert, F. X. Kärtner, and G. Chang, "Energetic ultrafast fiber laser sources tunable in 1030–1215 nm for deep tissue multi-photon microscopy," *Opt. Express*, vol. 25, no. 6, p. 6822, Mar. 2017, doi: 10.1364/OE.25.006822.

[147]   L. E. Myers and W. R. Bosenberg, "Periodically poled lithium niobate and quasi-phase-matched optical parametric oscillators," *IEEE J. Quantum Electron.*, vol. 33, no. 10, pp. 1663–1672, Oct. 1997, doi: 10.1109/3.631262.

[148]   D. J. Richardson, J. Nilsson, and W. A. Clarkson, "High power fiber lasers: current status and future perspectives [Invited]," *J. Opt. Soc. Am. B*, vol. 27, no. 11, p. B63, Nov. 2010, doi: 10.1364/JOSAB.27.000B63.

Bibliography

[149]   Y. Zhou, K. K. Y. Cheung, S. Yang, P. C. Chui, and K. K. Y. Wong, "Widely tunable picosecond optical parametric oscillator using highly nonlinear fiber," *Opt. Lett.*, vol. 34, no. 7, p. 989, Apr. 2009, doi: 10.1364/OL.34.000989.

[150]   E. S. Lamb, S. Lefrancois, M. Ji, W. J. Wadsworth, X. Sunney Xie, and F. W. Wise, "Fiber optical parametric oscillator for coherent anti-Stokes Raman scattering microscopy," *Opt. Lett.*, vol. 38, no. 20, p. 4154, Oct. 2013, doi: 10.1364/OL.38.004154.

[151]   J. H. Lee, J. van Howe, C. Xu, and X. Liu, "Soliton Self-Frequency Shift: Experimental Demonstrations and Applications," *IEEE J. Sel. Top. Quantum Electron.*, vol. 14, no. 3, pp. 713–723, May 2008, doi: 10.1109/JSTQE.2008.915526.

[152]   H.-Y. Chung, R. Greinert, F. X. Kärtner, and G. Chang, "Multimodal imaging platform for optical virtual skin biopsy enabled by a fiber-based two-color ultrafast laser source," *Biomed. Opt. Express*, vol. 10, no. 2, p. 514, Feb. 2019, doi: 10.1364/BOE.10.000514.

[153]   G. Zhou, Q. Cao, F. X. Kärtner, and G. Chang, "Energy scalable, offset-free ultrafast mid-infrared source harnessing self-phase-modulation-enabled spectral selection," *Opt. Lett.*, vol. 43, no. 12, p. 2953, Jun. 2018, doi: 10.1364/OL.43.002953.

[154]   Y. Hua, G. Zhou, W. Liu, M. Xin, F. Kaertner, and G. Chang, "Femtosecond two-color source synchronized at 100-as-precision based on SPM-enabled spectral selection," *Opt. Lett.*, May 2020, doi: 10.1364/OL.391161.

[155]   A. Demircan and U. Bandelow, "Analysis of the interplay between soliton fission and modulation instability in supercontinuum generation," *Appl. Phys. B*, vol. 86, no. 1, pp. 31–39, Nov. 2006, doi: 10.1007/s00340-006-2475-8.

[156]   J. P. Gordon, "Theory of the soliton self-frequency shift," *Opt. Lett.*, vol. 11, no. 10, p. 662, Oct. 1986, doi: 10.1364/OL.11.000662.

[157]   D. V. Skryabin, "Soliton Self-Frequency Shift Cancellation in Photonic Crystal Fibers," *Science*, vol. 301, no. 5640, pp. 1705–1708, Sep. 2003, doi: 10.1126/science.1088516.

[158]   G. Zhou, M. Xin, F. X. Kaertner, and G. Chang, "Timing jitter of Raman solitons," *Opt. Lett.*, vol. 40, no. 21, p. 5105, Nov. 2015, doi: 10.1364/OL.40.005105.

[159]   A. M. Heidt, "Efficient Adaptive Step Size Method for the Simulation of Supercontinuum Generation in Optical Fibers," *J. Light. Technol.*, vol. 27, no. 18, pp. 3984–3991, Sep. 2009, doi: 10.1109/JLT.2009.2021538.

[160]   J. C. Knight, T. A. Birks, P. St. J. Russell, and J. P. de Sandro, "Properties of photonic crystal fiber and the effective index model," *J. Opt. Soc. Am. A*, vol. 15, no. 3, p. 748, Mar. 1998, doi: 10.1364/JOSAA.15.000748.

[161]   J. Kim, J. A. Cox, J. Chen, and F. X. Kärtner, "Drift-free femtosecond timing synchronization of remote optical and microwave sources," *Nat. Photonics*, vol. 2, no. 12, pp. 733–736, Dec. 2008, doi: 10.1038/nphoton.2008.225.

[162]   A. J. Benedick, J. G. Fujimoto, and F. X. Kärtner, "Optical flywheels with attosecond jitter," *Nat. Photonics*, vol. 6, no. 2, pp. 97–100, Feb. 2012, doi: 10.1038/nphoton.2011.326.

[163]   M. Xin, K. Şafak, M. Y. Peng, P. T. Callahan, and F. X. Kärtner, "One-femtosecond, long-term stable remote laser synchronization over a 35-km fiber link," *Opt. Express*, vol. 22, no. 12, p. 14904, Jun. 2014, doi: 10.1364/OE.22.014904.

[164]   C. Manzoni *et al.*, "Coherent pulse synthesis: towards sub-cycle optical waveforms," *Laser Photonics Rev.*, vol. 9, no. 2, pp. 129–171, 2015, doi: 10.1002/lpor.201400181.

[165]   J. A. Cox, W. P. Putnam, A. Sell, A. Leitenstorfer, and F. X. Kärtner, "Pulse synthesis in the single-cycle regime from independent mode-locked lasers using attosecond-precision feedback," *Opt. Lett.*, vol. 37, no. 17, p. 3579, Sep. 2012, doi: 10.1364/OL.37.003579.

Bibliography

[166]   Q. Cao, F. X. Kärtner, and G. Chang, "Towards high power longwave mid-IR frequency combs: power scalability of high repetition-rate difference-frequency generation," *Opt. Express*, vol. 28, no. 2, p. 1369, Jan. 2020, doi: 10.1364/OE.28.001369.

[167]   L. E. Zapata, F. Reichert, M. Hemmer, and F. X. Kärtner, "250 W average power, 100 kHz repetition rate cryogenic Yb:YAG amplifier for OPCPA pumping," *Opt. Lett.*, vol. 41, no. 3, p. 492, Feb. 2016, doi: 10.1364/OL.41.000492.

[168]   N. Ter-Gabrielan, V. Fromzel, T. Sanamyan, and M. Dubinskii, "Highly-efficient Q-switched Yb:YLF laser at 995 nm with a second harmonic conversion," *Opt. Mater. Express*, vol. 7, no. 7, p. 2396, Jul. 2017, doi: 10.1364/OME.7.002396.

[169]   J. Limpert *et al.*, "Yb-doped large-pitch fibres: effective single-mode operation based on higher-order mode delocalisation," *Light Sci. Appl.*, vol. 1, no. 4, pp. e8–e8, Apr. 2012, doi: 10.1038/lsa.2012.8.

[170]   C. Ottenhues *et al.*, "Single-mode monolithic fiber laser with 200 W output power at a wavelength of 1018 nm," *Opt. Lett.*, vol. 40, no. 21, p. 4851, Nov. 2015, doi: 10.1364/OL.40.004851.

[171]   X. Qi, S.-P. Chen, H.-Y. Sun, B.-K. Yang, and J. Hou, "1016nm all fiber picosecond MOPA laser with 50W output," *Opt. Express*, vol. 24, no. 15, p. 16874, Jul. 2016, doi: 10.1364/OE.24.016874.

[172]   J. Boullet *et al.*, "High power ytterbium-doped rod-type three-level photonic crystal fiber laser," *Opt. Express*, vol. 16, no. 22, p. 17891, Oct. 2008, doi: 10.1364/OE.16.017891.

[173]   X. Xiao, Y. Hua, B. Fu, and C. Yang, "Experimental investigation of the wavelength tunability in all-normal-dispersion ytterbium-doped mode-locked fiber lasers," *IEEE Photonics J.*, vol. 5, no. 6, pp. 1502807–1502807, 2013.

[174]   D. B. Soh, J. Nilsson, and A. B. Grudinin, "Efficient femtosecond pulse generation using a parabolic amplifier combined with a pulse compressor II Finite gain-bandwidth effect," *J. Opt. Soc. Am. B*, vol. 23, no. 1, p. 10, Jan. 2006, doi: 10.1364/JOSAB.23.000010.

[175]   R. Paschotta, J. Nilsson, A. C. Tropper, and D. C. Hanna, "Ytterbium-doped fiber amplifiers," *IEEE J. Quantum Electron.*, vol. 33, no. 7, pp. 1049–1056, Jul. 1997, doi: 10.1109/3.594865.

[176]   A. Silva, K.-J. Boller, and I. D. Lindsay, "Wavelength-swept Yb-fiber master-oscillator-power-amplifier with 70nm rapid tuning range," *Opt. Express*, vol. 19, no. 11, p. 10511, May 2011, doi: 10.1364/OE.19.010511.

[177]   J. Wang *et al.*, "High-efficiency fiber laser at 1018 nm using Yb-doped phosphosilicate fiber," *Appl. Opt.*, vol. 51, no. 29, p. 7130, Oct. 2012, doi: 10.1364/AO.51.007130.

[178]   F. Beier *et al.*, "1009 nm continuous-wave ytterbium-doped fiber amplifier emitting 146 W," *Opt. Lett.*, vol. 39, no. 13, p. 3725, Jul. 2014, doi: 10.1364/OL.39.003725.

[179]   R. Royon, J. Lhermite, L. Sarger, and E. Cormier, "High power, continuous-wave ytterbium-doped fiber laser tunable from 976 to 1120 nm," *Opt. Express*, vol. 21, no. 11, p. 13818, Jun. 2013, doi: 10.1364/OE.21.013818.

[180]   R. Lindberg, P. Zeil, M. Malmström, F. Laurell, and V. Pasiskevicius, "Accurate modeling of high-repetition rate ultrashort pulse amplification in optical fibers," *Sci. Rep.*, vol. 6, no. 1, p. 34742, Dec. 2016, doi: 10.1038/srep34742.

[181]   C. Headley and G. P. Agrawal, "Unified description of ultrafast stimulated Raman scattering in optical fibers," *J. Opt. Soc. Am. B*, vol. 13, no. 10, p. 2170, Oct. 1996, doi: 10.1364/JOSAB.13.002170.

[182]   H. Tünnermann, J. Neumann, D. Kracht, and P. Weßels, "Gain dynamics and refractive index changes in fiber amplifiers: a frequency domain approach," *Opt. Express*, vol. 20, no. 12, pp. 13539–13550, Jun. 2012, doi: 10.1364/OE.20.013539.

[183]   H. Liu, J. Nees, and G. Mourou, "Diode-pumped Kerr-lens mode-locked Yb:KY(WO_4)_2 laser," *Opt. Lett.*, vol. 26, no. 21, p. 1723, Nov. 2001, doi: 10.1364/OL.26.001723.

Bibliography

[184] B. R. Washburn, J. A. Buck, and S. E. Ralph, "Transform-limited spectral compression due to self-phase modulation in fibers," *Opt. Lett.*, vol. 25, no. 7, p. 445, Apr. 2000, doi: 10.1364/OL.25.000445.

[185] S. Novak and A. Moesle, "Analytic Model for Gain Modulation in EDFAs," *J. Light. Technol.*, vol. 20, no. 6, p. 975, Jun. 2002.

[186] P. Gierschke, C. Jauregui, T. Gottschall, and J. Limpert, "Relative amplitude noise transfer function of an Yb^{3+}-doped fiber amplifier chain," *Opt. Express*, vol. 27, no. 12, pp. 17041–17050, Jun. 2019, doi: 10.1364/OE.27.017041.

[187] F. He, J. H. Price, K. T. Vu, A. Malinowski, J. K. Sahu, and D. J. Richardson, "Optimisation of cascaded Yb fiber amplifier chains using numerical-modelling," *Opt. Express*, vol. 14, no. 26, p. 12846, 2006, doi: 10.1364/OE.14.012846.

[188] S. Koke, C. Grebing, H. Frei, A. Anderson, A. Assion, and G. Steinmeyer, "Direct frequency comb synthesis with arbitrary offset and shot-noise-limited phase noise," *Nat. Photonics*, vol. 4, no. 7, pp. 462–465, Jul. 2010, doi: 10.1038/nphoton.2010.91.

[189] S. Koke, A. Anderson, H. Frei, A. Assion, and G. Steinmeyer, "Noise performance of a feed-forward scheme for carrier-envelope phase stabilization," *Appl. Phys. B*, vol. 104, no. 4, pp. 799–804, Sep. 2011, doi: 10.1007/s00340-011-4654-5.

[190] F. Lücking, A. Assion, A. Apolonski, F. Krausz, and G. Steinmeyer, "Long-term carrier-envelope-phase-stable few-cycle pulses by use of the feed-forward method," *Opt. Lett.*, vol. 37, no. 11, p. 2076, Jun. 2012, doi: 10.1364/OL.37.002076.

[191] B. Borchers, S. Koke, A. Husakou, J. Herrmann, and G. Steinmeyer, "Carrier-envelope phase stabilization with sub-10 as residual timing jitter," *Opt. Lett.*, vol. 36, no. 21, p. 4146, Nov. 2011, doi: 10.1364/OL.36.004146.

[192] C. Grebing, M. Görbe, K. Osvay, and G. Steinmeyer, "Isochronic and isodispersive carrier-envelope phase-shift compensators," *Appl. Phys. B*, vol. 97, no. 3, pp. 575–581, Nov. 2009, doi: 10.1007/s00340-009-3739-x.

[193] R. Ell, J. R. Birge, M. Araghchini, and F. X. Kärtner, "Carrier-envelope phase control by a composite plate," *Opt. Express*, vol. 14, no. 12, pp. 5829–5837, Jun. 2006, doi: 10.1364/OE.14.005829.